

Quantum coherence of ions in a microfabricated trap

PhD Thesis

Scott James Thomas

National Physical Laboratory

EQOP

Department of Physics

University of Strathclyde, Glasgow

11th December 2022

This thesis is the result of the author's original research. It has been composed by the author and has not been previously submitted for examination which has led to the award of a degree.

The copyright of this thesis belongs to the author under the terms of the United Kingdom Copyright Acts as qualified by University of Strathclyde Regulation 3.50. Due acknowledgement must always be made of the use of any material contained in, or derived from, this thesis.

Abstract

This thesis reports on experiments towards improving the quantum coherence of trapped ion qubits, such that coherent control of the qubit can be achieved. This is essential for the applications that ion traps have in the fields of quantum information processing, quantum metrology and for use in atomic clocks.

High RF potentials are applied to traps to give tight confinement and long storage times. Low-noise performance is essential for performing coherent control of the ion qubits with high fidelities. The ability for the trap to operate under these RF potentials can be compromised by the presence of electronic breakdown. Even the faintest amount of breakdown can severely diminish the trapping efficiency. An RF testbed has been developed to characterise the performance of newly fabricated microtraps is presented. Should any breakdown occur during testing it is detected optically. Image processing routines enhance the sensitivity of the measurement such that the onset of surface flashover type breakdown can be detected at amplitudes up to 90 V less than what is possible with unprocessed images. A calibrated pickup measurement allows for the RF voltage amplitude on the trap to be determined without perturbing the resonant circuit that is used to apply the high voltages. These techniques will be used to improve the development of future devices. The principles demonstrated here also have applications beyond ion microtraps to other types of MEMS devices.

One requirement of implementing fault-tolerant quantum information processing is that the Rabi frequency of the laser-ion interaction must have a fractional stability between 10^{-2} and 10^{-4} . Additionally to coherently control the state of a qubit the gate operations must be performed at timescales that are much faster the coherence time of the qubit. To achieve both of these the construction of an optical frequency tuner

for the qubit laser is presented. This subsystem utilises a direct digital synthesis RF source to apply fast detuning operations to the qubit laser over a ± 25 MHz range, whilst simultaneously stabilising the laser power to the extent that its Allan deviation reaches the more stringent level for fault-tolerant quantum gates over the 10 – 700 s time frame, which correspond to the approximate durations of spectroscopy experiments. To ensure that the tuner and downstream subsystems do not add excessive frequency noise onto the laser a beat measurement is made against the laser at the source. All noise and sidebands are observed to be < -36.5 dBc and the linewidth of the beatnote is < 0.21 Hz.

Fluctuations in the magnetic field that the ion is exposed to will induce modulations in the Zeeman shift of the ${}^2S_{1/2}(m_j = -1/2) - {}^2D_{5/2}(m_j = -5/2)$ qubit transition that is used here, which in turn causes decoherence in the qubit. Due to this transition having $\Delta m_j = 2$ the qubit transition will have a higher sensitivity to any fluctuations in the magnetic field, however the geometry of the apparatus results in this Zeeman component giving the highest laser-ion coupling. The apparatus used for the work in this thesis features a magnetic shield and a set of coils for nullifying any remaining field and applying a bias field. The ability of this setup to stabilise the field the ion experiences is investigated. Whilst investigating the stability of the magnetic field the effects of nearby devices on the magnetic field are considered. The shield is shown to attenuate the external field by a factor of $1065\times$, and the magnetic field is stabilised enough that the Allan deviation of the qubit transition frequency is < 10 Hz for 1 s – 7000 s timescales and < 1 Hz for 20 s – 350 s. Investigation into the magnetic field stability also revealed the presence of ground loops from the source of the trap DC potentials and the piezo electric transducers that are used to steer the qubit laser beam pointing.

Finally, spectroscopy experiments on a single ion and two-ion string are demonstrated. The motional frequencies of the single ion and two-ion string are measured and are found to agree with the calculated frequencies. The state initialisation into the $S_{1/2}(m_j = -1/2)$ Zeeman component is measured to be ≥ 99.6 %. A raster scan of the beam pointing is used to ensure that the laser intensity maximum of the laser is incident on the ion. Coherent control of a trapped ion qubit is demonstrated with

the generation of Rabi oscillations and Ramsey fringes. By fitting Bloch equations to the results of these experiments the unknown experiment parameters such as the Rabi frequency and mean vibrational number are able to be determined. The ability to initialise the ion into the motional ground state via sideband cooling is shown. Utilising amplitude shaped pulses to minimise off-resonant excitation has been demonstrated by applying pulses whose amplitude follows a Blackman profile in time. This pulse shape has reduced Fourier components that are far from resonance, which manifests as the suppression of spectral side-lobes. The data fitting routines used iterate on previous work to reduce the computational overhead and improve computation times. The experimental procedures to perform and optimise the Mølmer-Sørensen entanglement gate are presented, as is discussion on how the results of these experiments should be interpreted. However, demonstration of this routine remains the next step in the experiment's investigation.

Acknowledgements

I would like to give an immense thank you to Alastair Sinclair for his insight, guidance and encouragement over the course of this project. I have been incredibly fortunate to have been given the opportunity to conduct my postgraduate research under his supervision. In the same vein, I would like to thank Guido Wilpers for sharing his expertise and knowledge on a wide variety of Physics topics over the course of my studies, and for being so willing to share it. I would also like to thank Erling Riis, my supervisor at the University of Strathclyde, for his help and support on a host of academic and non-academic issues that I have faced. Additionally, I would like to thank Stefan Kuhr, also at Strathclyde, for initially recommending me to Professor Riis, and starting me on this journey.

Over the course of my time at the NPL I have been able to benefit from working alongside a number of skilled and dedicated scientists working on different aspects of the ion microtrap and other projects. For the first year and a half of my studies I was able to work with Kaushal Choonee on the fabrication of the microtrap devices, to whom I am thankful for his advice and assistance. I am incredibly grateful to David Szwer for all the LabVIEW and Matlab advice that he dispensed. It would have been impossible to do many of the coding tasks that this thesis features without it. It was a great pleasure to work with my predecessor, Mariam Akhtar, on the experiment. Mariam's encouragement and enthusiasm (and running of the NPL Cake Club) was a great support during my time there. I would also like to thank Micheal Larsson and Nathanaël Builler, for the support and guidance that they offered on my work. Outside of the microtrap project I would like to thank Robert Starkwood and Philip Dolan, both of whom helped to enhance my enjoyment of my time at the NPL.

Beyond the NPL, I would like to thank my friends: Darren Bell, Andrew Blair, Greg Coburn, Scott Cunningham, Aaron Delarue, Aaron Donald, Kyle Hancock, David McHale, Gina and Nicol Riggio, Connor Seaton-Mooney, Chris Shorts, Scott Stevenson and Gordon Weir. I am immeasurably grateful for the many years, in some cases over a decade, of rapport and camaraderie that we have shared.

Finally, I would like to thank all my family and especially my parents, Karen and James Thomas, for their unending support and encouragement throughout my studies.

Contents

List of Figures	x
List of Tables	xiii
List of Abbreviations	xiv
Optical Circuit Symbols Key	xvi
1 Introduction	2
1.1 Quantum Information Processing	4
1.2 Ion Traps for Quantum Metrology	8
1.3 Ion Trap Architecture and Qubit Implementation	9
2 Background Theory	11
2.1 Ion Trapping	11
2.1.1 Motion of the Ion in an RF Trap	11
2.1.2 Micromotion	17
2.2 Transitions and Energy Levels in $^{88}\text{Sr}^+$	18
2.3 Zeeman Effect	20
2.4 Laser Cooling Techniques	23
2.4.1 Doppler Cooling	23
2.4.2 Optical Qubit Transition	23
2.4.3 Sideband Cooling	26
2.5 Trapped Ion Qubits	27
2.6 Dechorence	31

Contents

2.6.1	Motional Dechorence	31
2.6.2	Electronic State Dechorence	32
2.6.3	Dechorence from the Qubit Laser	33
2.7	Entanglement	34
3	Background of Apparatus	37
3.1	Microtrap	37
3.2	Vacuum System	38
3.3	Magnetic Shielding	40
3.4	Trap Voltage Sources	41
3.5	405 nm & 461 nm Laser	42
3.6	422 nm Laser	43
3.7	674 nm Laser	44
3.8	1033 nm Laser	47
3.9	1092 nm Laser	50
3.10	Imaging Systems	51
3.11	Control Systems	52
3.12	Procedures and Results of Standard Operation	53
3.12.1	Loading Ions into the Trap	53
3.12.2	Micromotion Minimisation	54
3.12.3	Doppler Cooling Scans	55
3.12.4	Optical Pumping	57
3.12.5	Minimising the Magnetic field	57
3.12.6	Spectroscopy Sequencing	58
3.12.7	Ion Trapping Lifetimes	58
4	RF Characterisation of Microtrap Chips	62
4.1	Introduction	62
4.2	Apparatus	64
4.2.1	Radiofrequency System	64
4.2.2	Optical System	66

Contents

4.3	Testing Routine	69
4.4	Determining the Resonant Frequency	70
4.5	Voltage Calibration	70
4.6	Image Processing	73
4.7	Testbed Results	78
4.8	Summary	82
5	Optical Frequency Tuner for the 674 nm Qubit Laser	85
5.1	Introduction	85
5.2	Tuner Apparatus	86
5.3	Power Stabilisation Performance	89
5.4	Transfer of Frequency Stability	94
5.5	Summary	95
6	Magnetic Field Stabilisation	100
6.1	Introduction	100
6.2	Evaluation of the Magnetic Field Stability	101
6.3	Effect of the Hotplate on the Magnetic Field	107
6.4	Observed Ground Loops	112
6.5	Summary	112
7	Ion Spectroscopy	116
7.1	Introduction	116
7.2	Data Fitting	117
7.3	Beam Position Optimisation	120
7.4	Motional Spectra	123
7.5	Rabi Flopping	128
7.6	Ramsey Spectroscopy	131
7.7	State Initialisation	135
7.8	Spectroscopy with Amplitude-Shaped Pulses	137
7.9	Towards Entanglement	139
7.10	Summary	144

Contents

8 Conclusion	145
8.1 Summary	145
8.2 Conclusion	150
8.3 Future Work	151
Bibliography	152

List of Figures

2.1	Diagram showing the basic electrode structure of a linear Paul Trap . . .	12
2.2	Stability region of the Mathieu Equation	15
2.3	Diagram of the relevant optical transitions in ^{88}Sr and $^{88}\text{Sr}^+$	19
2.4	Diagram of the Zeeman components of the 674 nm Transition	22
2.5	Example Bloch vector rotations around the Bloch sphere	28
2.6	Mølmer-Sørensen Gate operation	36
3.1	Structure of the NPL microtrap	39
3.2	Ultra High Vacuum chamber assembly and optical access	40
3.3	Optical circuit for the 405 nm and 421 nm lasers	42
3.4	Optical circuit for the 422 nm laser	45
3.5	Optical circuit for the 674 nm laser source.	48
3.6	Optical circuit for the tuner and pulse control setup	49
3.7	Optical circuit for the 1033 nm laser	50
3.8	Optical circuit for the 1092 nm laser	51
3.9	Scans of the 422 nm laser frequency	56
3.10	Example control sequence used to perform spectroscopy with the 674 nm laser	59
4.1	Circuit diagram of the RF electronics used in the RF testbed	67
4.2	Angles of observation for the RF testbed cameras	69
4.3	Example of a frequency scan performed with the RF testbed	71
4.4	Flowcharts describing the breakdown detection algorithms	75

List of Figures

4.5	Images of breakdown produced by the RF testbed	81
5.1	Tuner apparatus with side view of AOM	87
5.2	Tuner output efficiency vs optical detuning with and without stabilisation	92
5.3	Tuner response time to a step change in the laser detuning	93
5.4	Allan deviations of the tuner output power operating at a fixed frequency	94
5.5	Beat of the pulse control setup output against an FNCS system that comes from the laser source output	96
5.6	Beat note linewidth obtained by fits	97
6.1	Power spectrum of the magnetic field inside and outside of the mu-metal shield	102
6.2	Allan deviations of the in loop magnetic field coil measurements from the high precision multimeters	105
6.3	Allan deviations of the out-of-loop magnetic field measurements inside the shield	106
6.4	Data used to calculate the out-of-loop Allan deviation of the magnetic field and the corresponding thermistor measurements	108
6.5	Effect of running the ion loading hotplate on the magnetic field	109
6.6	Out-of-loop magnetic field measurements after the hotplate is turned off.	110
6.7	Thermistor recordings after hotplate operation	111
6.8	Shift in the observed magnetic field caused by changing the DC voltages applied to the trap and changing the 674 nm pointing piezos	113
7.1	Raster scan of the beam pointing with one and two ions	122
7.2	Single ion carrier transition in a nullified B-field	124
7.3	Single ion motional spectrum with the bias field applied	126
7.4	Two ion motional spectrum with the bias field applied	127
7.5	Example of Rabi oscillations from applying a single pulse of increasing duration on the carrier.	131
7.6	Ramsey fringe pattern obtained by scanning the laser frequency over the qubit carrier transition.	133

List of Figures

7.7	Excitation probability at the centre of the qubit carrier transition as the phase shift between two Ramsey pulses is varied	134
7.8	Red and blue \hat{z} -motional sidebands of a single ion after sideband cooling is applied	136
7.9	Scan of the sideband cooling pulse detuning to characterise the quencher AC-Stark shift	137
7.10	Comparison of amplitude shaped pulses against square shaped pulses. .	139
7.11	Simulated outcome of the Mølmer-Sørensen gate with the obtained experimental parameters	142

List of Tables


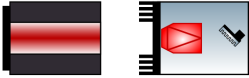







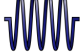
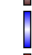
























2.1	Wavelengths, and radiative linewidths and excited state lifetimes of the transitions used in this experiment. The two photoionisation transitions at the top of the table are for an un-ionised ^{88}Sr atom and the remaining transitions are for the $^{88}\text{Sr}^+$ ion.	20
3.1	Names, functions and number of National Instruments cards used to control the apparatus	53
6.1	Magnetic field coil operating currents	101
6.2	Voltage to magnetic field conversion factors for the high precision multimeter readings for each coil and the out-of-loop Bartington sensor . . .	102
6.3	List of devices that were tested for influence on the magnetic field inside the magnetic shield	104
7.1	Calculated and measured secular frequencies for one and two ions	129

List of Abbreviations

AOM	- Acousto-Optical Modulator
CW	- Continuous Wave
NPL	- National Physical Laboratory
QIP	- Quantum Information Processing
RF	- Radio-Frequency
ECDL	- Extended-Cavity Diode Laser
PMT	- PhotoMultiplier Tube
FNCS	- Fibre Noise Cancellation System
CCD	- Charge-Coupled Device
EMCCD	- Electron Multiplying CCD
VCO	- Voltage Controlled Oscillator
HV	- High Vacuum
UHV	- Ultra High Vacuum
PCB	- Printed Circuit Board
TTL	- Truth Table Logic
EFG	- Electric Field Generator
NI	- National Instruments
DDS	- Direct Digital Synthesis
AC	- Alternating Current
DC	- Direct Current
APD	- Avalanche PhotoDiode
MLE	- Maximum Likelihood Estimation

Optical Circuit Symbols Key

Drawings of optical circuits in this thesis were made using Inkscape, including components based on the ComponentLibrary developed by Alexander Franzen [1]. The key below shows the meaning of the symbols used in this thesis.

	Mirror		Laser Source
	Mirror with piezo		Laser Diode
	Mirror offset into page		Laser beam
	Dichroic mirror		Fibre splitter
	Diffraction grating with piezo		Optical fibre
	High-pass filter		Fibre Coupler
	Low-pass filter		Fibre polarisation controller
	$\lambda/2$ wave plate		CCD Camera
	$\lambda/4$ wave plate		Photodetector
	Optical isolator		
	Polarising beamsplitter cube		
	Wollaston PBS cube		
	Beamsplitter plate		
	Retroreflector		Coaxial cable / electrical wire
	Glass wedge		RF Synthesiser
	EOM		RF Low-pass filter
	AOM		RF high-pass filter
	Mechanical shutter		RF mixer
	Beam dump		RF switch
			RF power combiner

Chapter 1

Introduction

In quantum mechanics two states that would be discrete classically can be superpositioned onto each other so that the system exists in both states simultaneously, such as in the famous Schrödinger's cat thought experiment where the cat could be alive or dead with its fate determined by whether a radioactive atom had decayed or not. Furthermore in cases where multiple particles are present it is possible to entangle them together so that they are dependent on each other. Experimental realisations of quantum physics are however difficult to achieve in practice as the quantum system can easily interact with the external environment. This causes the fragile quantum states to couple to external sources of noise that destroys the coherence of the quantum states contained within thus ruining the experiment.

Cooled ions trapped within a linear radio-frequency (RF) trap, a device originally created by Wolfgang Paul for mass spectrometry [2], present themselves as an ideal system for use in experimental quantum physics. The main reasons for this are that within the trap each ion is tightly confined by the trapping potential whilst simultaneously being well isolated from its external environment which minimises the coupling of any deleterious, external noise sources to the fragile quantum states stored in each ion's electronic and motional states. This environmental isolation allows for the quantum states to be robustly stored with long coherence times and for precise and rapid manipulation of these quantum states using external radiation from a resonant laser or microwave source. The quantum information stored within these states can be trans-

Chapter 1. Introduction

ferred amongst multiple ions through their collective motion where the motion of each ion is strongly coupled to that of other ions through the mutual Coulombic repulsion the ions exert on each other. The numerous research groups around the world who study and develop ion traps for a wide range of different experiments, including Quantum Information Processing (QIP) and precision metrology, is testament to how robust and versatile this system is. This is further acknowledged by half of the 1989 Nobel Prize in Physics being jointly awarded to Hans G. Dehmelt and Wolfgang Paul for “for the development of the ion trap technique.” and again in 2012 where half of the that year’s prize was awarded to David J. Wineland “for ground-breaking experimental methods that enable measuring and manipulation of individual quantum systems” which he achieved using trapped ions.

This thesis is organised as follows:

The remainder of this chapter will review the historic and ongoing status of ion trap research; focusing on QIP and quantum metrology. A short summary of ion trap setups in use by other groups is also presented.

Chapter 2 will examine the relevant background theory and concepts for the work undertaken in this thesis.

Chapter 3 will summarise the main experimental setup used for most of the work in this thesis.

Chapter 4 will examine the issue of high voltage breakdown of the microfabricated ion traps and describes a setup that is utilised to characterise the high RF voltage tolerance of these devices.

Chapter 5 describes a tuner element that is included into the qubit laser. This element simultaneously performs fast frequency shifting operations whilst stabilising the optical power of the laser.

Chapter 6 discusses the magnetic field noise that the ion is exposed to and the work that was done to characterise it.

Chapter 7 covers the spectroscopy routines and the results that are generated. Also discussed here are improvements to the data fitting routines that have been made.

1.1 Quantum Information Processing

In 1982 Richard Feynman [3] wrote an article which explained that it would rapidly become too difficult, if not impossible, to model an extensive quantum system on a classical computer. Instead a computer based upon quantum mechanics, where information is stored in a two-state $\{|g\rangle, |e\rangle\}$ quantum system, would be able to exploit the same properties that a classical computer would struggle to process, to effectively simulate a different quantum system. Despite this prediction there was little interest in creating a quantum computer until 1994 when Peter Shor developed his factorisation algorithm [4] which required a quantum computer to perform. Since then other QIP algorithms that would require a quantum computer have emerged, such as Grover's search algorithm [5] and the Deutsch-Jozsa algorithm [6] that determines whether an unknown binary function is constant or balanced (i.e. whether the function always return the same answer, a 0 or a 1, for any input combination or a 0 for half the input domain and a 1 for the other half respectively). In 1996 David DiVincenzo [7] defined a set of stringent requirements that would need to be fulfilled in order to create a functioning quantum computer:

- 1) *A scalable system with well defined qubits.*

Scalable means that the number of basic computational units can be increased with minimal losses in performance and with little increase in the cost, energy consumption and physical size of the quantum computer [8]. In the context of trapped ions this refers to the trap architecture and the method that qubits are encoded in the ions. This topic is looked in more detail in chapter 1.3

- 2) *The ability to initialise the register to a simple fiducial state.*

For the ion qubits used here this involves Doppler and sideband cooling to the motional ground state and optical pumping to the desired electronic level. The theory behind these are covered in chapter 2.4.1 and 2.4.3, and the implementation in chapters 3.12.3, 3.12.4, 3.12.6, 7.4 and 7.7.

- 3) *Long relevant decoherence times, much longer than the gate operation time.*

The coherence time of a qubit refers to the length of time over which the information

described by the state is preserved; specifically it is the time in which the probability of retaining the value of the state has decayed by $1/e$ [9]. Ion qubits based on hyperfine or Zeeman sub-levels can have long qubit lifetimes as these are stored in the electronic ground state of the ion and are not subject to spontaneous decay. An example of each being coherence times greater than 10 minutes have been achieved for a single qubit based on the hyperfine sub-levels of Yb^+ [10] and a $^{40}\text{Ca}^+$ Zeeman qubit achieving a coherence time of 2.1 s [11]. In contrast to these, qubits encoded in an optical metastable excited state have decoherence times in the hundreds of milliseconds [12]. The fundamental limitation for the decoherence time for trapped ion QIP is that the states used for encoding the qubit have a natural lifetime, with optical qubits generally having the shortest lifetimes. For the quadrupole transition of $^{88}\text{Sr}^+$, the ion species used for the work done in this thesis, this lifetime is 390 ms [13]. In practice, the decoherence time for the qubit will be less than this due to the qubit coupling to noise in the environment. Ideally these lifetimes should be chosen to be as long as possible to maximise the number of operations that can be performed before the qubit is lost to decoherence. Typically gate operations for trapped ion qubits are of the order of ten to a few hundred microseconds [14–16] in duration although recently qubit gates that require hundreds of nanoseconds have been demonstrated [17]. These gate times are at worst three orders of magnitude lower than the qubit lifetimes; such that the coherence times far exceed the time required to execute simple QIP algorithms that consist of several qubit gates concatenated together [18].

4) *A universal set of quantum gates*

If any single arbitrary operation can be broken down into a specific set of operations this set can be called “universal” and any more complex operations could be achieved by performing these universal gates a different number of times, on different inputs in different orders. In classical Boolean logic the NAND gate is the “universal” logic gate as any Boolean logic operation on any number of inputs can be composed of a sequence of NAND gates. In QIP the “universal” quantum gates are single qubit operations and the two qubit controlled-NOT (C-NOT) gate, the QIP equivalent of the classical XOR gate [18–20].

5) *The ability to measure the state of a specific qubit*

State readout for ion based qubits is carried out using Dehmelt's electron shelving technique [21, 22]. In this technique the ion's state is determined by rapidly cycling photons on a secondary transition that is only resonant when the ion is in the ground state. Typically this is performed on the Doppler cooling transition due to the short lived excited state that this cooling technique utilises. After just a few microseconds of photons being cycled the state of the ion can be determined with near 100 % accuracy [23]. This method has been able to perform single qubit state detection with error rates of 5×10^{-4} for hyperfine qubits [24] and 1.8×10^{-4} for optical qubits [25]. In the cases where multiple ions are trapped in a linear string, the state of each ion in the string can be imaged by illuminating all ions in the string and imaging their fluorescence with a CCD camera [26] or by moving the laser focus across the string [16].

In 1995, Cirac and Zoller [27] were the first to propose that ions stored within a linear RF trap would serve as an ideal system to make a quantum computer. In their description of the ion trap quantum computer the internal states of the ions are used as the qubits, the state of the whole quantum computer is the superposition state of all the confined ions and each qubit would be manipulated by addressing its corresponding ion with a laser. C-NOT gates, which are used to implement the quantum computer algorithms, would be applied by exciting the collective motion of the ion string in the linear trap, in which the ions' motion is coupled together through their mutual Coulombic repulsion. Kielpinski et al expanded on this outlining what an ion trap quantum computer would look like in practice [28]. A more recent proposal [29] is to use a vast 2-dimensional array of microfabricated X-shaped ion traps, where each trap is a single cell in the array, in conjunction with globally and locally applied magnetic and RF fields. In this design each cell contains a small number of ions that are used for qubit operations with a second ion species being used for sympathetic cooling of the primary ions. Here the single and multi-ion gate operations are performed using these fields with only simple lasers being required for the remaining operations; these being state detection and preparation, photionisation and sympathetic cooling.

Trapped ions present one of the more promising systems on which to implement

QIP. This is due to trapped ion qubits having coherence times that are much longer than the time it takes to perform each gate operation [30,31] when compared against similar systems [32,33], an accurate and easy to perform method of measuring the state of the qubit [22]. As a result numerous qubit operations can be performed consecutively before the qubit decoheres. It should also be noted that whilst fast qubit gate operations are desirable, the actual increase in processing power from QIP, when compared against classical computers, arises from the exponential scaling from entangling qubits and the ability to put the qubit into a superposition state. In addition to this, QIP systems can also be used to solve certain computational problems, which are impossible to do with a classical computer at practical timescales [18,34]. Qubit operations just have to be fast relative to the coherence time of the qubit; although generally there is a trade off between increasing the speed that qubit operations are performed at and fidelity of those operations [35].

Although trapped ions remain one of the most promising methods of implementing quantum information processing, other methods are also being investigated, with some examples being;

- 1) QIP methods similar to those with trapped ions have been implemented on trapped neutral atoms [36],

- 2) Solid state systems based upon Josephson junctions such as SQUIDS [37] and Transmons [38–40] and other solid state systems involving quantum dots [41,42],

- 3) Systems of entangled photons [43–45],

- 4) Adiabatic methods previously mentioned [46] where the qubits of the system are evolved from the ground state of a simple Hamiltonian to the ground state of the desired Hamiltonian via the adiabatic theorem [47,48]

- 5) Measurement-based quantum computation [49,50] methods where the qubit value is teleported through ancillary qubits in a matrix of entangled qubits. With this type of QIP the computational algorithm is performed by sequentially measuring ancillary the qubits with the answer to the algorithm stored in the final set of qubits that are measured.

1.2 Ion Traps for Quantum Metrology

Beyond QIP ion traps have numerous metrological uses some of which are detailed here.

Due to atomic transitions being highly repeatable they make ideal reference standards for atomic clocks. Currently the SI definition of the second is defined by the 9.2 GHz hyperfine transition in ^{133}Cs . In the future the second could be defined by an optical frequency transition of a trapped ion [51] or a trapped ion that is referenced to a separate trapped atom or atoms [52, 53]. The principle behind this being that optical transitions have higher Q factor ($\sim 10^5$) than those in the microwave frequency region and thus have a lower inherent instability, which would allow for relative uncertainties down to the 10^{-18} level to be reached [54–57]. To achieve this level of uncertainty particular interest has been given to the utilisation of forbidden quadrupole transitions of trapped ions that have electron configurations similar to those of alkali metals; these, depending on the species, have linewidths of single-digit hertz or lower [58–60]. Work has also been done examining the extremely narrow octupole transition in $^{171}\text{Yb}^+$, which possesses a 1 nHz natural linewidth, as a potential standard [61–63]. Applications for this include most uses that are covered by atomic clocks such as GPS navigation [64, 65], characterising other less precise clocks [66] and the use as a reference clock for the Network Time Protocol [67].

Beyond their possible use in frequency standards ion traps have a wide range of other potential uses, one of which is the original purpose that Wolfgang Paul originally created his RF trap for [2], namely, use in mass spectrometers. Some of the recent developments in ion trap mass spectrometry are covered in the review by Snyder et al [68]. Other potential metrological applications for ion traps that have been proposed or investigated include: use as highly sensitive force sensors [69], rotation sensing [70], magnetometry [71], measurement of the branching ratios of dipole transitions [72] and as a quantum lock-in amplifier [73].

1.3 Ion Trap Architecture and Qubit Implementation

In the 1990s when interest in trapped ion QIP started, the first proof-of-principle trap designs were mostly millimetre scale custom made traps [74–76] that were only capable of utilising ~ 10 ions. To create scalable traps that could contain more ions, enable mass production and improve the qualitative consistency of the traps, a considerable amount of effort has been invested to miniaturise these designs. Generally two different types of linear trap architectures have been used.

The first of these are two-dimensional architectures where the electrodes of the ideal linear Paul trap are arranged into a single plane and the ions are suspended above the ion trap. The advantage of this type of design is that the manufacturing process is relatively easy compared to three-dimensional traps described below, which in turn allows for more complex designs to be created such as traps with X shaped [77, 78] and Y shaped [79] junctions with additional features and modifications being easy to implement [80]. Some of these designs are intended to be used as “cells” in an array that link together via shuttling junctions that together function as a quantum information processor [28, 29]. In these proposals different cells or parts of each cell are used for different functions such as memory, state readout, etc. However, a significant flaw in two-dimensional trap architectures is that the harmonicity of the trapping field is significantly reduced, compared to the ideal case, as the trapping field is only supplied from one direction, yielding lower trapping efficiencies [81]. Some examples of this architecture are the trap designs used by NIST [82] and the research group at Georgia Tech [83].

The other main type of architecture used are of a bulk three-dimensional form, that more closely resembles the ideal linear Paul trap. Traps made in this architecture are usually millimetre scale or larger due to the difficulty of manufacturing the required three dimensional structure at microscale levels. The ion traps used for the work done in this thesis are of this type of architecture, implemented at microscale, the full description and properties of which are detailed in chapter 3.1. Other research groups at Oxford [84] and Innsbruck [85] have recently used traps based on the three-dimensional

architecture.

Reviews of different manufacturing techniques and modifications have been performed which detail the current architectures used by different research groups [86,87]. Additionally a review by Eltony et al [88] examines several added features and modifications to trap architectures that have been attempted.

In addition to the scaling of the ion traps themselves, there is also a need to scale the optical systems to address each trapping zone. Promising developments with waveguides and microscale lenses [89–92] could be implemented to overcome this.

The actual implementation of trapped ion qubits have been realised in three separate ways:

1) Qubits are encoded between two hyperfine energy levels in the ground state. These qubits require the ion to have an odd nuclear spin and are controlled and manipulated by either microwaves or Raman fields. The Maryland group has encoded their qubits using $^{171}\text{Yb}^+$ [93,94], the NIST group uses $^9\text{Be}^+$ [95] and the group at Oxford has also encoded their qubits this way using $^{43}\text{Ca}^+$ [96,97],

2) Qubits encoded in two Zeeman sub-levels of the electronic ground state such as the way in which the Oxford and Mainz groups uses $^{40}\text{Ca}^+$ [11,96],

3) Qubits encoded in the optical transition of a ground state and a metastable excited state. The group at MIT encode their qubits [98,99] in this way. The Weizmann Institute previously encoded their qubits in Zeeman sub-levels [100] but now use optical this type of qubit [101].

Chapter 2

Background Theory

2.1 Ion Trapping

2.1.1 Motion of the Ion in an RF Trap

Fundamentally a charged particle cannot be trapped by purely static electric fields [81]. The linear Paul trap used for the work done in this thesis dynamically traps ions by applying an RF potential that is oscillating at a frequency, Ω_{RF} , and a maximum amplitude, U_{RF} , to a pair of diagonally opposite electrodes combined with DC potentials, V_{DC} , from a set of four endcap electrodes. Figure 2.1 summarises the layout of this configuration with greater detail on the trap architecture described in section 3.1. The potential that an ion confined in this trap experiences is:

$$\Phi(x, y, z, t) = \frac{V_{\text{DC}}}{2}(\alpha_x x^2 + \alpha_y y^2 + \alpha_z z^2) + \frac{U_{\text{RF}} \cos(\Omega_{\text{RF}} t)}{2}(\beta_x x^2 + \beta_y y^2 + \beta_z z^2) \quad (2.1)$$

where α_i and β_i are geometric factors that are defined by the trap architecture. From this the equations of motion for the ion in the trap can be obtained [81]. Along one axis this is:

$$\frac{d^2 u_i}{dt^2} = -\frac{Q_e}{m} \frac{\partial \Phi}{\partial u_i} = -\frac{Q_e}{m} [V_{\text{DC}} \alpha_i + U_{\text{RF}} \cos(\Omega_{\text{RF}} t) \beta_i] u_i \quad (2.2)$$

where u is the ion's displacement along the $i \in \{x, y, z\}$ axis, Q_e and m are the charge and mass of the ion respectively, $\alpha_i = (\epsilon_i \kappa) / r_{\text{DC}}^2$ and $\beta_i = \eta_{\text{trap}} / r_{\text{RF}}^2$, with η_{trap} and κ being factors that consider effects of the trap geometry on the trapping

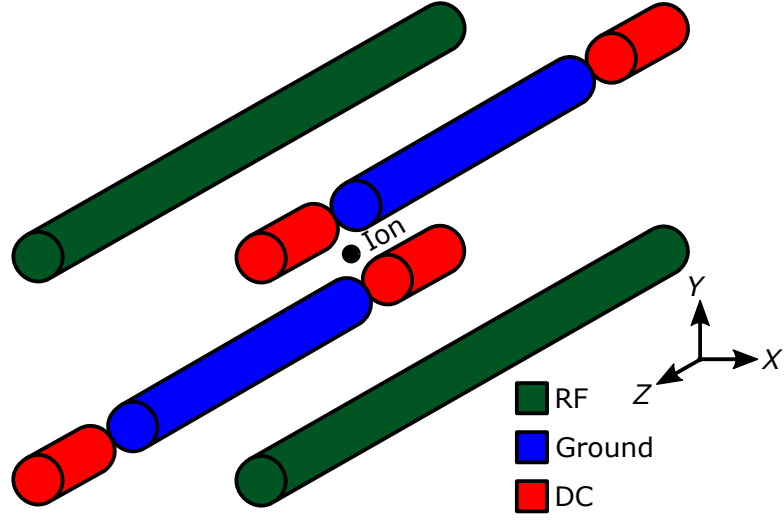


Figure 2.1: Example electrode structure of a linear Paul trap.

efficiency [102, 103]. Here r_{RF} and r_{DC} are the distances from the ion to the RF and endcap electrodes respectively.

Using the substitutions on each axis

$$a_i = \frac{8Q_e V_{\text{DC}} \kappa}{m r_{\text{DC}}^2 \Omega_{\text{RF}}^2} \quad (2.3a)$$

$$q_i = \frac{2Q_e U_{\text{RF}} \eta_{\text{trap}}}{m r_{\text{RF}}^2 \Omega_{\text{RF}}^2} \quad (2.3b)$$

the equations of motion become a form of the Mathieu equation [23, 81, 104]:

$$\frac{d^2 u_i}{dt^2} + [a_i - 2q_i \cos(\Omega_{\text{RF}} t)] \frac{\Omega_{\text{RF}}^2}{4} u_i = 0 \quad (2.4)$$

where the dimensionless terms a_i and q_i are now the stability parameters of the Mathieu equation.

A solution to the Mathieu equation can be found using Floquet's theorem [81, 105]:

$$u_i(t) = A_i \sum_{n=-\infty}^{\infty} C_{2n,i} \cos\left((2n + \beta_i) \frac{\Omega_{\text{RF}}}{2} t\right) + B_i \sum_{n=-\infty}^{\infty} C_{2n,i} \sin\left((2n + \beta_i) \frac{\Omega_{\text{RF}}}{2} t\right) \quad (2.5)$$

where A_i and B_i are constants that satisfy boundary conditions, the coefficients C_{2n} represent a recursion relation that describe the amplitude of the ion's motion and here

Chapter 2. Background Theory

β_i is the characteristic exponent that dictates the frequency of the ion's motion. n here are integer values corresponding to higher orders of the ion's motion induced by the RF field. Both $C_{2n,i}$ and β_i are functions of a_i and q_i only.

For the Mathieu equation there is a range of a_i and q_i values for which the motion of the ion is stable. This area of the parameter space corresponds to solutions where β_i from equation 2.5 has non-integer values. For parameter values that result in β_i being an integer the motion of the ion is periodic but unstable. This limits the allowed values of a_i and q_i to an area of the parameter space enclosed by “characteristic curves” that serve as the boundaries between the stable and unstable regions of the parameter space [106, 107].

For the electrode configuration shown in figure 2.1 the q_i parameters are

$$q_x = q_y = \frac{2Q_e\eta_{trap}U_{RF}}{m\Omega_{RF}^2r_{RF}^2}, \quad q_z = 0, \quad (2.6)$$

and the a_i parameters are

$$a_x = -\epsilon a_z, \quad a_y = -(1 - \epsilon)a_z, \quad a_z = \frac{8Q_e\kappa V_{DC}}{m\Omega_{RF}^2r_{DC}^2} \quad (2.7)$$

where ϵ is an anisotropic effect that arises from the endcaps being off diagonal relative to the $\hat{x}\hat{y}$ plane that the RF is applied on [102].

The C_{2n} terms outside of $n = 0, \pm 1$ provide only small contributions to the ion motion when the stability parameters are within the limit of $(|a_i|, q_i^2) \ll 1$ [108]. This allows for the lowest-order approximation [23, 81] ($C_{\pm 4} \simeq 0$) to be made. This removes higher order terms of the ion's motion and combined with the boundary condition of $A_i = B_i$, provides a solution of the form:

$$u_i(t) \approx 2A_i C_{0,i} \cos\left(\beta_i \frac{\Omega_{RF}}{2} t\right) \left[1 - \frac{q_i}{2} \cos(\Omega_{RF} t)\right] \quad (2.8)$$

In this case $\beta_i = \sqrt{a_i + q_i^2/2}$ describes an oscillation at a frequency known as the

“secular” or “motional” frequency;

$$\omega_i = \beta_i \frac{\Omega_{\text{RF}}}{2} = \frac{\Omega_{\text{RF}}}{2} \sqrt{a_i + \frac{q_i^2}{2}} \quad (2.9)$$

Comparing the secular frequencies given by equation 2.9 against data obtained experimentally reveals a poor match between the predicted frequencies and what is observed in practice. Considering β_i to higher order than that just given by the lowest-order approximation gives more accurate values for ω_i . A higher order approximation of β_i given in [109];

$$\omega_i = \frac{\Omega_{\text{RF}}}{2} \left[a_i - \frac{(a_i - 1)q_i^2}{2(a_i - 1)^2 - q_i^2} - \frac{(5a_i + 7)q_i^4}{32(a_i - 1)^3(a_i - 4)} - \frac{(9a_i^2 + 58a_i + 29)q_i^6}{64(a_i - 1)^5(a_i - 4)(a_i - 9)} \right]^{\frac{1}{2}} \quad (2.10)$$

provides secular frequencies that are much closer matches for what is observed experimentally¹.

In addition to the “ideal” stability conditions mentioned above, secondary sources of instability exist in the Mathieu equation; where the ion’s motion is parametrically excited by the RF field, heating the ion out of the trap. These instabilities exist when the secular frequencies match the resonance condition [103, 108]

$$n_x \omega_x + n_y \omega_y = \Omega_{\text{RF}} - k_z \omega_z \quad (2.11)$$

where n_x , n_y and k_z are positive integers. Figure 2.2 depicts the range of values for a_x and q_x that would provide stable trapping with the trap architecture used in this thesis.

If multiple ions are confined within the trap then the mutual Coulombic repulsion will induce further motional frequencies that can be observed; for N ions in the trap $3N$ motional frequencies will be observed, adding one extra motional mode per axis [111–113]. These in turn will add in additional instabilities in a form similar to that

¹With the trap architecture used in this thesis, with a single ion these parameters are typically $m = 88 \times 1.661 \times 10^{-27}$ kg, $\Omega_{\text{RF}} = 29.8$ MHz, $U_{\text{RF}} = 200$ V, $V_{\text{DC}} = 3.0$ V, $\kappa = 0.098$ $r_{\text{DC}} = 223.44$ μm , $\eta_{\text{trap}} = 0.690$ and $r_{\text{RF}} = 240.42$ μm which gives secular frequencies of $\omega_x \approx 1.44$ MHz, $\omega_y \approx 1.58$ MHz and $\omega_z \approx 570$ kHz

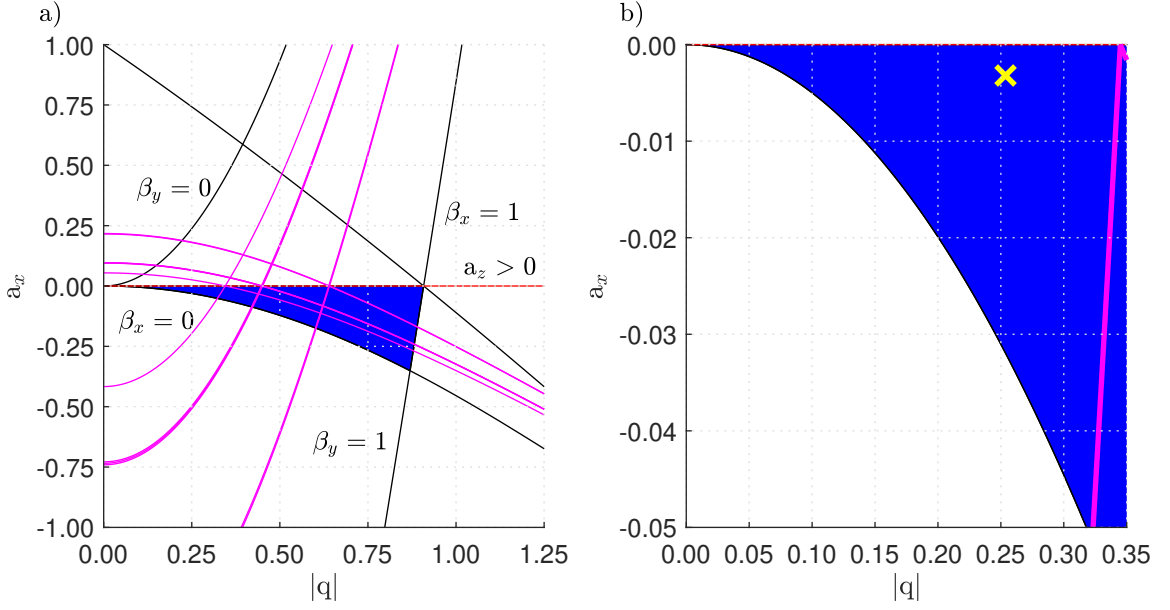


Figure 2.2: a) Stability diagram of the ion trap described in section 3.1 along the \hat{x} -axis, with the coloured area representing the stable region of the trapping parameters [110]. The instabilities from the resonance conditions given by equation 2.11 are indicated with magenta lines. Here a_x is limited to negative values due to the requirement of the DC voltages, and thus a_z , being positive to confine positively charged ions. b) Enlarged region of the stability diagram with the yellow X corresponding to the typical values of a_x and q_x used for the work done in the later chapters of this thesis.

given by equation 2.11; making storage of multiple ions more difficult than for a single ion, with the difficulty increasing with the number of ions being trapped. For two ions the three single ion frequencies now correspond to the collective motion of the ion string and an extra frequency, known as either the stretch or breathing mode, will be observed at

$$\omega_{str} = 3\sqrt{\omega_z} \quad (2.12)$$

and two frequencies that correspond to rocking modes will be found at

$$\omega_{roc, j} = \sqrt{\omega_j^2 - \omega_z^2} \quad (2.13)$$

where $j \in \{x, y\}$.

In addition to this classical treatment of the ion's motion, a quantum mechanical view of the ion's motion can be considered. When an ion has been laser cooled the

kinetic energy of its motion becomes comparable to $\hbar\omega_i$ with the motion being described by the Schrödinger equation. Cook et al [114] showed that in this regime solving the Schrödinger equation becomes reduced to solving the classical Mathieu equation, verifying that this is a valid way to examine the motion. With the Schrödinger equation the motion of the ion is expressed as

$$-\frac{\hbar^2}{2m} \frac{\partial^2}{\partial u_i^2} \psi + \frac{1}{2} m \omega_i^2 \psi = i \hbar \frac{\partial}{\partial t} \psi \quad (2.14)$$

Defining the creation, \hat{a}^\dagger , and annihilation, \hat{a} , operators as

$$\hat{a}^\dagger = \sqrt{\frac{m\omega_i}{2\hbar}} \hat{u}_i - \frac{i}{\sqrt{2m\hbar\omega_i}} \hat{p}_i \quad (2.15a)$$

$$\hat{a} = \sqrt{\frac{m\omega_i}{2\hbar}} \hat{u}_i + \frac{i}{\sqrt{2m\hbar\omega_i}} \hat{p}_i \quad (2.15b)$$

with \hat{u}_i and \hat{p}_i the position and momentum operators respectively, allows equation 2.14 to be re-written as [115, 116]

$$H |\psi\rangle = \hbar\omega_i (\hat{a}^\dagger \hat{a} + \frac{1}{2}) |\psi\rangle = E_n |\psi\rangle \quad (2.16)$$

where E_n are the energy eigenvalues, which take the usual form for a quantum harmonic oscillator:

$$E_n = (n + \frac{1}{2}) \hbar\omega_i \quad (2.17)$$

where $n = 0, 1, 2, \dots$ are the vibrational numbers of the ion's motion. Even though the motion of an ion is quantised by n the exact motional state is not actually known. Instead it is described as a thermal distribution that depends on the mean vibrational number, \bar{n} (which can be a non-integer). The probability of the ion being in the n^{th} vibrational level for any single measurement is [81]

$$P_n(\bar{n}) = \frac{\bar{n}^n}{(1 + \bar{n})^{(1+n)}} \quad (2.18)$$

This complicates attempts to perform spectroscopy on the ion as the coupling to between the laser and ion depends on the value of n (see section 2.4.2). As a consequence

performing spectroscopy on an ion that is in a thermal ($\bar{n} \neq 0$) state will result in a loss of coherence from the ion-laser couplings giving different excitation results.

2.1.2 Micromotion

On top of the secular motion is a faster, secondary motion known as “micromotion”, so called due to it oscillating at a smaller amplitude than the secular motion. The origins of the micromotion can be understood by considering an ion in an RF field at a location that is not at the null; when the field is confining it gives the ion a large and sudden “kick” towards the RF null. This causes the ion to move a small amount and gain velocity. The RF field then changes to be anti-confining; this change imparts a second “kick” away from the RF null. Since the RF field alternates faster than the secular motion of the ion the RF field drives this smaller, faster motion on top of the secular motion. This driving effect on the micromotion will cause it to be 180° out-of-phase with the RF field. This micromotion is intrinsic to the movement of the ion in the trap and cannot be compensated for or suppressed. In equation 2.5 this corresponds to the terms that arise when $n = \pm 1$; these give faster frequencies at $(\pm 2 + \beta_i)\Omega_{\text{RF}}/2$ which also have a smaller amplitude due to $|C_{0,i}| > |C_{\pm 2,i}|$ [81].

Stray DC patch potentials on surfaces that have line of sight to the ion, such as the electrodes, vacuum chamber windows, etc, can displace the ion from the RF null [104], inducing further, excess micromotion [117]. These patch potentials can originate from flaws in the electrodes during manufacture, laser induced charging of the surfaces [118] (although this is not expected to be the case for the apparatus described in chapter 3 [118]) or contaminants on these surfaces. The effect of the patch potentials can be considered by modifying equation 2.8 to account for the ion’s displacement from the RF null at the centre of the trap ($u_{i,0}$):

$$u_i(t) \approx \left[u_{i,0} + 2A_i C_{0,i} \cos\left(\beta_i \frac{\Omega_{\text{RF}}}{2} t\right) \right] \left[1 - \frac{q_i}{2} \cos(\Omega_{\text{RF}} t) \right] \quad (2.19)$$

which when multiplied gives the following equation that fully describes the motion of

the ion in the trap (at least in the lowest-order approximation):

$$\begin{aligned}
 u_i(t) \approx & u_{i,0} + 2A_i C_{0,i} \cos(\omega_i t) \\
 & + \frac{A_i C_{0,i} q_i}{2} [\cos((\Omega_{\text{RF}} + \omega_i)t) + \cos((\Omega_{\text{RF}} - \omega_i)t)] - \frac{q_i u_{i,0}}{2} \cos(\Omega_{\text{RF}} t)
 \end{aligned}
 \tag{2.20}$$

In this the penultimate term represents the intrinsic micromotion, defined above, and the final term defines the excess micromotion [81, 104, 119]. As this term shows, the excess micromotion is proportional to $u_{i,0}$; as the ion is further displaced from the RF null the excess micromotion will take up a larger fraction of the ion's total motion. Without compensation this can become significant enough that it can couple to the interacting laser light; leading to a degradation in the performance of any attempted spectroscopy [104, 117]. Hence, it is important to minimise the excess micromotion. Typically this done by applying DC voltages onto compensation electrodes in the same plane as the RF potential (like those marked as being grounded in in figure 2.1) that rectify the position of the ion.

The driven nature of the micromotion can induce uncontrolled heating onto a cooled ion [23, 104] or in cases where multiple ions are being used the micromotion of one ion can couple to the motion of other ions inducing further heating [120]. The modulation of the ions' motion from the micromotion also adds extra sidebands to the motional spectrum at $\pm\Omega_{\text{RF}}$. This not only reduces the strength of the laser-ion carrier interactions but it can also cause laser heating of the ion due to off-resonant excitations on blue detuned micromotion sidebands near the transitions that are being utilised [104].

2.2 Transitions and Energy Levels in $^{88}\text{Sr}^+$

In the work detailed here atomic strontium (isotope: $^{88}_{38}\text{Sr}$) is ionised using the transitions shown in figure 2.3a [121]. After ionisation the $^{88}\text{Sr}^+$ ions have an alkali metal like electronic structure. Figure 2.3b shows the transitions in $^{88}\text{Sr}^+$ that are relevant for this work and table 2.1 provides some of their key properties.

The two-photon process shown in Figure 2.3a is used to convert a ^{88}Sr atom into a

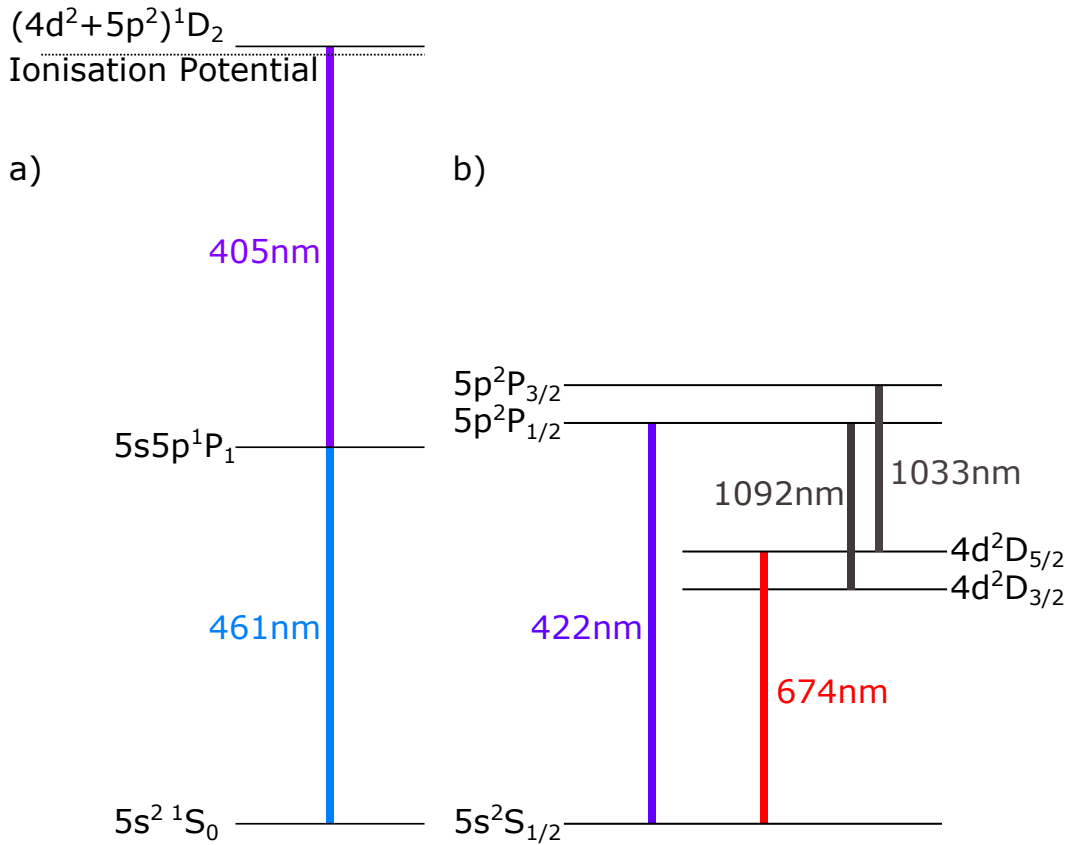


Figure 2.3: a) Selected energy levels of neutral atomic ^{88}Sr . b) Lowest energy levels of $^{88}\text{Sr}^+$. Each transition is labelled with the wavelength associated with that particular transition

$^{88}\text{Sr}^+$ ion. The $(4d^2 + 5p^2)^1D_2$ state is auto-ionising; when the atom enters this state each electron is excited and bound but together their energy is greater than the first ionisation potential of ^{88}Sr . As a result one electron is ejected from the atom, ionising it, and the other electron returns to the ground state.

The $5s\ ^2S_{1/2} - 5p\ ^2P_{1/2}$ transition in $^{88}\text{Sr}^+$ is used for Doppler cooling and state readout. The state readout utilises Dehmelt’s electron shelving method [22] to verify that the ion is in the ground state, $^2S_{1/2}$, or not. If it is in the ground state then the ion will fluoresce when 422 nm light is applied from the $^2S_{1/2} - ^2P_{1/2}$ transition being cycled. If it is in the long-lived $^2D_{5/2}$ state then the ion is considered to be “shelved” and will be unable to fluoresce. Due to the 1/13 possibility of the $P_{1/2}$ decaying down to the dark $D_{3/2}$ state ($\tau = 435\text{ ms}$ [127]) 1092 nm laser light that

Transition	Wavelength [nm]	$\Gamma/2\pi$ [Hz]	$\tau = 1/\Gamma$ [s]
$5s^2\ ^1S_0 - 5s5p\ ^1P_1$	460.8620 [122]	32×10^6	5×10^{-9} [123]
$5s5p\ ^1P_1 - (4d^2 + 5p^2)\ ^1D_2$	405.2 [122] [124]	Ionising	Ionising
$5s\ ^2S_{1/2} - 5p\ ^2P_{1/2}$	421.6706 [122]	20.22×10^6	7.35×10^{-9} [125]
$5s\ ^2S_{1/2} - 4d\ ^2D_{5/2}$	674.02559 [126]	0.41	0.391 [13]
$4d\ ^2D_{3/2} - 5p\ ^2P_{1/2}$	1091.7860 [122]	1.52×10^6	105×10^{-9} [125]
$4d\ ^2D_{5/2} - 5p\ ^2P_{3/2}$	1033.01 [122]	1.38×10^6	115×10^{-9} [125]

Table 2.1: Wavelengths, and radiative linewidths and excited state lifetimes of the transitions used in this experiment. The two photoionisation transitions at the top of the table are for an un-ionised ^{88}Sr atom and the remaining transitions are for the $^{88}\text{Sr}^+$ ion.

excites the $4d\ ^2D_{3/2} - 5p\ ^2P_{1/2}$ transition is continually applied to the ion to prevent optical pumping into this dark state.

The optical qubit is encoded on the narrow $5s\ ^2S_{1/2} - 4d\ ^2D_{5/2}$ transition. The $D_{5/2}$ state is metastable and can only be driven through the weak, forbidden quadrupole transition, which arises from the long lifetime ($\tau = 391$ ms [13]) of the state. However, in certain circumstances it would be impractical to wait for the ion to decay naturally back to the ground state. To get around this, the $4d\ ^2D_{5/2} - 5p\ ^2P_{3/2}$ transition at 1033 nm is used to return the ion to the ground state via the much shorter lived, otherwise unused $5s\ ^2S_{1/2} - 5p\ ^2P_{3/2}$ transition. The $S_{1/2} - D_{5/2}$ transition is also used to perform sideband cooling.

2.3 Zeeman Effect

In the presence of a magnetic field the $S_{1/2}$ level splits into two components ($m_j = \pm 1/2$) and the $D_{5/2}$ level splits into six ($m_j = \pm 5/2, \pm 3/2, \pm 1/2$). The strength of the splitting is defined by the equation:

$$\Delta E = g_j \mu_B B m_j \quad (2.21)$$

Chapter 2. Background Theory

with $\mu_B = (e\hbar)/(2mc)$ the Bohr magneton, B the magnitude of the magnetic field, m_j the magnetic quantum number. g_j is the Landé g-factor and is defined as

$$g_j = \frac{3}{2} + \frac{S(S+1) - L(L+1)}{2J(J+1)} \quad (2.22)$$

where S is the spin quantum number, L is the orbital angular momentum quantum number and $J = L + S$ is the total angular momentum [128–130]. This has the effect of splitting the $S_{1/2} - D_{5/2}$ into different components, with the energy shift of each being given by:

$$E_{S-D} = \mu_B B (m_{5/2} g_{5/2} - m_{1/2} g_{1/2}) \quad (2.23)$$

Although the splitting of the $S_{1/2}$ and $D_{5/2}$ would imply that there are 12 components to the transition, the $m_j = \pm 1/2$ to $m_j = \mp 5/2$ ($\Delta m_j = 3$) components cannot be utilised due to quadrupole selection rules only permitting $\Delta m_j = 0, \pm 1, \pm 2$ [129, 130]. The coupling strength of each Zeeman component to the laser are scaled by [111, 113]

$$\mathcal{S}_{(\Delta m_j=0)} = \frac{1}{2} |\cos(\chi) \sin(2\zeta)| \quad (2.24a)$$

$$\mathcal{S}_{(\Delta m_j=\pm 1)} = \frac{1}{\sqrt{6}} |\cos(\chi) \cos(2\zeta) + i \sin(\chi) \cos(\zeta)| \quad (2.24b)$$

$$\mathcal{S}_{(\Delta m_j=\pm 2)} = \frac{1}{\sqrt{6}} \left| \frac{1}{2} \cos(\chi) \sin(2\zeta) + i \sin(\chi) \sin(\zeta) \right| \quad (2.24c)$$

where ζ is the angle of the laser \hat{k} -vector relative to the direction of the magnetic field and χ is the angle of the laser polarisation with respect to the plane created by magnetic field and \hat{k} -vector. The Zeeman components, their accompanying frequency shift and the relative coupling intensity of each are depicted in figure 2.4 using the parameters used in the experimental apparatus. There is no hyperfine splitting of $^{88}\text{Sr}^+$ due to it having a nuclear spin of zero.

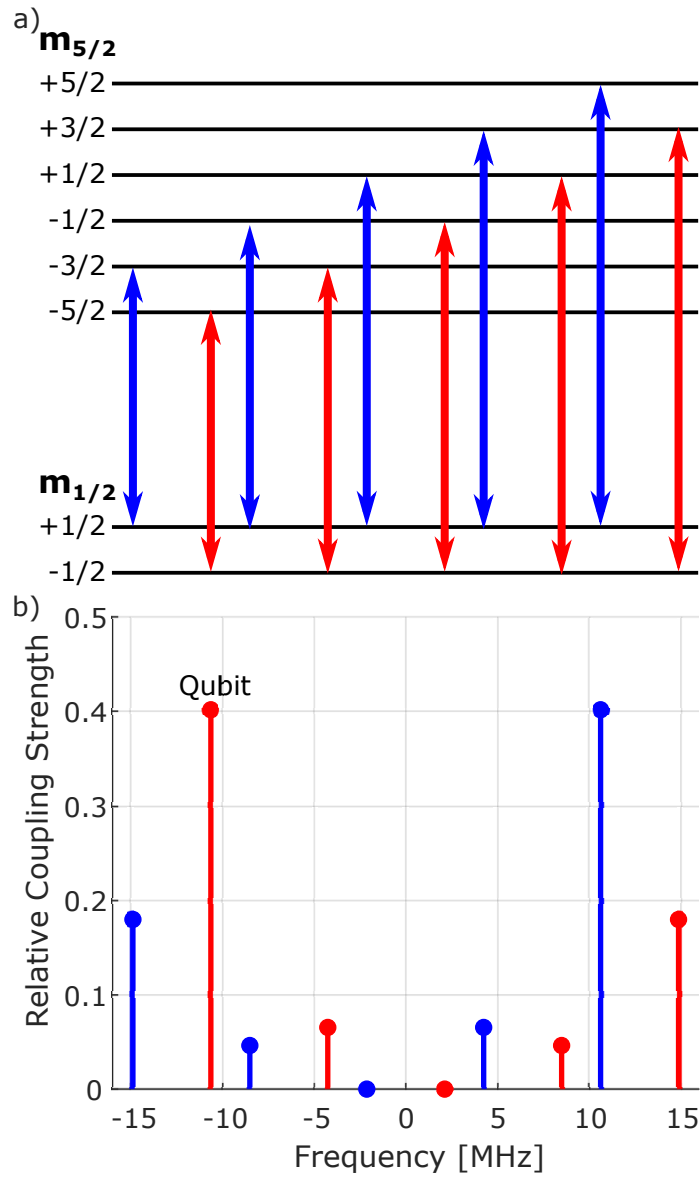


Figure 2.4: a) The 10 Zeeman components of the 674 nm transition with b) their corresponding relative coupling strengths calculated via equations 2.23 and 2.24 using $B = 380 \mu\text{T}$, $\zeta = 100.3^\circ$ and $\chi = 90^\circ$. Red components are transitions that involve the $S_{1/2}(m_j = -1/2)$ state and blue are ones that involve the $S_{1/2}(m_j = +1/2)$ state. The component used for the qubit transition is marked with text.

2.4 Laser Cooling Techniques

2.4.1 Doppler Cooling

The principle of Doppler cooling [81, 128, 131–133] is that a moving ion has its kinetic energy reduced by absorbing a photon that is propagating towards the direction of the ion’s motion. In absorbing this photon the ion also undergoes a change in momentum in the direction the photon is propagating. After absorption, the ion spontaneously decays back down to the ground state, emitting a photon in a random direction, resulting in the ion recoiling in the opposite direction. When averaged over many absorption-emission cycles the ion’s kinetic energy in the direction of the laser beam is reduced (as the random direction of the emission results in an average of zero net change in velocity). This has the effect of “cooling” the ion. Eventually the cooling effect from the mono-directional absorption is balanced with heating from the random-walk recoil caused by each emission. At this point no further net cooling occurs. In order to achieve the lowest possible kinetic energy with this method, known as the Doppler limit, the laser detuning is set to be $-\Gamma_{eff}/2$ [128, 132, 133] from the stationary resonance transition, where Γ_{eff} is the effective linewidth due to saturation broadening and Zeeman splitting. Doing so gives a mean vibrational level of [133]

$$\bar{n}_{\min} = \frac{\frac{\Gamma_{eff}}{\omega_s} - 1}{2} \quad (2.25)$$

With $\omega_s/2\pi \approx 0.569$ MHz this gives $\bar{n}_{\min} \approx 17.3$. Thus in order to initialise the motional qubit into the ground state ($\bar{n} = 0$) a second stage of cooling must be applied.

2.4.2 Optical Qubit Transition

To describe the interaction of the laser light with the internal electronic states of the ion, the Hamiltonian

$$H = H_{ge} + H_m + H_L \quad (2.26)$$

can be considered [81, 115]. The first term represents the two-level electronic states of ion (the ground state, g and the excited state, e) without the presence of the driving light field

$$H_{ge} = \frac{\hbar\omega_0}{2}\sigma_z \quad (2.27)$$

with ω_0 the optical frequency that is resonant with the energy difference between the two electric states and σ_z is the Pauli matrix. The second term represents the motion of the ion in the trap

$$H_m = \hbar\omega_i\left(a^\dagger a + \frac{1}{2}\right) \quad (2.28)$$

and comes from equation 2.16. The third time-dependent term describes the laser-ion interaction:

$$H_L = \frac{\hbar\Omega_R}{2}(\sigma^+ + \sigma^-)(e^{i(k\hat{x} + \omega_L t)} + e^{-i(k\hat{x} + \omega_L t)}) \quad (2.29)$$

where $\sigma^\pm = 1/2(\sigma_x \pm i\sigma_y)$ are the raising and lowering operators [81], ω_L and k are the frequency and wave vector of the laser and Ω_R is the Rabi frequency [113] that specifies the coupling strength between the light field and the ion.

H_L can be simplified by making the substitution $e^{ik\hat{x}} = e^{i\eta(a^\dagger + a)}$ and applying the unitary operator, $U_0 = \exp(-iH_0 t/\hbar)$ (and its adjoint, U_0^\dagger), to bring the equation into the interaction picture, then applying the rotating wave approximation to remove the fast terms at $\omega_L + \omega_0$ [81, 115]:

$$H_{L,int} = U_0^\dagger H_L U_0 = \frac{\hbar\Omega_R}{2}(\sigma^+ e^{i\eta(\hat{a}^\dagger + \hat{a})} e^{-i\delta t} + \sigma^- e^{-i\eta(\hat{a}^\dagger + \hat{a})} e^{i\delta t}) \quad (2.30)$$

Here $\delta = \omega_L - \omega_0$, the detuning of the laser, $\hat{a}^\dagger = a^\dagger e^{i\omega_i t}$, $\hat{a} = a e^{-i\omega_i t}$ and

$$\eta = k \cos(\theta) \sqrt{\frac{\hbar}{2M\omega_i}} \quad (2.31)$$

is the Lamb-Dicke parameter which relates the spatial extent of the ion's motion to the wavelength of the light driving the transition [81, 134]. When the ion is cooled such that the amplitude of its motion is small compared to the wavelength of the light the

ion is said to be within the Lamb-Dicke regime. When the condition

$$\eta\sqrt{2\bar{n}+1} \ll 1 \quad (2.32)$$

is met the ion is considered to be in this regime. Doppler cooling with the apparatus described in chapter 3 is sufficient to place an ion of $^{88}\text{Sr}^+$ in this regime².

With the right detuning, equation 2.30 shows the Hamiltonian will couple the electronic states of the ion to the vibrational levels of its motion. Expanding the $e^{\pm i\eta(\hat{a}^\dagger + \hat{a})}$ terms [81, 119] as a power series changes the equation into

$$H_{int} = \frac{\hbar\Omega_R}{2} \left(\sigma^+ \left(\sum_{\kappa=0}^{\infty} \frac{(i\eta)^\kappa (\hat{a}^\dagger e^{-i\omega_i t} + \hat{a} e^{i\omega_x t})^\kappa}{\kappa!} \right) e^{-i\delta t} + \text{conj.} \right) \quad (2.33)$$

Here the oscillating motion of the ion creates sidebands that couple the electronic states to the vibrational levels of the ion's motion. The terms produced by the sum in this equation create a series of ladder operators that allow the ion to drive the $|g, n\rangle - |e, n'\rangle$ transition if the laser is detuned to be near resonant with the corresponding sideband. The coupling strength of the laser to these transitions is given by [23, 81, 135]

$$\Omega_{n,n'} = \Omega_{n',n} = \Omega_R e^{-\frac{\eta^2}{2}} \sqrt{\frac{n_{<}!}{n_{>}!}} \eta^{|n'-n|} L_{n_{<}}^{|n'-n|}(\eta^2) \quad (2.34)$$

where $n_{>}$ and $n_{<}$ are larger and smaller values n and n' respectively and $L_n^\alpha(X)$ is the generalised Laguerre polynomial.

Since the Rabi frequency depends on the value of n , attempts to perform coherent excitation of the ion will be complicated by the ion being in a thermal ($P(n) \neq 1$) distribution of states (see the end of section 2.1.1). Instead of a single value of n determining the final value of the state the final excitation probability will be given by the weighted average of the Bloch vector rotations at Rabi frequencies $\Omega_R(n)$. The weightings for this average being determined by equation 2.18.

Hence the importance of cooling the ion to the motional ground state since $\bar{n} \rightarrow 0$ maximises the probability of n being in one state and minimises the contributions from

² $\eta\sqrt{2\bar{n}+1} \approx 0.12 \ll 1$, with $\omega_i = \sim 0.57$ MHz, $k = \frac{2\pi}{674 \text{ nm}}$, $\theta = 52.3^\circ$ and $\bar{n} \approx 17.3$

other values of n .

2.4.3 Sideband Cooling

After Doppler cooling the ion is subjected to resolved-sideband cooling [136–138] to complete the process of placing the ion into the vibrational ground state ($\bar{n} = 0$). In order to perform this technique the ion must be in the Lamb-Dicke regime [81, 134]. Here first order sidebands appear on each side of the main carrier transition at the motional frequencies of the ion as described in section 2.4.2. Detuning the laser to absorb on the red sideband has the vibrational number being reduced by one on each absorption-emission cycle as each the ion predominantly emits photons on the carrier (which has a higher photon energy compared to the photons absorbed on the red sideband). Likewise absorbing on the blue-detuned sideband will raise n by one per photon cycled. Here the coupling strength between the carrier, red and blue sidebands are [81, 135];

$$\Omega_{carrier} = \Omega_R \left[1 - \left(n + \frac{1}{2} \right) \eta^2 \right] \quad (2.35a)$$

$$\Omega_{red} = \Omega_R \eta \sqrt{n} \quad (2.35b)$$

$$\Omega_{blue} = \Omega_R \eta \sqrt{n+1} \quad (2.35c)$$

From these it can be seen that at as $n \rightarrow 0$, $\Omega_{red} \rightarrow 0$ and $\Omega_{blue} \rightarrow \Omega_R \eta$. As a consequence of this when \bar{n} is low the asymmetry between the two sidebands can be used to determine the value of \bar{n} . After sideband cooling, the mean vibrational quantum number can simply be calculated by examining the ratio of the peak excitation probabilities of the two sidebands [81, 119, 138, 139]:

$$\bar{n} = \frac{\frac{P_{red}}{P_{blue}}}{1 - \frac{P_{red}}{P_{blue}}} \quad (2.36)$$

This technique can also be used to measure the heating rate of the trap, $d\bar{n}/dt$. This measurement is made by applying a sideband cooling pulse and measuring the peak

excitation rate of each sideband whilst varying the delay between the cooling and probing pulses. This measurement will also reveal if the sideband cooling is unable to place the ion into the motional ground state, which can arise from either an excessively high heating rate or inefficient sideband cooling.

When the excited state has a long lifetime, the wait time for the ion to spontaneously decay can severely impact the efficiency of the sideband cooling, to the extent that it can prevent cooling. To bypass this problem the excited state can be quenched by coupling it to an auxiliary, short-lived state that quickly decays back to the ground state. This gives a cooling rate of [81, 135]

$$R_{SBC} = \Gamma_{eff} \frac{\eta\sqrt{n}\Omega_R}{2(\eta\sqrt{n}\Omega_R)^2 + \Gamma_{eff}^2} \quad (2.37)$$

where Γ_{eff} is the effective linewidth:

$$\Gamma_{eff} = \frac{\Omega_Q^2 \Gamma^2}{(\Gamma + \Gamma_Q)^2 + 4\delta_Q^2} \quad (2.38)$$

with Ω_Q and δ_Q being the Rabi frequency and detuning of the quenching laser and Γ_Q is the linewidth of the quenching transition.

2.5 Trapped Ion Qubits

As previously mentioned, the qubit is the quantum mechanical equivalent of the classical bit. The qubit consists of two distinct states, $|g\rangle$ and $|e\rangle$, that can be used to store and represent a single unit of binary information. However unlike the classical bit, the states of the qubit can be placed into a superposition of each other. A generic qubit state can be written as:

$$|\Psi\rangle = a_0 |g\rangle + a_1 |e\rangle \quad (2.39)$$

where a_0 and a_1 are complex numbers representing the probability of the qubit being in either state and satisfy the condition $|a_0|^2 + |a_1|^2 = 1$. Equation 2.39 can be rewritten as:

$$|\Psi\rangle = \cos\left(\frac{\alpha}{2}\right)|g\rangle + e^{-i\beta}\sin\left(\frac{\alpha}{2}\right)|e\rangle \quad (2.40)$$

In this form the qubit state can be visualised as a three-dimensional unit-vector, known as the Bloch vector, with polar coordinates α, β which represent the vertical and horizontal angles of the vector respectively. The allowed values for the Bloch vector lie on the surface of a sphere, known as the Bloch sphere. The north and south poles of this sphere represent the $|e\rangle$ and $|g\rangle$ states respectively. Any point outside of the two poles represent a superposition of the two qubit states. Here α represents the population of the qubit states and β the phase of the coefficient a_1 with respect to a_0 . Single qubit gate operations have the effect of rotating the Bloch vector across the surface of the Bloch sphere, with the final position described by equation 2.40.

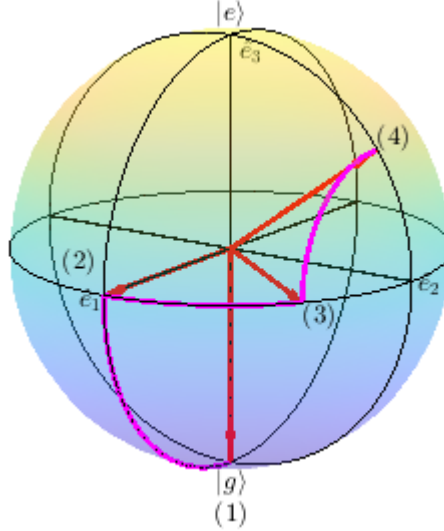


Figure 2.5: Example of a pulse sequence rotating the Bloch vector around the Bloch sphere; 1) The qubit is initialised into the $|g\rangle$ state, 2) a $\pi/2$ pulse puts the qubit into the $\frac{1}{\sqrt{2}}(|g\rangle + |e\rangle)$ state, 3) the pulse source is turned off and its frequency is detuned to allow a phase difference between the pulse source and the resonant atomic transition to accumulate, 4) A second pulse with the same Ω_R as the first pulse, with the same detuning as used in the gap period, applies a final rotation after which the qubit population is measured.

A single measurement of the qubit does not reveal all the information contained in the qubit state, but rather is a projective measurement that will yield either $|g\rangle$ or $|e\rangle$ with the probability of the qubit being in each state determined by a_0^2 and a_1^2 respec-

tively. Thus many cycles of the same initialisation, qubit rotations and measurement must be performed in order to accurately determine the qubit state. For trapped ions applying laser light that causes the ion to undergo a transition not used to encode the qubit will project the qubit into either $|g\rangle$ or $|e\rangle$. This corresponds to the collapse of the qubit wavefunction into one of its eigenstates.

For the trapped ion qubits used here, gate operations are applied via laser pulses, each with a unique duration $2T$, a frequency ω_L and phase ϕ_L whose coupling strength to the ion is described by Ω_R . Figure 2.5 depicts the Bloch sphere with series of example qubit rotations. The evolution of the Bloch vector can be described via differential equations similar to those derived by Letchumanan [135, 140, 141]:

$$\dot{\tilde{\rho}}_{eg} = [i\delta - (\Gamma_L + \frac{1}{2}\Gamma_{eg})]\tilde{\rho}_{eg} - i\frac{\Omega_R}{2}e^{-i\phi_L}(\rho_{ee} - \rho_{gg}), \quad (2.41a)$$

$$(\dot{\rho}_{ee} - \dot{\rho}_{gg}) = -\Gamma_{eg}[1 + (\rho_{ee} - \rho_{gg})] + i\Omega_R(e^{-i\phi_L}\tilde{\rho}_{eg}^* - e^{i\phi_L}\tilde{\rho}_{ge}) \quad (2.41b)$$

where $\delta = \omega_L - \omega_0$ is the detuning of the laser from the ion's transition frequency, Γ_{eg} is the linewidth of the quadrupole transition, Γ_L is the contribution to the observed transition linewidth from the laser, $\rho_{i,j}$ are the $(i, j)^{\text{th}}$ elements of the density matrix and

$$\dot{\tilde{\rho}}_{ge} = e^{-i\omega_L t}\rho_{ge}, \quad (2.42a)$$

$$\dot{\tilde{\rho}}_{eg} = e^{i\omega_L t}\rho_{eg} \quad (2.42b)$$

Setting $\tilde{\rho}_{eg}^* = \tilde{\rho}_{ge}$, $\phi = 0$ and separating $\tilde{\rho}_{ge}$ into its real and imaginary parts so that $\tilde{\rho}_{ge} = 1/2(u - iv)$ allows for equation 2.41 to be rewritten as the optical Bloch equations (OBEs):

$$\dot{u} = \delta v - (\Gamma_L + \frac{1}{2}\Gamma_{eg})u, \quad (2.43a)$$

$$\dot{v} = -\delta u + \Omega_R w - (\Gamma_L + \frac{1}{2}\Gamma_{eg})v, \quad (2.43b)$$

$$\dot{w} = -\Omega_R v - \Gamma_{eg}(w - 1) \quad (2.43c)$$

Chapter 2. Background Theory

These describe the motion of the Bloch vector \vec{R} around the Bloch sphere that is induced by excitation from a near resonant laser field; u represents the dispersive component of the vector's movement, v represents the absorptive component and $w = (\rho_{ee} - \rho_{gg})$ is the population difference. This vector can thus be expressed as:

$$\vec{R} = u\hat{e}_1 + v\hat{e}_2 + w\hat{e}_3 \quad (2.44)$$

where \hat{e}_j are the axes of the Bloch sphere depicted in figure 2.5.

A laser pulse applied to the qubit will rotate the Bloch vector around the axis $\vec{W} = \Omega_R\hat{e}_1 + \delta\hat{e}_3$ with at an effective Rabi frequency, $\Omega'_R = \sqrt{\Omega_R^2 + \delta^2}$. In cases where $\Omega_R = 0$ the Bloch vector will rotate around \hat{e}_3 with a frequency of δ , with no change to the populations of $|g\rangle$ and $|e\rangle$. Varying duration of the laser pulse produces Rabi oscillations where the Bloch vector rotates around the the sphere at a frequency of Ω_R .

If there is no decoherence in the qubit ($\Gamma_L = \Gamma_{eg} = 0$) then the Bloch vector will remain at its unit length ($u^2 + v^2 + w^2 = 1$) and will remain on the surface of the Bloch sphere, pointing at a position that corresponds to a pure state. In cases where decoherence is present it has the effect of reducing the magnitude of the Bloch vector as time progresses, causing the vector to point to a position inside the Bloch sphere corresponding to a mixed state. Looking at the Rabi oscillations obtained by measuring the qubit this has the effect of damping the probability of the qubit being in either state towards 1/2, which corresponds to the Bloch vector decaying to the centre of the sphere. In practice it is impossible to eliminate decoherence in an optical qubit (even if one could obtain a laser with an infinitely small linewidth, $\Gamma_L = 0$) due to the finite lifetime of the excited state. However despite this it is still possible to implement high-fidelity qubit operations on the ion as long as the sequence is on a timescale that is much faster than the time it takes for the ion to decay ($T_{operation} \ll 1/\Gamma_{eg}$) which can be done by either employing fast qubit gates or by utilising long-lived excited states for the $|e\rangle$ state of the qubit.

Experimentally the excitation probability, $P_{ee} = (1 + \rho_{ee} - \rho_{gg})/2$, is measured;

to determine the effect of a laser pulse on the excitation probability equations 2.41 can be numerically integrated over the duration of the pulse being applied and fitting the final value of $(1 + \rho_{ee} - \rho_{gg})/2$ to the results. For more complex pulses, such as those with time-varying amplitudes, the effects can be determined by numerically integrating over modified versions of these equations that replace the fixed, time-independent, parameters with time dependant ones that describe how the pulse evolves, such as replacing Ω_R with $\Omega_R(t)$ [142]. This is discussed in greater detail more in chapter 7 which utilises this to perform data fitting on experimental spectroscopy results.

2.6 Dechorence

The upper boundary for the coherence time of an optical qubit is the natural lifetime of the excited state. For these qubits this lifetime is typically of the order of hundreds of milliseconds to single digit number of seconds [13, 143, 144] and for hyperfine and Zeeman transitions the lifetimes can be longer than a year [144]. However in practice the actual coherence time will be reduced by environmental factors, which originate from one of three sources, each of which will be discussed in subsequent sub-sections [23].

2.6.1 Motional Dechorence

As mentioned at the ends of sections 2.1.1 and 2.4.3 the heating of the ion causes \bar{n} to increase, which increases probability of the ion being in different vibrational levels. This in turn leads to larger contributions from different Rabi frequencies when the qubit rotations are performed. These cause the qubit to dephase if the ion heating occurs on a scale that is comparable to the time taken to perform the qubit operation being done. This heating of the ion comes from noise in the confining electric fields. Although the sources for this noise are not well understood with multiple origins being proposed [23, 136, 145–150], it is convenient to just consider the motion of the ion being coupled to spurious electric fields originating on the surfaces that the ion is exposed to. The effects these noisy electric fields have on the heating rate of the ion can be calculated using a method similar to the one used by Savard, O’Hara and

Thomas [23,139,149–151]. It should be noted that several in-depth studies on the effects of electric field noise spectral density concluded that the magnitude of the noise scales as $\sim 1/d^4$ [139,149,150], where d is the ion-electrode separation. As a consequence of this the effects of the electric-field noise in microfabricated ion trap architectures is much greater than in macro-scale trap designs [16,137,150].

Three commonly considered sources of the spurious electric field noise are [23,81,139]:

1) Johnson noise [152,153], which can be reduced by utilising electronic filtering [112,154,155],

2) Thermal blackbody radiation [23,139,156]. In cases where this is a major concern this source of noise can be minimised via cryogenic cooling [157–161]. However this is not expected to be an issue for the trap devices used here [156,162] and

3) Surface patch-potentials on the electrodes [163–165]; the effects from which can be reduced by a factor of two [166] to two orders of magnitude [164] by either cryogenic cooling of the trap [160] or performing *in situ* cleaning of the electrodes [112,148,160,164,166].

A fourth, less likely, potential source for electric field noise is the onset of electrical breakdown, in the form of surface flashover, between high voltage RF electrodes and grounded surfaces that the ion is exposed to. Although the mechanisms behind surface flashover are poorly understood it has been observed that it involves both the emission of electrons from the dielectric-electrode-vacuum triple point and damage to the surfaces of the electrodes on which the potential is applied; distorting the electric fields applied to the ion [23,150]. Thus even small amounts of flashover will induce significant heating of the ion [167]. The subject of surface flashover is covered in more detail in chapter 4.

2.6.2 Electronic State Dechorence

Any fluctuations in the magnetic field that the ion experiences can be a source of decoherence for the internal electronic states of the ion [23] due to the energy separation between the two levels being dependent on B as described in equation 2.23. One of the main sources of magnetic field fluctuations is at 50 Hz and the associated harmonics that

originate from the mains electricity supply. Multiple methods have been attempted to minimise or compensate for this 50 Hz noise, such as feed-forwards [168–170], feedback [169, 171], synchronising the experiment to the mains power cycle [11, 172] or utilising magnetic shielding [11, 144, 170]. Often multiple techniques are used in conjunction with each other to minimise these fluctuations. The apparatus used here utilises a magnetic shield and a set of coils to nullify the field at the ion and apply a quantising bias field, with the last of these used to separate the Zeeman components. All coils possess a feedback mechanism to stabilise their driving currents (setup described in section 3.3 and performance evaluated in chapter 6).

A further way to reduce the decoherence induced by noise in the magnetic fields is to utilise superconducting coils [170] to nullify and generate the bias magnetic field, however this requires cooling the apparatus down to cryogenic temperatures; vastly increasing the complexity of apparatus.

If the fluctuations in the magnetic field are slow relative to the timescales of gate operation then spin echo techniques [142, 173, 174] can be used to reduce the error.

2.6.3 Dechorence from the Qubit Laser

Fluctuations and noise in the parameters of the laser light that interacts with the ion leads to decoherence in the qubit. The two main sources of decoherence originating from the laser are from the laser frequency stability (via its finite linewidth and any drift in the laser frequency) of the laser and fluctuations in the laser intensity.

The finite laser linewidth will possess Fourier components that are away from the transition of interest and may induce off-resonant excitations from nearby components of the ion’s spectrum, as will drifts in the laser frequency. These are of particular concern with regards to interacting with the motional sidebands as the non-resonant Fourier components of the laser may induce off-resonant excitations on the carrier due to the carrier having much stronger coupling to the laser, as equations 2.35 demonstrate. Thus it is important to minimise the power spectral density of these Fourier components that are far from the transition being probed in order to maximise the coherence of the operation being performed. Amplitude shaped pulses [17, 175], such

as a Blackman profile [176], with the same pulse area as they would under a square pulse, can achieve this as described later in chapter 7. A second, less favourable method to avoid off-resonant excitations is to adjust the trapping parameters to increase the secular frequency of the ion and thus the spacing between the components of the ion's motional spectrum. This can be done by adjusting the RF voltage amplitude, RF frequency and the endcap voltages. The primary problem with implementing this is that the radial secular frequencies are proportional to the RF amplitude, which if continually increased can result in the breakdown or damage to the trap device, as described in chapter 4. Furthermore changing the trapping parameters can change a_i and q_i such that ion motion becomes unstable and the trap becomes unable to confine ions. On the laser side of the apparatus the linewidth and drift of the laser can be reduced by stabilising the laser to a stable frequency reference such as a cavity [64, 101, 177, 178].

Intensity fluctuations arise from instability in either the optical power or laser pointing. Both induce fluctuations in the Rabi frequency, causing decoherence of the qubit. The effects of the pointing instabilities can be reduced by using mechanically stable optics mounts, keeping the laser beam enclosed to minimise air currents and environmental temperature [179, 180] and utilising an adjustable mirror with feedback via a quadrant photodiode [181]. Instabilities in the optical power of the laser can be reduced by implementing a feedback onto the laser [175, 180, 181]. Chapter 5 describes the feedback mechanism that has been implemented for the laser apparatus described in section 3.7.

2.7 Entanglement

Qubit entanglement here is achieved using the Mølmer-Sørensen gate operation [182, 183], which maximally entangles two or more ions that are in the Lamb-Dicke regime. Implementing this gate operation has numerous advantages over the entanglement gate proposed by Cirac and Zoller [27], namely that it does not require single-ion addressing and the maximally entangled state that it produces is insensitive to the value of n at the start of the gate operation. The latter of these means that the ions do not

require ground state cooling. It should be noted that despite the independence from the initial value of n , the entanglement fidelity is affected by any heating that occurs during the gate operation [182, 183]. Although the Mølmer-Sørensen gate can be used for many ions here, for simplicity, only two ions will be considered. Here bichromatic laser light of frequencies $\omega_{\pm} = \omega_0 \pm \Delta$ that are symmetrically detuned from the carrier transition is applied to the ion. The detunings of the two lasers are chosen such that the following conditions apply: $2\omega_0 = \omega_+ + \omega_-$ and that Δ is close to but not equal to ω_i . These conditions allow the ion to undergo a two-photon transition through four possible pathways, depicted in figure 2.6, without populating the intermediate states. As a consequence, the gate operation finishes with the same value of n that it begins, making it independent of n as the ion must follow a pathway that both increases n by one and reduces it by one. This can also be shown by considering the interaction of the bichromatic light with the ion in a similar manner to equations 2.26 - 2.30. Here the interaction is described by the Hamiltonian [182, 184]:

$$H_{int} = \sum_{I,J} \frac{\hbar\Omega_j}{2} (\sigma_I^+ e^{i\eta_J(\hat{a}^\dagger + \hat{a})} e^{-i\Delta t} + \sigma_I^- e^{-i\eta_J(\hat{a}^\dagger + \hat{a})} e^{i\Delta t}) \quad (2.45)$$

where $I \in \{1, 2\}$ are the ions exposed to the laser and $J \in \{+, -\}$ indicates which of the two lasers is being considered. Ideally the two components of the bichromatic laser would have the same Rabi frequency ($\Omega_+ = \Omega_- = \Omega_R$) and wave vector ($\eta_+ = \eta_- = \eta$). From this emerge terms that raise the value of n by one that are proportional to $(\sqrt{n+1}\Omega_R\eta)^2/(\Delta - \omega_i)$ and terms that lower it by one that are proportional to $(\sqrt{n}\Omega_R\eta)^2/(\omega_i - \Delta)$, similar to the monochromatic laser case in sections 2.4.2 and 2.4.3. Summing these terms describes the possible paths shown in figure 2.6 and gives the coupling strength of the interaction to be [182, 184]

$$\Omega_{MS} = \frac{2(\Omega_R\eta)^2}{\omega_i - \Delta} \quad (2.46)$$

This sum results in “miracle” outcome where the pathways destructively interfere and become independent from n due to the different signs on the denominators. Utilising a bichromatic laser pulse adds in two additional resonant transition pathways from

$|ge\rangle \leftrightarrow |eg\rangle$. These possess a Rabi frequency that is the negative (i.e. is out of phase) of the $|gg\rangle \leftrightarrow |ee\rangle$ transitions [184]. The evolution of the qubits from each possible initial state can thus be described by:

$$|gg\rangle \rightarrow \cos\left(\frac{\Omega_{\text{MS}}T}{2}\right) |gg\rangle + e^{i\phi} \sin\left(\frac{\Omega_{\text{MS}}T}{2}\right) |ee\rangle, \quad (2.47a)$$

$$|ee\rangle \rightarrow \cos\left(\frac{\Omega_{\text{MS}}T}{2}\right) |ee\rangle + e^{i\phi} \sin\left(\frac{\Omega_{\text{MS}}T}{2}\right) |gg\rangle, \quad (2.47b)$$

$$|ge\rangle \rightarrow \cos\left(\frac{\Omega_{\text{MS}}T}{2}\right) |ge\rangle - e^{i\phi} \sin\left(\frac{\Omega_{\text{MS}}T}{2}\right) |eg\rangle, \quad (2.47c)$$

$$|eg\rangle \rightarrow \cos\left(\frac{\Omega_{\text{MS}}T}{2}\right) |eg\rangle - e^{i\phi} \sin\left(\frac{\Omega_{\text{MS}}T}{2}\right) |ge\rangle \quad (2.47d)$$

Initialising the qubits into the $|gg\rangle$ state and applying pulses with a duration that is an integer multiple of $T = \frac{\pi}{2|\Omega_{\text{MS}}|}$ maximally entangles the qubits into either the $\frac{1}{\sqrt{2}}(|gg\rangle - e^{i\phi}|ee\rangle)$ or $\frac{1}{\sqrt{2}}(|ee\rangle - e^{i\phi}|gg\rangle)$ states.

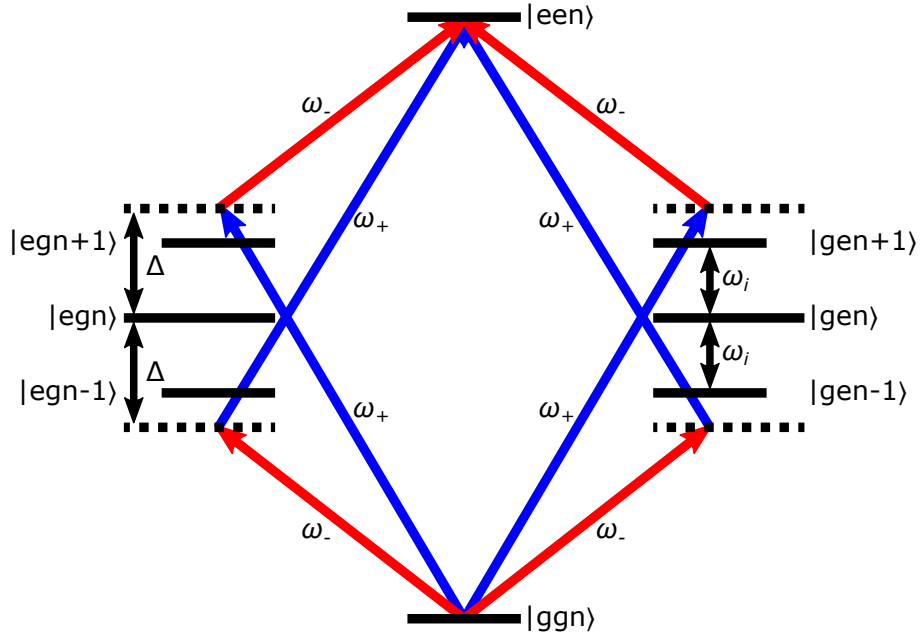


Figure 2.6: The Mølmer-Sørensen Gate operation couples the $|ee\rangle$ and $|gg\rangle$ states together via a bichromatic laser with frequencies at ω_- (red) and ω_+ (blue) that are near resonant with the red and blue sidebands at ω_i respectively. This drives a two-photon transition via four pathways that destructively interfere with each other. As a consequence the intermediate states ($|XYn \pm 1\rangle$) are left unpopulated and effectively serve as virtual states.

Chapter 3

Background of Apparatus

3.1 Microtrap

The ion trap devices used in this work are a linear array of three-dimensional, rotationally-symmetric, Paul traps (depicted in figure 3.1). These traps use a similar design to previous iterations and are microfabricated from silicon wafers using processes which are almost identical to those used to create the previous designs [156, 162, 185, 186]. The main differences between previous designs and the current implementation is the inclusion of more trapping segments, changes to some of the trap aperture dimensions (relevant dimensions from the current iteration are specified in figure 3.1b) and the addition of cleaning steps at the end of the fabrication process. The trap geometry is designed such that the RF and DC electrodes have a unit aspect ratio with each other giving it a high trapping efficiency for ions along the trap axis.

After fabrication, the trap is joined to a ceramic leadless chip carrier (CLCC) via an intermediate substrate. The CLCC, when made part of the vacuum system, allows for external, air-side, electrical connections to be made to the trap which are only ~ 15 mm away from the trap aperture. Additionally an atomic flux shield is added to the CLCC to restrict the flow of strontium from the atom source to only a pre-designated loading zone (pictured in figure 3.1c). Without this, strontium flux can deposit onto the surfaces of other zones which form patch-potentials and leads to degradation of the trap performance. Figure 3.1d gives a schematic of each electrode's function. The

transport zone consists of DC electrodes that have been elongated to the length of three single segments to further isolate the loading zone from the segments where ions are to be stored or have spectroscopy performed. To store an ion in an operational zone, DC voltages are applied to the DC electrodes in the zones adjacent to the one that the ion is stored in. One of the compensation electrodes (marked Co in figure 3.1b) and one of the DC electrodes, both from the zone that the ion is stored in, can be used to minimise the excess micromotion of the ion (process described in section 3.12.2). This excess micromotion can arise from imperfections in the trap manufacturing or from stray electric fields, such as from deposited strontium or other contaminants on the electrode surfaces [148, 163].

Each compensation electrode is capacitively coupled through the SiO_2 to the RF electrode on the internal surface of the SiO_2 , as shown in the inset of Figure 3.1b. The overlap of a single zone compensation electrode with a single RF electrode results in a capacitance $C_1 \approx 50$ fF. This capacitive coupling can be utilised to sense the RF voltage, U_{RF} , applied to the RF electrode [154].

Deficiencies or flaws that occur in the microfabrication process can result in the electrical breakdown of the ion trap devices, meaning that the U_{RF} desired for optimum ion trapping cannot be achieved. Breakdown could happen through the SiO_2 dielectric layer or via flashover across its surface from the RF electrode to the compensation electrodes or the grounded Si (see Figure 3.1b). The detection of these breakdown modes motivated the apparatus and techniques described in chapter 4.

3.2 Vacuum System

To keep the trap in Ultra High Vacuum (UHV) the trap device is kept within a custom made stainless steel chamber. On one side the CLCC, a steel spacer and window are cold welded together onto the chamber with a larger window cold welded onto the other side. These windows are sized and positioned such that any laser that passes through the trap aperture from the larger window side can pass through the smaller window as depicted in figures 3.2b-d, allowing for a wide range of optical access angles. The chamber setup is made in clean-room conditions to minimise the trap exposure to potential

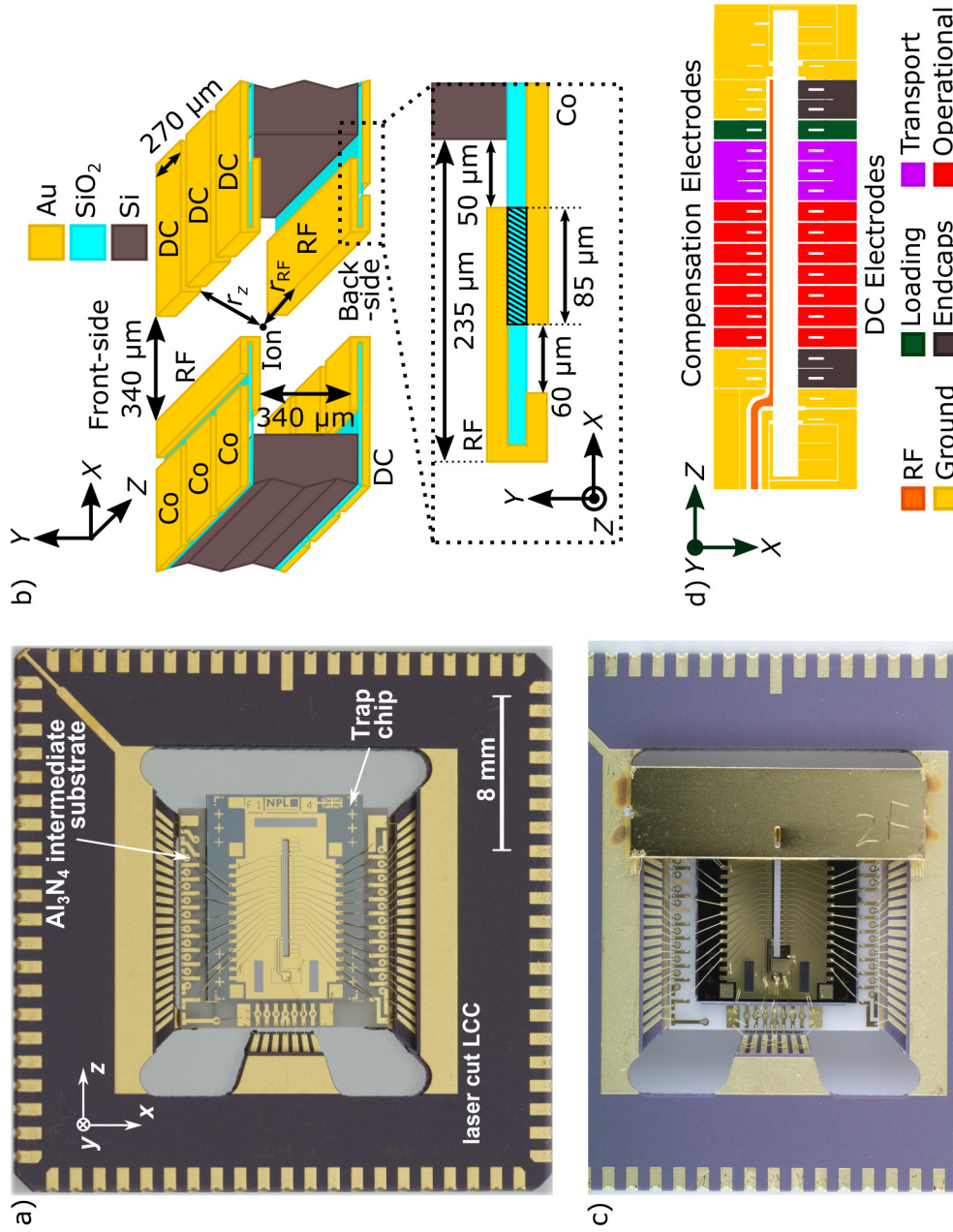


Figure 3.1: a) Picture of an ion trap that has been assembled with the intermediate substrate and CLCC. b) Three dimensional cross section of the trap revealing the rotationally-symmetric structure with the dimensions that are relevant to an individual trapping segment included. The inset highlights the origin of the microtrap capacitance from the overlap of the RF and compensation electrodes through the SiO_2 (shaded area).c) Photograph of the trap with the atomic flux shield attached. d) Not to scale schematic of the function of each segment along the trap aperture.

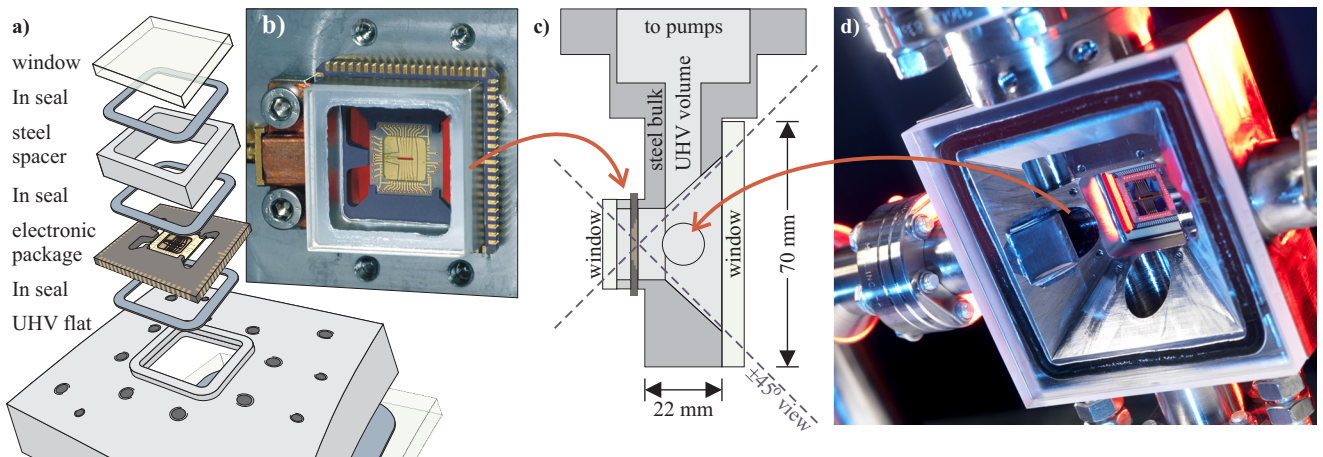


Figure 3.2: UHV chamber of the microtrap. a) Detail of the assembly layers from the trap side of the chamber. All cold-welds are made with indium wire. b) Photograph showing the view of the trap from the small window side once the vacuum chamber is assembled. c) Cross-section of the optical access provided by the vacuum chamber. d) View of the trap from the larger window. Images taken from [154] with author permission.

contaminants and ensure that the cold-welds take. This chamber in conjunction with a non-evaporable getter and ion pump obtain an internal pressure of $\sim 1 \times 10^{-11}$ mbar. The vacuum chamber additionally has a selection of screw-holes drilled into it that allow for the external electronics to be mounted onto the vacuum chamber directly.

3.3 Magnetic Shielding

The vacuum chamber, vacuum pump and a small amount of optics components are contained within a triple layer mu-metal magnetic shield. Together these provide $\sim 1000 \times$ attenuation of external magnetic fields at 50 Hz. The shield is designed such that two adjacent sides can be removed and replaced for access to the inside of the shield.

In addition to the other components, inside the magnetic shield is a set of four magnetic field coils. Three of these are orthogonal to each other to compensate for the ambient magnetic field inside the shield and the fourth set to apply a bias field. The \hat{z} -axis compensation coil is aligned along the axis of the trap aperture and the \hat{x} -axis coil is perpendicular to the floor. Each coil is connected to a high precision source measure

unit (NI PXIe-4139) that supplies DC currents up to 3 A with a maximum DC output power of 20 W with seven digit resolution. Additionally each of the compensation coils is connected in series to a $1\ \Omega$ precision resistor (Wika Instruments CER6000A). The voltage over each resistor is measured with a 7.5 digit digital multimeter (NI PXI-4071) which is used to stabilise the coil currents. The bias coils are positioned such that they create a magnetic field on the zy -plane at an angle of 48° from the \hat{z} -axis. These coils are connected to a similar supply and measurement setup as the other coils except the $1\ \Omega$ resistor is replaced with two resistors in parallel with each other due to the bias coil requiring higher driving currents. Further details of the coils and evaluation of their performance is given in chapter 6.

3.4 Trap Voltage Sources

The RF potential is applied to the trap electrodes by making the ion trap part of a resonant tank circuit. An RF source (HP 8647A) is amplified (via Minicircuits ZHL-1-2W-S+) to $1 - 2$ W of power. The output of this amplifier is fed into a helical resonator [155] (unloaded resonant frequency of 18 MHz) which along with a 7 cm coaxial cable creates the tank circuit. When fully assembled the tank circuit has a resonant frequency of 19.7 MHz and is typically operated with $U_{\text{RF}} = 150\ \text{V}_{\text{pp}}$. A bi-directional coupler samples the RF signal going forwards to the tank circuit as well as the signal that is reflected back.

The DC potentials which are applied to both the DC electrode and compensation electrodes are controlled via an Electric Field Generator (EFG) developed by the Wunderlich group in Siegen [187] which is capable of supplying $\pm 9\ \text{V}$ with 16 bit resolution. These outputs are routed through a re-configurable termination board [112] that maps the EFG output channels to the DC and compensation electrodes on the trap. This gives the possibility of one EFG channel supplying voltages to one or multiple electrodes with those not connected to an EFG channel being grounded. The output of the termination board connects to a DC filter board [112] that is mounted onto the vacuum chamber and makes the contact to the CLCC pins. On the filter board, each

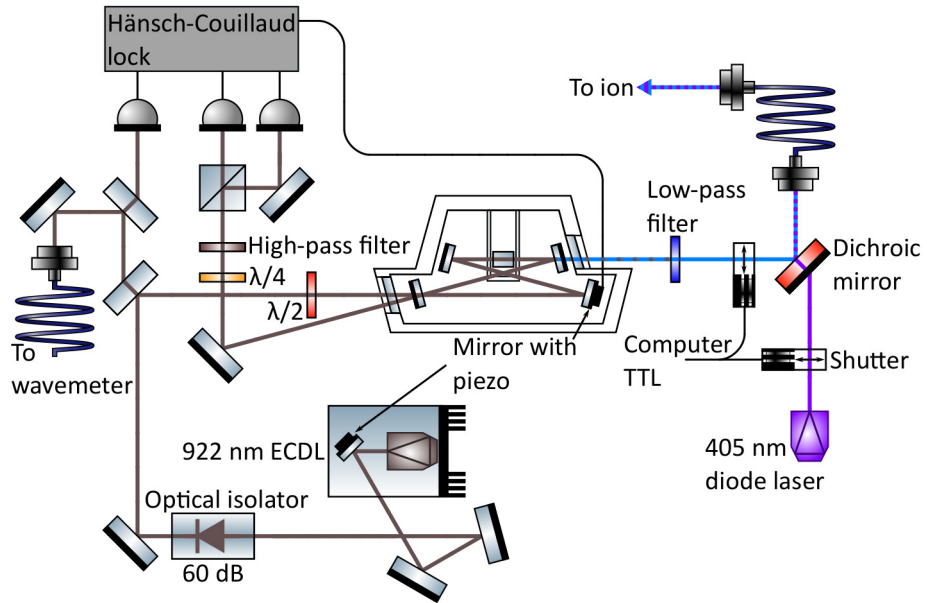


Figure 3.3: Schematic of the 405 nm and 461 nm lasers. At the dichroic mirror the two laser beams are overlapped and coupled into the same fibre.

of the CLCC pins is preceded by a 2nd order RC filter with a -3 dB point of 6 Hz [112].

3.5 405 nm & 461 nm Laser

As described in chapter 2.2 the ion is photo-ionised using a two photon transition. This is achieved using two lasers that are super imposed onto each other before being transmitted down a fibre to the loading zone of the trap. The laser setup (schematic in figure 3.3) utilises 461 nm light that is created from frequency doubling a 922 nm ECDL laser via a frequency doubling cavity with a potassium niobate (KNbO_3) crystal [121]. One mirror in this cavity is attached to a piezoelectric mount that is used to tune the cavity length. This piezo is controlled via a Hänsch-Couillaud polarisation lock [188] to keep the cavity locked to the 922 nm laser. The 461 nm light is delivered to the trap by coupling it into a single mode polarisation maintaining (PM) fibre. Typically the ECDL laser outputs 35 mW of light, which produces up to 2 mW of 461 nm out of the

cavity and $\sim 330 \mu\text{W}$ out of the fibre with waist of $2w_0 = 200 \mu\text{m}$ at the ion. The ECDL has sufficient passive laser stability to not require active stabilisation. A small amount of 922 nm light is picked off for monitoring purposes on a wavemeter.

The second photo-ionisation laser is a simple free running laser diode operating at 405 nm. Due to this transition having a very broad linewidth (0.9 nm) no frequency stabilisation is required for this laser. A dichroic mirror is used to overlap both lasers and couple them into into the same fibre (see figure 3.3). This provides 5 mW of 405 nm light to the trap with a waist of $2w_0 = 180 \mu\text{m}$ at the ion. A pair of mechanical shutters, controlled via the same TTL signal, are used to switch the lasers' on-off state.

3.6 422 nm Laser

The 422 nm laser that is utilised for Doppler cooling, optical pumping and state detection on the $S_{1/2} - P_{1/2}$ transition is generated from frequency doubled laser light at 844 nm (schematic in figure 3.4). A Toptica DL-pro which is capable of emitting $\sim 51 \text{ mW}$ of 844 nm light is used as the laser source. A portion of this light is picked off from the main beam for monitoring on the wavemeter and frequency drift compensation. This compensation is achieved with a side of fringe lock on a tunable etalon (finesse = 115).

The main path of the 844 nm laser ($\sim 45 \text{ mW}$) goes onto a frequency doubling cavity of similar design to the one that produces the 461 nm light. As with the 461 nm doubling cavity, a Hänsch-Couillaud polarisation lock [188] is used to lock the doubling cavity to the fundamental laser. This configuration is capable of providing $\sim 7 \text{ mW}$ of 422 nm light.

The side-of-fringe lock does not provide sufficient frequency stability to maintain Doppler cooling and thus requires further stabilisation. A saturated absorption lock [76] provides this stability using the nearby $5s^2S_{1/2} - 6p^2P_{1/2}$ transition of ^{85}Rb as an absolute frequency reference [189]. The error signal from this lock is applied to the tunable etalon. A double pass AOM at 270 MHz and other downstream AOMs are used to bridge the 440 MHz gap between the two transitions and to detune the laser.

A zero-order output of the double pass AOM is coupled into a fibre that goes to a 2×4 PM fibre splitter to produce three far-detuned beams that are used only to cool hot ions immediately after loading. The fourth output of the splitter leads to an avalanche photodiode (APD) that is used to monitor the power of the beams going to the trap. Each of these three beams has $\sim 2 \mu\text{W}$ of power in them and come to a waist of $2w_0 = 70\mu\text{m}$ at the ion.

The main path of the 422 nm beam is split into two further paths each of which features two double-pass AOMs operating at fixed frequencies which serve as fast, high extinction (~ -80 dB each) optical switches. On one path the output is coupled into a fibre which goes to the other input port of the fibre splitter. Two of the Doppler cooling beams have powers of $3.0 \mu\text{W}$ and one has $3.5 \mu\text{W}$. All three beams are used for micromotion minimisation however only one beam is used during spectroscopy experiments. Between the fibre splitter and the output couplers that direct the beams onto the trap is a fibre switcher that currently is only used to independently control the on/off state of the cooling beams. The second branch of the main path is used to produce σ^- polarised light for optical pumping the ion into the $S_{1/2}(m_j = -5/2)$ state. This beam enters a different fibre that provides $1.5 \mu\text{W}$ of light to the ion with a beam waist diameter of $2w_0 = 70\mu\text{m}$. A Glan-Taylor prism and Berek compensator (required for bi-refringence phase shifts from the vacuum chamber window) are used to control the polarisation of this beam.

3.7 674 nm Laser

Light at 674 nm is used for spectroscopy of the $S_{1/2} - D_{5/2}$ transition and for sideband cooling. Up to 1.3 W of 674 nm light is produced by pumping an M² SolsTiS with 15.5 W of 532 nm light from a Coherent Verdi-V18 (laser schematic in figure 3.5). A small portion (~ 1.5 mW) of the output from the SolsTiS is picked off for power monitoring with a photodiode (PD₀). The main branch of the output passes through an AOM that is used to provide frequency feedback. A fraction of the main beam (~ 7 mW) is then split off for generating the error signal that is used for the frequency stabilisation with an ultra-stable cavity. In this path the beam passes through a variable

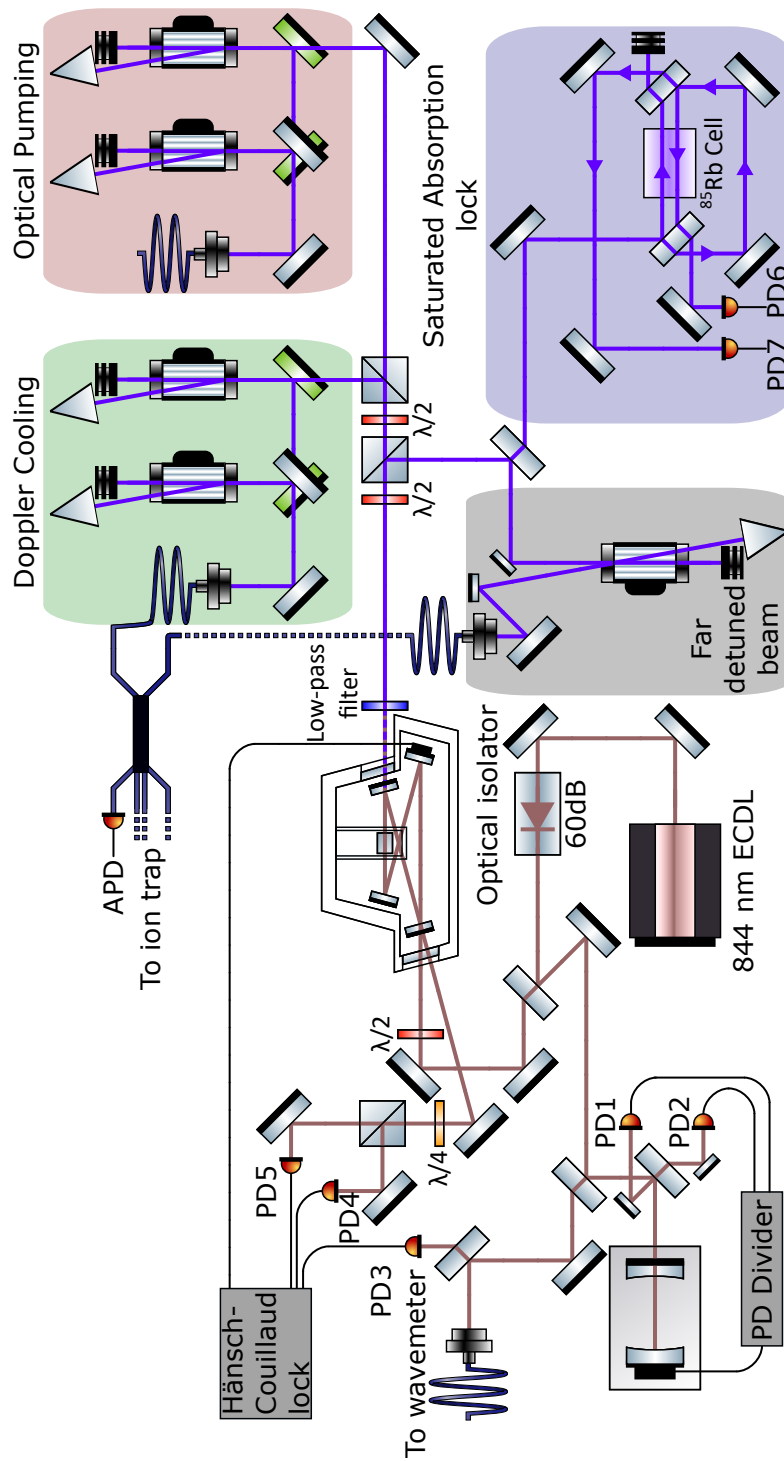


Figure 3.4: Schematic of the 442 nm laser. Here green mirrors are vertically offset from the white coloured mirrors, with the retro-reflectors applying a vertical offset to the beam passing through the AOM. Not pictured are lenses that are used to make a telescope around the AOMs to focus the beams through the AOM crystal and have the offset beams be parallel to each other at the input and output of the telescopes. In practice the two beams to each that pass through the ^{85}Rb cell are superimposed over each other. Here they are separated for visibility of the beam paths and their directions of propagation.

frequency AOM in a double pass configuration that applies ~ 1.6 GHz frequency shift to the laser to bridge the gap between the ion transition and the cavity. Around $200 \mu\text{W}$ of this beam is coupled into a fibre that passes through an electro-optical modulator, which adds 5 MHz sidebands to the laser. The output from this fibre is input to the cavity, which is made from ultra low expansion (ULE) glass and a pair of mirrors whose substrates are made from fused silica on ULE backings. The cavity is encased in a double layer thermal shield, both layers of which are temperature stabilised and mounted on a vibration-isolation stage. A Pound-Drever-Hall lock [190] creates the error signal that is fed back to the VCO that supplies RF to the feedback AOM to give the laser a linewidth of ≤ 0.2 Hz. Additionally a frequency ramp of 85.6 mHzs^{-1} is applied to the RF source of the double pass AOM to account for the ageing drift in the resonant frequency of the cavity. A camera on the output of the cavity is used to check the output mode and to assist in locking the laser to the cavity.

The mainline of the beam after the stabilisation signal has a fraction picked off with a half wave-plate and polarising beamsplitter that serves as a variable power attenuator. Next the beam is divided to go down three similar paths, each of which has a single pass AOM, interferometer setup and a 22 m optical fibre that are used as fibre noise cancellation systems (FNCS). The interferometer measures the phase changes in the laser light between the beam at the input of the FNCS system and the light that is reflected off of the output surface of the fibre. This is then used as the error signal to perform phase modulation on the AOM [191] at the input of the fibre to compensate for any fluctuations induced by the fibre.

At one fibre output ~ 180 mW of light goes through the tuner setup (see chapter 5 for details) to perform fast frequency detuning and power stabilisation. This is followed by a setup used for both fast amplitude shaping and phase control of pulses and for making the pulse bichromatic as required for the Mølmer-Sørensen gate (hereafter referred to as the “pulse control setup”) [142, 175]. The full post-fibre setup schematic is demonstrated in figure 3.6. Bichromatic light is created by applying two RF sources (two HP 8647A synthesisers, HP1 and HP2) to a single-pass AOM. Two variable attenuators are used to finely adjust the RF amplitudes to maximise the bichromatic beat

signal. Some of the light at the output of the pulse control setup is picked off and beat against the output of one of the other FNCS setups. The main output of the pulse control setup is coupled into a fibre that leads to the inside of the magnetic shield.

The third FNCS system is intended to be used as an out-of-loop measurement of the laser frequency stability by performing a beat measurement against a frequency comb setup in the adjacent laboratory [192].

Inside the shield the fibre output is split with a fraction of the beam power being incident on an APD used for monitoring the laser power. The main beam path is reflected off of a mirror mounted on a pair of piezo adjusters that are used for fine adjustment of the beam pointing. After this the beam passes through the ion trap delivering up to 12 mW of 674 nm light that is focused to a waist of $2w_0 = 45 \mu\text{m}$ at the ion. After the trap a quadrant photodiode (QPD) is used to monitor the beam pointing when the piezo adjusters are being altered. The 674 nm probe beam is $\sim 52.3^\circ$ from the trap aperture axis which corresponds to it being $\sim 100.3^\circ$ from the bias magnetic field vector.

3.8 1033 nm Laser

The 1033 nm laser is required to return the ion to the ground state after it is excited to the metastable $D_{5/2}$ state via the $^2D_{5/2} - ^2P_{3/2}$ and $^2P_{3/2} - ^2S_{1/2}$ transitions. A Toptica DL-pro, similar to the one used to generate the 844 nm light (figure 3.7) supplies light at this wavelength. The output of the laser is split into two paths. One goes to an input of a 2×2 fibre coupler; one output of which goes to the wavemeter and the other goes to a side-of-fringe lock provided by a low drift cavity [142]. The other fibre takes light to a pair of double-pass AOM setups, one of which is used as the quencher and the other as the clearout with the two beams being 300 MHz detuned from each other, which is required to perform sideband cooling optimally [81, 138] (from equation 2.37). These two beams are coupled back into fibres which lead to a 2×2 fibre splitter. One of the splitter outputs goes to a photodiode for monitoring and the other leads to the trap, providing up to 700 μW and 100 μW of clearout and quench light respectively that is focused to a waist of 180 μm at the ion. With this setup each beam can be

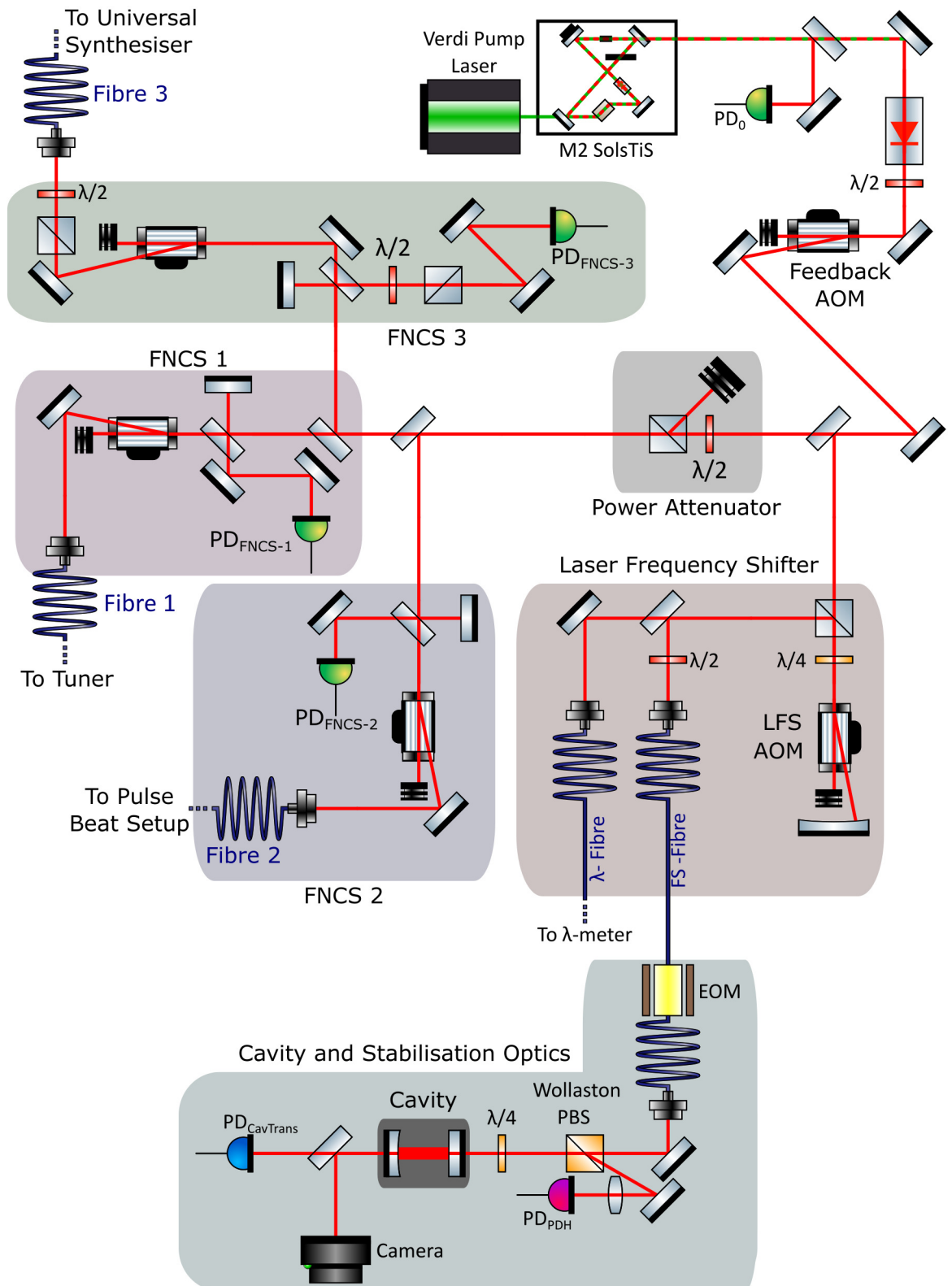


Figure 3.5: Schematic of the 674 nm laser up to the three FNCS setups.

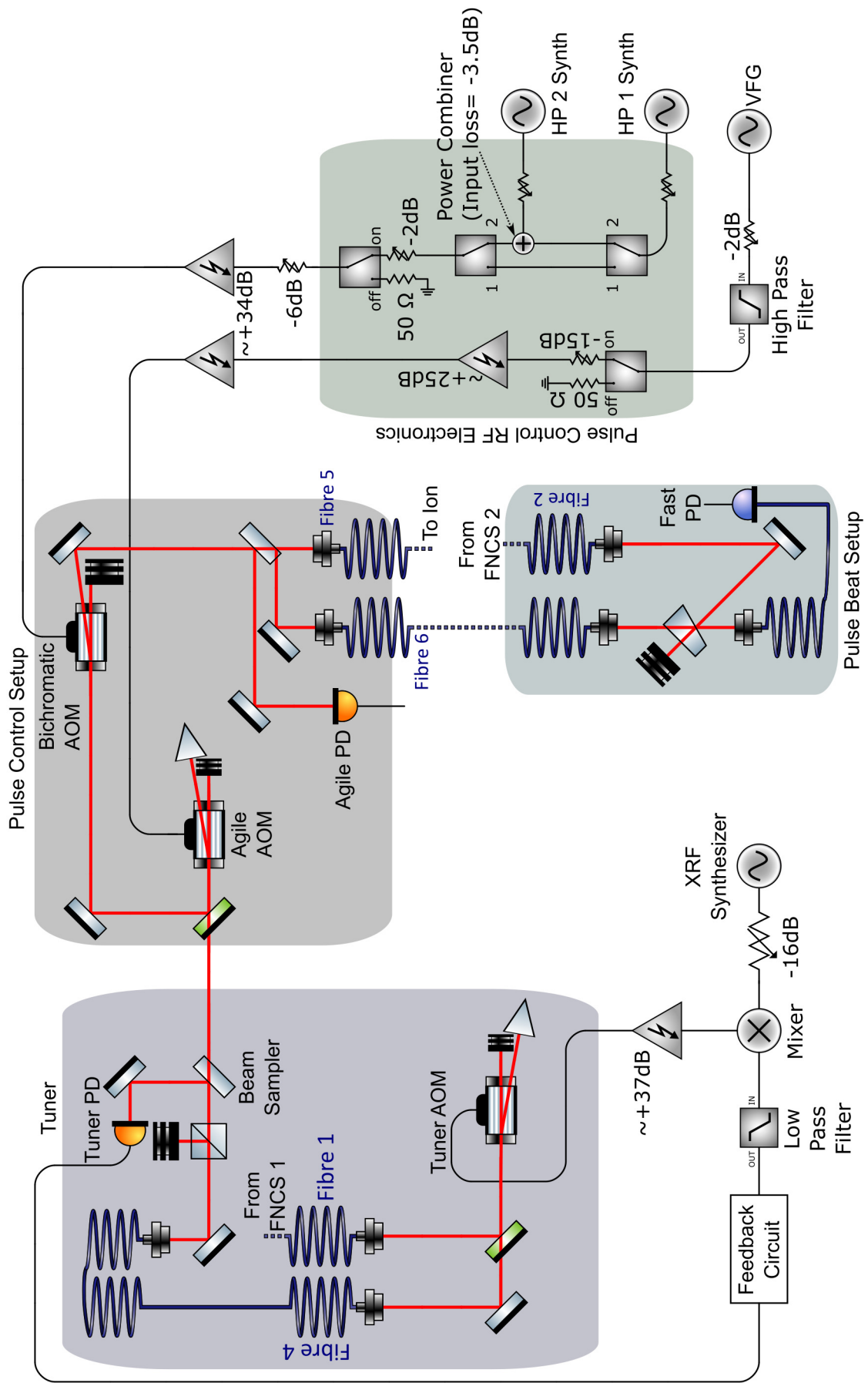


Figure 3.6: Optical circuit for the tuner and pulse control setup. Schematic for the RF control electronics are also included.

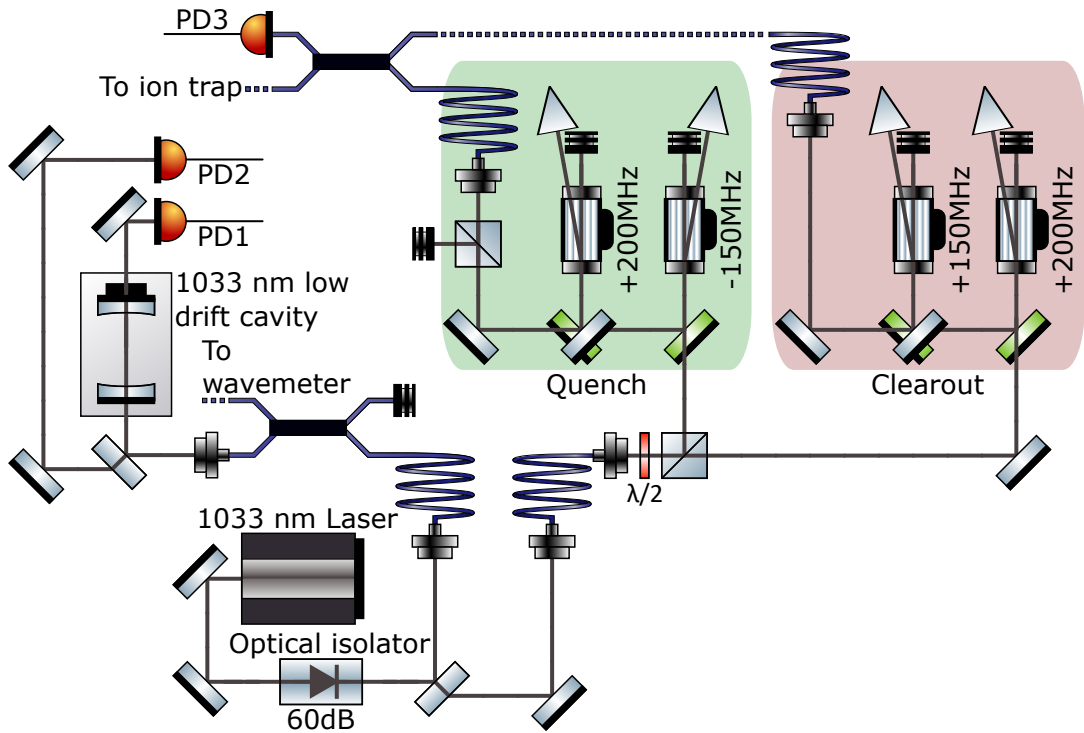


Figure 3.7: Schematic of the 1033 nm laser. Here green mirrors are vertically offset from the white coloured mirrors, with the retro-reflectors applying a vertical offset to the beam passing through the AOM. Not pictured are lenses that are used to make a telescope around the AOM to focus the beams through the AOM crystal and have the offset beams be parallel to each other at the input and output of the telescopes.

independently switched on and off with a high degree of extinction.

3.9 1092 nm Laser

The 1092 nm laser light is used to depopulate the $D_{3/2}$ dark state that the ion can decay into from the $P_{1/2}$ excited state. The light is generated from a neodymium-doped laser fibre [76], with a 825 nm diode laser as the pump (figure 3.8). A diffraction grating couples light back into the doped fibre to form the laser cavity. This laser has a large number of cavity modes, which have 15 MHz separation under a ~ 1.5 GHz envelope. The laser does not feature any form of active frequency stabilisation as when one mode drifts out of resonance with the ${}^2D_{3/2} - {}^2P_{1/2}$ transition an adjacent mode will drift into resonance. A polarisation controller is used to match the polarisation of the output

to the angle at which the reflection from the grating is maximised.

A small amount of the output light is picked off for monitoring on a photodiode and the wavemeter. Coarse adjustments to the wavelength can be made by adjusting the intra-cavity etalon and finer levels of adjustment are made by controlling a piezo servo on the diffraction grating.

The output of the laser is coupled into a 1×2 fibre splitter that provide two outputs to the trap, each of which provides ~ 1.8 mW to the ion with a spot size of $2w_0 \approx 580$ μm . One output of the fibre splitter goes through a half-wave plate and Glan-Taylor prism that is used when coarsely minimising the magnetic field to which the ion is exposed (see section 3.12.5). The second beam passes through free space and is utilised to maintain fluorescence when the magnetic field is minimised.

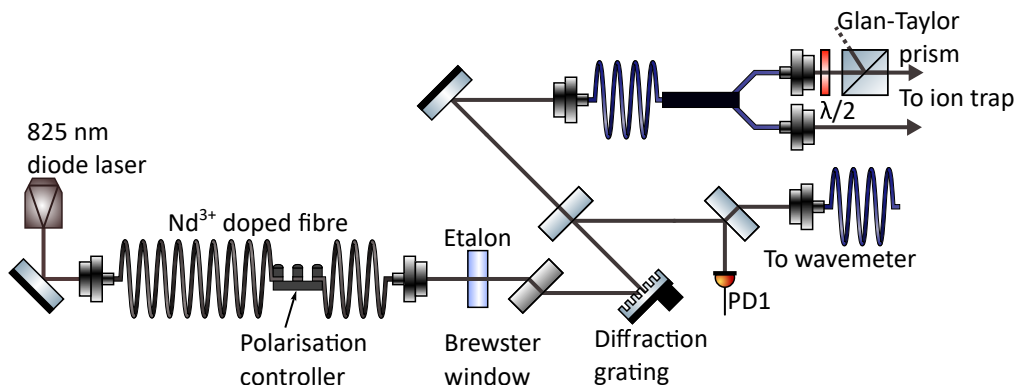


Figure 3.8: Schematic of the 1092 nm laser. The two output beams are setup to be roughly orthogonal to each other.

3.10 Imaging Systems

In order to determine the state of the ion after probing with the 674 nm laser, fluorescence from the 422 nm light that is used to perform electron shelving must be collected and detected. A pair of high numerical aperture ($\text{NA} = 0.43$) lenses are placed facing the windows of the vacuum chamber to give a $\sim 10\times$ magnification of the focal point in the trap aperture. A photomultiplier tube (PMT) (Electron Tubes 9893/350A photo-multiplier tube) and an electron multiplying CCD (EMCCD) camera (Andor iXon Ultra 860) are positioned to observe fluorescence from the small and large

windows of the chamber respectively so that each observes a different side of the ion trap. Both devices are fitted with optical filters that block light from the 674 nm, 1033 nm and 1092 nm lasers reaching the detectors. Light at 405 nm and 461 nm can still reach the sensors of both instruments, however these lasers are only used during trap loading. When these lasers are incident on the trap, the PMT is not in use and the EMCCD camera has its shutter closed to prevent the sensor from being degraded by light at these wavelengths. The PMT, with all lasers off, has a dark count of $\sim 10 \text{ s}^{-1}$.

In order to determine the ion's state a thresholding operation is applied to the PMT reading such that a count rate above the threshold is counted as the ion being in the ground state and below is counted as being in the excited state [22]. This threshold, \mathcal{T} is calculated as

$$\mathcal{T} = \frac{(L - S\sqrt{L}) + (D + S\sqrt{D})}{2} \quad (3.1)$$

with D is the count rate when the ion is not fluorescing, L is the count rate when fluorescing and

$$S = \frac{L - D - 2}{\sqrt{D} + \sqrt{L}} \quad (3.2)$$

is an additional safety factor that places the threshold an equal number of standard deviations between L and D . For multiple ions a separate threshold is calculated for the different number of ions that could be fluorescing at once; Here L is replaced with L_N/n where L_N is the measured fluorescence when all ions are fluorescing and $n = 1, 2, \dots, N$ is the number of ions that are expected to fluoresce. In the future the Andor camera will be used to determine which individual ion(s) are fluorescing for a particular measurement, but this is yet to be implemented.

3.11 Control Systems

All experiment control sequences and data collection are performed by a single National Instruments (NI) PXI machine, containing an embedded control unit (PXIe-8133) and 13 PXI cards that are listed in table 3.1.

The high precision timer card serves two purposes; first to measure the count rate from the PMT, which is first converted to a digital signal by an ORTEC am-

Card	Description	Quantity
NI PXI-6608	High precision timer	1
NI PXIe-6537	High speed digital I/O	1
NI PXI-6733	Analogue output	2
NI PXI-6254	Analogue input	1
NI PXIe-4139	Source measure unit	4
NI PXI-4071	Digital multimeter	4

Table 3.1: Table of National Instruments PXI cards that are mounted into the PXI machine to control the experiment.

plifier/discriminator, photon signals from the PMT so that the photon count rate can be determined and secondly to generate the clock signal for the digital I/O card. The digital I/O card provides 32 independent channels that are used to provide TTL signals that control the mechanical shutters, RF switches that control the AOM on/off states and trigger other devices that are required to run the experimental routines. One of the analogue output cards is used to control the VCO which controls the 422 nm laser frequency. The analogue input card is used to measure photodiode signals as well as thermistors that are embedded in the oven and hotplate used to load ions. Each source measure unit is used to supply current to a magnetic field coil, which in turn is monitored with one of the digital multimeter cards.

All of the experimental techniques in the next section of this chapter are controlled from this PXI machine with control software written in LabVIEW, with the exception of the micromotion minimisation. For this the EFG and lasers are controlled through LabVIEW and proprietary software reads the time-to-amplitude converter of the PMT. All RF voltage sources and the master oscillator of the PXI machine are phase-locked via a stable 10 MHz reference signal derived from a local hydrogen maser.

3.12 Procedures and Results of Standard Operation

3.12.1 Loading Ions into the Trap

The setup used to generate the flux of atoms required to generate ions is a two stage oven-hotplate system similar to the one described by DeVoe [193].

To load ions into the trap a tantalum hotplate containing a reservoir of Sr is heated

to 190 – 230 °C, evaporating atoms towards the trap [112, 121]. A thermistor inside the hotplate provides a feedback signal that controls the on/off state of the hotplate preventing the temperature from exceeding the above temperature range.

If the reservoir of Sr becomes depleted then an oven containing a reservoir of SrO:Ta can be heated to ~ 800 °C to replenish the hotplate [112]. A thermistor inside the oven controls the oven temperature in the same manner as the hotplate. The oven is setup such that it has no direct line of sight to the trap aperture. This two stage system is required due to free Sr being reactive with the atmosphere.

The two photo-ionisation lasers are alternated with detection periods of the PMT in conjunction with the EFG shuttling newly loaded ions into the operation zone. In the operation zone the Doppler cooling lasers and far detuned beam are continually applied to both cool any loaded ions and detect if an ion has been loaded. Typically it takes ~ 180 s to load an ion after beginning the load routine.

3.12.2 Micromotion Minimisation

As mentioned in section 2.1.2, stray DC potentials can shift the ion away from the RF null at the centre of the potential well and induce excess micromotion on the ion. Applying a DC voltage onto one the compensation electrodes and one of the DC electrodes of trap zone that the ion is trapped in allows for the position of the ion to be fine tuned to the location of the RF null. This can be used in combination with different methods of evaluating the severity of the excess micromotion to minimise it. Here a summary of three methods, of varying sensitivity, are presented.

The first and least sensitive is to adjust the ion position whilst observing the ion fluorescence on the EMCCD camera. When the position of the ion is least affected by changes in the RF voltage amplitude then the micromotion is considered reduced as far as this method will allow [104].

The second method is to use the RF-photon correlation technique [76, 104, 194]. Here the ion's fluorescence is modulated at Ω_{RF} due to the Doppler shift from the micromotion, with the modulation amplitude being proportional to the severity of the excess micromotion. Due to the high frequency of the modulation, a histogram of

photon arrival times is created with a time-to-amplitude converter which correlates the photon arrival times in the PMT to the phase of the RF drive [104,135]. This technique relies on the lifetime of the $^2P_{1/2}$ state ($\tau = 7.35$ ns) being shorter than the period of the micromotion ($1/\Omega_{\text{RF}} = \sim 51$ ns), which permits multiple scattering events per micromotion cycle. Thus by adjusting the ion's position towards the RF null, the amplitude of the micromotion can be minimised. It should be noted that minimising the modulation amplitude on just a single cooling beam may project components of the micromotion onto the plane perpendicular to the laser's \hat{k} -vector. Thus to completely minimise the micromotion this process must be iterated on all three cooling beams. To perform this technique the 422 nm laser is detuned to $-\Gamma_{\text{eff}}/2$, to the steepest part of the lineshape, so that the modulation amplitude from the Doppler shift is maximised. However, if the micromotion is severe enough it can become a significant component of the ion's motion; this has the effect of "flattening" the lineshape [104]. This decreases the lineshape gradient, which can create the impression that the micromotion has been minimised when it actually has significantly increased. Thus to confirm that the micromotion has been minimised frequency scans of the 422 nm lasers are performed (see section 3.12.3).

The third and most sensitive technique is to scan of the 674 nm probe laser over the micromotion sidebands in the motional spectrum of the ion to measure the coupling strength of the probe laser to the micromotion directly. Adjusting the position of the ion to minimise these sidebands will minimise the micromotion. Although this method is the most sensitive the apparatus only provides a single 674 nm beam and as a consequence can result in part of the micromotion being projected onto the plane that is normal to the \hat{k} -vector of the laser.

3.12.3 Doppler Cooling Scans

With the micromotion minimised via the RF correlation technique (section 3.12.2) the lineshape of the cooling transition for each of the three cooling beams are sequentially obtained. To do this the frequency of the double pass AOM that inputs light to the saturated absorption lock (see section 3.6) is varied to scan the cooling laser over the

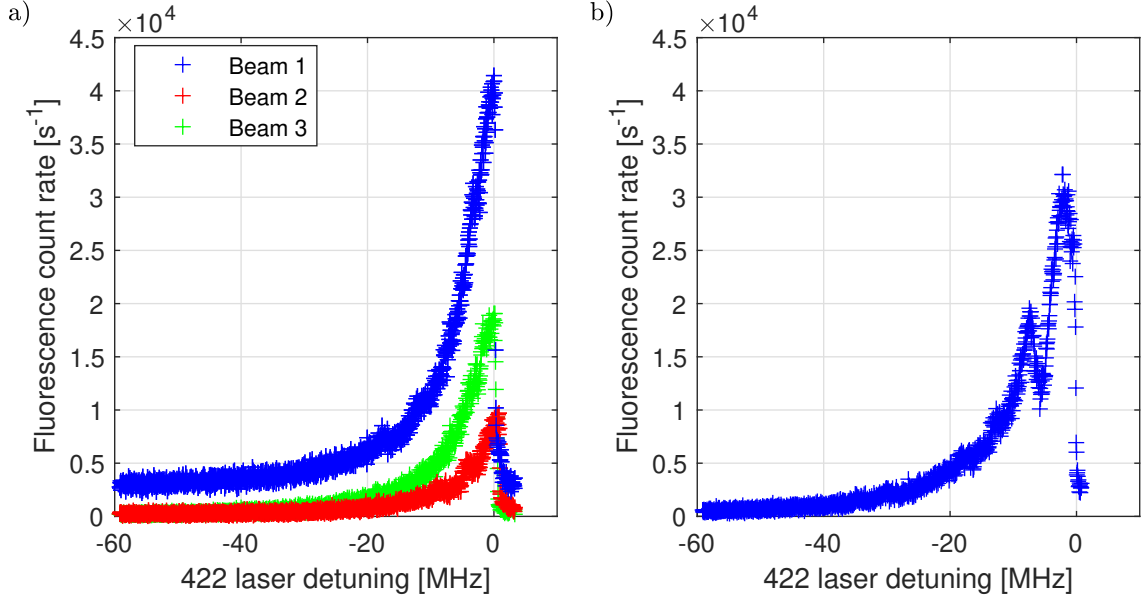


Figure 3.9: a) Cooling transition for each of the three cooling beams. b) Cooling lineshape with coherence null. Here the 1092 nm laser would have a detuning of ~ 6 MHz.

$S_{1/2} - P_{1/2}$ transition (example depicted in figure 3.9a). At zero detuning and above the transition begins to mostly cycle blue detuned photons, adding momentum to the ion rather than removing it. As the ion is heated from this it undergoes an increase in velocity and shifts the cooling transition out of resonance with the laser causing the reduction in fluorescence. If the excess micromotion is poorly compensated then the lineshape will not be a purely singular Lorentzian profile and may appear to be broadened or flattened. Once the cooling scans have been taken, the laser is detuned to $\Gamma_{eff}/2$ so that the cooling efficiency of the ion is maximised.

An additional feature that can sometimes be observed in the scans of the 422 nm are coherence nulls (example in figure 3.9b). Here the ion is driven from the $S_{1/2}$ state into the $D_{3/2}$ and back without scattering a 422 nm photon. This occurs when the detuning of both the cooling and 1092 nm repumper are equally detuned from the $P_{1/2}$ state [119,195]. This can occur with this apparatus due to the 1092 nm laser not featuring frequency stabilisation.

3.12.4 Optical Pumping

To ensure that the ion begins in the $S_{1/2}(m_j = -1/2)$ state the ion undergoes optical pumping where circularly polarised 422 nm light drives the $S_{1/2} - P_{1/2}$ transition. This method of optical pumping exploits the selection rules [128] of the $^{88}\text{Sr}^+$ ion which dictate that the polarisation of the light and its \hat{k} -vector relative to the magnetic field will only drive certain transitions between the m_j sub-levels of the two states. With σ^- light the only allowable transitions have $\Delta m_j = -1$. Once in the $P_{1/2}$ state the ion can spontaneously decay into either of the $S_{1/2}$ sub-levels. If the ion decays into the $S_{1/2}(m_j = +1/2)$ sub-level then it will be re-excited and if it decays into the $S_{1/2}(m_j = -1/2)$ state then no further excitation is possible. The efficiency of the optical pumping is measured by comparing the number of excitation events that occur during a detuning scan of the $S_{1/2}(m_j = -1/2) - D_{5/2}(m_j = -5/2)$ and $S_{1/2}(m_j = +1/2) - D_{5/2}(m_j = +5/2)$ transitions. After 10 μs the ion is initialised into the $S_{1/2}(m_j = -1/2)$ state with a probability measured to be $\geq 99.5\%$.

3.12.5 Minimising the Magnetic field

The motional spectrum of the $S_{1/2} - D_{5/2}$ transition possesses ten Zeeman components each consisting of a carrier and motional sidebands (as well as far detuned micromotion sidebands). In order to perform precise spectroscopy experiments the quantisation axis must be well defined. This requires the ambient magnetic field from the Earth, ion pump, etc to be minimised prior to applying the bias magnetic field which separates out these components.

A coarse method of minimising the magnetic field can be undertaken by exploiting the selection rules of the quadrupole transition [195]. The unpolarised 1092 nm is blocked and the remaining 1092 nm beam's polarisation is alternated between vertical and horizontal; minimising the fluorescence each time by coarsely adjusting the coil currents. By iteratively repeating this process the Zeeman splitting is reduced to ~ 200 kHz (≈ 2 μT) when the motional spectrum of the ion is measured with the 674 nm laser. With the coarse adjustments complete the unpolarised 1092 nm beam is unblocked so that the ion may be able to cycle the 422 nm transition in the reduced

magnetic field.

Next, fine adjustments are made to the compensation coil currents to further minimise the magnetic field by making small changes to the current in one coil followed by scanning of the 674 nm, then iteratively repeating through all the coils until the Zeeman components overlap with each other. As the components become overlapped the scan range is reduced to scanning over only the carrier and the currents are adjusted until the Zeeman components of the carrier appear to be fully superimposed over each other (which occurs at ~ 15 kHz $\hat{=}$ ~ 0.15 μ T).

Once the ambient magnetic field is minimised a 290 μ T field is applied to the ion with the bias coils.

3.12.6 Spectroscopy Sequencing

With both the micromotion and ambient magnetic field minimised and the bias field applied the ion is coherently manipulated on the $S_{1/2} - D_{5/2}$ quadrupole transition. A typical spectroscopy experiment is shown in figure 3.10 and proceeds as follows. Beginning with a Doppler cooled ion (step 1), the ion is optically pumped into the $S_{1/2}(m_j = -1/2)$ state with σ^- 422 nm light (2), then sideband cooled into the $n = 0$ vibrational state (3 & 4). Extra optical pumping pulses are periodically applied during step 3 to prevent the ion decaying into the $S_{1/2}(m_j = +1/2)$ state. During steps 3 & 4 1033 nm light is applied to maintain efficient cooling. Following this the experiment probe pulses are applied (5). Once complete the state of the ion is read out (6) using Dehmelt's electron shelving method [22] with the 422 nm light to the ion. After state detection the ion is returned to the ground state by applying 1033 nm clearout light (7). This sequence is repeated for a user specified number of iterations and state readout results are averaged together to determine the excitation probability. The results of specific spectroscopy routines are discussed in chapter 7.

3.12.7 Ion Trapping Lifetimes

One key metric of evaluating the performance of ion trap devices is the duration for which one or more ions may be contained within the trap without being lost. Multiple

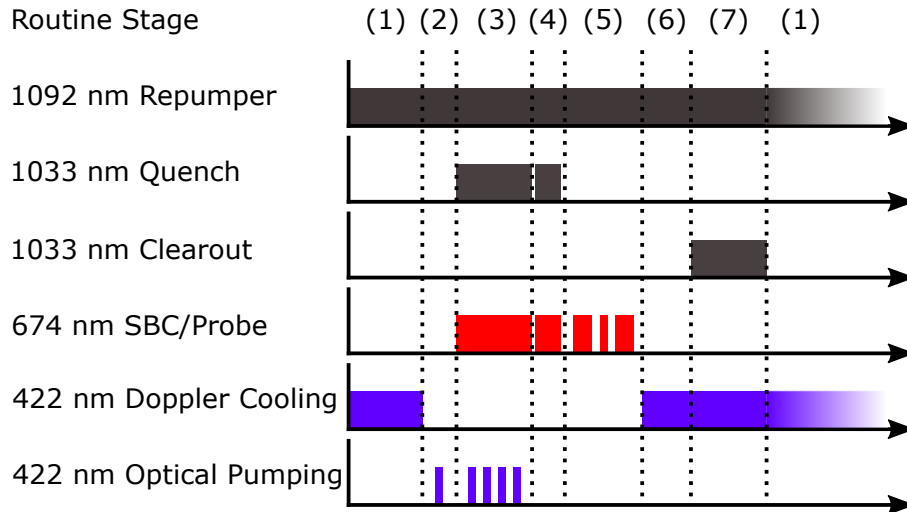


Figure 3.10: Example control sequence of which lasers are used at different stages of the routine: 1) Doppler Cooling, 2) Optical pumping, 3) Sideband cooling with additional optical cooling pulses, 4) Additional sideband cooling without optical pumping, 5) Experimental probe routine, 6) Ion state readout, 7) State clearout. 1092 nm light is applied throughout the whole sequence. The full experimental routine can be executed in less than 10 ms. Once the routine is completed it resets to stage 1. Typically a sequence is repeated 100 to 500 times per experiment.

possible mechanisms exist that can eject ions from the trap, with the three most likely to occur in this apparatus being

- 1) instabilities in the trapping parameters coinciding with the harmonics of the secular frequencies (as outlined in section 2.1.1),
- 2) background gas collisions and
- 3) the Doppler cooling laser going out of lock in such a manner that its frequency drifts to the blue side of the $S_{1/2} - P_{1/2}$ transition and heats ions out of the trap.

Points (1) and (2) become more prominent as the number of ions being stored in the trap increases. In the first case due to the increasing number of secular frequencies and in the second the increasing number of ions allow for an increased number of collision events to take place along the length of the ion string. It should be noted that whilst background gas collisions can destabilise and destroy large strings of ions, it is possible that the collision does not end up ejecting all ions from the trap but instead removes only a fraction of the string or, if the string is small enough, only heats the ions without removing them, allowing the string to reform. Although the laser lock is independent

of the number of ions in the string, increasing number of ions will eventually result in the string becoming long enough that some ions (namely those far from the centre of the cooling beam) may not receive enough scattering events to be sufficiently cooled. The effects of sympathetic cooling [196,197] can mitigate this, as adjusting the pointing of the Doppler cooling beams such that each beam illuminates a different part of the string.

The number of ions in the trap is monitored by observing the fluorescence from the string as it is illuminated by the Doppler cooling laser on the EMCCD. A dedicated LabVIEW routine, written for this monitoring purpose, retrieves an image from the EMCCD once per second. Each single-shot image then has the grey levels of its columns summed, such that any columns where the ion is present will contain a higher value than those that do not. Next a peak finding algorithm is used to determine the number of peaks that are visible amongst the summed columns. A threshold is applied to discount any small peaks that may arise from the image background.

It would be expected that a simpler method to determine the number of ions would be to use the fluorescence signal on the PMT. In this, it would be expected that each ion would provide a similar fluorescence signal and thus the number of ions could be counted by dividing the measured signal by the one-ion fluorescence count. However, due to the unequal, spatially dependent illumination of the ions, combined with the inter-ion spacing being determined by the number of ions in the trap [113] a change in the number of ions may result in the fluorescence counts per ion changing as well. This can also be further complicated by the different Doppler beams possessing differing intensities. Despite this it is possible to simply monitor both at the same time.

With this the storage times for one, two and six ions were monitored. A single ion could be held in the trap seemingly indefinitely (storage times exceeding five days) and is only lost when the apparatus is shutdown or deliberately removed from the trap. Two ions could be stored for several days without being lost. Additionally the trap is capable of storing a single ion for over 12 hours without the application of the Doppler cooling lasers. For six ions, the string was maintained for 11.2 hours before one ion was lost from the string, after which the remaining five ions were held for a further

Chapter 3. Background of Apparatus

17.9 hours after which the string was lost by the cooling laser going out of lock and heating the ions out of the trap. Examining the fluorescence counts reveals that after a background gas collision onto a two ion string will recrystallise after ~ 2 s.

Chapter 4

RF Characterisation of Microtrap Chips

4.1 Introduction

As described in section 2.6.3, when a laser pulse is applied to the ion, the various Fourier components of the pulse may induce off-resonant excitations onto other nearby transitions. Increasing the RF voltage applied to the trap will increase the separation of each of the motional sidebands and the carrier from each other and reduce the likelihood of off-resonant excitations from occurring. Substituting equation 2.6 into equation 2.10 shows that the \hat{x} - and \hat{y} -axis secular frequencies of the ion are proportional to the RF voltage amplitude, U_{RF} , that is applied to the trap; thus it is desirable to maximise the applied RF voltage to the trap. Furthermore, operating the trap with higher U_{RF} values requires larger RF frequencies to be applied, so as to retain low values for the q_i parameters (and additionally, requires adjustments to the DC voltages to retain a consistent value for the a_i parameters). This in turn also gives higher secular frequencies due to the linear Ω_{RF} term at the start of equation 2.10. A secondary benefit to operating with a larger value for U_{RF} is that the stronger electric field provides greater isolation from the external environment and improves the ion storage time. For storing strings of multiple ions, the extra motional modes added by the ion-ion Coulombic interactions can be parametrically excited via the same effects described by equation

2.11, making it difficult to retain the strings for long periods of time. Therefore, the ability to keep the q_i parameter low, with higher U_{RF} and Ω_{RF} , allows for the trap to be operated in the low q_i region of the stability diagram (see figure 2.2b), away from these instabilities. This, together with the improved environmental isolation provided by the higher U_{RF} , enables long storage times for strings of ions.

In practice however, the RF voltage cannot be increased indefinitely; eventually the ion trap device will experience breakdown across the gaps between the different electrodes or between the electrodes and nearby grounded surfaces across exposed dielectric sections of the trap. Micro-scale ion traps in particular are at risk from this due to the short distances involved between the high voltage RF and grounded parts of the device. This breakdown manifests either as a change in the electrical properties of the trap due to breakdown through the bulk material, or as surface flashover between the RF electrode and exposed features at low DC or ground potentials [150,198–200]. Manufacturing techniques to improve electrical breakdown performance include the etching and milling of the exposed dielectric surfaces [201] or redesigning the device with alternative material systems [202]. To aid with device development, including the microfabrication process, it is essential to accurately characterise the RF performance of each individual device as they are manufactured. Measurements have shown that the heating rate of a trapped ion is dependent on U_{RF} as increasing this voltage results in an increase in the surface flashover [167] if it is present in the device. The onset of even the faintest breakdown likely generates excessive electric field noise in the region it occurs. In turn this will increase the ion heating rate and lead to reduced coherence in controlling the sensitive quantum states of the trapped ions. It has also been observed that surface flashover, if significant enough, can reduce the trapping times and trap reliability [199]. It is therefore important to determine the bounds of breakdown-free operation for ion microtrap devices.

The following sections of this chapter will describe the RF testbed that was developed to evaluate the ability of ion microtraps with the 3D structure described in section 3.1 to withstand high RF voltage amplitudes. The testbed is designed for the sensitive detection of surface flashover, whilst measuring the U_{RF} being applied to the

RF electrodes of the trap in order to determine the suitability of each device for ion trapping. Much of the testbed operation is automated to provide straightforward measurements of the trap resonance, calibration of U_{RF} and the value of U_{RF} that flashover is detected at.

4.2 Apparatus

For testing under the application of large RF amplitude U_{RF} , the microtrap device being tested is contained within an RF setup similar to the main experiment. The traps are kept in high vacuum (HV) below 10^{-4} mbar to avoid gas-based discharges. This was achieved using a stainless steel chamber, similar to the form of that detailed in section 3.2 where the ceramic carrier forms the electrical feed through for the vacuum. This procedure is almost identical to that used to package a device for ion trapping experiments [154]. In the apparatus described here, butyl rubber under pressure forms the vacuum seal between the stainless steel and ceramic chip carrier in place of the indium seals. This sealing method is sufficient for pumping down to pressures of 10^{-7} mbar yet it permits rapid and straightforward swapping of devices under test.

4.2.1 Radiofrequency System

The RF circuit for driving the microtraps and measuring the applied amplitude U_{RF} is illustrated in Figure 4.1. The output of the synthesiser (HP 8647A) is amplified by 36 dB (by a Minicircuits ZX60-100VH+) before being transmitted to the input of the helical resonator. Directional couplers (Minicircuits ZMDC-10-1) prior to the helical resonator sample the forward and reflected powers to and from the resonant circuit (*i.e.* the LC tank circuit formed by the resonator and microtrap under test, in a similar configuration to what is used on the main experiment apparatus) respectively. RF power tolerances of the components limit the resultant U_{RF} to ≤ 500 V. The front- and back-side compensation electrodes are each connected to ground via a 50Ω resistor, forming RF potential dividers with trap capacitances $C_{1,F}$ and $C_{1,B}$ (see section 3.1) respectively. Since the reactance of the capacitors dominates the potential divider

($X(C_1) \geq 310 \text{ k}\Omega$ at $\Omega_{\text{RF}}/2\pi \approx 10 \text{ MHz}$), U_{RF} can be sensed across the $50 \text{ }\Omega$ resistors with negligible perturbation to the resonant frequency of the tank circuit. Calibration of the divider performed at Ω_{RF} enables the value of U_{RF} to be measured in the same way as in [154]. An RF switch enables U_{RF} to be measured on two separate compensation electrodes, typically from equivalent positions on each side of the trap, which is important to establish that both sides of the device operate as expected. A custom PCB, designed to fit onto the vacuum chamber in a similar fashion to the RC filter board described in section 3.4 [112], containing in-line $50 \text{ }\Omega$ resistors connects the CLCC pins to SMA jacks for straightforward use and aids in the ease and speed of changing over the trap under test. The detected RF signals from the $50 \text{ }\Omega$ resistors are amplified by a second 36 dB amplifier and transmitted forwards to the power meters. A digitally controlled step attenuator (Minicircuits ZX76-31R5-PN+) is used to prevent downstream components from being damaged when higher RF powers are in use.

The testing sub-routines used for this apparatus require the RF power to be measured over a wide range, and thus requires two separate power meters; one for a low-power range ($-60 \text{ dBm} \leq P_{\text{meas}} \leq +5 \text{ dBm}$) and the other for a higher-power range ($-30 \text{ dBm} \leq P_{\text{meas}} \leq +20 \text{ dBm}$). RF switches are used to select the relevant power meter as well as the desired path to measure. The circuit provides four signal paths to measure:

- 1) The forward-going signal to the helical resonator (P_{fwd}),
- 2) The signal reflected from the resonator (P_{rfl}),
- 3) The signal sensed from the front-side of the device ($P_{\text{p},f}$) and
- 4) The signal sensed from the back-side of the device ($P_{\text{p},b}$).

All the RF switches and the step attenuator are controlled via a multiform I/O device (NI USB-6001) that is also used as an analogue-to-digital converter for the analogue signal from the low-range power meter. The choice of RF power meters over a spectrum analyser for power measurements was motivated by cost considerations. The low-range power meter outputs an analogue voltage signal that is proportional to the power it measures in dBm. An automated calibration of this power meter is performed by matching its output to the digital, high-range one in the region of measured powers

where their responses are both linear (-30 dBm to 0 dBm). The calibration routine is iterated so that in the region of overlap the two power meters have less than 0.2% in the difference between the RF powers they measure. Every power measurement that is taken is an average of 10 readings from the power meters. The control software chooses which power meter to use based on what the last individual power measurement was. If the recorded power crosses a -5 dBm threshold then the setup will switch to use the appropriate power meter for measuring above or below this power threshold. This threshold is chosen as the response of both power meters is still linear at powers around this value with enough of the low-range power meter's measurement range above it for an accurate first measurement to be made. During normal operation large step changes in the power that would potentially damage the low-range power meter are not expected to occur. The control software is also setup to remember which power meter was last used for each measurement path so as to prevent the circuit damaging the low-range power meter by switching from a path that measures low-power to one where high-powers are present.

4.2.2 Optical System

To detect breakdown in all locations across SiO_2 gaps, two distinct areas around each RF electrode must be observed: 1) at the external surface between the RF and compensation electrodes at normal incidence, and 2) at the internal surface between the RF electrodes and the doped Si of the microstructure at an oblique angle of $\sim 45^\circ$ (see Figure 4.2). Four independent, identical imaging systems afford simultaneous observations of each location on the device as the applied U_{RF} is ramped up. All systems can detect light emitted from surface flashover, but those looking at external surfaces are better suited to detecting light from bulk breakdown. In each system, an aberration-corrected objective lens ($f = 80$ mm, $f/4$, $\text{NA} = 0.12$) images the internal and external surfaces with magnification = -1.1 and -0.57 respectively, and corresponding depths of focus = $80\ \mu\text{m}$ and $77\ \mu\text{m}$, onto a high-sensitivity monochrome CMOS camera (Thorlabs DCC3240M). These properties are more than sufficient to detect bulk breakdown through the $15\ \mu\text{m}$ thick SiO_2 dielectric layer and surface flashover across its surface.

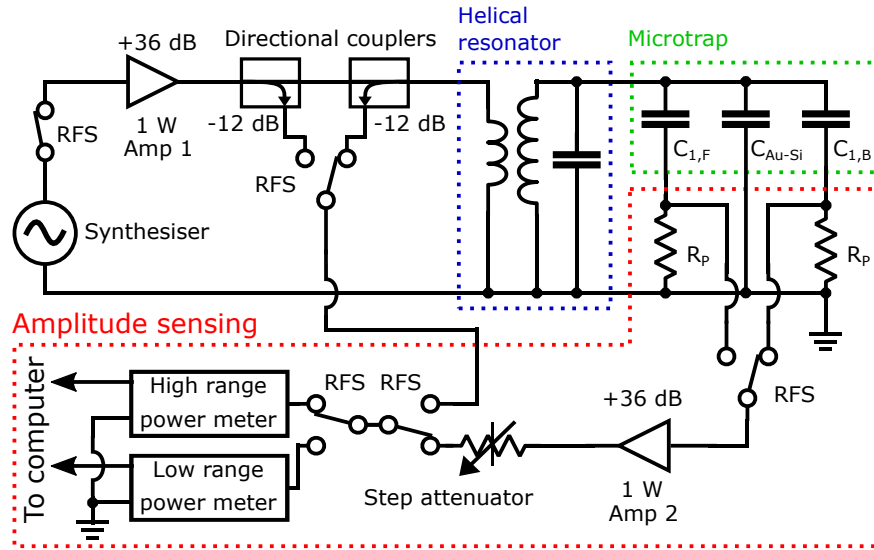


Figure 4.1: Circuit diagram of the RF test setup. The high range power meter can measure powers over the range -30 dBm to $+20$ dBm and the low range power meter measures powers over -60 dBm to $+5$ dBm, RFS refers to the radiofrequency switches (all of which are Minicircuits ZASWA2-50DR-FT+), R_p are the $50\ \Omega$ resistors. The step attenuator is required to prevent high powers from damaging the RF switches after Amp 2 whilst also allowing low RF powers to be measured when needed. The test setup is designed to measure the voltage on both sides of the trap, hence there being two trap capacitors in the circuit, where $C_{1,F} = C_{1,B} = 50$ fF. C_{Au-Si} is the capacitance that arises from the coupling of the RF electrodes to the silicon bulk and is ~ 4 pf. Power meters are Minicircuits ZX47-60LN+ (lower) and PWR-4GHS (higher).

Each camera has two sets of parameters that they operate under; the first being used for room-light conditions to aid in focusing the cameras onto the regions of interest, which is required for each trap device under test as the gluing of the trap to the intermediate substrate and the substrate to the CLCC results in small deviations in the position of the electrodes from the camera on all three axes. The second set of parameters are set to maximise the detection sensitivity for low-light measurements described later in section 4.6. The analogue gain of the sensor is maximised (at $8\times$) and the pixel clock rate is set to its minimum value of 7 MHz to minimise the read noise. The single-image exposure time is set to 1 s. The gamma value ($\gamma = 1/2.2$) characterises the image transfer function $S_{out} = \beta\Phi^\gamma$, where Φ is the photon flux, β is a constant and s_{out} is the camera pixel's associated output signal. The black-level offset, k_{BL} , was independently optimised for each camera using a device known to strongly emit flashover (to such an extent that it could be seen without image processing). The value of k_{BL} was varied as U_{RF} was gradually reduced until flashover could no longer be observed using the image processing techniques described in section 4.5. The effect of k_{BL} is that a constant DC signal is applied to each pixel in the camera CCD array; by doing so, any faint background noise that would produce a signal is offset below the minimum signal required for the analogue-to-digital converter to generate a grey level of one. This process was repeated for each of the four cameras then repeated with three other traps known to produce flashover to verify the optimisation. The full equation for determining digital grey level value for the i^{th} pixel, Γ_i that camera reads is:

$$\Gamma_i = \lfloor (8 \times (\beta\Phi_i + k_{BL}))^\gamma \rfloor \quad (4.1)$$

which is limited to a range of $0 \leq \Gamma_i \leq 255$.

To minimise background on the sensor signals and enable 1 s exposures, a light-tight enclosure, made from black acrylic, surrounds the imaging systems and the vacuum-contained microtrap. All active electronic components (i.e. those producing heat) except the cameras are located outside of the enclosure to minimise ambient heating of

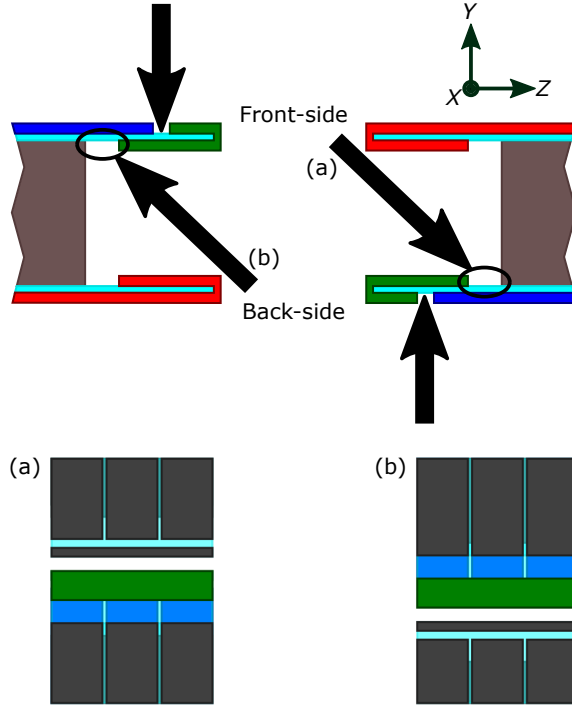


Figure 4.2: Cross section of the electrodes in the microtrap device to illustrate the camera observation directions. The front- and back-side external surfaces are observed along directions with unit vectors $-\hat{y}$ and \hat{y} respectively. The oblique viewing directions are $\frac{1}{\sqrt{2}}(-\hat{y} + \hat{z})$ and $\frac{1}{\sqrt{2}}(\hat{y} - \hat{z})$, corresponding to the internal surfaces of the front- and back-side RF electrodes respectively. The colour scheme from figure 3.1c is used to colour the electrode surfaces. In **(a)** & **(b)** the external surfaces, which the cameras are not focused on are coloured grey.

the cameras and an increase in their sensor noise level. All instrumentation and data acquisition is controlled by LabView software routines. The entire testbed apparatus is located in a cleanroom environment to avoid device contamination.

4.3 Testing Routine

To test the electronic performance of each device, a specific routine is followed. First, the resonant frequency of the circuit depicted in Figure 4.1 is measured. Second, the part of the circuit sensing U_{RF} by electronic pickup is calibrated. Finally, images of the device electrode gaps are captured as U_{RF} is ramped up; these images are processed

by an algorithm optimised to detect the onset of surface flashover. For the parameters associated with the test routines described here, typical values are quoted.

4.4 Determining the Resonant Frequency

The resonance frequency of the tank circuit is determined by scanning the frequency of the synthesiser; both forward and reflected powers are measured and their ratio P_{rfl}/P_{fwd} calculated at each frequency step. To perform the scan with adequate resolution throughout, the frequency increments $\delta\nu$ are coarser in the wings and finer at the resonance. Changes to the frequency increments occur at thresholds of $P_{rfl}/P_{fwd} = \{0.6, 0.1\}$. Typically, $\delta\nu = 5$ kHz for $P_{rfl}/P_{fwd} \geq 0.6$, 3 kHz for $0.6 > P_{rfl}/P_{fwd} > 0.1$, and 1 kHz for $P_{rfl}/P_{fwd} \leq 0.1$.

The measured data is expected to match the transfer function of the tank circuit

$$\frac{P_{rfl}}{P_{fwd}} = k \left(1 - \frac{1}{1 + \left(\frac{\nu^2 - \nu_0^2}{\nu \Delta\nu} \right)^2} \right) \quad (4.2)$$

where $\nu = \Omega_{RF}/2\pi$, ν_0 is the resonance frequency, $\Delta\nu$ is the linewidth (full-width at half maximum) and k is a scaling factor that accounts for there being less than 100 % reflection far from resonance (due to system losses). By fitting this function to the data with the Levenberg–Marquardt algorithm, ν_0 is determined. An example data set is displayed in Figure 4.3. The coarse value of ν_0 is determined by the particular helical resonator used in the apparatus; higher resonant frequencies can be achieved using alternative resonators. These scans are typically done at low input powers to avoid inducing unintentional flashover when the scan passes over the resonant frequency.

4.5 Voltage Calibration

Determining U_{RF} relies on the capacitive coupling of this signal from the RF electrodes to the compensation electrodes whose origin is explained in section 3.1. Typically this capacitance is $C \approx 0.05$ pF (corresponding to a reactance of ~ 310 k Ω at $\nu \sim 10$ MHz)

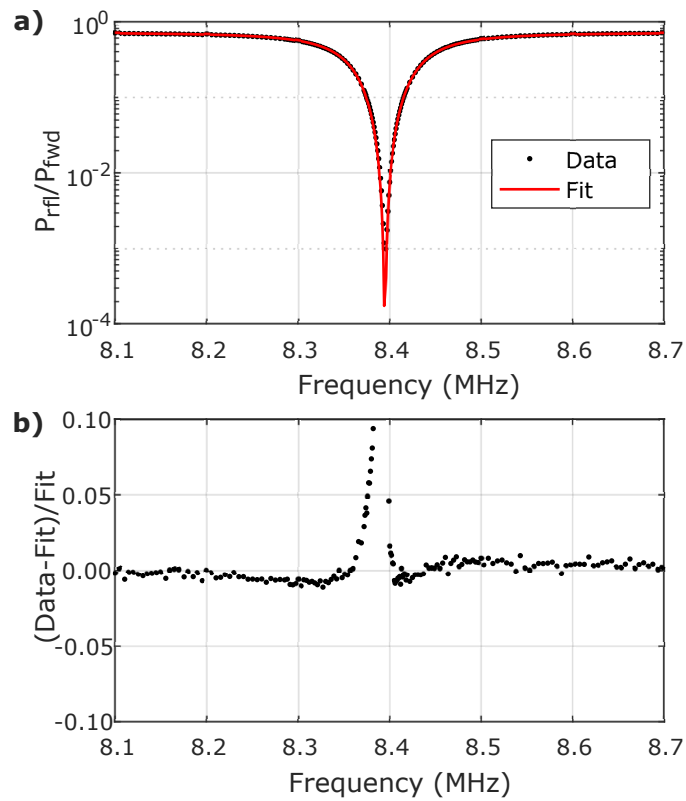


Figure 4.3: **a)** Example of a resonance scan that the test setup performed. The resolution of the frequency sweep changes when the ratio crosses 0.6 and again at 0.15. **b)** Residuals of the data from the fit of equation 4.2.

with variations from where on the wafer the trap was created, which side (front or back) of the trap is being considered, and variations on a wafer-to-wafer level. Calibrating the sensing circuit permits accurate measurements of U_{RF} with a technique similar to that described in [154]. This stage of the routine is performed at ν_0 due to the reactance of the trap being dependent on the RF frequency; thus this stage of the routine must be done after a frequency scan establishes what ν_0 is.

In order to obtain the value of U_{RF} , the amount of attenuation on the pickup signal that is measured on the compensation electrodes, relative to U_{RF} , must be known. To measure this attenuation, the helical resonator element of the circuit (see Figure 4.1) is replaced by a 50Ω resistive load in parallel with the RF electrodes of the device to maintain impedance matching. A calibration signal of frequency ν_0 and amplitude U_{cal} (known by measuring P_{fwd}) is applied across this load; this is the same amplitude present on the RF electrodes (to within 1 %) as the reactance between the resistor and the device is negligible. The capacitively-coupled pick-up signal of power $P_{p,i}$ and amplitude $U_{p,i}$ is measured across a resistive load $R_{p,i} = 50 \Omega$. This is done separately for front- and back-side RF electrodes to determine their attenuation factors α_i ($i \in \{f, b\}$) using the equations

$$U_{p,i} = 10^{(P_{p,i}/20 \text{ dBm})} \quad (4.3)$$

$$\alpha_i = \frac{U_{\text{cal}}}{U_{p,i}}. \quad (4.4)$$

Designating the voltage amplitude across the device capacitance as $U_{c,i}$ (*i.e.* between the RF and compensation electrodes), then $U_{\text{cal}} = U_{c,i} + U_{p,i}$. Since $U_{p,i} \ll U_{c,i}$, then the approximation $U_{\text{cal}} = U_{c,i}$ is made. So far traps from two wafers have been analysed with the setup. Traps from the first wafer had α_i in the range of 3000-3400 and those from the second wafer were within 2500-2900, which verifies that this assumption can be made. Therefore equation 4.4 can be rearranged to convert a pickup power measurement to the voltage on the trap for any RF voltage at that frequency. It is prudent to perform the calibration routine for both sides of the device, since small

differences in capacitances can arise due to fabrication tolerances. Once the α_i values are established the resonant circuit is restored. To ensure that the resonant frequency has not been perturbed by this process, and to verify that the electrical connections are properly re-established, a second frequency scan with reduced range is performed. This step of the routine is performed at low input powers, as even though the helical resonator is removed and thus the voltage on the trap cannot reach the voltages required for flashover, high input powers can begin to saturate Amp 1. At this point the amplifier will output harmonics of ν_0 which can distort the power that is measured by the power-meters. When the resonator is included these harmonics are filtered out and do not make significant contributions to the voltage on the trap.

4.6 Image Processing

After α_i are determined and the circuit has been returned to its standard configuration the cameras are focused on the electrode gap surfaces of interest and their detection parameters are set at optimal values. For the trap architecture used here the devices are limited by surface flashover rather than breakdown through the bulk SiO₂. However the detection routine and apparatus presented here is suitable for detecting both bulk breakdown as well as surface flashover, since the camera depth of focus (which is 80 μm) is sufficient enough to see through the 15 μm thick SiO₂ that would undergo bulk breakdown. The general principle of the breakdown detection procedure is detailed below. With $U_{\text{RF}} = 0$, a background image is recorded by taking the average of 20 single-shot 1 s exposures. U_{RF} is then increased in 5 V increments, with each value measured using the sensing circuit and the α_i determined in section 4.5. This U_{RF} is used to calculate the subsequent synthesiser setting to achieve the required increment. At each U_{RF} , a single-shot and averaged camera images are analysed with image processing algorithms for the presence of breakdown. The averaged image is calculated first as a cumulative average, then as a 20-shot simple moving average when sufficient single-shot images are acquired. If breakdown is detected, then U_{RF} is switched off and the final value of U_{RF} and the accompanying images (background, last single-shot, averaged and processed) are recorded. If no breakdown is detected, U_{RF} is incremented

and the image analysis is repeated. If breakdown has not been detected before U_{RF} reaches a user-specified threshold (typically this is set to $U_{\text{RF}} = 250 \text{ V}$), then the test is considered complete.

Two types of breakdown can be observed and detected: a) a bright transient spark that is captured only in a single image, and b) a faint, persistent glow along the length of the RF electrode, whose onset is only visible in the processed average of many sequential images. If the RF voltage is continually increased, the faint glow type of breakdown increases in brightness and can become visible without the image processing; however by this point the breakdown is likely to have caused some damage to the trap microstructure. Two separate image processing routines have been developed to detect these events (see flowcharts in figure 4.4); both were implemented using the LabVIEW IMAQ module. They begin by recording the background reference signals on each camera sensor for 1 s exposures and $U_{\text{RF}} = 0$. Each sensor may be subject to an uneven background, shot-to-shot fluctuations in individual pixel signals, as well as hot pixels. Thus an average of many (*e.g.* 20) consecutive exposures forms the reference images; examples are shown in Figure 4.5b. Both algorithms [203, 204] are constructed from standard image processing techniques with both algorithms featuring thresholding and filtering operations, and the detection of faint glow breakdown also using morphology operations. Additionally a region of interest is applied to the images, so that the algorithms only consider the high voltage RF electrode and the surrounding grounded surfaces; reducing the computational overhead from processing regions of the image where breakdown cannot occur and preventing false detection events in these regions.

Detecting transient sparks relies on measuring signal on small numbers of adjacent pixels that is significantly above their background values in a single-shot image. The first stage of that detection algorithm applies a basic global thresholding operation and a spatial low-pass filter [203] to both the background reference and single-shot images (the same processing parameters are applied to each image). The thresholding operation compares the grey level Γ_i of each pixel to a threshold $\Gamma_{t1} = 40$, leaving Γ_i unchanged if $\Gamma_i \geq \Gamma_{t1}$, or setting to zero if $\Gamma_i < \Gamma_{t1}$. This has the effect of removing

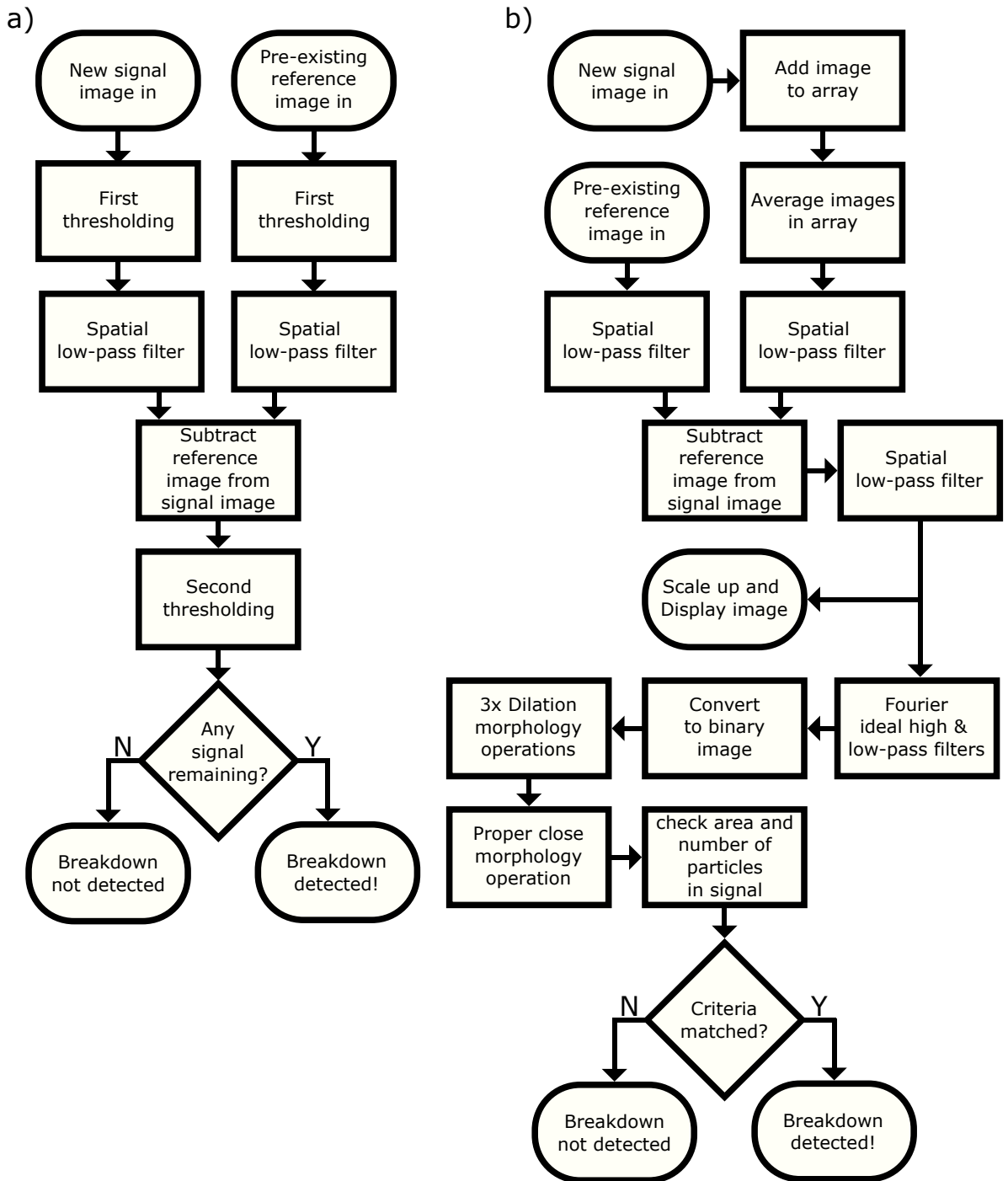


Figure 4.4: Flowcharts summarising **a)** the transient single image based algorithm and **b)** the averaged, faint glow-like breakdown detection algorithm.

low level fluctuations from the background of both images so that only pixels with high signal values are considered. A low-pass spatial (*i.e.* pixel-based) filter is next applied to both reference and single-shot images. The grey level Γ_i of each pixel is compared to the mean value $\bar{\Gamma}_n$ of its first- and second-order neighbours' grey levels using a tolerance factor η_s . If $\Gamma_i > \eta_s \bar{\Gamma}_n$, then the pixel grey level is set to $\bar{\Gamma}_n$, otherwise it remains at Γ_i (for transient spark detection, $\eta_s = 0$; so that each pixel is always set to the average value). This minimises the effects of single pixel fluctuations and hot pixels. This does not affect either algorithm's ability to detect breakdown as in both cases the signal is detected across a large number of contiguous pixels, which outside of the pixels at the borders of these regions, will have average values above their equivalents in the background image. Following this, the difference between the filtered signal and background images is computed. The transient spark signal is likely much greater than the lower noise of the shot-to-shot background; thus a second thresholding operation is applied to remove low level shot-to-shot fluctuations and drift in the background. Note that this threshold Γ_{t2} is not directly comparable with Γ_{t1} due to the former being applied after the difference operation. Thereafter any remaining signal is considered to be detection of breakdown.

The algorithm to detect faint, persistent-glow breakdown analyses the moving averages of single-shot images (see Figure 4.5c). This detection routine begins once the cumulative average has reached the 15th image and proceeds until the simple moving average has reached 30th image. The background reference image and averaged signal images are both processed by a low-pass spatial filter ($\eta_s = 0.4$) and difference operations. Following this, a second low-pass spatial filter ($\eta_s = 1$) is applied to the difference image to remove single pixels with non-zero values due to small differences between background and averaged signal. Some of these occur at spatial frequencies that are not removed by the subsequent Fourier frequency filters. A Fourier transform creates an image spectrum containing high spatial frequencies in the centre and low frequencies at the edges. This permits application of ideal low- and high-pass filters in the frequency domain [203]. The ideal filters remove the lowest 0.5% (high-pass) and the highest 10% (low-pass) of frequencies from the Fourier image by applying circular

masks to the Fourier images that multiply the frequencies to be kept by one and the discarded ones are multiplied by zero. In doing this, spatial frequencies composing the background of the original image are filtered out, while those remaining are due to breakdown signal and noise at similar spatial frequencies. Thereafter an inverse Fourier transform reconstructs the filtered image. The grey levels of pixels containing any faint breakdown signal occurs at similar grey levels to the remaining noise, thus a simple thresholding operation will be ineffective for breakdown detection (*cf.* transient spark algorithm). Analysing the spatial distribution of signal in the filtered image provides a means to do this. First, the image is transformed to a binary form by setting pixels with grey level $\Gamma_i \neq 0$ to 1 and leaving those with $\Gamma_i = 0$ unchanged. This binary image contains clusters of adjacent pixels showing a 1; hereafter these are referred to as particles. These correspond to breakdown as well as noise that is located away from the region of interest on the device. A dilation operation is applied to this image; where each pixel is checked if one of its eight neighbours has a value of 1. If it does then that pixel has its value set to one and is left as unchanged if it does not. When repeated a further two times, it enlarges the spatial extent of particles where the signal is sparsely distributed. A proper close operation enlarges as per a single dilation, then contracts around the perimeter but not within it. Both morphology operations have the effect of restoring any edges that were truncated during the thresholding and filtering operations. Moreover, they fill the gaps between particles in proximity; this will be the case for those due to breakdown, but not for isolated particles remote from the region of interest. If breakdown is present, particles will merge and a larger group of contiguous particles will be evident within the region of interest in the image. The final stage of the algorithm to detect faint-glow breakdown analyses the area of all particles in the processed image. Within each particle, the number of signal pixels, n_{sig} , is counted and used as a measure of particle area. Particles are classified by their area and the number of particles N_p in each class is counted. If there is a sufficient number with large areas, or indeed a single particle with a much larger area, then breakdown is deemed to be present. The detection criterion applied is that $N_p \geq x_i$ when $n_{sig} \geq y_i$, for one combination of $x \in \{1, 2, 3, 4, 5\}$, $y \in \{3250, 2500, 2250, 2000, 1750\}$. In

comparison, particles away from region of interest that are considered to be noise have typical areas $n_{sig} \leq 1000$. Upon detection, the triggering particle(s) are highlighted in the processed image. Statistical analysis of particles considers particles of largest areas first. If detection arises from these, then other smaller particles which also fit the criteria are not explicitly highlighted by the procedure; if required, this could be done in subsequent post-test analysis of the data.

The algorithm for detecting faint, persistent-glow breakdown was developed using a device exhibiting signal visible to the eye in the averaged image. The parameter values for each step of the routine were optimised by iterating with the same device at successively lower values of U_{RF} (and thus fainter breakdown), until the breakdown signal was no longer evident. These parameter settings were confirmed by performing the same optimisation routine on an additional two devices.

4.7 Testbed Results

The transient spark type of breakdown is caused by a particulate contaminant on the surfaces of the device at the location of the particulate on the gap between the RF electrode and the grounded surfaces. Here the particulate acts like an antenna between the RF electrode and the grounded surfaces, with the high voltages incinerating the particulate. Persistent faint-glow flashover is usually observed thereafter at that location. Larger particulates can fragment with subsequent sparks at different locations on the electrode being caused by these fragments. These behaviours were observed in early manual testing of microtrap devices and motivated the development of the detection algorithm described here. Upon introducing more thorough cleaning procedures for devices (that were introduced prior to the development of the image processing algorithm), transient sparks were no longer detected or observed.

Example results showing detection of persistent faint-glow flashover from two separate microtrap devices are shown in Figure 4.5. These show: (a) the oblique view of the device, where the internal surface containing an RF electrode and the SiO_2 insulator runs laterally in this view; (b) a background image with $U_{RF} = 0$; (c) the unprocessed, signal-averaged image when breakdown was detected; (d) partially-processed

image (taken prior to Fourier transform and morphology operations and with the pixel grey levels multiplied by 50 for visibility); and (e) fully processed image with detected breakdown highlighted.

The processed detection image can be superimposed upon the image recorded under ambient light to reveal the spatial location of the detected breakdown. Figure 4.5f shows the extent of this breakdown along the internal edge of the RF electrode, where particles on the electrode/insulator surface are coloured magenta and those outside this spatial region are coloured green. This correlation between signal particles and the expected spatial location is evidence that the detection algorithm is correctly identifying signal attributed to breakdown. Results from other devices not presented here show that the particle detection criteria consistently detects the breakdown signal at the correct spatial location in the device.

There are only a few occasions when the detection algorithm is triggered by a particle (or group of particles) remote from the spatial regions of interest on the device. These infrequent events are easily assessed by the user and are not found to be repeatable. It is observed that genuine breakdown results in a signal that is repeatable in the position and applied voltage $U_{\text{RF,flash}}$ at which it occurs.

The effectiveness of the faint-glow breakdown detection algorithm is evidenced by comparing (b) and (c) in Figure 4.5. To an observer's eye, there is no perceptible signal above the background between these. After detection of flashover when the location of the trigger signal is known, the grey levels on the relevant pixels can be compared between signal and background images. Typically, the signal is on average only 2 grey level counts above the background (estimating that ~ 40 incident photons correspond to an increment of 1 count in the grey level). Thus using only statistical methods as a threshold discriminant would not achieve the sensitivity demonstrated here. The result of the detection algorithm was compared to simple detection by a user's eye discriminating between Figures b) and c). Performed using a few devices, it was found that the algorithm would detect the faint-glow flashover at a amplitude $U_{\text{RF,flash}}$ between 60 V and 90 V lower than was possible by manual eye detection.

Under these faint-glow conditions, there is no detectable electronic signature of this

weak breakdown in the reflected power signal from the resonant circuit. Changes in that signal are only detectable when there is a change in the impedance of the resonant circuit. Large enough changes to device impedance usually arise with breakdown through bulk material, although strong surface flashover would also give rise to this. It has been established that the voltage required to induce surface flashover is a factor of 2.5 less than the voltage required to induce electrical breakdown severe enough to change the traps' impedance [150]. Any minor change to device impedance during faint-glow flashover would require further detailed investigation into more sensitive electronic measurements to detect changes in the reflected power.

While the results presented here were with $\Omega_{\text{RF}}/2\pi = 8.4$ MHz, tests at higher values (*i.e.* ~ 20 MHz) are straightforward with an alternative resonator. In earlier investigations based on manual detection, no noticeable dependence of $U_{\text{RF,flash}}$ on Ω_{RF} was observed in this range. A second set of tests performed with RF frequencies in the 1 kHz – 100 kHz with voltage amplitudes up to 250 V resulted in no breakdown being produced on traps that had previously produced flashover at voltages below this threshold. In this case the Amp 1 in figure 4.1 was replaced with a high voltage RF amplifier, the directional couplers were replaced with a pair that were capable of sampling RF voltages over this frequency range and the helical resonator was bypassed such that the directional coupler output connected directly to the trap.

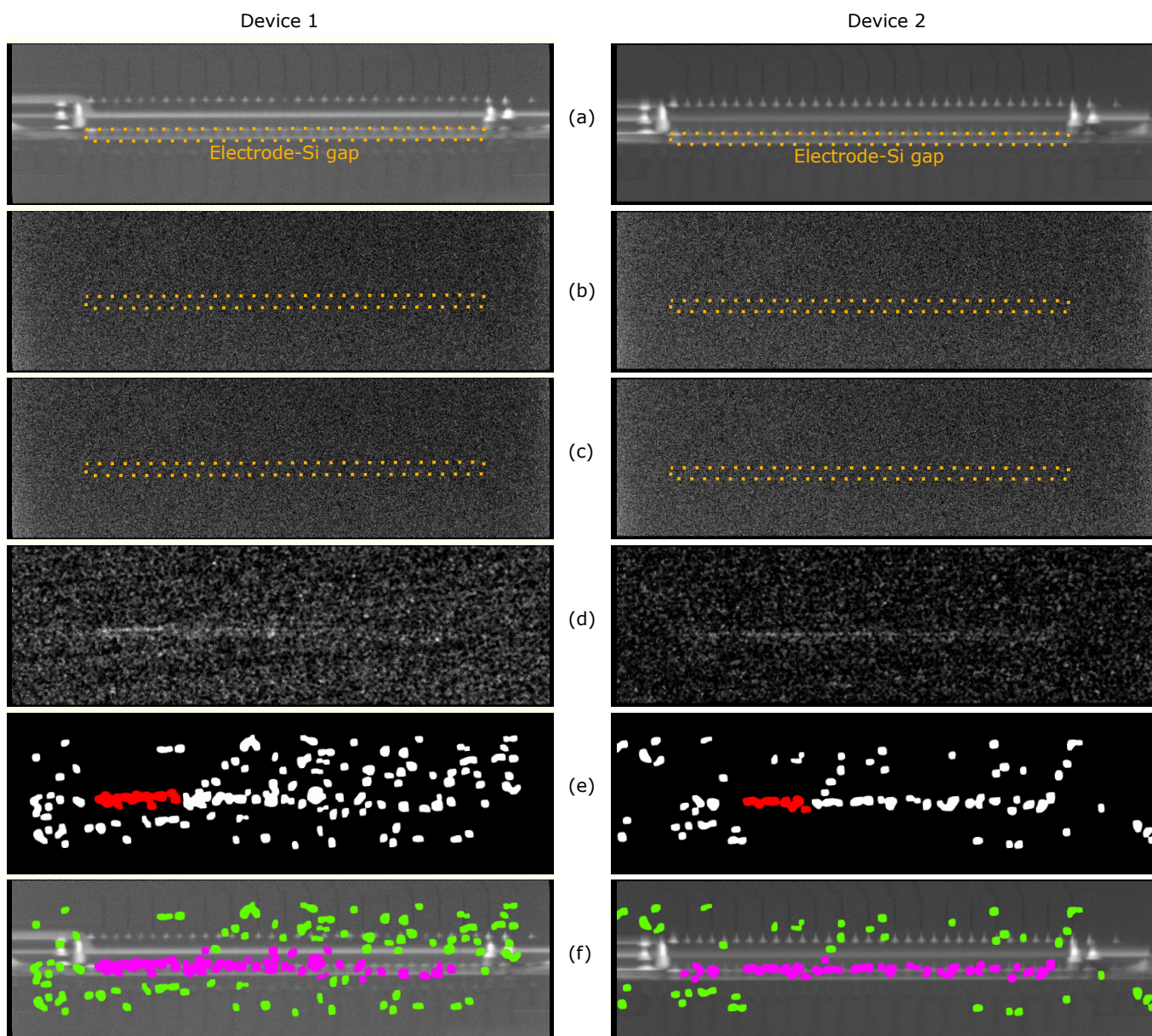


Figure 4.5

Figure 4.5: Recorded images from two devices that produced breakdown in the form of surface flashover. The algorithm detected faint-glow breakdown at $U_{\text{RF,flash}} = 198$ V for device 1 and 176 V for device 2. In all images, the device aperture is viewed obliquely with the same perspective as in figure 4.2a. The gap in the internal surfaces between the bulk Si and the RF electrode has been annotated with dotted, orange lines for clarity, with the exposed SiO_2 surface between the lines. In figures (a)-(c).

a) Image under ambient illumination conditions. The camera is focused on the internal surface of the front-side RF electrode, which here is the side of the trap furthest from the camera. The viewing direction means that the external electrode surfaces in the upper part of the image are closer to the camera than those in the lower part.

b) Reference image produced with $U_{\text{RF}} = 0$.

c) Signal image produced by averaging 20 single-shot images together. To the eye, there is no observable difference between the preceding reference image and the signal despite breakdown being present.

d) Image from c) partially processed by the algorithm, (taken after the second spatial low-pass filter but prior to the Fourier transformation). The grey levels in this image have been multiplied by 50 to help the user determine the presence of breakdown. The scaling also results pixels with $\Gamma_i \geq 6$ being scaled to the maximum value of $\Gamma_i = 255$.

e) Fully processed image after the detection of breakdown. The particle that triggered the detection is highlighted in red.

f) Particle data from e) superimposed on image a). Magenta particles occupy the space where one would expect to observe the breakdown whereas those in green are particles outwith this space.

4.8 Summary

This chapter has presented an electrical testbed for ion microtrap devices for the purpose of aiding developments in their fabrication and to determine their suitability for purpose once fabricated. The hardware used for the apparatus was designed to be cost-effective and fit for cleanroom use. The techniques to calibrate the electronic circuit that is used to sense the RF amplitude present on the device under test have been described. Also described are the principles for the sensitive optical detection of the onset of persistent faint-glow breakdown in these devices as well as the detection of any transient sparks that may arise from any particulate contaminants on the surface of the device. After establishing the principles of image processing routines for this purpose, the detection system parameters were optimised empirically.

The principal result of this work is a testbed which can detect the onset of faint-glow

breakdown at a much more sensitive level than by straightforward analysis of unprocessed images. The algorithm for processing images and sensing breakdown resulted in detection at RF amplitudes between 60 V and 90 V lower than was possible by manual eye detection (where $120 \text{ V} \leq U_{\text{RF,flash}} \leq 300 \text{ V}$). This enhancement in sensitivity is important for assessing the operating bounds of devices expected to achieve minimised ion heating rates. This device performance metric has been shown to be dependent on visible breakdown [167] thus it is reasonable to expect that faint-glow breakdown will also be detectable in the behaviour of the trapped ions. Knowledge of $U_{\text{RF,flash}}$ and the position(s) where it occurred on the device can be correlated with optical or electron microscope images of the specific device and used to interpret and inform steps in the microfabrication process. Similarly, knowledge of devices where no breakdown was observed up to a defined test limit of U_{RF} is also informative for future developments.

There are several possible improvements to the testbed that can be considered. Replacing the power meters with a spectrum analyser, whilst considerably more expensive, would provide frequency information about the RF voltages applied, reflected and picked up from the trap. Reducing the temperature of the camera sensors through cooling would achieve a modest reduction in sensor noise and permit detection of fainter emission from the breakdown site. This could be achieved via a Peltier device but would necessitate engineering measures to control condensation and heat dissipation, which could be cumbersome to implement. A more significant reduction in sensor noise could be achieved by using an electron-multiplying CCD with spectral sensitivity chosen to match breakdown emission; however this is an order of magnitude more expensive than the cameras used in this work. The consistency, ease and speed of focusing the cameras onto the relevant areas of the trap could be improved by attaching a step motor to each of the cameras to enable computer control and automation of this process. In the present setup this is a difficult and time consuming process to do and due to the position of the trap varying on each tested trap, must be done for every device that is tested. In the present image processing algorithm, the Fourier low- and high-pass filters are circular in the image spectrum and thus relatively simple. The geometry of the device, in particular that of the RF electrode (on both internal or external surfaces),

suggests that breakdown will occur along a particular direction. A bespoke Fourier filter could be tailored to account for this. That would require that each device under test was located identically or that the exact alignment was quantified and a specific filter calculated for that device such as by utilising machine learning to fit a template to an ambient light image.

Although the testbed described here was developed for ion microtrap devices with a 3D electrode microstructure, the principles are directly applicable to such devices with 2D electrodes geometries [150]. The underlying principles of the testbed and methods described here could be used to analyse performance of other MEMS devices that are susceptible to breakdown, such as micro-and nano-thrusters [205, 206] for spacecraft, as well as miniature RF light sources [207] in which the occurrence of flashover is desirable. These principles may also be useful for investigations into material properties, such as dielectric barrier breakdown studies where most previous studies seem to have investigated catastrophic breakdown [208] and its aftermath [209] or on the high speed formation of breakdown [210, 211] rather than the onset of the breakdown. The image processing routine could also be adapted for other types of electrical breakdown that can produce a faint glow such as corona discharges [212].

Chapter 5

Optical Frequency Tuner for the 674 nm Qubit Laser

5.1 Introduction

Trapped ion spectroscopy, along with other laser applications [213,214] requires the ability to quickly change the laser frequency over a wide range to manipulate the quantum state of the ion (here the apparatus needs to cover a detuning range of $\sim \pm 20$ MHz). To practically implement qubit gate operations these detuning operations need to be performed at sub-millisecond timescales, so as to complete the gate sequence at timescales that are practical relative to the qubit coherence times. Additionally, in performing the detuning operations the frequency stability of the laser must be preserved in order to fully exploit the narrow linewidths [13,63,143,215] of the transitions into which the qubits are encoded. Furthermore these qubit operations require that the Rabi frequency remains stable for the whole experimental routine; both throughout the duration of the routine (which can require repeating the specific gate sequence hundreds of times consecutively) and over the previously specified frequency range. This is of crucial importance to the goal of achieving fault tolerant QIP [30,216], which requires that the Rabi frequency has a minimum fractional stability between 10^{-4} and 10^{-2} [172,217–219], depending on the task being performed.

In terms of implementation, this can be done by stabilising the qubit laser power, as

the Rabi frequency is proportional to the square root of the qubit laser’s intensity. One method of stabilising the laser power is to control parameters of the laser source such as the driving current to the lasing medium [220]. However if this method is being used to stabilise the frequency of the laser [177, 221, 222] then simultaneously implementing power feedback here could induce the cross-talk between the two feedback sources and destabilise both the laser frequency and its power. For the qubit laser described in section 3.7 the frequency stabilisation is performed at the laser source by locking to an ultra-stable cavity, which prevents both fast detuning operations and optical power stabilisation via the laser source parameters. Therefore these must be performed downstream from the laser source. In this chapter the development and evaluation of an optical tuner apparatus that simultaneously performs both the fast frequency detuning operations and laser power stabilisation will be described.

5.2 Tuner Apparatus

The output of FNCS-1 (figure 3.5a) is input into the tuner setup (figure 5.1a) via a 22 m optical fibre. Here it passes through a variable frequency AOM (Isomet 1250C) that is placed at the focal point of a telescope composed of two 200 mm focal length lenses. A retro-reflector is used to return the $+1^{\text{st}}$ order beam back through the AOM to create a double pass setup with the second order $+1^{\text{st}}$ beam being used as an output. The AOM is positioned and angled to maximise the double pass transmission efficiency. After being setup, the resonant circuit inside the AOM was adjusted to minimise the reflected RF power and thus further optimise AOM’s double-pass transmission efficiency. These give the AOM a single pass transmission efficiency of 79 % and a double pass efficiency of 60 %. The lenses of the telescope are raised by 1.5 mm so that the output beam is 3 mm above and parallel to the input beam as depicted in figure 5.1b. Doing this allows the output beam to travel over the mirror used to steer the fibre output into the telescope. Similar double-pass setups to this have used wave plates and a polarising beam splitter to separate the input and output beams without the spatial offset [223–225]. However these introduce further losses in optical power from the added components and introduce the risk of a small number of photons that have not passed through the

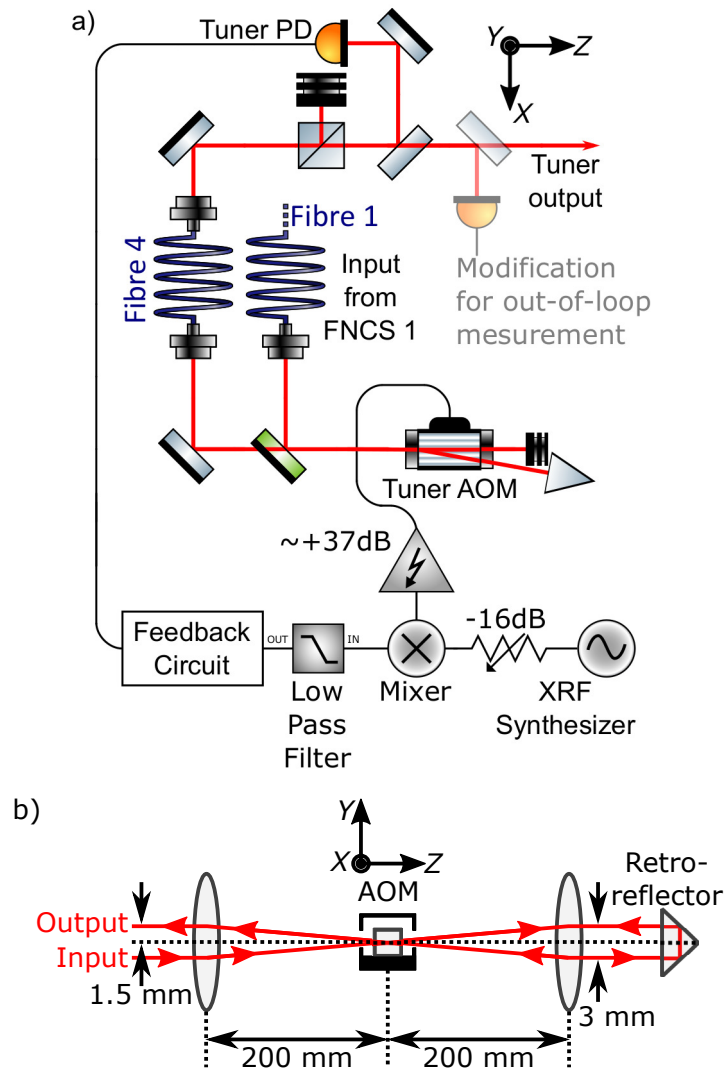


Figure 5.1: a) Optical Circuit for the tuner setup. b) Side on view of the AOM showing the path of the beam in the vertical direction.

AOM being reflected into the output beam. By utilising the setup described the probability of these non-detuned photons entering the output beam is minimised. When the frequency of the AOM is varied the angle of the single beam is changed in proportion to the magnitude of the change. This can cause small deviations in the output beam pointing from imperfections in the retro-reflector alignment, the effects of which would become more pronounced on optical components further downstream. To compensate for this the output beam from the double pass AOM is input into a fibre (fibre 4 in figure 5.1) so that any deviations in beam pointing are converted into deviations in the optical power due to more or less of the beam being coupled into the fibre. At the output of the fibre the beam has its polarisation cleaned by a Glan-Taylor prism. A beam sampler at the tuner output then takes $\sim 5\%$ of the optical power and re-directs it onto a photodiode (Hamamatsu C10439-07) that is used as the sensor for providing power stabilisation feedback.

Feedback is implemented by inputting the photodiode output to a Proportional-Integral feedback circuit (that was created from a repurposed Moglabs B3120 signal-conditioning board which was modified to have a higher integrator bandwidth) to create an error signal. This signal is then used to attenuate the RF drive of the AOM through an RF mixer (Minicircuits ZLW-1). This mixer was chosen to be the servo mechanism in preference of other components, such as variable voltage attenuators, due to its high bandwidth. A Direct Digital Synthesis (DDS) (Moglabs XRF) is used to supply the RF which, after the mixer, is amplified (by a Minicircuits ZHL-03-5WF+) before being applied to the AOM. The DDS source permits frequency changing at $1\ \mu\text{s} - 1\ \text{s}$ timescales and can queue up to 8000 detuning operations, which should be more than sufficient for performing gate sequences. To ensure that small amounts of the RF drive do not bleed through the mixer input port to the feedback circuit a 5 MHz low-pass filter is inserted between the mixer and the feedback circuit. Additionally RF attenuators are placed on the output of the DDS to ensure that the maximum power applicable to the AOM is limited to +31.4 dBm, keeping the applicable power below the AOM damage threshold of +33 dBm.

To ensure that the frequency stability of the laser is maintained by the tuner and

pulse control setup, a small portion of the light is picked off from the output of the pulse control setup, prior to the input of fibre 5, and sent to the pulse beat setup. This is a simple optical circuit that superimposes the picked off light onto the output of FNCS-2 via a glass wedge. The superimposed lasers are input into a fibre that goes to a fast photodiode (Thorlabs DET02AFC) that has a 1 GHz bandwidth for measurement. The two beams produce a beat with a frequency of $f_b = 184.8$ MHz, which arises from the detunings imposed by the different AOMs that they pass through. Detecting the signal from the photodiode on a spectrum analyser will show the Fourier spectrum of the beat and reveal any unwanted features or noise in the spectrum.

5.3 Power Stabilisation Performance

The issue of power fluctuations is expected to be a major limiting factor in implementing high-fidelity gates. Due to the AOM being a resonant circuit, detuning the RF frequency away from the centre frequency will reduce the transmission efficiency. The effect of this reduction is squared due to the AOM being used in a double pass configuration. Additionally, as mentioned in the previous section, the detuning of the AOM also causes changes in the input coupling efficiency of fibre 4 which in turn influences the output power. Scanning the frequency of the DDS source, whilst comparing the tuner output power against the input power (measured at the output of fibre 1), reveals how the RF frequency affects the overall efficiency of the system. The central frequency of the tuner, which corresponds to zero detuning, is chosen to provide the optimum output efficiencies for the required ± 20 MHz optical detuning range (here this occurs at 161 MHz in the RF domain). The feedback setpoint is chosen such that the output power can be successfully stabilised over an extended ± 25 MHz scan range. This extended range is utilised so that the limits of the required ± 20 MHz detuning range are not at the edge of what the system can stabilise and not liable to fluctuations if the laser power decreases below the setpoint power, taking it out of lock at the edges of the detuning range. The results of this scan with and without the feedback enabled are shown in figure 5.2a and b. With the feedback disabled, the output of the tuner has ~ 43 % of the optical power that comes out of fibre 1 over much of the detuning range.

The output efficiency then begins to decrease after ± 15 MHz, lowering by ~ 1.3 % at ± 20 MHz and ~ 2.5 % at 25 MHz, with the change in efficiency decreasing at a higher rate as the detuning is further increased. With the feedback on at the typical setpoint the output efficiency is 40.7 %. The output efficiency also remains consistent (to within ± 0.031 %) over the whole scan range in this case. Here a typical input power of 170 mW allows the tuner system to output ~ 70 mW of 674 nm light, which corresponds to ~ 8.5 mW at the ion with the pulse shaping AOM operating at full power. This output is far more than the micro- and nanowatt level powers that most of the experiments in chapter 7 require. To compensate for this, lower RF powers are used in the downstream pulse control setup when generating pulses. This has the benefit of reducing the RF amplitude that needs to be applied to the pulse shaping AOM, which lessens the effects of heating in the pulse control AOM's crystal. Should the detuning range ever need to be extended then setpoint value can be lowered to cover a wider detuning range and higher RF powers applied to the pulse shaping AOM to provide pulses of the same output power. The feedback has been implemented such that as long as the unlocked laser power is above the feedback setpoint then the servo will remain locked.

A more aggressive means of testing the stabilisation capacity of the tuner is to apply a sequence of randomly generated detuning steps that are within the ± 25 MHz stabilisation range. A sequence of 2000 random frequency steps, each separated by $1/2$ ms, was created to test the setup and applied via the DDS source. The same sequence was used to test for both the the feedback being enabled and disabled. A subset of the tuner output whilst running this sequence is depicted in figure 5.2c. With the feedback disabled, step changes in the output power can be observed when at the points in time where the detuning is altered; with the feedback enabled the output power remains mostly constant over each detuning step, with spikes in the power occurring at the times where the detuning is initially changed. The polarity and magnitude of the step changes and spikes here are determined by the size and direction of the corresponding detuning change according a change in the unstabilised efficiency from figure 5.2a. The magnitude of the step changes and spikes is roughly

proportional to $||\delta_2| - |\delta_1||$. To establish the time constant of the servo system, a fit to the 10 largest spikes was made. This established the time constant of the servo after experiencing a change in the laser detuning to be $45.5 \mu\text{s}$ (figure 5.3 shows a typical example), corresponding to a bandwidth of 22.0 kHz. This limitation was found to originate from the bandwidth of the servo circuit. Replacing the servo circuit could bring this down to $t < 10 \mu\text{s}$. The spikes, which a feedback servo cannot fully remove, could be reduced by implementing a feed-forward into the DDS source.

To evaluate the tuner's improvement to the stability of the laser power, the optical circuit in figure 5.1 is modified to have a glass plate sample a portion of the output and a second photodiode (also a Hamamatsu C10439-07) is used to take out-of-loop measurements of the beam power. With this modified setup an Allan deviation is calculated using the equation [226],

$$\sigma_y^2(\tau) = \frac{1}{2m^2(M - 2m + 1)} \sum_{j=1}^{M-2m+1} \left[\sum_{i=j}^{j+m-1} (y_{i+m} - y_i)^2 \right] \quad (5.1)$$

where $\tau = m\tau_0$ is the averaging time with τ_0 the smallest time between measurements, m the averaging factor and y_i is the i^{th} of M consecutive power measurements averaged over τ . The Allan deviations of the in-loop and out-of-loop data, with and without feedback are given in figure 5.4. These show the tuner reducing the power fluctuations by almost two orders of magnitude at 10^3 s and achieving 10^{-4} out-of-loop fluctuations at times between 10 s and 700 s, which are the approximate timescales needed for the experimental routines. Implementing the previous suggestion of an improved feedback circuit would likely improve this further with major gains to be made at shorter timescales.

It was noticed that after a period of operation that the tuner output power would periodically drop by up to 30 %, going below the stabilisation setpoint for times that could last up to several minutes. Examining the transmission of each component in the tuner revealed that the laser polarisation was rotating in a fast and uncontrolled manner. As a consequence the Glan-Taylor prism was dumping a significant fraction of the beam power. Further examination of the laser polarisation revealed that these

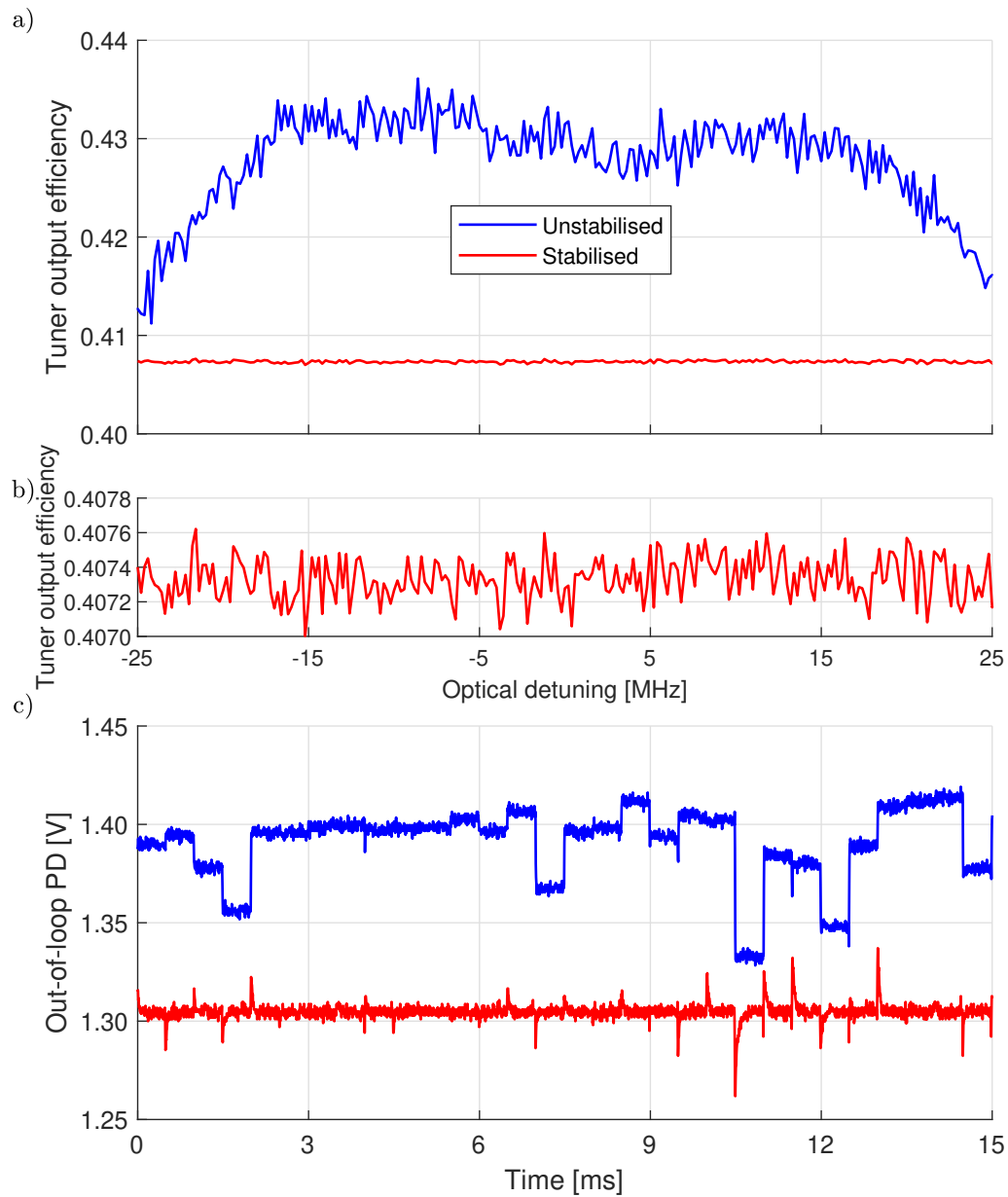


Figure 5.2: a) Tuner output efficiency with and without stabilisation over the range of frequencies required for the experiments described in chapter 7. Each data point is the average of 50 measurements with a scan resolution of 200 kHz. b) Subsection of (a) that only shows the stabilised efficiency. c) Tuner output with a random change in frequency made every half millisecond with and without stabilisation, using the same sequence in both cases. The magnitude of the step changes and spikes correspond to the change in efficiency on the unstabilised curve in (a).

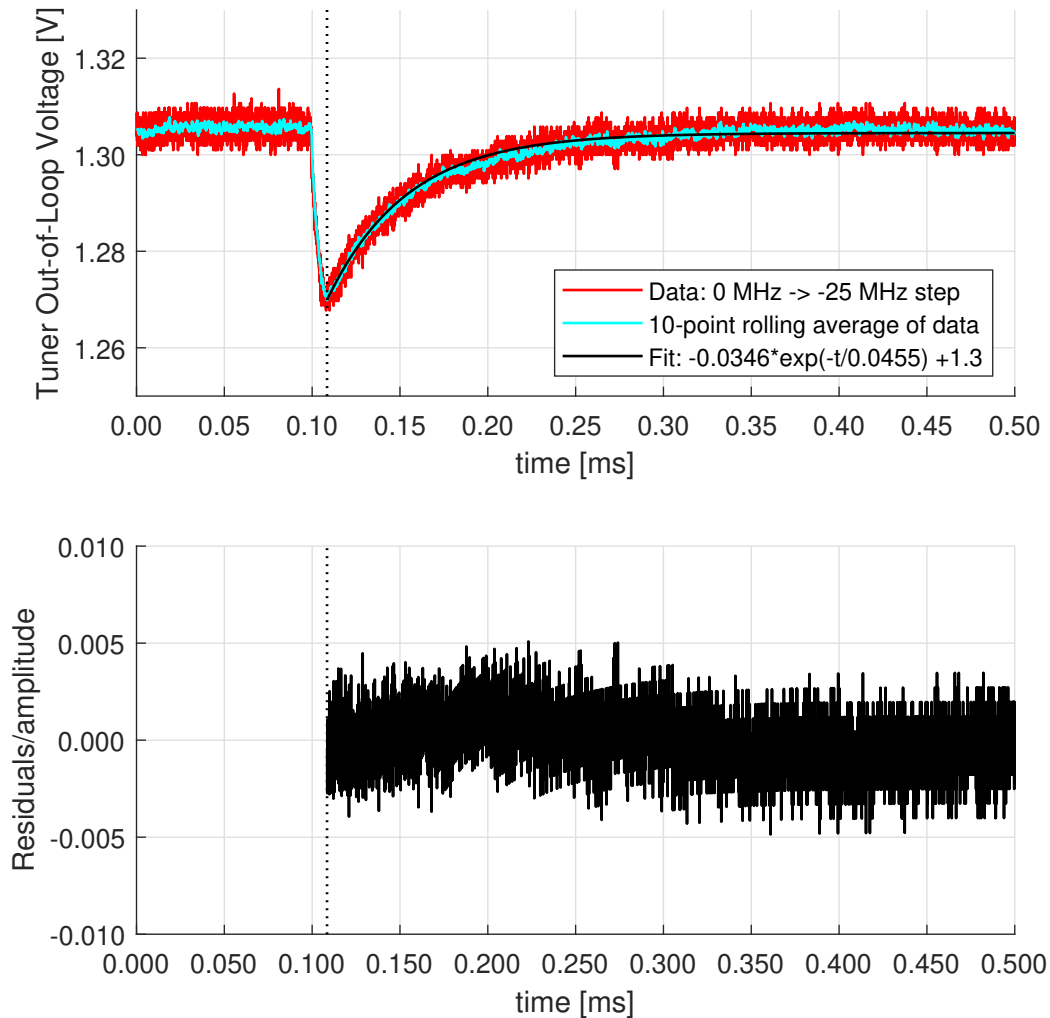


Figure 5.3: A single detuning step change going from 0 MHz to -25 MHz, showing the largest possible detuning change and thus the largest possible step change in the laser power. The time constant was determined by averaging the value from the 10 largest spikes, each obtained via a Levenberg-Marquardt algorithm, to be $45.5 \mu\text{s}$. A fit created with the averaged time constant is shown here. Data recorded before the dotted line was not used in the fit either because it was before the step change or the data was dominated by the bandwidth of the photodiode. A rolling average of the recorded data is included to increase the visibility of how the out-of-loop data evolves.

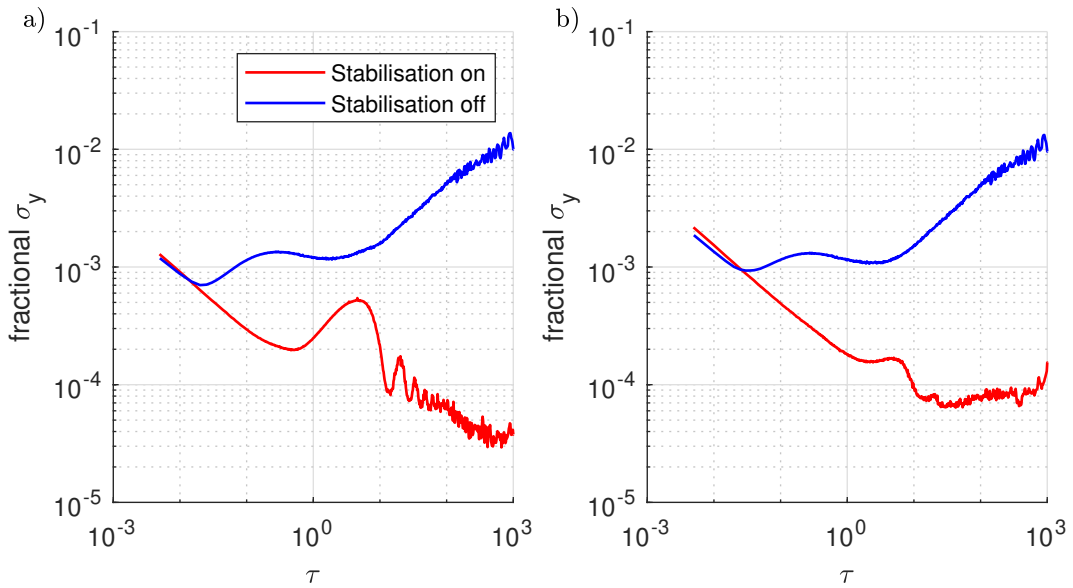


Figure 5.4: a) In-loop and b) Out-of-loop Allan deviations for the tuner operating at a fixed frequency.

polarisation fluctuations originated in fibre 1. It was discovered that the input interface of the fibre had been damaged by fluctuations in the source laser power, which periodically exceeded the fibre’s damage threshold. Replacing the fibre and reducing the input power to the present values has solved this issue. Without the monitor of the tuner servo signal it would have been likely that spectroscopy experiments would have been compromised by the damaged fibre.

5.4 Transfer of Frequency Stability

Experiments utilising optical qubits require the laser being used to manipulate the internal state of the ions to possess a high degree of frequency stability. To ensure that the addition of new subsystems into the laser, namely the tuner and pulse control setup, do not reduce the spectral purity of the laser, a beat measurement is made between a sample of the output from the pulse control setup and the output of FNCS-2 with the pulse beat setup (described in section 5.2). The spectral purity of this beat is then examined on a Tektronix RSA5103B spectrum analyser with the results this shown in figure 5.5. It should be noted that this measurement does not give an

absolute measurement of the laser linewidth, nor does it factor in the effects of drift and fluctuations at the laser source and thus the laser spectrum as observed by the ion may be different than what is depicted in figures 5.5. Instead this measurement shows the relative stability between the laser at the point that the subsystems have been added and the laser as it is when it is delivered to the magnetic shield.

Figure 5.6 reveals that the beat has a linewidth of at most 0.21 Hz up to the fibre that goes to the trap by fitting a Gaussian function to the main peak from figure 5.5d via the Levenberg–Marquardt algorithm. Since the observed linewidth is a little above the resolution bandwidth of the spectrum analyser, it is likely that this is the main limitation on the ability to obtain this linewidth. To verify this a second fit was made using a Blackman-Harris function, which was used as the window function on the spectrum analyser that was used for this measurement. Since this second fit also produces small residuals and a similar linewidth, this confirms the finite resolution of the instrument as being the main limitation on the measurement, as a linewidth narrower than the resolution bandwidth would be expected to reproduce the window function that was used. This combined with the fact that the sidebands present in the spectra depicted in figure 5.5 are smaller than -36.5 dBc are strong indicators the tuner and pulse control systems do not add significant noise onto the qubit laser and thus are suitable for use in spectroscopy experiments. In order to maintain the frequency stability of the laser, the tuner and pulse control setup are encased in a metal enclosure to minimise the effects of air currents and temperature drifts [179,180]. Without this the laser linewidth increases to ~ 6 Hz.

5.5 Summary

This chapter described the construction and characterisation of a frequency-agile tuner system that is designed to perform fast laser detuning operations whilst maintaining a stable optical power. The feedback servo allows for laser detuning operations to be performed over a 50 MHz optical frequency range without losing the power stabilisation lock. The main limitation on the system is the 22 kHz servo bandwidth arising from the electrical circuit being used to generate the servo signal. After improving

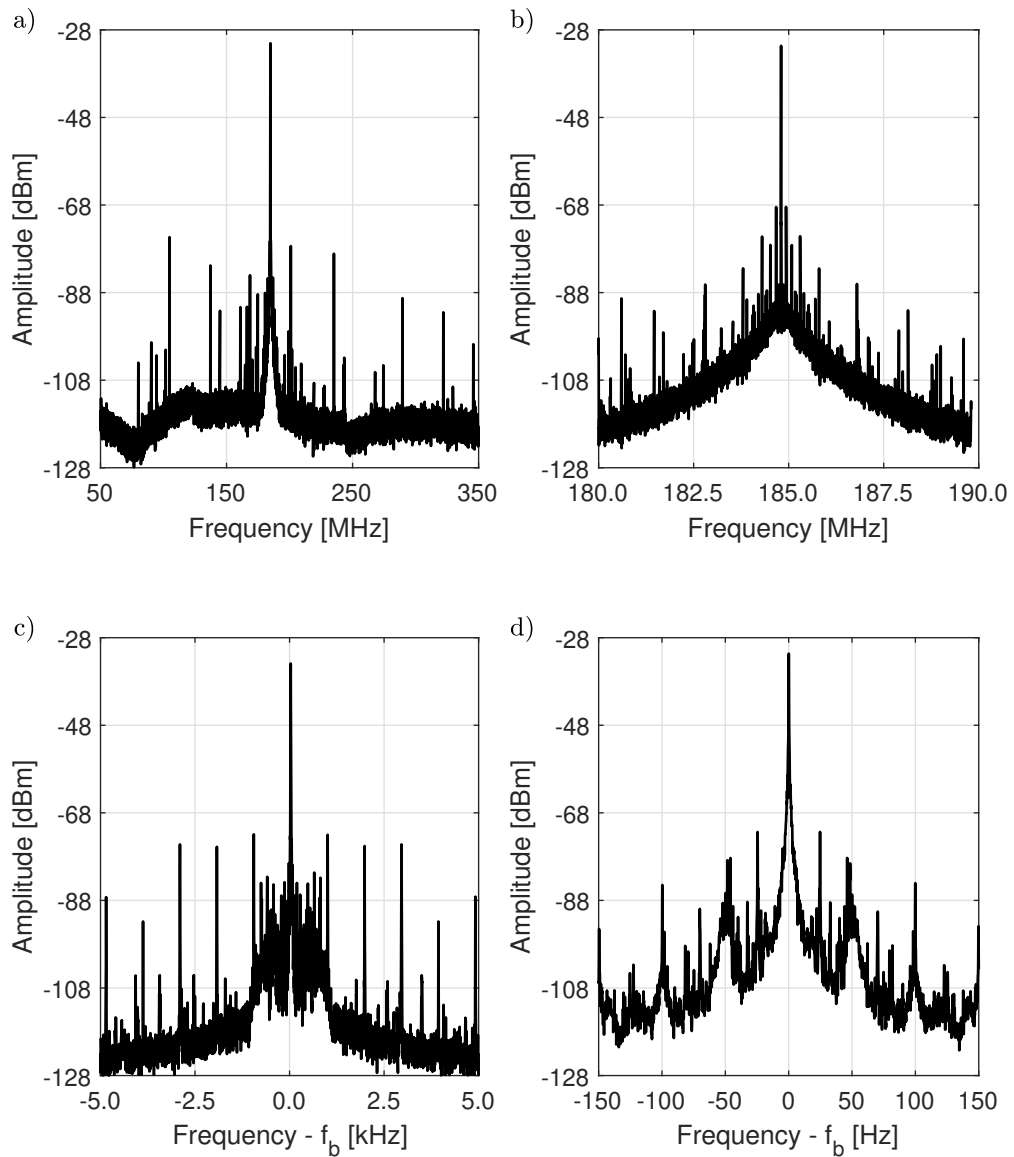


Figure 5.5: a) RF spectrum of the beat note. b-d) beat measurements with reduced scan ranges and higher bandwidths around f_b . In all cases the largest sidebands and noise features are at least -36.5 dBc. The acquisition times, over which ten averages were taken, and bandwidths used for each plot are a) 8.9 s & 10 kHz, b) 1.1 s & 1 kHz, c) 24.4 s & 1 Hz and d) 115 s & 0.2 Hz.

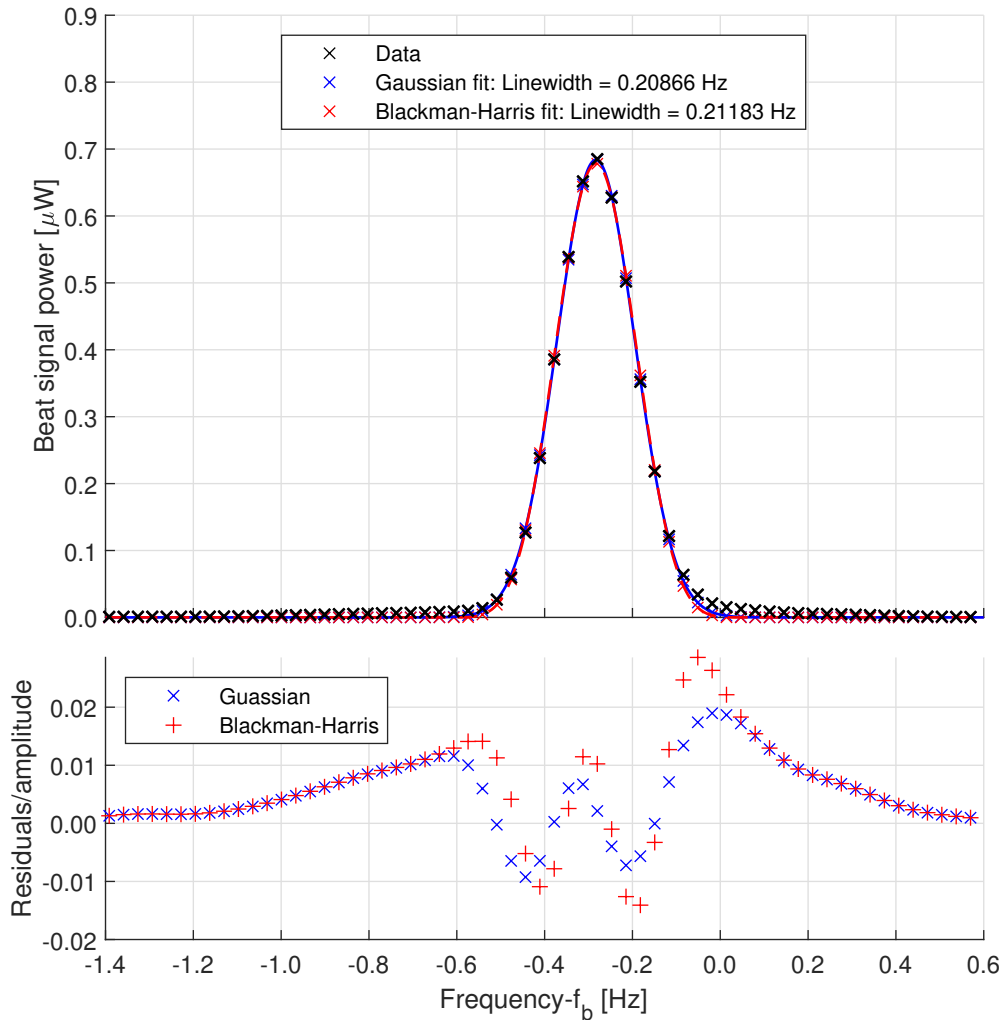


Figure 5.6: Gaussian and Blackman-Harris fits to the main peak in figure 5.5d reveals that the beat note has a linewidth of 0.21 Hz that is maintained at least up to the fibre input that delivers light to the trap (fibre 5 in figure 5.6). Both functions produce good fits as the residuals are small ($\leq 2.6\%$)

this, the next limitation on the servo bandwidth would be the 100 kHz bandwidth of the servo photodiode. At this stage the feedback mechanism could be further improved by implementing a two-stage feedback system that utilises a faster photodiode for short timescale corrections in conjunction with the existing photodiode correcting to correct longer term drifts. Implementing a feed-forward onto the DDS source would also improve performance at short timescales; where the power suddenly changes at the frequency step and the feedback is unable to immediately compensate. The Allan deviation of an out-of-loop photodiode at the output of the tuner reveals that the feedback stabilises the fractional optical power to the $< 10^{-4}$ level over the 10 – 700 s range; below the more stringent threshold for fault-tolerant QIP and does so for the required duration of the experimental routines performed in chapter 7. This also corresponds to a factor of seven improvement over the unlocked laser stability for 1 – 10 s timescales, increasing up to a two order of magnitude of improvement at 1000 s. It should be noted that the performance of the tuner system was evaluated at its output rather than at the ion, due to the pulse shaping AOM that immediately follows the tuner converting the laser from continuous operation to microsecond timescale pulses, which additionally can have varying amplitudes depending on the pulse sequence required for the given experiment. The power-stabilised laser that is input to the pulse control setup ensures that the pulses created by this system are consistent throughout the whole experimental routine. Furthermore, the pulse control setup also features a power stabilisation [142,175] subsystem that facilitates cleanly shaped optical pulses and would improve the power stability of the laser at pulse length timescales. Evaluating this is beyond the scope of the work done in this chapter.

The frequency stability of the tuner and pulse control setup was also verified by measuring a beat between a sample of the output light prior to the fibre that leads to the trap and light from the other active FNCS system at the laser source. At this point the beat note linewidth was measured to be at most 0.21 Hz, with the measurement being limited by the resolution bandwidth of the spectrum analyser that was used to make the measurement. Additionally the measurement showed that any noise and sidebands present in the beat were at least -35 dBc. These together show that the

Chapter 5. Optical Frequency Tuner for the 674 nm Qubit Laser

tuner system (and pulse control setup) do not add significant noise onto the power spectrum of the laser and thus the qubit laser should be suitable for performing fault tolerant QIP gates and for use in the spectroscopy experiments in chapter 7. In the future a second tuner and pulse control setup are intended to be created on the output of the other FNCS system to create a second qubit laser for a new ion trap setup.

Chapter 6

Magnetic Field Stabilisation

6.1 Introduction

As described in sections 2.3 and 2.6.2 the application of a magnetic field to the ion will lift the degeneracy of the quadrupole transition via the Zeeman effect. This makes the transition frequency susceptible to noise in the magnetic field, which now becomes a source of decoherence.

This chapter will evaluate the performance of the magnetic field system described in section 3.3 that is used to nullify the background magnetic field and apply the bias field to the ion. A LabVIEW control programme is used for setting the currents in each of the coils and for applying software based PI feedback to the set currents based on the 7.5 digit readings from the high precision digital multimeters (each one is a single NI PXI-4071 card). The readings from these multimeters are used as in-loop measurements of each coil's performance. Out-of-loop measurements are made with a Bartington MAG-03IE500 magnetic field sensor. Previous measurements with these sensors revealed the presence of cross talk between the different sensor probes in the ribbon cable connecting the main sensor unit, limiting the sensitivity of the measurements made. To compensate for this only a single probe is connected which measures the field parallel to the \hat{k} – vector of the 674 nm laser. At this angle the probe has a degree of sensitivity to the field from all four sets of coils. Additionally whilst recording, the sensor probes generate a 15.625 kHz, ~ 1 mG magnetic field that

Coil	Operating current [mA]
\hat{x} -axis	70
\hat{y} -axis	397
\hat{z} -axis	18
Bias	2000

Table 6.1: Coil operating currents for the measurements taken here in this chapter where the coils are on. For the x-axis, z-axis and bias coils these are close to the typical operating values for the experimental routines used in chapter 7. For the measurements in this chapter the \hat{y} -axis coil is being operated at half of the typical operating current due to the typical current producing a magnetic field that saturates the Bartington sensor.

prevents their use for out-of-loop measurements of the magnetic field during experiment operation.

6.2 Evaluation of the Magnetic Field Stability

The magnetic shield's ability to attenuate the external magnetic field has been evaluated by examining the power spectrum of the magnetic field inside and outside the shield with the Bartington sensor. For these measurements the coils were operated at the values specified in table 6.1. The results of the measurements are depicted in figure 6.1 as both the magnetic field and as the optical frequency modulation that the magnetic field spectrum would impart onto the $S_{1/2}(m_j = -1/2) - D_{5/2}(m_j = -5/2)$ transition. These were calculated from the voltage measurements using the Bartington conversion factors specified in table 6.2 and the corresponding frequency shifts were calculated using equation 2.23. At 50 Hz, the largest component of the power spectrum, the fluctuations are reduced by a factor of 1065, which meets the specification given in section 3.3.

A series of measurements were undertaken to verify that none of the devices and external power supplies which were located inside or near the shield produced a magnetic field strong enough to perturb the ion under standard operating conditions. The only exceptions to this were the ion pump that provides the UHV in the vacuum chamber and the strontium oven that is used to replenish the hotplate once depleted [112].

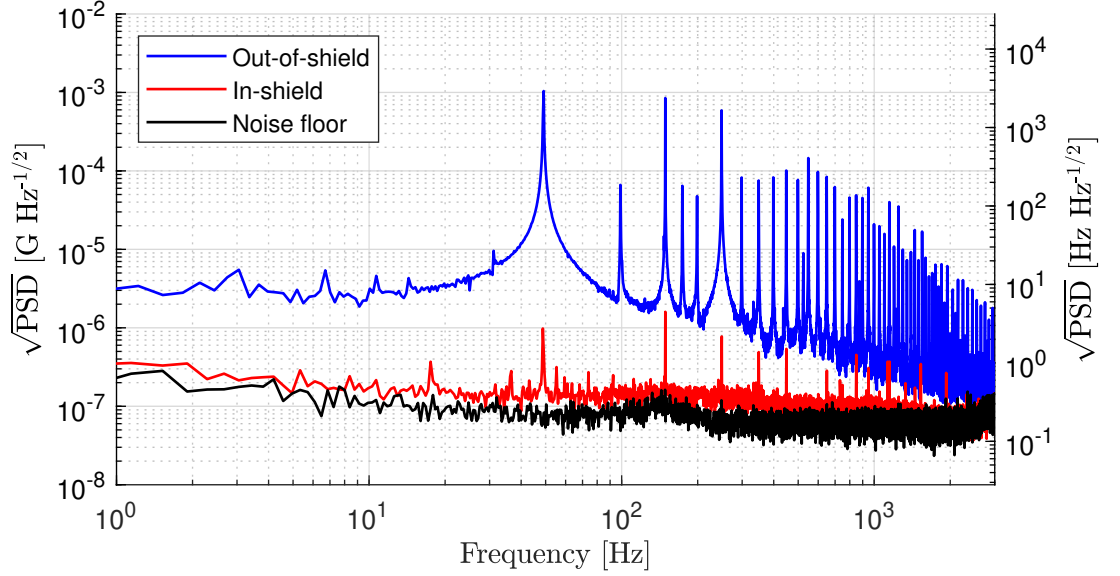


Figure 6.1: Power spectrum of the magnetic field inside and outside of the shield. The left scale shows the magnetic field that the ion is expected to experience as measured by the sensor and the scale on the right shows the corresponding frequency shift in the $S_{1/2}(m_j = -1/2) - D_{5/2}(m_j = -5/2)$ transition. The magnetic field at 50 Hz is reduced by a factor of 1065. Here Gauss ($1 \text{ G} = 10^{-4} \text{ T}$) is used as the unit for magnetic field, as a $1 \mu\text{G}$ field corresponds to a Zeeman shift on the order of a single hertz ($\sim 2.8 \text{ Hz}$) for the $S_{1/2}(m_j = -1/2) - D_{5/2}(m_j = -5/2)$ transition.

Meter	Factor [G V^{-1}]
\hat{x} -axis	$3.00 \times V_x$
\hat{y} -axis	$1.88 \times V_y$
\hat{z} -axis	$1.31 \times V_z$
Bias	$0.725 \times V_{bias}$
Bartington mag-03	$0.1 \times V_{OoL}$

Table 6.2: Calibration factors for converting the high precision multimeter readings for each coil and the out-of-loop Bartington sensor to convert the voltage measurements to the magnetic field at the ion. These factors were calculated from measurements of the magnetic field generated by each coil taken by Guido Wilpers and the specified resistance of the precision resistors. The frequency shift that these impart onto the qubit transition can be calculated by multiplying these by $2\mu_B/\hbar$ via equation 2.23.

The ion pump was left on during all tests due to the long pump down time required to reach UHV and with that, its steady state operation. The oven was left untested due to the rarity of its use and a desire to avoid depleting its SrO:Ta reservoir. The device testing was split into two categories: “passive”, where each device was left on in a steady state fashion, without user input for ≥ 8 hours both alone and in different combinations with the other devices that are passively tested, and “active”, where the main parameter of the device was adjusted to observe its immediate effect on the magnetic field. The devices investigated and the type of tests that were carried out for each are listed in table 6.3. For passive testing the in- and out-of-loop recordings were compiled into Allan deviations (see equation 5.1 on page 91). The results of these tests were then compared against a background measurement that served as the noise floor of the apparatus. In the background measurement all of the devices were disconnected from their power supplies and the source measure units that supply current to the coils were bypassed and disconnected from their circuits. In these tests there was no noticeable difference in the Allan deviations between the background measurement and the individual devices operating in their steady state. For measurements taken when the source measurement units were connected the tests were performed twice, once with the feedback off and once with it on to evaluate the ability of the feedback to compensate for fluctuations in the coil current under the given apparatus configuration. Figures 6.2 and 6.3 show the Allan deviations produced when the apparatus is fully operating under steady state conditions, with and without the feedback engaged. The latter of these two figures shows that the magnetic field is stabilised to < 10 Hz over 1 s to 7000 s timescales and manages to reach < 1 Hz for times between 20 s and 350 s; although for times greater than ~ 400 s the measurement becomes limited by the noise floor of the out-of-loop sensor. This also prevents accurately describing the effectiveness of the software feedback during standard operating conditions. Despite this, the level of stability achieved should be sufficient for the experiments described in chapter 7.

The active tests were carried out in the span of minutes and were not used to create Allan deviations, as in all three of these tests, a noticeable effect on the out-of-loop measurement of the magnetic field was observed. The results of these tests are

Device	Test Type
Hotplate	Active
EFG & DC electrodes	Passive & active
Qubit laser piezo adjusters	Passive & active
Source measure units	Passive
Trap RF drive	Passive

Table 6.3: List of devices that were tested for influence on the magnetic field inside the magnetic shield. An “active” test refers to a test where the main parameter of the device (applied voltages for the EFG and piezo adjusters and source current for the hotplate) was varied during the device operation, whilst a “passive” test refers to a test where the device was left in steady state operation, without being manually adjusted. Passive tests lasted for times ≥ 8 hours and were used to produce Allan deviations that were compared against a background Allan deviation that was obtained with all devices switched off.

presented and discussed in sections 6.4 and 6.3.

The out-of-loop sensor is specified to have a temperature scaling sensitivity of $\sim \pm 20$ ppm/ $^{\circ}\text{C}$. As a consequence variations in the temperature inside the magnetic shield will impose drift onto the magnetic field measurements taken with this sensor. Thus, the temperature inside the shield is recorded to check for any correlations that may appear in the Allan deviations created from the out-of-loop measurements. For this, one thermistor is glued onto the \hat{y} -axis coil, a second to the outside of the ion pump heat sink and a third is suspended in the air above the coils, near the top of the inside of the shield. The out-of-loop magnetic field data used to calculate the Allan deviations in figure 6.3 and the corresponding thermistor measurements are presented in figure 6.4. Here the \hat{y} -coil and suspended thermistors show a temperature change of 0.3 $^{\circ}\text{C}$ and 0.45 $^{\circ}\text{C}$ in the feedback off case, which was recorded prior to the feedback on case, indicating that the inside of the shield had yet to thermalise at the time of recording, caused by the coils having been set to their standard operating currents immediately prior to the beginning of the measurement. By the time of the second measurement began the system had thermalised. The thermistor measurements in the feedback off case would indicate that the magnetic field readings would increase by ~ 4 μG over the course of the recording, which as can be seen in figure 6.4a is factor of ~ 7.5 lower than the drift of the out-of-loop sensor over the same duration (~ 30 μG).

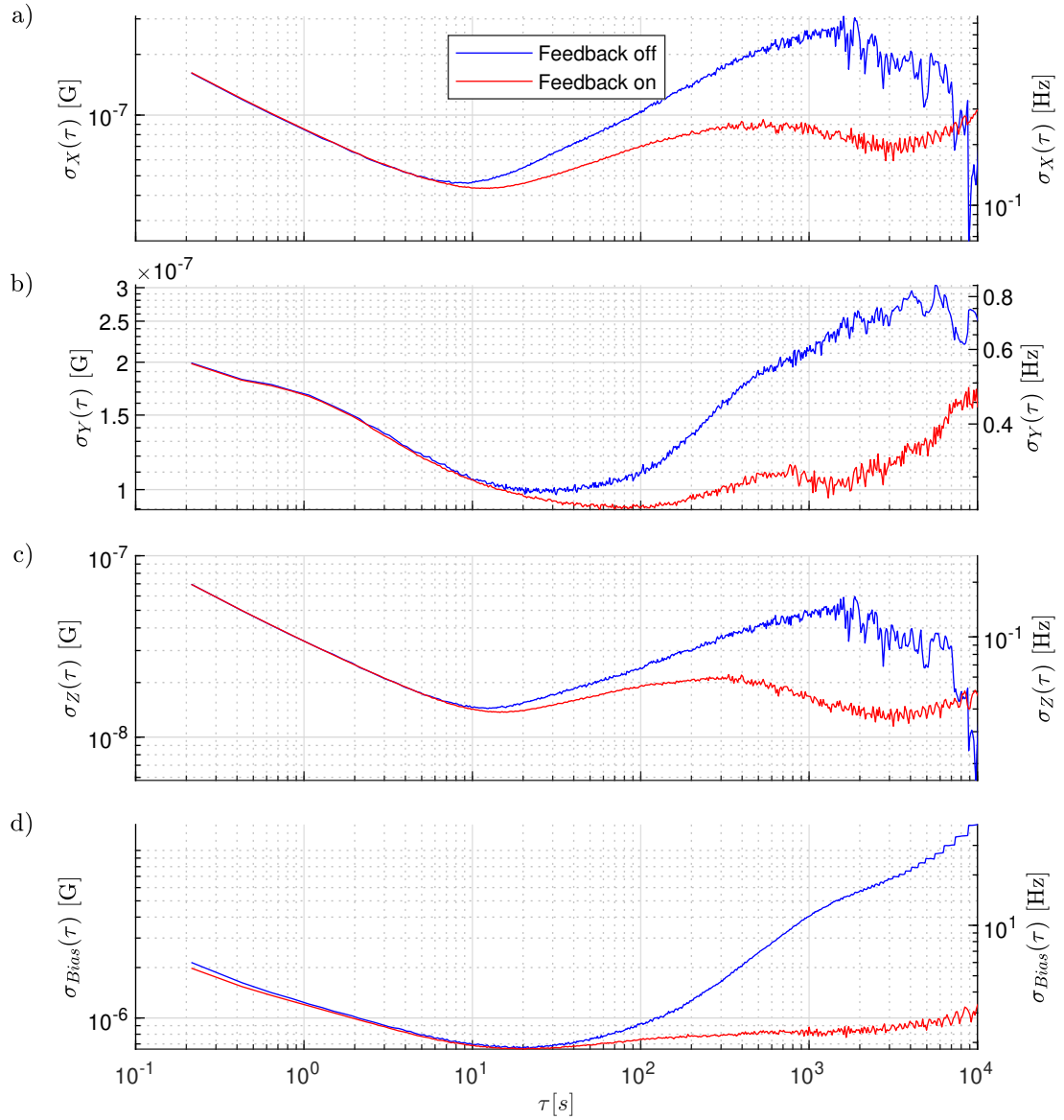


Figure 6.2: Allan deviations of the in-loop measurements from the high precision multimeters. The voltage measurements from these meters are converted into the expected magnetic field using the factors given in table 6.2 and the conversion to the expected frequency shift of the qubit transition is calculated from these via equation 2.23.

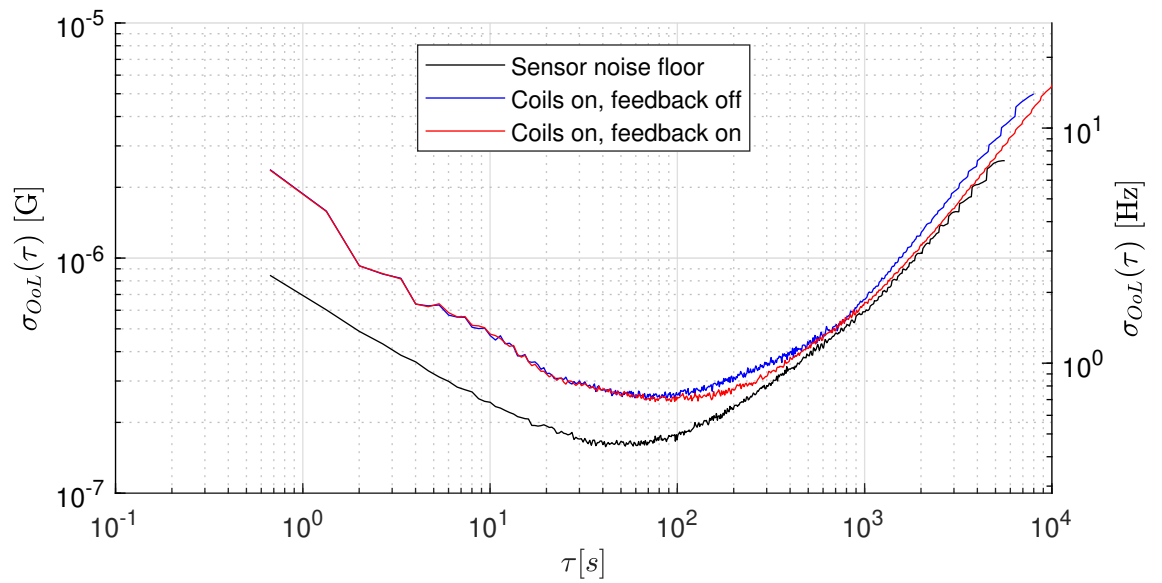


Figure 6.3: Allan deviations of the out-of-loop measurements from the Bartington sensor inside the shield. The Allan deviation indicates that between < 1 s and 7000 s the system is able to stabilise the magnetic field such that it only induces fluctuations at the < 10 Hz level in the qubit transition and to the < 1 Hz level for 20 s – 350 s timescales. This measurement is limited by the noise floor of the sensor at the timescales over which the software feedback is expected to work limiting the ability to evaluate its effectiveness.

This would suggest that thermal effects are unlikely to be the main limiting factor on the noise floor of the Allan deviation. This is reinforced by the measurement where the feedback is on, where the same rate of change in the magnetic field can be seen, despite the temperature being thermalised according to the thermistor recordings.

6.3 Effect of the Hotplate on the Magnetic Field

In addition to measuring the passive stability of the setup, the effect on the magnetic field from running the strontium hotplate, as if it was being used during a loading sequence, was tested. Due to the high currents (up to 6 A) involved in running the hotplate there is no surprise that there is an effect on the magnetic field whilst ions are being loaded into the trap (figure 6.5). In addition to the magnetic field changing during hotplate operation there is also a settling time for the magnetic field after the ion loading sequence is completed. Figure 6.6 shows that after the hotplate operation is ceased the magnetic field slowly returns to its pre-loading value. Fitting a two phase exponential determines the fast time constant of the decay to be 15.2 minutes and the slow time constant to be 2.13 hours. Examining the thermistors inside the magnetic shield (figure 6.7) show that the temperature decreases after the hotplate is switched off, with the \hat{y} -coil thermistor showing the largest change at 0.6 °C, corresponding to an expected 5 μ G decrease in the magnetic field. A two phase exponential fit to the \hat{y} -coil data gives time constants similar to those of the fit to the out-of-loop sensor data. This indicates that either the out-of-loop sensor is more sensitive to variations in temperature than specified in the manual or that there is a slight temperature dependent variation in the magnetic field inside the shield. The corresponding frequency shift induced on the ion by these effects is small ~ 300 Hz/°C as shown by the figures 6.6 and 6.7. Further investigations into this could be carried out by placing a heating element inside the magnetic shield and examining the effect this has on the ion's motional spectrum in a nullified field. If this effect turns out to be significant for future work then it may be possible to use the thermistor measurements as part of a feedback mechanism to compensate for any temperature induced change in the qubit transition frequency.

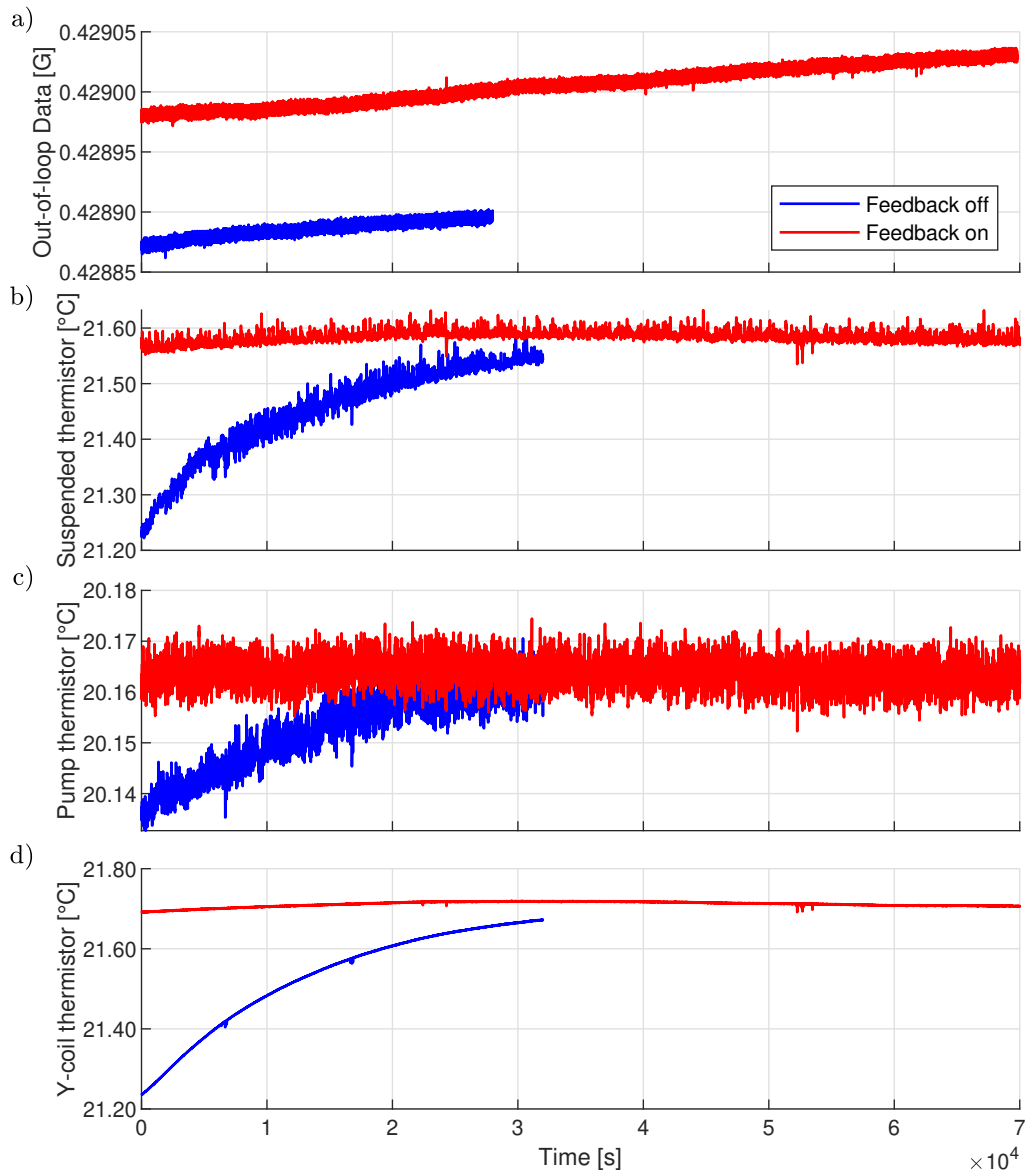


Figure 6.4: a) Data used to calculate the out-of-loop Allan deviation of the magnetic field and b-d) the corresponding thermistor measurements. The feedback off data was recorded prior to the feedback on data, hence why the temperature readings are stabilised in the case where feedback is on but not so when the feedback is off. Fitting an exponential function to the feedback off data in (d) determined that the time constant of the coil was 13760 s.

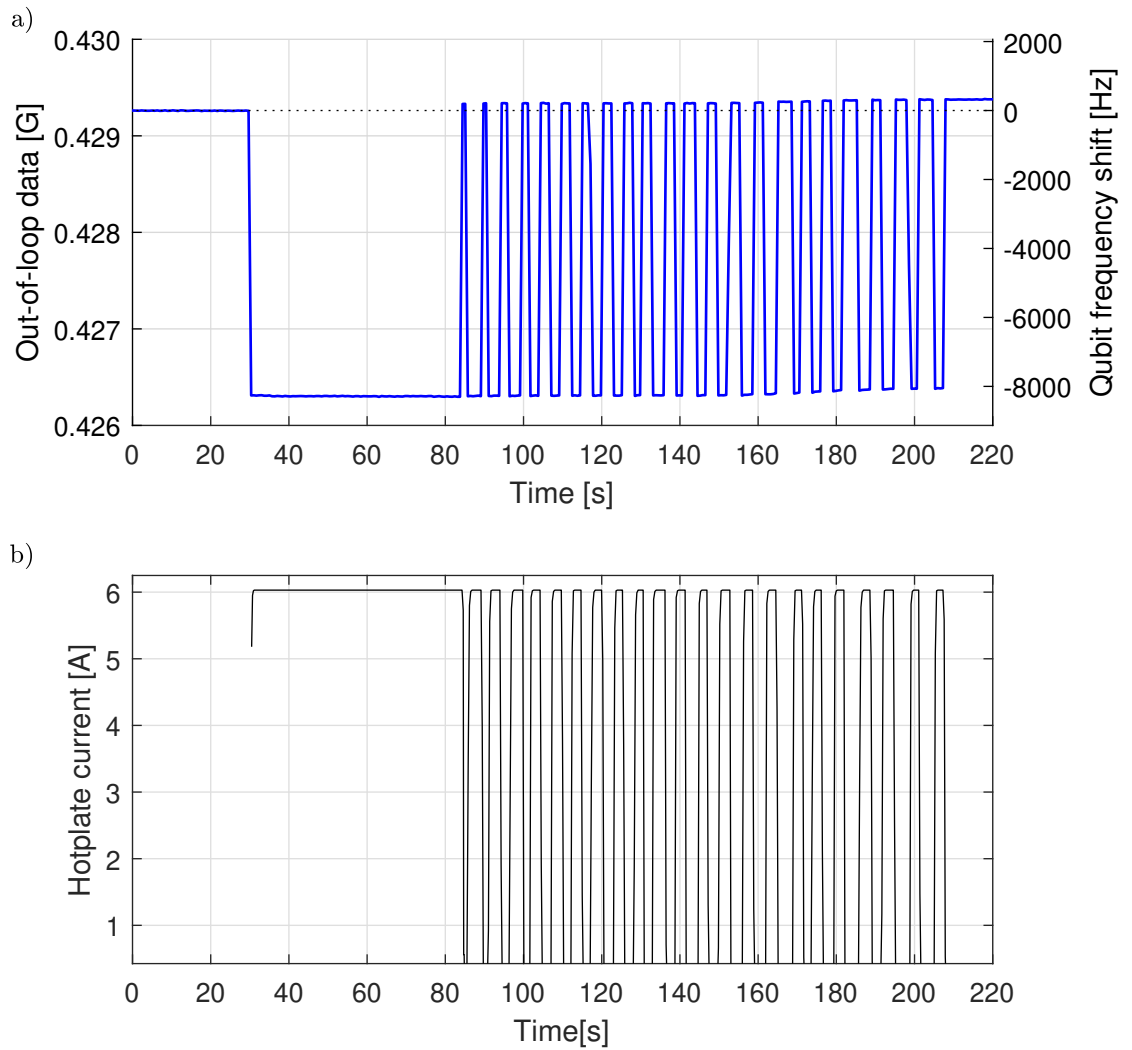


Figure 6.5: a) Out-of-loop measurement whilst running the strontium hotplate as if it were loading an ion. At the end of the sequence the magnetic field does not fully return to its initial value. b) Current applied to the hotplate during a loading sequence.

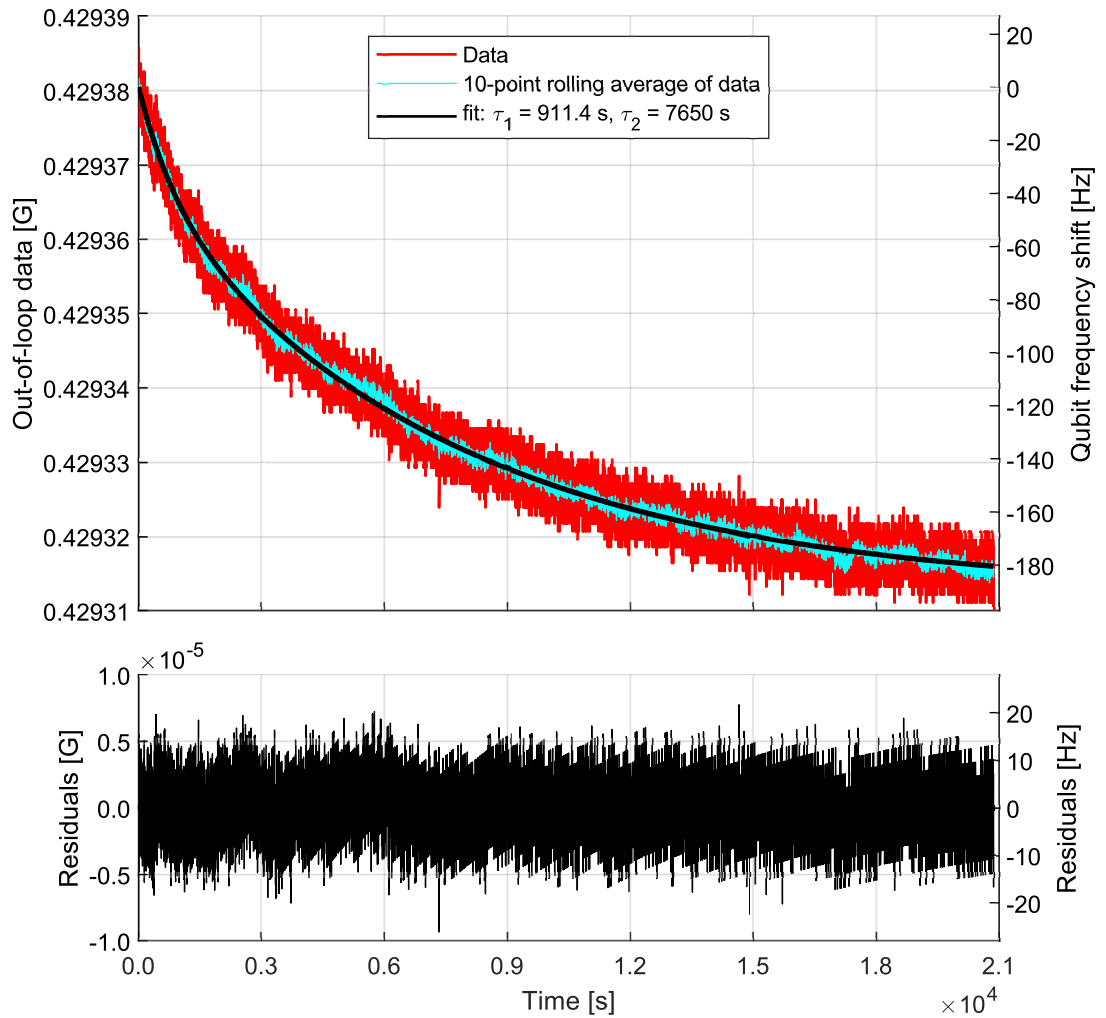


Figure 6.6: Out-of-loop measurements that were continued after the hotplate was switched off in figure 6.5. Fitting a two phase exponential to these readings with a Levenberg-Marquardt algorithm gives time constants of 911.4 s and 7650 s. A rolling average of the recorded data is included to increase the visibility of how the out-of-loop data evolves.

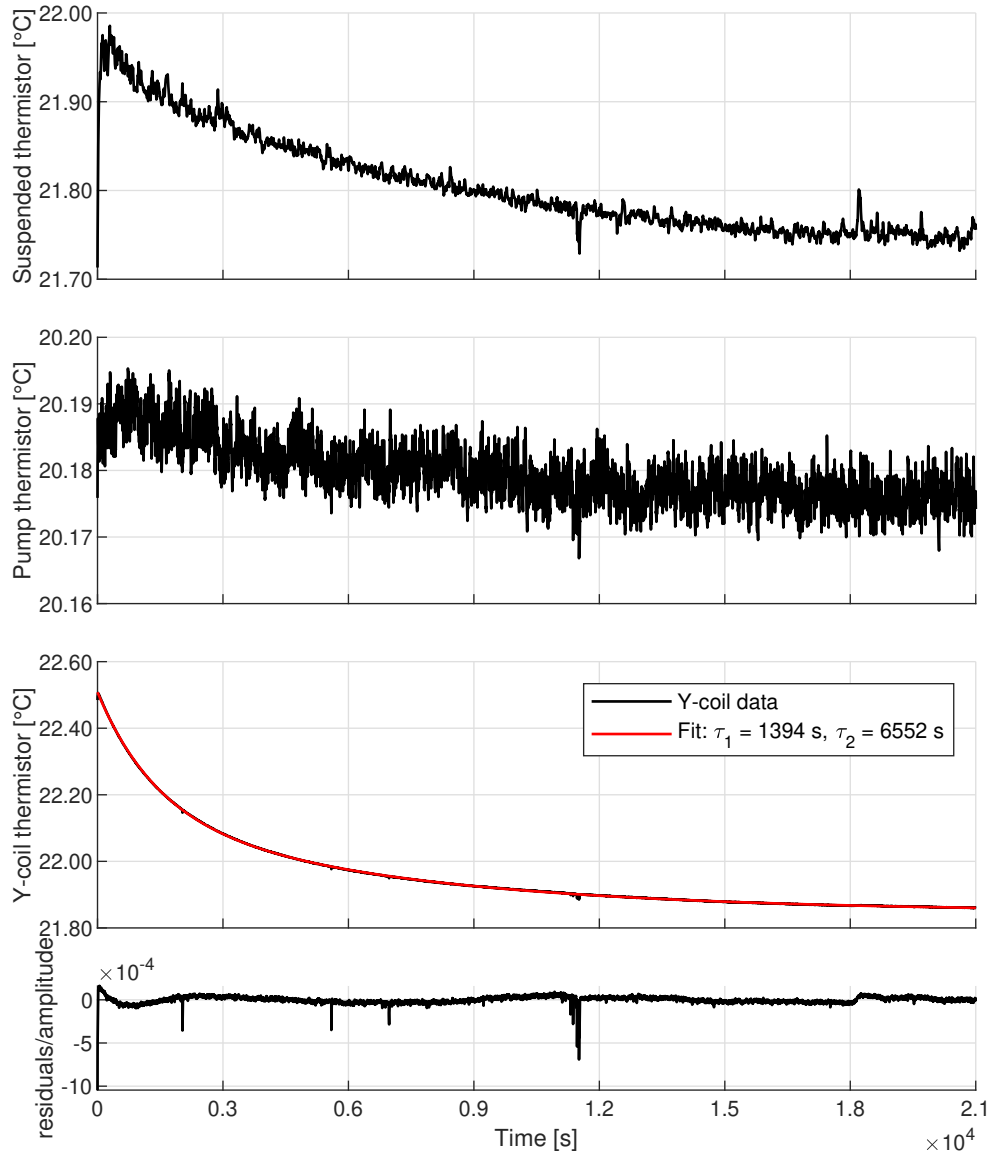


Figure 6.7: Thermistor readings taken after the hotplate loading routine is completed. Each thermistor shows a change in temperature with a time constant of the same order of magnitude as that seen by the out-of-loop sensor in figure 6.6. A two phase exponential fit to the \hat{y} -coil data gives time constants $\tau_1 = 1394$ s, $\tau_2 = 6552$ s.

6.4 Observed Ground Loops

During testing of the magnetic field stabilisation system it was observed that changing the DC voltages applied to the trap electrodes produced a small change in the magnetic field (see figure 6.8a). Each electrode imparted the same magnitude of change onto the field and changing multiple electrodes produced a cumulative change in the field. There also appears to be no hysteresis when changing these voltages. Together these implied the presence of a ground loop, which was confirmed by removing the ground connection between the EFG and the filter board and applying the same sequence of voltage changes to the trap. With this, changing the DC voltages produced no change in the out-of-loop sensor reading. Unfortunately this change rendered the trap unable to load ions and thus the ground connection, and with it the ground loop, had to be re-instated. As a consequence of this the magnetic field is re-nullified after any shuttling sequence or changes to the DC voltages are made that do not end with the electrodes having the same voltages as they did when the field was initially nullified.

A similar observation was made when changing the pointing of the 674 nm laser with the piezo transducers inside the shield (figure 6.8b). Unlike the DC voltages applied to the trap changes to these induce large amount of hysteresis. Due to the beam pointing rarely being adjusted no further changes or investigations were made other than to re-nullify the magnetic field if the beam pointing is adjusted.

6.5 Summary

The efficacy of the magnetic field stabilisation for the purpose of reducing decoherence has been evaluated in this chapter. The ability for the magnetic shield to attenuate the external magnetic field was evaluated and found to meet its specification of nullifying noise at 50 Hz by a factor of 1065.

The possibility of devices inside and located near the magnetic shield influencing the magnetic field that the ion would be exposed to were investigated by comparing Allan deviations calculated from > 8 hours of measurements from the in- and out-of-loop sensors. Each device that could possibly influence the magnetic field, except the stron-

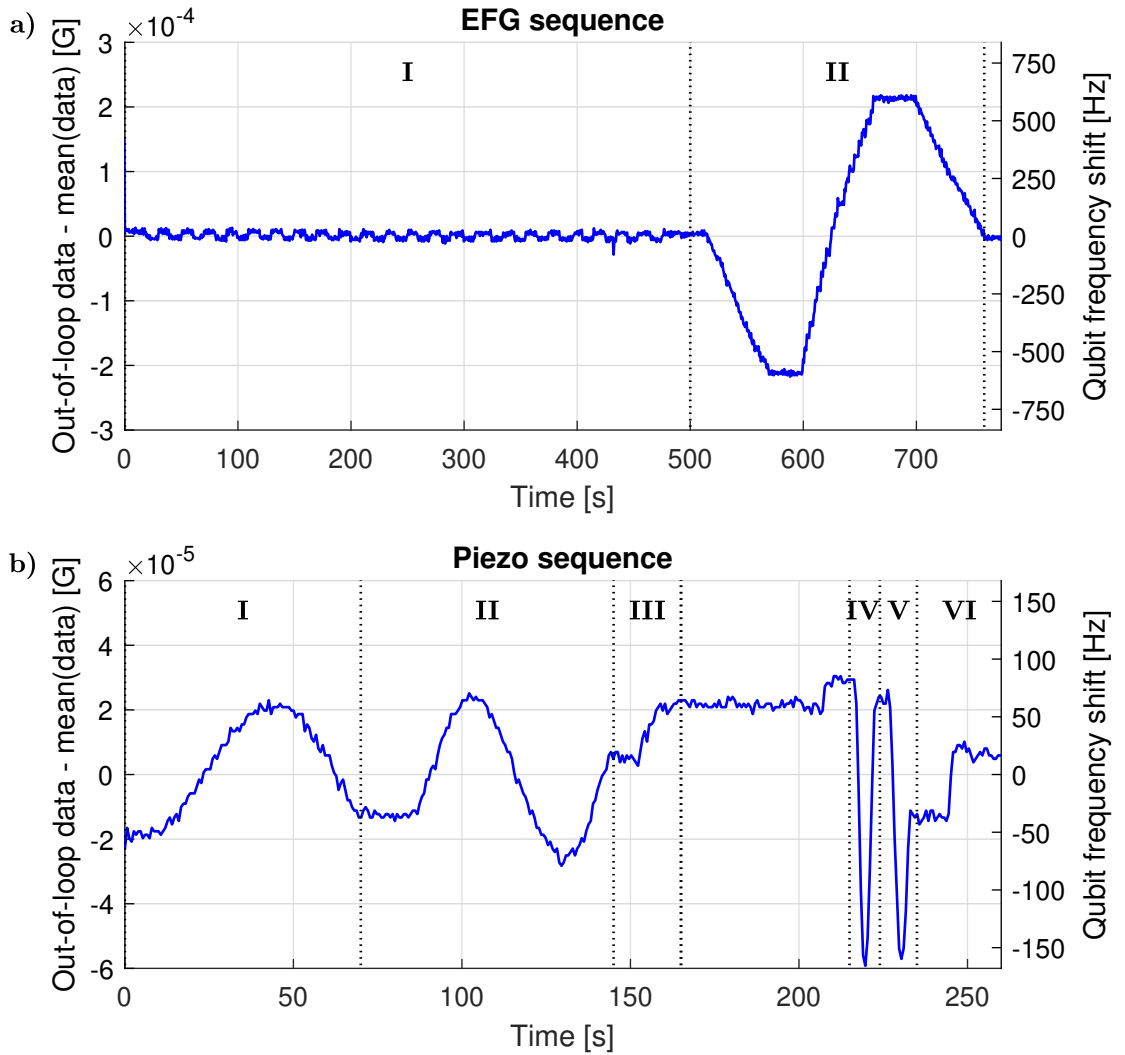


Figure 6.8: a) Out-of-loop sensor readings whilst changing the DC voltages on the trap DC and compensation electrodes. A change of ± 8 V, the limits of applicable voltages, on an electrode impart a cumulative $\sim \mp 10 \mu\text{G}$ change onto the magnetic field ($\sim \mp 28$ Hz qubit transition frequency shift). The testing sequence used here was I) sequentially setting each electrode to $+8$ V for 10 s then back to 0 V for 10 s, II) setting each electrode to $+8$ V then to -8 V and back to 0 V with a pause after setting all electrodes to ± 8 V.

b) Out-of-loop sensor readings whilst changing the voltages applied to the 674 nm beam pointing piezo transducers. Here the testing sequence was I) Ramp the beam horizontally across the full width of the QPD in one direction. II) Ramping with the reverse motion. III) Moving the beam to the centre of the QPD. IV) Ramping the beam position from the top of the QPD to the bottom. V) Ramping the beam position from the bottom to the top. VI) re-centring the beam again.

tium oven and ion pump, was investigated under its steady state operating conditions in isolation and in combination with the other potential sources by comparing against a background measurement in which all devices were disconnected. These measurements found no noticeable differences between the steady state measurements and the background reference. Out-of-loop Allan deviations of the nullified magnetic field with the bias field applied show that the field can be stabilised to a degree that corresponds to < 10 Hz fluctuations in the qubit transition for $1 \text{ s} - 7000 \text{ s}$ timescales and < 1 Hz for $20 \text{ s} - 350 \text{ s}$. However for times greater than $\sim 400 \text{ s}$ this measurement became limited by the noise floor of the out-of-loop sensor. This limitation also prevented an accurate assessment of the performance of the software feedback system. Despite this the system is sufficiently stable for the timescales that the experiments in chapter 7 are performed over. The possibility of thermal effects affecting the measurement were investigated and were found not be a major limiting factor on these measurements.

In addition to these steady state tests, the effects on the magnetic field when running the hotplate as if loading an ion was tested. It was found that after the hotplate finishes the loading routine the magnetic field does not immediately return to its pre-routine value, but instead is offset by $\sim 1.2 \times 10^{-4} \text{ G}$ at the end of the sequence before settling back to the steady state value. A fit with a two phase exponential gives a decay with fast time constant of ~ 15 minutes and a slow time constant of ~ 2.12 hours. The possibility of thermal effects either being the source of the offset and decay or otherwise influencing the sensor due to the hotplate heating the inside of the magnetic shield were also considered. Fitting the same formula as before to the thermistor attached to the \hat{y} -axis coil, which measured the greatest change in temperature ($\sim 0.6 \text{ }^\circ\text{C}$), gave similar time constants to the fit of the magnetic field over the same duration ($\tau_{fast} = 23$ minutes and $\tau_{slow} = 1.82$ hours), which combined with the magnitude of the change in the magnetic field being only slightly above the expected change from the sensors temperature sensitivity, leave this as a probable origin of the effect. The possibility of further investigations into this effect were considered, however due to the small effect that this has on the ion's Zeeman splitting ($\sim 300 \text{ Hz}/^\circ\text{C}$), it is not considered an immediate priority. Additionally, ongoing work to replace the

oven-hotplate based ion loading mechanism [112] with a laser ablation based method [227,228] may render further investigations unnecessary. With this loading method the high current heating element inside the shield will not be required for routine operation of the apparatus and will thus increase the thermal stability inside the shield in addition to removing the magnetic field from the high current.

Tests on the voltages applied to the DC and compensation electrodes revealed the presence of a ground loop between the EFG which supplies the DC voltages and the vacuum chamber that serves as ground for the trap electrodes. Attempts to remove this ground loop resulted in the trap being unable to load ions, thus the ground loop has been left in the system with further investigation required on how to effectively remove this problem. A similar issue was observed with the piezo transducers that are used to steer the 674 nm beam pointing. Due to the rarity of these being used it was decided that no further investigation was to be done and the magnetic field was to be re-nullified in the event that they are altered. Implementing chip-scale waveguides [91,229] that would remove the need and ability to adjust the beam pointing would circumvent this problem. Until then re-nullification of the magnetic field after adjusting the beam pointing of the qubit laser is required.

Chapter 7

Ion Spectroscopy

7.1 Introduction

The universal set of QIP gates is composed of the single qubit rotation and the two qubit C-NOT gate [18–20]. Thus the ability for the apparatus to perform the component operations that would comprise these gates serves as the fundamental benchmark of its performance. The key metrics used to evaluate this are the coherence times of the qubits and the fidelities of the gates applied to the qubits. The coherence time of the qubit serves as an indicator for how many qubit gates can be applied before the qubit decoheres. For qubits encoded in an optical transition the lifetime of the excited state serves as the ultimate limit for what this value is; however other sources of decoherence can reduce this further, such as those described in section 2.6. The gate fidelity is simply how well the output state of the gate operation agrees with the ideal outcome [230]. The ability for two qubit gates to perform entanglement operations extends beyond QIP to uses in metrology, as it offers faster and more sensitive measurements than that offered by uncorrelated single qubits [231, 232].

This chapter will feature investigations into the coherent control and manipulation of the states of one and two ions that are encoded in the $S_{1/2}(m_j = -1/2) - D_{5/2}(m_j = -5/2)$ Zeeman component of the quadrupole transition. These experiments were performed using the apparatus described in chapter 3. As demonstrated in chapters 5 and 6 the apparatus should be sufficiently capable of performing the experimental routines

presented here. These experimental sequences, unless otherwise stated, follow a similar formula to that outlined in figure 3.10 (page 59):

- 1) Doppler cooling,
- 2) Optical pumping into $S_{1/2}(m_j = -1/2)$,
- 3) Spectroscopy pulse(s),
- 4) State readout and
- 5) State clear out.

Each experimental sequence utilised applies a different set of spectroscopy pulses for stage three. Each measurement is taken by repeating the sequence many times (minimum of $100\times$) and averaging the state readouts to obtain an excitation probability for each value of the parameter that the apparatus is scanning.

First a discussion on the data fitting routines via the numerical simulation of the Bloch equations (equations 2.41 on page 29) is presented. Following this section 7.3 demonstrates that the qubit laser beam pointing was optimised for one and two ion spectroscopy. Section 7.4 presents the motional spectra of one and two ions obtained via frequency-resolved spectroscopy, where the laser detuning is varied. Section 7.5 demonstrates coherent control of the qubit by the use of time-resolved spectroscopy to create Rabi oscillations. Further coherent control is demonstrated with Ramsey spectroscopy in section 7.6 where a sequence of laser pulses are used to control the qubit state. The ability to cool the ion into the motional ground state with sideband cooling is demonstrated in section 7.7. In this section the experimental routine uses the full experimental sequence described in figure 3.10. Section 7.8 covers the effects of applying amplitude-shaped pulses to a single ion. Finally section 7.9 covers considerations that have been made for performing the entanglement of two ions via the Mølmer-Sørensen gate operation and how the expected results are to be interpreted.

7.2 Data Fitting

The rotation of the Bloch vector around the Bloch sphere and its decay due to decoherence can be modelled by numerically integrating the Bloch equations (equations 2.41, on page 29) over a pulse of duration T_L with the ion initialised into $\rho_{gg} = 1$ and

$\rho_{ee} = 0$ at $t = 0$. The effects of an experimental sequence with multiple pulses, such as the Ramsey spectroscopy techniques used in section 7.6, can be simulated by simply simulating each section of the routine in sequence using the output of the numerical integration from the end of the first part as the initial condition for the second part and so on. The effects of free precession times where the ion is not exposed to the laser can be simulated by setting the Rabi frequency to zero for the duration of the period. Fitting the final state values of the whole sequence to data sets acquired from the experimental spectroscopy routines allows for unknown experimental parameters to be found. However due to the projective nature of the experimental state measurement only the excitation probability, P_{ee} , is measured. The population difference ($\rho_{ee} - \rho_{gg}$) from the Bloch equations can easily be converted to P_{ee} via

$$P_{ee} = \frac{((\rho_{ee} - \rho_{gg}) + 1)}{2} \quad (7.1)$$

When numerically integrating the Bloch equations, any dephasing that originates from the apparatus (such as the laser linewidth and any fluctuations or drift in the magnetic field, laser frequency or intensity) is encoded into the parameter for the observed laser linewidth Γ_L [135, 140]. However, it should be noted that the fitted values of Γ_L have large uncertainties as the pulse durations being used here are much smaller than the coherence time of the qubit (i.e. $T_{pulse} \ll 1/(\Gamma_L + \Gamma_{eg}/2)$ from equations 2.41). Due to this the decay from Γ_L will only make a small contribution to the evolution of the Bloch vector and thus the determined value for the effective laser linewidth is unlikely to be accurate. The effects of imperfect state initialisation and measurement can be factored into the model by simply multiplying the simulated P_{ee} by an efficiency factor, A , which in section 7.4 is determined to be 0.996. The different vibrational levels that ion can occupy provide different Rabi frequencies, which complicates accurate simulations of the excitation probability. By numerically integrating equations 2.41 for each n that have a realistic occupation probability (where the occupation probability is given by equation 2.18 and such that $\sum P_n \geq 0.9999$), allows for the effects of each $\Omega_{n,n'}$ (via equation 2.34) to be considered. This, more accurate, representation of P_{ee} is then

determined by calculating $P_{ee} = \sum_n P_n P_{ee}(n)$.

Due to the binomial statistical nature of the measurement, where the excitation probability is determined by the average of N binary measurement outcomes, least squares algorithms cannot be used to perform the fitting to the data. Instead the more general maximum likelihood estimation (MLE) must be used [233, 234]. In this method the point in the parameter space that maximises the probability of producing the observed data set is determined to be the best fit. Here to evaluate this, the log-likelihood is calculated with

$$L(\xi) = \sum_i [\ln(N!) - \ln((N - X_i)!) - \ln(X_i) + X_i \ln(AS_i) + (N - X_i) \ln(1 - AS_i)] \quad (7.2)$$

where $X_i = P_{ee,i}N$ is the number of excited state detection events for the i^{th} data point and S_i are the results of the numerical integration with the given parameter set, ξ . This particular method of evaluation is utilised for ease of computation and the large increase in the value of $|L(\xi)|$ for values of S_i that poorly correspond to the value of X_i . Due to the large number of calculations involved in performing each iteration of the MLE routine it can be inefficient to raster scan through the parameter space if two or more parameters are considered free and there is a large parameter space to scan through. The implementation of parallel computing for the simulation can reduce the required computation time, however scanning over the parameter space with sufficient resolution can still be time consuming. To get around this, it can be more computationally efficient to search through the parameter space for the maximum value of $L(\xi)$. After evaluating a pre-provided initial condition the fitting routine takes a small step in each direction of the parameter space to establish an initial gradient on each axis of the space. Next the search routine iteratively tries to maximise equation 7.2 by reaching the point in the parameter space where the derivative on all axes is either zero or the gradients between successive measurements become smaller than a given tolerance factor. This routine was implemented in a Matlab code that performs the parameter space search and numerical integration with the considerations discussed above.

Uncertainties in parameters determined by the fitting routine are calculated by

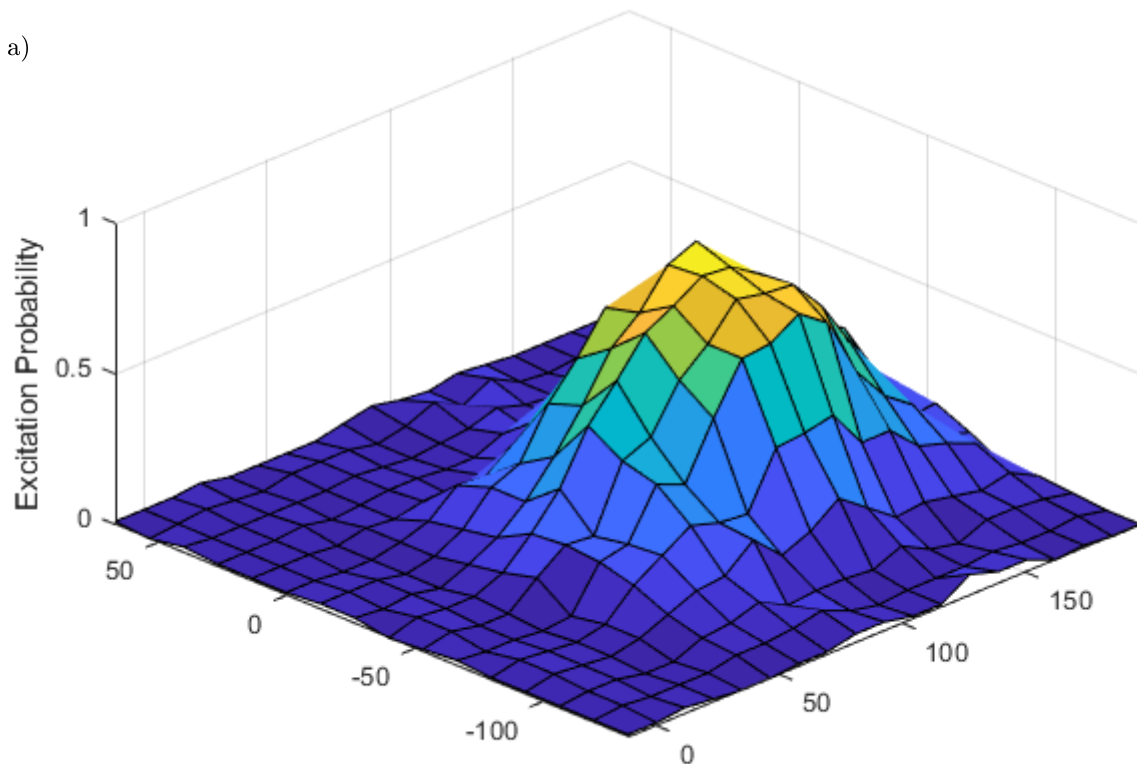
determining the Hessian matrix, the second derivatives on each axis of the parameters space around the ξ_{\max} that give the maximised $L(\xi)$, which is then inverted to give the covariance matrix. This details how inter-related the parameters are with each other, with the diagonal elements providing the variance of each parameter, and from which the confidence region around ξ_{\max} can be calculated. In the parameter space, the confidence region take the form of an ellipsoid centred on ξ_{\max} that is rotated by the parameters inter-dependency. To establish the uncertainties for each parameter the ellipsoid is projected onto each axis of the parameter space [135, 235]. In this chapter the uncertainties correspond to the 68 % confidence intervals given by a one-tailed χ^2 distribution with a number of degrees of freedom equal to the number of parameters being fitted.

7.3 Beam Position Optimisation

To ensure that the ion is exposed to the centre of the qubit laser, a raster scan of the beam pointing was conducted by varying the voltages applied to the piezo adjusters on the final mirror before the ion trap. For each measurement, the pointing of the beam was determined and set by using measurements from the QPD (Thorlabs PDQ80A) on the far side of the trap as feedback for the adjusters. Next the experimental routine was performed with a 100 μs , 16 μW spectroscopy pulse of 674 nm light being applied to the ion and then recording the excitation probability. These pulse parameters were chosen such that the maximum the excitation probability would be less than one and thus the maximum recorded excitation probability would correspond to the optimum beam position. Figure 7.1a depicts the results of this scan. Once completed the adjusters were set to settings that produced the maximum excitation probability. It would be expected that when more ions are added into the trap the centre of their common motion would lie at the same location as the single ion's maximum excitation probability. It should be noted that due to neither of the ions being at the centre of the beam, the two ions will experience slightly lower, but still approximately equal, laser intensities than in the case of the single ion. Attempting to repeat the raster scan with two ions (figure 7.1b) however only reveals that the PMT observes the maximum excitation when both

ions are illuminated and lacks the sensitivity to spatially resolve each individual ion. In cases where three or more ions are trapped the laser will provide higher intensities (and thus higher Rabi frequencies) for ions closer to the centre of the string, which may complicate the implementation of qubit operations or introduce a reduction in gate fidelity. Future developments in integrating laser-written waveguides [91,229] that mate to the vacuum chamber may aid in overcoming this. This would also remove the need to perform this routine as the optimum beam pointing would be pre-written into the waveguide. This could work by either supplying multiple qubit lasers to the operation zone of the trap with waveguides written for different numbers of ions, or each ion could be trapped in a separate zone with a single qubit laser being used for each.

a)



b)

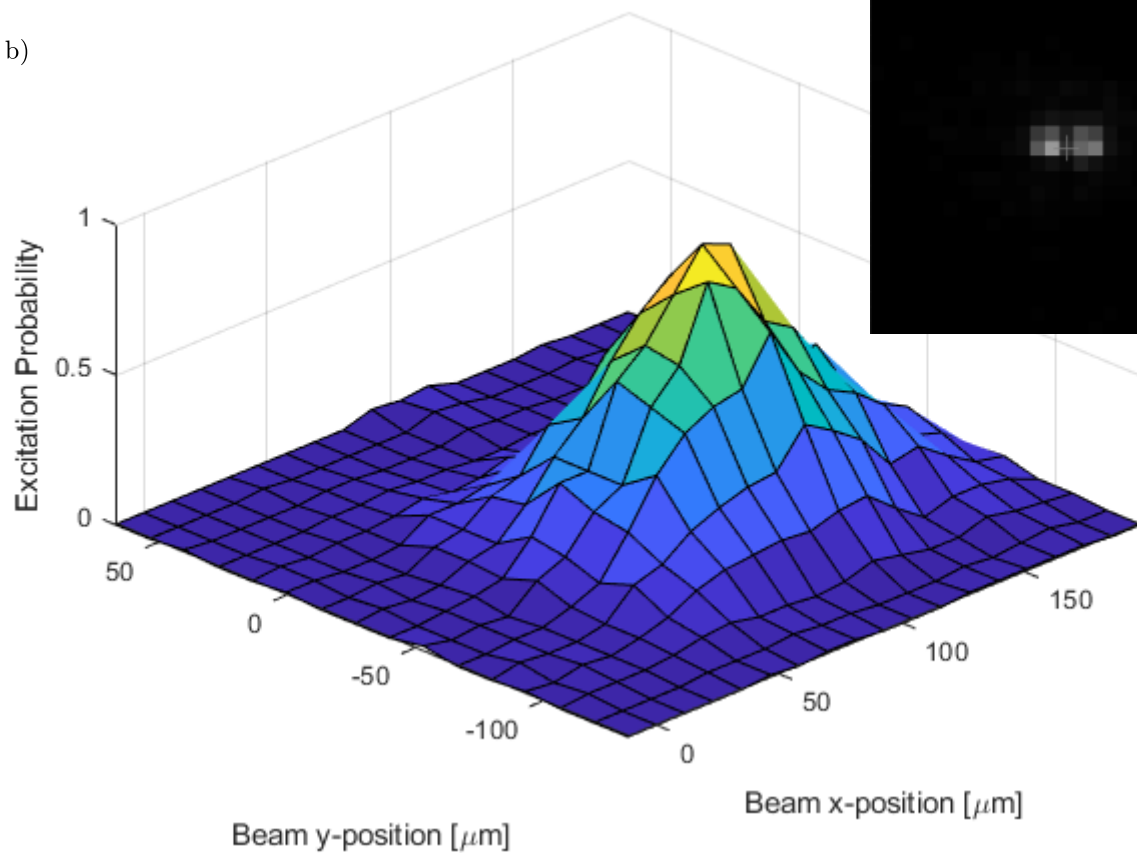


Figure 7.1

Figure 7.1: Raster scan of the beam pointing with a) a single ion and b) two ions confined within the trap. Here an increment of one on the \hat{x} -axis of the QPD corresponds to the beam centre moving by 463 nm on the plane at the ion and the same increment on the \hat{y} -axis corresponds to a 534 nm shift of the beam position and $(0, 0)$ corresponds to the centre of the QPD. Each data point was acquired with 100 interrogations using 780 nW, 100 μ s pulses for the measurement phase. In b) the EMCCD image of the two ions under Doppler cooling that was taken after the scan was completed is provided in the inset.

7.4 Motional Spectra

To verify that the magnetic field has been sufficiently nullified the second method from section 3.12.5 is typically used, unless significant changes have been made inside the magnetic shield. An example of the end product of this process is shown in figure 7.2, where all 10 Zeeman components are superimposed on top of each other such that they cannot be differentiated.

Once the magnetic field has been nullified a bias field of 3.8 G is applied to separate the Zeeman components. Under this field the carrier transition of the $S_{1/2}(m_j = -1/2) - D_{5/2}(m_j = -5/2)$ Zeeman level is shifted by -10.5 MHz from its 0 G bias field frequency. This particular frequency shift was chosen to minimise the possibility of off-resonant excitations from the motional spectrum of adjacent Zeeman components, within the limits that the bias-coil current source can apply.

Next the ability for the apparatus to initialise the ion into the $S_{1/2}(m_j = -1/2)$ state via optical pumping with σ^- 422 nm laser light is evaluated. The theory behind this process is described in section 3.12.4 (page 57). The effectiveness of the pumping is evaluated by comparing the carrier transitions of the $S_{1/2}(m_j = -1/2) - D_{5/2}(m_j = -5/2)$ and $S_{1/2}(m_j = +1/2) - D_{5/2}(m_j = +5/2)$ Zeeman components. The positions of these are first located by performing a frequency scan of the qubit laser without optical pumping. Next the scans are repeated with the optical pumping pulse preceding the qubit laser frequency scan. The optical pumping pulse duration is varied to optimise the state initialisation by minimising the number of excited state detection events from the $S_{1/2}(m_j = +1/2) - D_{5/2}(m_j = +5/2)$ transition. The effectiveness is gauged by

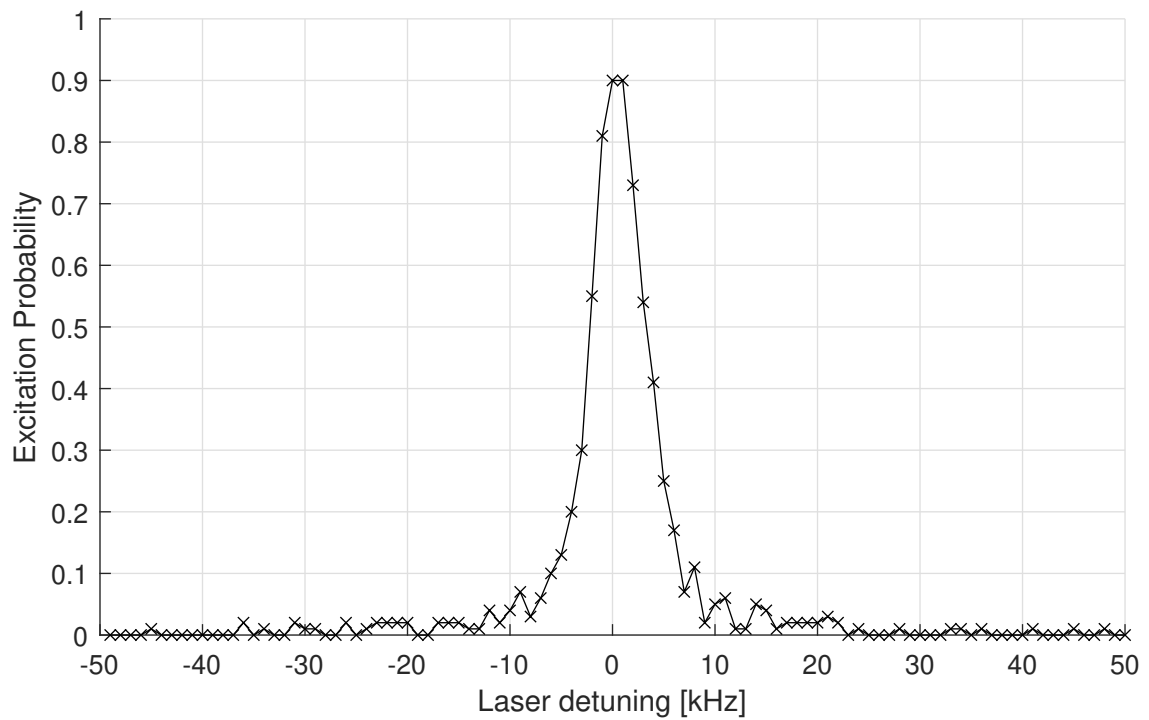


Figure 7.2: Carrier transition of all 10 Zeeman components in a nullified magnetic field and zero bias field. Each data point is the average of 100 interrogations of the ion with each interrogation consisting of a ~ 50 nW, $200 \mu\text{s}$ pulse, with the scan incrementing in 1 kHz steps. The full-width half maximum of the observed lineshape is ~ 14 kHz, indicating that the magnetic field is well nullified.

using the formula

$$A = \frac{c_{-1/2}}{c_{-1/2} + c_{+1/2}} \quad (7.3)$$

where c_i is the total number of excited state detection events from the transition beginning in the $i \in \{-1/2, +1/2\}$ m_j level of the ground state. Typically these scans are conducted over a 50 kHz scan range around the carrier with a 1 kHz resolution, 500 interrogations per scan increment and a ~ 300 nW spectroscopy pulse, that has a 200 μ s duration. With a single 10 μ s optical pumping pulse an efficiency of $A \geq 99.6\%$ is typically achieved.

Figure 7.3 depicts the motional spectrum of the ion centred on the carrier of qubit transition in a 2.8 G bias field. In this magnetic field the $\Delta m_j = +2$ Zeeman component is shifted by +10.5 MHz. The measured secular frequencies obtained here match up well to those predicted by equation 2.10 (page 14), which are shown in table 7.1a. The \hat{x} - and \hat{z} -axis frequencies show very good agreement between the calculated and measured values, to the extent that the differences are comparable to the scan resolution. The \hat{y} -axis frequencies, whilst still close, have a larger difference of 17 kHz. Similar results were obtained for the case with two ions confined in the trap, with an example of the two ion spectrum of the same transition presented in figure 7.4 with the six secular frequencies indicated on the figure. Again the secular frequencies measured here show good agreement with the expected values from equations 2.10, 2.13 and 2.12, which are shown for comparison in table 7.1b. Like in the single ions case the calculated \hat{y} -axis motional frequency is off by 15 kHz (and as a consequence, the \hat{y} -rocking frequency is also off from the predicted value), whilst the other frequencies show good agreement. The observed difference between the calculated \hat{y} -axis frequency and the measured value may be originate from an imperfection in the trap fabrication or an error in the definition of the electrode anisotropy used in equation 2.7.

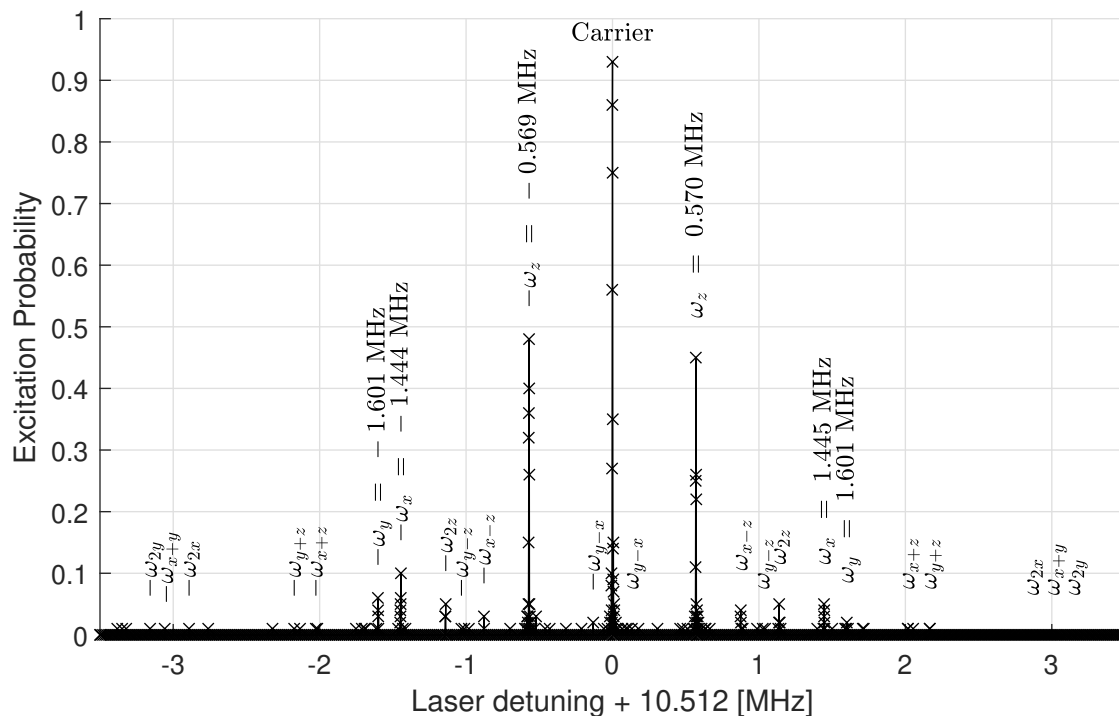


Figure 7.3: Motional spectrum of a single ion in a bias field of 3.8 G that has been centred on the $S_{1/2}(m_j = -1/2) - D_{5/2}(m_j = -5/2)$ carrier transition. Laser pulses with a pulse power of 260 nW and duration of 200 μ s were applied to the ion, with a scan resolution of 1 kHz, 3.0 V applied to the endcap electrodes and an RF amplitude of 200 V was applied to the RF electrodes at 29.781 MHz. The measured secular frequencies and the expected locations of the first-order sum and difference terms are annotated.

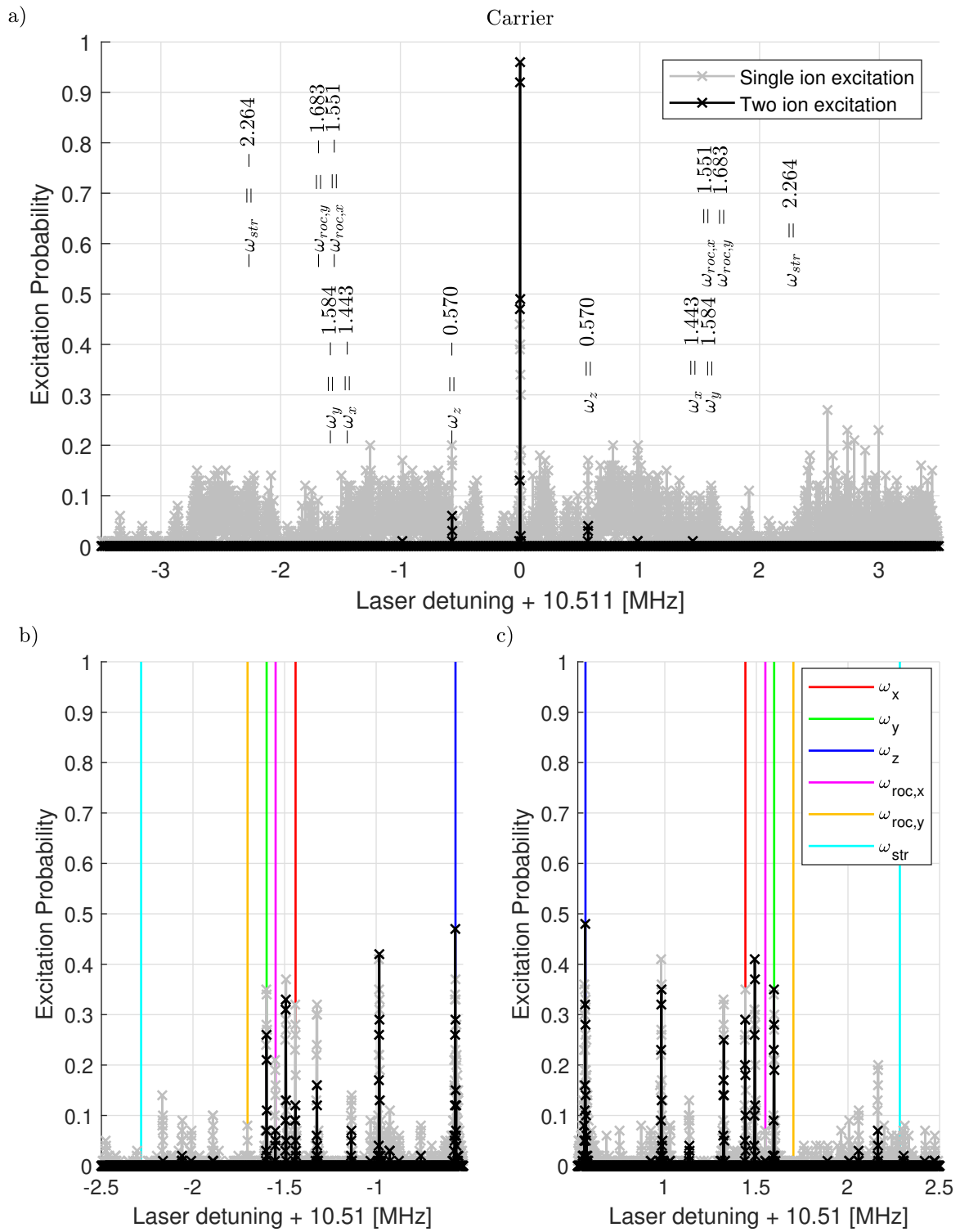


Figure 7.4

Figure 7.4: a) Full motional spectrum of two ions in a bias field of 3.8 G that has been centred on the $S_{1/2}(m_j = -1/2) - D_{5/2}(m_j = -5/2)$ carrier transition. The laser pulse power used was 260 nW with a duration of 200 μs and had a scan resolution of 1 kHz. Voltages applied to the trap electrodes were the same as in figure 7.3 and no sideband cooling was applied for this scan. The text markers indicate the expected frequencies. At this point the beam power was too low to detect the motional sidebands through the two ion excitations and the large number of sum and difference terms make it difficult to determine the frequencies from the single-ion excitations. Furthermore, the many nearby and overlapping features from sum and difference terms make determining the motional frequencies from the single ion excitations impossible. By repeating the experiment with a higher pulse power (2.2 μW) and the same pulse duration, the sidebands from the motional modes can be measured for the b) lower and c) upper sidebands. Due to the close proximity of the frequencies on the two rocking, \hat{x} - and \hat{y} -axis frequencies, their locations on the spectrum are indicated with coloured lines and the measured values are displayed in table 7.1b.

7.5 Rabi Flopping

Although the motional spectrum of the ion has dependencies on the coherence of the states, it is not by itself an explicit demonstration of the coherent control of the ion. Rabi flopping, which demonstrates Rabi oscillations, is an explicit demonstration of the coherence. Here the excitation probability is measured as a function of the pulse duration for $\delta = 0$ on the carrier, with a fixed laser intensity. Since the ion has been initialised into the $S_{1/2}(m_j = -1/2)$ state, the oscillations should begin from zero excitation probability. In an ideal system, which possesses an infinitely long coherence time, the population of the two states would oscillate with full contrast as the increasing pulse length drives the Bloch vector further around the meridian of the Bloch sphere. In this excitation probabilities that are not exactly one or zero correspond to superposition states of $|g\rangle$ and $|e\rangle$. In practice however the oscillation between the two states will be dampened from two sources. The first cause being dephasing from the thermal distribution of the vibrational levels, where each vibrational level gives a different Rabi frequency (see sections 2.4.2 and 2.4.3). Here longer pulses impart larger dephasing of the qubit as the different Rabi frequencies cause the ion to be driven by increasingly different amounts around the Bloch sphere. This can be overcome by applying sideband cooling prior to the spectroscopy pulse to ensure that the ion only occupies a single

a) Single ion		
Secular frequency	Calculated [MHz]	Measured [MHz]
ω_x	± 1.443	-1.444, 1.445
ω_y	± 1.584	-1.601, 1.601
ω_z	± 0.570	-0.569, 0.570
b) Two ions		
Secular frequency	Calculated [MHz]	Measured [MHz]
ω_x	± 1.443	-1.441, 1.440
ω_y	± 1.584	-1.597, -1.597
ω_z	± 0.570	-0.567, 0.567
$\omega_{roc,x}$	± 1.551	-1.55, -1.548
$\omega_{roc,y}$	± 1.683	-1.702, 1.702
ω_{str}	± 2.264	-2.268, 2.268

Table 7.1: Calculated and measured secular frequencies for a) one and b) two ions. The parameters used to calculate the one and two ion secular frequencies are specified in figures 7.3 and 7.4.

($n = 0$) vibrational level for the spectroscopy pulse. The second of these sources being finite coherence time from the apparatus and excited state lifetime, which cause the decay of the Bloch Vector (see section 2.5). The effects of the apparatus, namely the laser linewidth and fluctuations in the magnetic field, on the coherence can be considered as random detuning errors that are imparted onto the qubit rotations. These build up a cumulative decrease in the contrast of the Rabi oscillations as pulse duration is increased. Demonstrations of the Rabi flopping are shown in figure 7.5. The error bars associated with each data point represent the statistical noise given by the (1σ) quantum projection noise [236];

$$QPN(1\sigma) = \sqrt{\frac{P_{ee}(1 - P_{ee})}{N}} \quad (7.4)$$

where N here is the number of interrogations performed with each measurement. These are statistical errors associated with rotations of the Bloch vector around the Bloch sphere, with smaller errors at the poles and larger errors near the equator. If the error bars obtained from measuring the excitation probabilities are significantly greater than those predicted by the quantum projection noise, then it would imply that there is some facet of the apparatus that requires either improvement or maintenance. How-

ever, the measurements detailed in chapters 5 and 6 demonstrate that the apparatus should possess a sufficiently high stability such that the quantum projection noise is the dominant source of uncertainty in the recorded data. To verify this, the outcome of each interrogation of the ion at the end of the spectroscopy sequence would need to be recorded to calculate the error bars for each data point, however the apparatus has not yet been configured to record these. Additionally, to fully grasp the long-term stability of the apparatus and witness the effects of any longer term drifts the spectroscopy routine (i.e. the full scan) would be repeated several times to observe any emerging differences between scan results. The simulated fit for figure 7.5 determines the value of $\bar{n}_z = 19.2 \pm 3.8$, which overlaps with the expected Doppler cooling limit of 17.3 that is predicted in section 2.4.1 for the \hat{z} -axis, $\Omega_R/2\pi = 15.257 \pm 0.001$ kHz and an equivalent laser linewidth of $\Gamma_L/2\pi = 113 \pm 1990$ Hz, which corresponds to a coherence time of 1.4 ± 24.8 ms. As described in section 7.2 the large uncertainty in Γ_L arises from the pulse durations used here being much shorter than the coherence time of the qubit and thus an accurate value cannot be extracted from this fit. The dephasing here is expected to be dominated by the axial, \hat{z} -axis, motion of the ion as the secular frequency along this axis is $2.5\times$ smaller than the frequencies of the other motional modes (and thus has the largest Doppler cooling limit) and furthermore the \hat{x} - and \hat{y} -motional sidebands also have much weaker coupling to the laser (see figure 7.3). Attempting to factor the two other motional modes to the fitting routine also results in a massive increase in the computational overhead of the fitting routine; more than cubing the total number of operations that need to be performed. Were this to be attempted then rather than just considering the the probability of the ion occupying each n_z vibrational level the calculation would need to consider the occupation probability of each n_z level for each n_y and then calculate these for each n_x level, whilst also expanding the parameter space that must be searched through by two dimensions in order to get the values of \bar{n}_x and \bar{n}_y . Therefore the \hat{x} - and \hat{y} -axis contributions to the numerical simulations are not considered for the data fitting here, nor in the rest of the chapter. For Doppler cooled ions the n_x and n_y values can be estimated using

the ratios of the Doppler cooling limits (pg 23):

$$\bar{n}_i = \bar{n}_z \frac{\frac{\Gamma_{eff}}{\omega_i} - 1}{\frac{\Gamma_{eff}}{\omega_z} - 1} \quad (7.5)$$

where $i \in x, y$. Utilising this the values of \bar{n}_x and \bar{n}_y can be estimated to be 7.23 and 6.47 respectively.

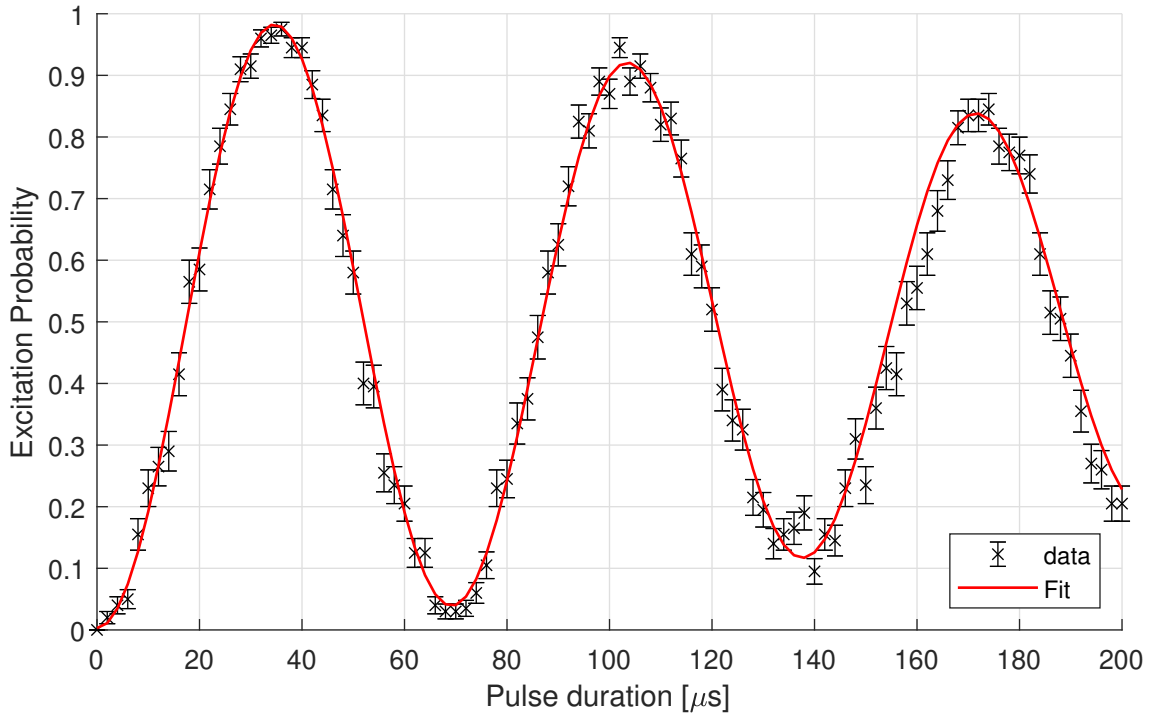


Figure 7.5: Rabi Flopping on the carrier of the qubit transition produced from a Doppler cooled ion with no sideband cooling. The pulse duration is incremented in steps of 2μ s with a pulse power of 7.5μ W.

7.6 Ramsey Spectroscopy

As demonstrated in the previous section the qubit laser can drive the ion qubit into a superposition state of $|g\rangle$ and $|e\rangle$. This implies that more complex pulse sequences, such as Ramsey's method of separated oscillatory fields [237, 238], can be used to demonstrate further coherent control of the qubit. In this technique the ion is interrogated

by two pulses of laser light, of equal duration τ , that are separated by a period of free precession, T , without exposure to the laser. Here the two pulses have their duration and power chosen such that $\Omega_R\tau = \pi/2$, becoming “ $\pi/2$ -pulses”. The first of these pulses prepares the ion into the $\frac{1}{\sqrt{2}}(|g\rangle + |e\rangle)$ superposition state. Should there be any frequency difference between the laser and the atomic transition frequency, then a relative phase difference will accumulate during the free precession period, corresponding to the Bloch vector rotating around the equator of the Bloch sphere. As a consequence of this the second $\pi/2$ -pulse would rotate the Bloch vector around a non-prime meridian of the Bloch sphere, leaving the qubit in a superposition state unless the accrued phase difference meets one of two conditions. In first case where there is no net accumulated phase difference or the phase difference is an even multiple of π the Bloch vector would rotate around the Bloch sphere as if no precession period had occurred, ending in the $|e\rangle$, whilst if the phase difference is an odd multiple of π it will return the qubit to the $|g\rangle$ state. Since the phase difference accrued over T is linearly dependent on the laser detuning, scanning the frequency of laser (keeping the frequency the same for all three time periods) will create fringes in the spectral lineshape, with the approximate separation between them being $1/(\tau + T)$. An example of these fringes is shown in figure 7.6. Due to the laser frequency being kept the same for all three time periods here, the initial pulse does not drive the Bloch vector fully to the equator except when $\delta = 0$. Instead during the free precession period the Bloch vector will precess around the line of latitude that the initial pulse ends at, with the second pulse driving the vector from the end point of the precession, hence why the fringes are observed in figure 7.6. As the dephasing of the qubit causes the Bloch vector to recede from the surface of the Bloch sphere towards its centre the second pulse will become unable to fully drive the Bloch vector to the $|e\rangle$ or $|g\rangle$ states. This manifests in the spectrum as a decrease of the fringe contrast towards an excitation probability of $1/2$. In figure 7.6, the fitting routine had Γ_L and \bar{n}_z as free parameters and determined that the values that maximised the likelihood of generating the data to be $\Gamma_L/2\pi = 31.2 \pm 1730$ Hz and $\bar{n}_z = 17.4 \pm 2.7$. As in the case of the Rabi flopping, the value of \bar{n} overlaps with the expected Doppler cooling limit value of 17.3 and little meaningful information can

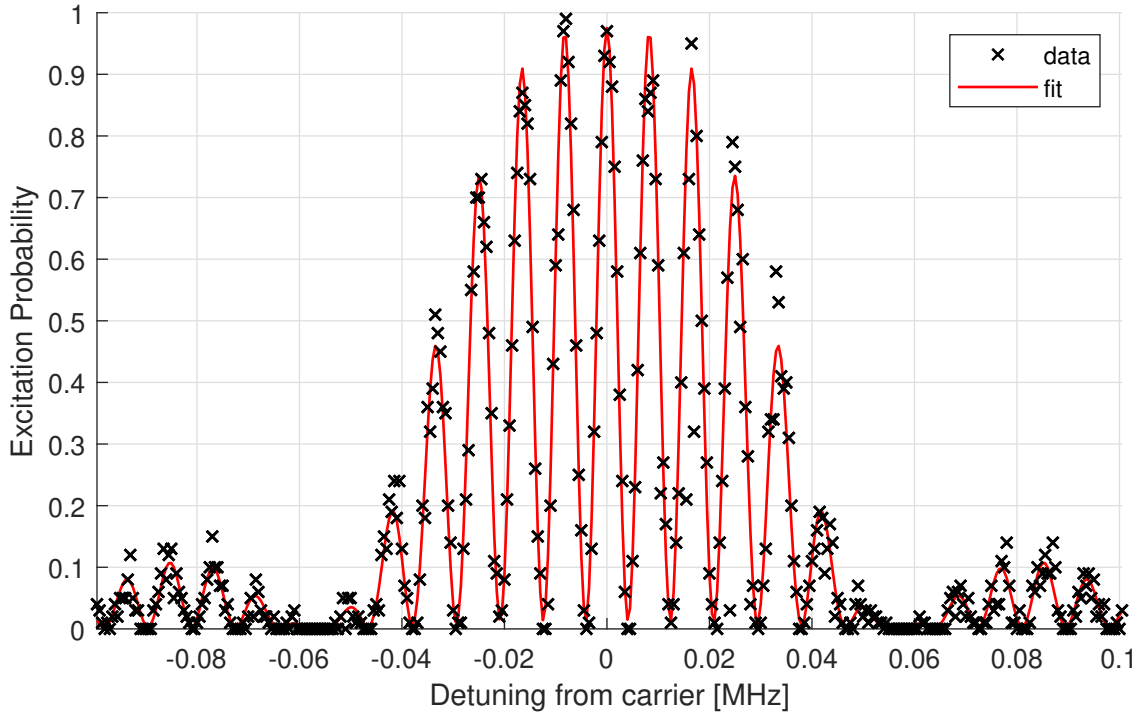


Figure 7.6: Ramsey fringe pattern obtained by scanning the laser frequency over the carrier transition. Two $7.5 \mu\text{W}$ pulses of duration $\tau = 17 \mu\text{s}$ are used with a $T = 100 \mu\text{s}$ free precession period. The scan resolution was 500 Hz and each data point was composed of 100 interrogations of the ion.

be extracted from the determined value of Γ_L due to the duration of the pulse sequence being much shorter than the coherence time given by the laser linewidth. Since the pulse power used here is the same as that used in figure 7.5 the Rabi frequency has been left as a fixed parameter with the same value as in figure 7.5.

Since the fringe pattern is a result of the phase difference accrued between the interrogation fields, it is expected that introducing an extra phase offset, $\Delta\phi_L$, to the second pulse will affect the observed fringe pattern. The degree to which this affects the fringes can be observed by setting the laser to a fixed detuning and varying $\Delta\phi_L$. This rotates the trajectory of the Bloch vector to move at an angle proportional to $\Delta\phi_L$ from the start of the second pulse allowing for the phase of the fringes to be controlled as demonstrated in figure 7.7, where two $\pi/2$ -pulses are applied with the phase offset of the second pulse being incremented for each data point.

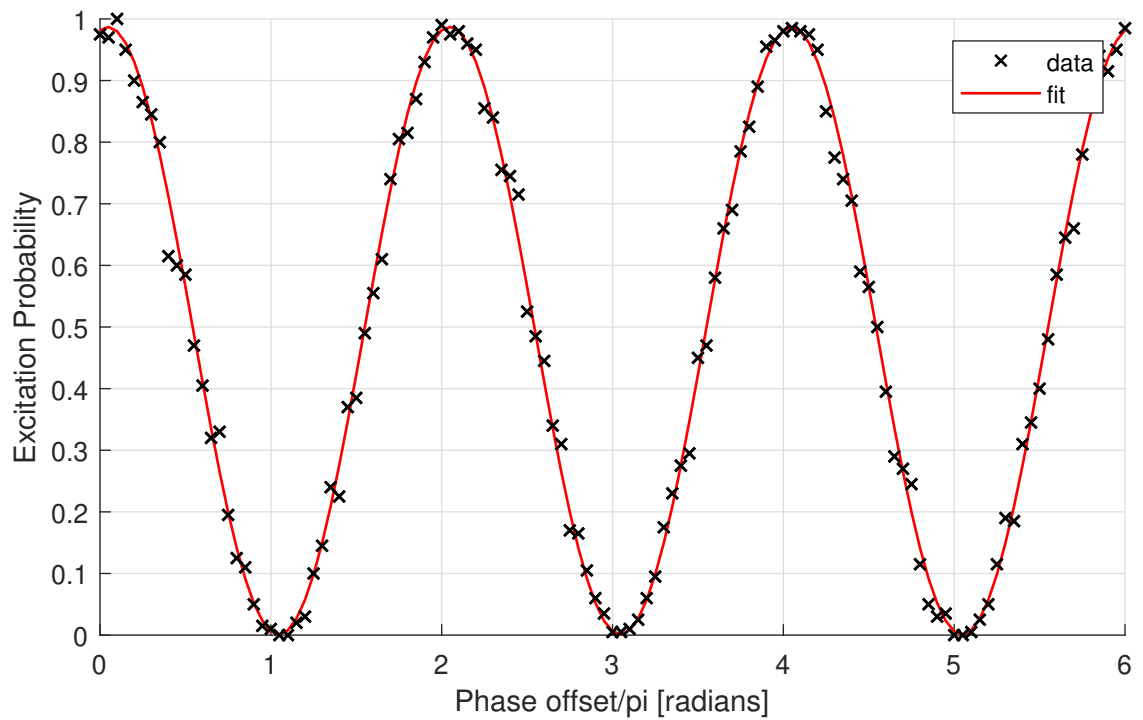


Figure 7.7: Excitation probability at the centre of the qubit carrier transition as the phase shift between the Ramsey pulses is varied. For this experimental routine $7.5 \mu\text{W}$, $17.5 \mu\text{s}$ pulses were used with a $200 \mu\text{s}$ free precession period. Each data point is composed of 200 interrogations and the scan had a resolution of 0.05π .

The results presented in this section demonstrate the coherent control of a single qubit via the use of the laser detuning and phase of the interrogating pulses relative to the ion. Furthermore the demonstration of Ramsey spectroscopy also demonstrates that the apparatus can apply a series of pulses to the ion, which can easily be scaled up to include more complex pulse sequences. Additionally any desired phase shift can be introduced, either for qubit control purposes or to counteract unwanted drift in the laser frequency that could exist for longer pulse sequences.

7.7 State Initialisation

The sideband cooling efficacy, whose theory is discussed in sections 2.4.2 and 2.4.3 (beginning on pages 23 and 26 respectively), is determined by comparing scans of the red and blue sidebands to each other after the application of a sideband cooling pulse. For these the detuning of the spectroscopy probe pulse was scanned whilst a preceding sideband cooling pulse is kept at a constant frequency, at the peak of the red motional sideband. Additionally four extra $10 \mu\text{s}$ optical pumping pulses are applied during the sideband cooling pulse, followed by a period where only the sideband cooling is applied. The efficiency is determined by the value of \bar{n} obtained from equation 2.36 (page 26) [135]. An example of this for the \hat{z} -motional sidebands of a single ion is given in figure 7.8 and gives $\bar{n}_z = 0.041 \pm 0.015$. This routine can also be used to evaluate the heating rate of the trap by varying the time between the end of the sideband cooling pulse and the probe pulse and calculating $d\bar{n}/dt$.

As described in section 2.4.3 and chapter 3, quenching light at 1033 nm is applied in conjunction with the sideband cooling pulse to achieve efficient cooling. This quenching light induces an AC-Stark shift in the $D_{5/2}$ state and as a consequence the frequency of the motional sidebands is altered whilst the cooling pulse is applied. To characterise the AC-Stark shift induced by the quencher, the frequency of the sideband cooling pulse was scanned whilst the detuning of the probe pulse was kept constant on the red motional sideband at -0.893 MHz. When the cooling pulse is scanned over the shifted sideband the excitation probability will drop as the cooling efficiency increased. The sideband cooling pulse duration and power were varied to create the largest flat-bottom region

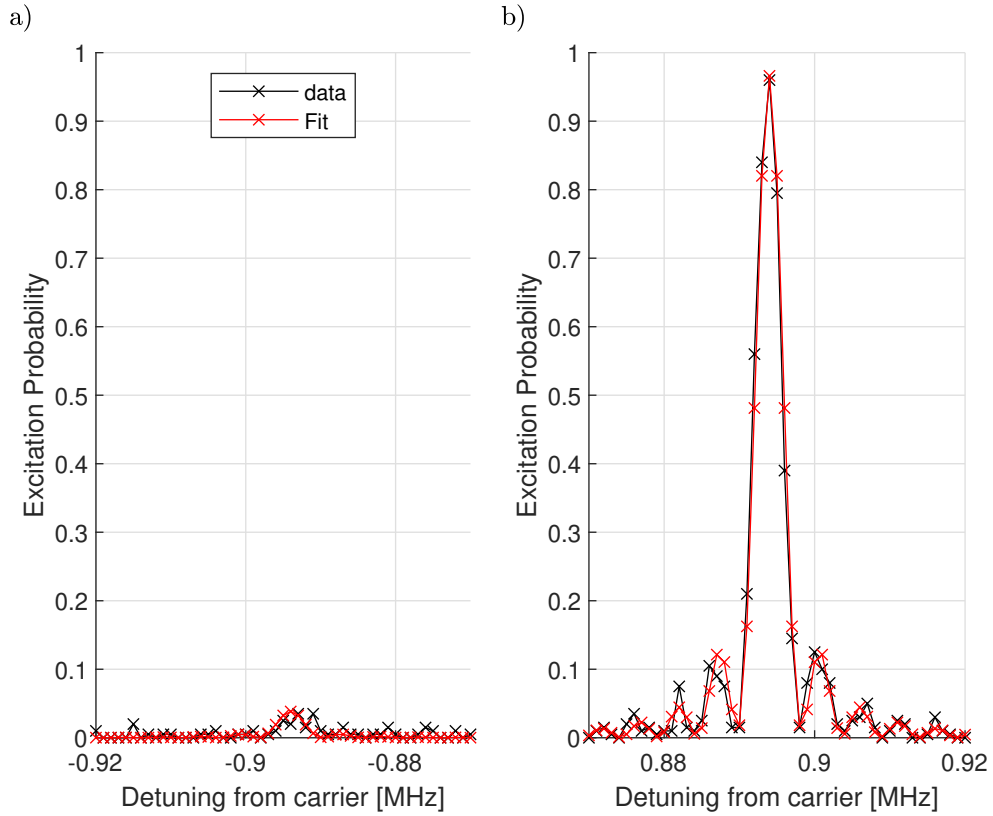


Figure 7.8: a) Red and b) Blue \hat{z} -motional sidebands after a 10 ms, 3.95 mW sideband cooling pulse was applied to the red \hat{z} -motional mode of a single ion. The probe pulse had a duration of 200 μs and a power of 85.8 μW . The probe beam was scanned in 1 kHz steps, with 200 interrogations per step and five 10 μs optical pumping pulses applied during the sideband cooling. There was a 230 μs gap between the end of the cooling pulse and the start of the spectroscopy probe pulse. Here the endcap voltages had been increased to 7.5 V

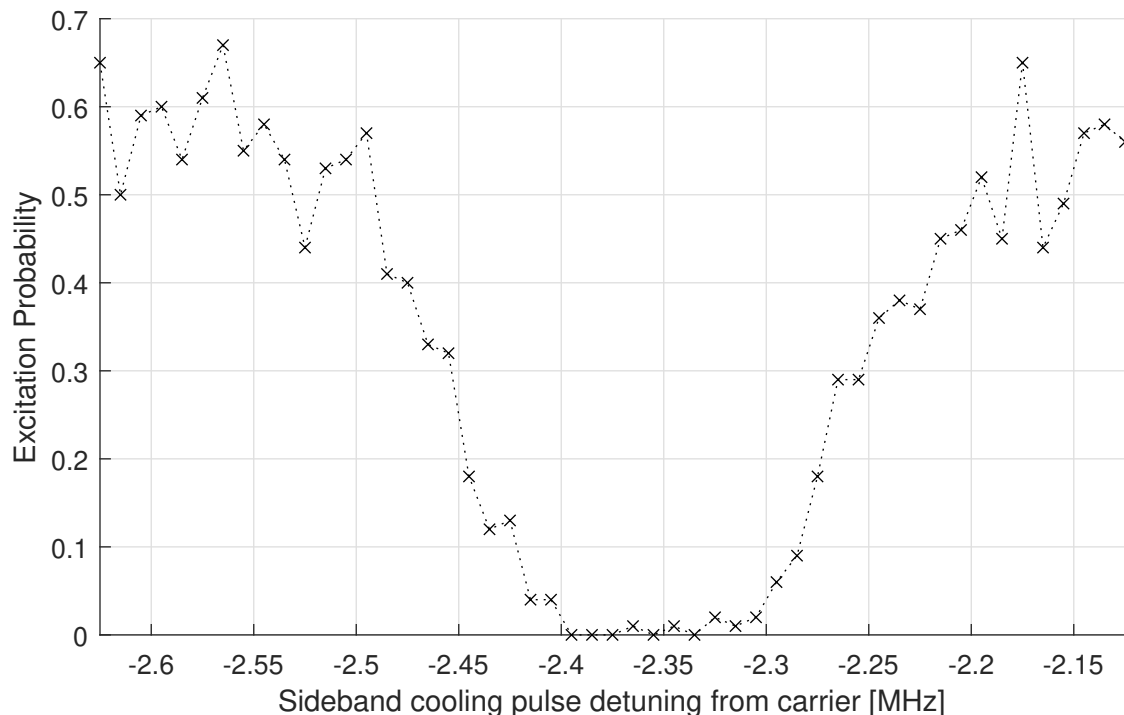


Figure 7.9: Scan of the sideband cooling pulse detuning with fixed probe pulse detuning with optimised parameters. The cooling and probe parameters were the same as those specified for figure 7.8, except for the probe pulse detuning, which was kept on the peak of the unshifted red sideband and the number of interrogations per step which were reduced to 100.

possible, so that any drift or fluctuations in the quenching beam parameters would have minimal impact on the efficacy of the cooling. An example of this scan with the optimised parameters is shown in figure 7.9. The effects of this AC-Stark shift were accounted for in the sideband cooling pulses used to generate figure 7.8, where the sideband cooling pulse was set to the centre of the flat region at -2.35 MHz.

7.8 Spectroscopy with Amplitude-Shaped Pulses

Thus far the spectroscopy experiments have been conducted utilising only square-shaped probe pulses. However by utilising shaped pulses, whose amplitude varies with time, the power spectral density at frequencies far from the resonance can be reduced by a significant amount. Reference [176] lists many potential pulse windows and their prop-

erties. Of these Blackman shaped pulses are commonly chosen for spectroscopy due to their high side-lobe suppression and minimal broadening near resonance [172, 239, 240]. With this pulse window the electric field amplitude follows the function

$$E(t) = \begin{cases} E_0(0.42 - 0.5 \cos(2\pi t/T_L) + 0.08 \cos(4\pi t/T_L)), & \text{for } 0 \leq t \leq T_L \\ 0, & \text{elsewhere} \end{cases} \quad (7.6)$$

This property is highly desirable when interacting with weaker components of the motional spectrum, such as the motional sidebands, as off-resonant components of the pulse can couple to parts of the motional spectrum with higher laser-ion coupling, namely the carrier, and introduce infidelities in the applied qubit operation [142, 175].

Figure 7.10 shows the comparison between two scans of the carrier transition, one with a standard square pulse and the other with a Blackman-shaped pulse. The slight difference in the Rabi frequencies that give the best fits ($\Omega_{(\text{square})} = 2630$ Hz for the square pulse and $\Omega_{(\text{Blackman})}(t = T/2) = 2960$ Hz for the Blackman) may be due to thermal effects in the AOM building up during the longer pulse. It can be seen that the side-lobes of the spectral line are suppressed in the case where shaped pulses are utilised. When creating the shaped pulses, the non-linear response of the pulse-shaping AOM is accounted for by an automated calibration routine performed by the experiment control software at the start of the experiment sequence. This calibration routine correlates the RF output of the pulse-shaping AOM's DDS source to the optical power measured on the APD inside the magnetic shield. A ninth order polynomial is then used as a calibration function for creating pulses of arbitrary amplitude shape relative to the maximum applicable power. A full description of how the pulse-shaping setup is calibrated is described in references [142, 175]. The implementation of the pulse shaping is of particular importance for the Mølmer-Sørensen entanglement gate as the bichromatic pulses need to be detuned near to, but not on the motional sidebands; without the suppression it is more likely that these side-lobes can couple to the motional sidebands as well as the carrier and reduce the fidelity of the entanglement gate.

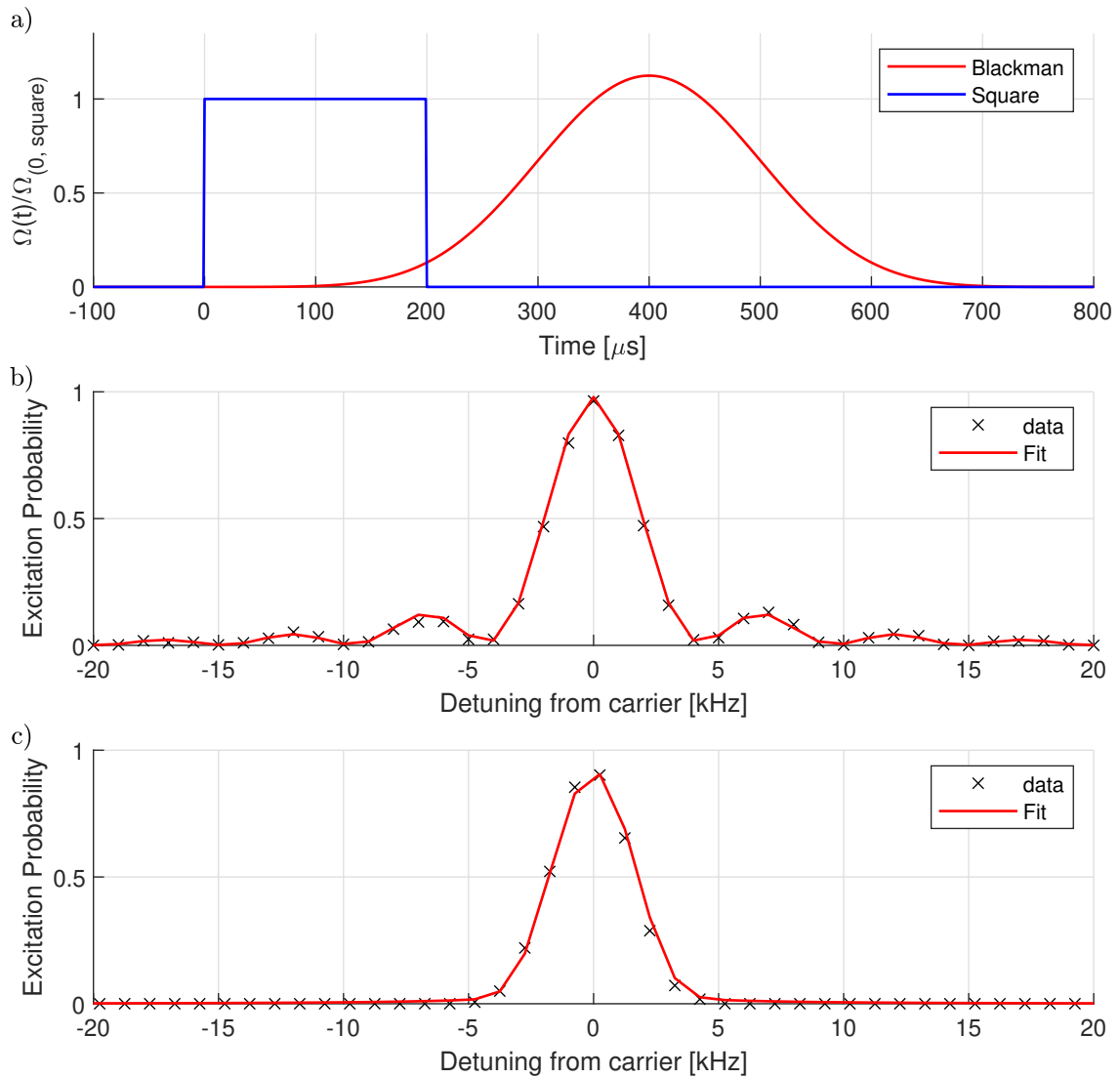


Figure 7.10

7.9 Towards Entanglement

The next stage for the apparatus would be to demonstrate the entanglement of two qubits via the Mølmer-Sørensen gate operation [182–184] described in section 2.7. The work done in previous sections of this chapter has established the required techniques for state initialisation and determined the relevant experimental parameters that would

Figure 7.10: A laser frequency scan of the carrier transition with square pulses and Blackman shaped pulses. Both scans and use the pulses of power 210 nW. Both scans are conducted with a 1 kHz resolution with 500 interrogations per step. The square pulse uses a 200 μs pulse whilst the Blackman pulse has a duration of 800 μs . a) Recreation of the pulse envelopes used for this experiment. The simulated fits to the data from (b) the square pulse and (c) the Blackman utilise the pulse envelopes from (a) in the numerical integration of equations 2.41. The equations have been modified to utilise time varying Rabi frequencies, $\Omega(t) \rightarrow \Omega_R E(t)$, to generate these fits.

be required to perform this operation. The initial experimental routine here would be to verify the parameter set that maximally entangles the qubits from their ground states, $|gg\rangle$, into the $(|gg\rangle + i|ee\rangle)/\sqrt{2}$ Bell state. To do this the duration of the gate pulse, T_{gate} , is varied to find the optimal gate time, τ , that gives equal probability of detecting both ions in either the $|ee\rangle$ or $|gg\rangle$ state and at the same time the minimal probability of detecting the ions in the $|eg\rangle$ or $|ge\rangle$ states.

The results of this experimental routine are described by the analytic equations [101, 172, 183, 239, 241]

$$P_2(t) = \frac{1}{8} \left[3 + 4e^{-|\alpha^2|(\bar{n} + \frac{1}{2})} \cos(\gamma) + e^{-4|\alpha^2|(\bar{n} + \frac{1}{2})} \right] \quad (7.7a)$$

$$P_1(t) = \frac{1}{4} \left[1 + 4ie^{-|\alpha^2|(\bar{n} + \frac{1}{2})} \sin(\gamma) - e^{-4|\alpha^2|(\bar{n} + \frac{1}{2})} \right] \quad (7.7b)$$

$$P_0(t) = \frac{1}{8} \left[3 - 4e^{-|\alpha^2|(\bar{n} + \frac{1}{2})} \cos(\gamma) + e^{-4|\alpha^2|(\bar{n} + \frac{1}{2})} \right] \quad (7.7c)$$

where P_j is the probability of observing j ions in the excited state and

$$\alpha = \frac{\eta\Omega_{MS}}{\epsilon} (e^{i\epsilon T_{gate}} - 1) \quad (7.8a)$$

$$\gamma = \frac{\eta\Omega_{MS}^2}{\epsilon} T_{gate} - \frac{\eta^2\Omega_{MS}^2}{\epsilon^2} \sin(\epsilon T_{gate}) \quad (7.8b)$$

in which Ω_{MS} is the effective Rabi frequency given by equation 2.46 and here $\epsilon = \omega_i - \Delta$ is the symmetric detuning of the bichromatic light from the chosen motional frequency. Outside of the weak field regime (the weak field regime is defined as $\eta\Omega_{MS} \ll \epsilon$) the electronic state of the ion is strongly coupled to the vibrational level of the ion over the

duration of the gate. Here the maximally entangled state is created when

$$\frac{\eta\Omega}{\epsilon} = \frac{1}{2\sqrt{\mathcal{K}}} \quad (7.9)$$

where \mathcal{K} is an integer greater than zero [183] that is used to ensure that the system returns to its initial vibrational level. To ensure that this is the case the condition

$$\epsilon\tau = \mathcal{K}2\pi \quad (7.10)$$

must be met. Combining this with the condition from 7.9 gives the required gate time to be

$$\tau = \frac{\pi}{\eta\Omega_{\text{MS}}} \sqrt{\mathcal{K}} \quad (7.11)$$

Experimentally this value and the optimum value of ϵ can be determined via an iterative process described in [101]. In this procedure first a scan of ϵ is performed with an arbitrary T_{gate} to find the value of ϵ that gives $P_0 = P_2$. Next T_{gate} is scanned with this value of ϵ to find the gate time that minimises P_1 . The second and third steps are then repeated until the two parameters converge on values that simultaneously minimise P_1 and give $P_0 = P_2$.

A simulated example of these using the parameters obtained from previous sections is depicted in figure 7.11, with the expected optimal gate time being $\tau = 215 \mu\text{s}$ for a pulse with $\Omega_{\text{MS}}/2\pi = 50 \text{ kHz}$.

After establishing τ the creation of the Bell state should be verified by performing a parity measurement. Here the parity, $\mathcal{P} = P_0 + P_2 - P_1$, is measured as a function of the phase of an extra $\pi/2$ pulse that is applied after the entanglement gate. From this the gate fidelity \mathcal{F} , of the gate operation is calculated using the equation [101]

$$\mathcal{F} = \frac{P_0(\tau) + P_2(\tau)}{2} + 2|\rho_{gg,ee}| \quad (7.12)$$

where $2|\rho_{gg,ee}|$ is the amplitude of the observed parity oscillations.

Beyond this a further condition, $\Omega_{\text{MS}}/\omega_i^2 \ll 1$, should be met to avoid off-resonant

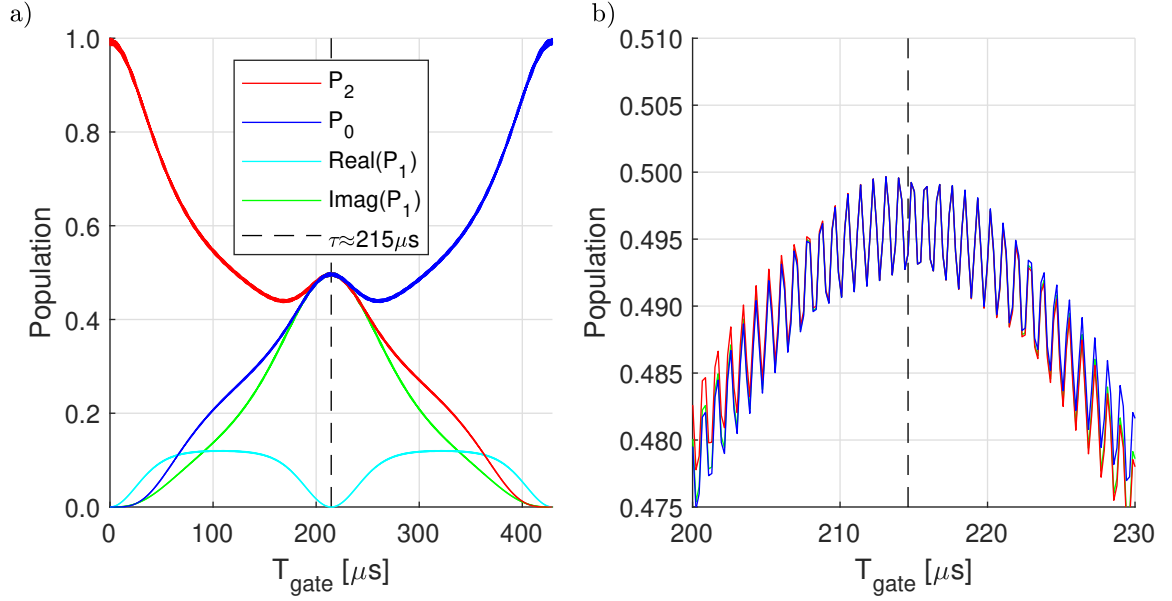


Figure 7.11: a) Simulated outcome of the Mølmer-Sørensen gate operation using equations 7.7 and 7.13. Here a pulse with $\Omega_{\text{MS}}/2\pi = 50$ kHz would be applied to the \hat{z} -axis motional sidebands. It is assumed from section 7.7 that the ions will be sideband cooled to $\bar{n} = 0.027$. The pulse duration and symmetric detuning are determined via equations 7.11 and 7.10 respectively gives $\epsilon = 4660$ Hz and $\tau = 215 \mu\text{s}$. b) Section of part (a) around the point of maximal entanglement. It can be seen that the fast modulation from of the signal from off-resonant excitations prevents the gate from fully entangling the qubits into the ideal Bell state, which occurs at $P_2 = P_0 = 0.5$.

excitations. Adding this as a consideration produces a term for the the fidelity

$$\mathcal{F}_{OR} \approx 1 - \frac{\Omega_{MS}}{\delta^2}(1 - \cos 2\delta T_{gate}) \quad (7.13)$$

that is multiplied onto equations 7.7 [183], adding a fast modulation on top of the signal. These effects can be mitigated by employing the amplitude shaped pulses from section 7.8.

In practice the bichromatic laser is created by simultaneously applying two RF sources to an AOM downstream of the pulse-shaping AOM, as described in section 3.7. Should the two components of the bichromatic laser have different intensities (and thus different Rabi frequencies), the gate will suffer a loss of fidelity from the reduced destructive interference in the pathways that the gate can take between the $|gg\rangle$ and $|ee\rangle$ states. This imbalance can arise from either differences in the RF powers used to drive the AOM or the AOM responding differently to the two RF frequencies, or from a difference in the fibre coupling efficiencies for the final fibre that delivers light into the magnetic shield. This modifies the effective Rabi frequency of the gate to become [239]

$$\Omega = \sqrt{\frac{\Omega_{MS,red}\Omega_{MS,blue}}{1 - \xi^2}} \quad (7.14)$$

where ξ is a parameter that describes the imbalance in the Rabi frequencies of the red ($\tilde{\Omega}_{red}$) and blue ($\tilde{\Omega}_{blue}$) Rabi frequencies. This imbalance, if detected, can be rectified by adjusting the variable voltage attenuators on the RF output of the driving sources.

The experimental control routines required to implement the Mølmer-Sørensen gate and perform the parity measurement have been made and implemented however data acquisition was prevented by the failure of the 532 nm pump for the qubit laser. The replacement of the pump and the required re-characterisation of the qubit laser once it is installed mean that performing these measurements remains a subject for future work.

7.10 Summary

In this chapter spectroscopy of a one and two ion string has been demonstrated. The ability for the apparatus to nullify the magnetic field and initialise the ion into the $S_{1/2}(m_j = -1/2)$ state with efficiencies exceeding 99.6 % has been shown. Once in a bias field the one and two ion motional frequencies have been recorded and show good agreement with the expected values obtained from calculation. The ability for the apparatus to apply shaped pulses was demonstrated with square and Blackman shaped probing pulses; the latter of which showed suppression of the spectral side-lobes by suppressing the pulses Fourier components that were far from resonance. Coherent control of the ion was demonstrated by the generation of Rabi oscillations on the carrier transition and via Ramsey spectroscopy. The ability for the apparatus to initialise the ion into the motional ground state was demonstrated with the use of sideband cooling; with the mean vibrational number at the end of the sequence determined to be $\bar{n}_z = 0.041 \pm 0.015$. A discussion on the Mølmer-Sørensen gate and the expected results that it should generate has also been presented, however the failure of the pump laser for the qubit laser has prevented further spectroscopy experiments from occurring, including the performing the two qubit entanglement. When the pump laser is replaced and re-characterised the next stages of the spectroscopy experiments can continue. The experimental routines and the rest of the required apparatus has been implemented.

Chapter 8

Conclusion

8.1 Summary

This thesis has described research into improving the coherent control of trapped ion qubits. Specifically, methods to investigate the maximum applicable voltage to micro-fabricated ion traps without inducing break down, perform fast detuning operations on the qubit laser whilst simultaneously stabilising the laser power and characterising the stability of the magnetic field that the ion is exposed to have all been investigated. The work presented here is relevant to the long term goal of this project; to develop microfabricated ion traps and test them for uses in quantum computing and metrology.

To minimise the probability of off-resonant excitations and thus improve the coherence time of the qubit, high RF voltage amplitudes need to be applied to the trap. Additionally, a high RF voltage amplitude improves the trapping efficiency, providing long ion storage times. However, the voltage cannot be increased indefinitely, as eventually the device will electronically breakdown. Microfabricated ion traps in particular are likely to experience this due to the high voltages involved combined with the short distances between the high voltage components and those that are either grounded or used to apply low DC potentials. To verify that newly produced microfabricated ion traps are capable of withstanding these voltage amplitudes an RF testbed was created. When testing for breakdown all possible locations that are expected to experience electrical breakdown are observed by a set of cameras. The testbed firstly establishes that

the electrical properties of the trap are functioning as expected by establishing the resonant frequency of a tank circuit made by connecting the trap to a helical resonator. The voltage amplitude on the tested trap is determined via a pickup measurement that exploits an innate capacitance that exists in the device. This pickup measurement is performed by measuring the voltage across a small resistor, whose resistance is small enough that the resonant circuit is essentially unchanged. This resistor is connected to the input of the CLCC that is usually used to apply voltages to the trap compensation electrodes. To ensure that both sides of the trap device function as expected a pickup measurement is made from each side of the trap. A calibration routine is used to ensure that these measurements are accurate, this compensating for device-to-device variations in the device capacitance. The voltage on the trap is then gradually increased whilst two image processing algorithms examine the images from the cameras, one for detecting short transient sparks and another for detecting faint glow. These algorithms enable spatial correlation of the breakdown to a physical location on the trap. In addition determining if the device can withstand the required voltages. This also provides feedback that can be utilised to improve the fabrication process. The image processing algorithm that detects faint glow like breakdown is capable of detecting this type of breakdown 60 V and 90 V lower than was possible by manual eye detection.

In order to implement qubit gate operations, the qubit laser must be able detune its frequency by ± 20 MHz, and to be able to address all Zeeman components of the motional spectrum once the ion is subjected to the bias magnetic field. These operations must be performed at timescales that are much shorter than the qubit coherence times to practically implement QIP gates, meaning that these frequency changes must be made at sub-millisecond timescales. In addition to this, performing fault-tolerant QIP requires the Rabi frequency have a fractional instability of $10^{-2} - 10^{-4}$ depending on the particular gate operation [172, 217–219]. Since the Rabi frequency is proportional to the square root of the laser intensity, this requirement can be achieved by stabilising the laser power. To achieve both of these tasks an optical frequency tuner subsystem was created for the qubit laser. This system achieves both of these by utilising an AOM in a double pass configuration; the DDS source for the AOM permits detuning

operations at $1 \mu\text{s} - 1 \text{s}$ timescales and a feedback mechanism, whose error signal is sourced from a pickup measurement at the tuner output. This is used to attenuate the amplitude of the AOM's driving voltage, which in turn controls the optical power. An optical fibre between the AOM and the the output pick-off converts any deviations in beam pointing, that occur due to small misalignments in the optical components, when the AOM frequency is adjusted into deviations in the laser power, which are then compensated for by the feedback. To ensure that the power feedback can reliably compensate for the required detuning range the setpoint for the feedback was chosen such that the tuner could stabilise the laser power over an extended $\pm 25 \text{ MHz}$ range. With the feedback engaged at this setpoint the tuner efficiency is 40.7% to within $\pm 0.031 \%$ and without the feedback it has a peak efficiency of $\sim 43 \%$ that decreases to $\{41.2, 41.6\} \%$ at $\{-25, +25\} \text{ MHz}$.

A second test of the feedback system where a sequence random detuning operations was applied to the laser was also performed. This test revealed the presence of spikes when the frequency of the AOM was altered with the feedback enabled, which correspond to the step change in the output efficiency of the tuner. These spikes had a time constant of $45.5 \mu\text{s}$ which was found to arise from the bandwidth of the feedback circuit. A replacement circuit could improve the time constant to $\leq 10 \mu\text{s}$. After this further improvements at shorter timescales may be achieved by implementing a two stage feedback system using a faster photodiode in conjunction with the existing one. Additionally, to remove the spikes a feed-forward system would need to be implemented. The long term improvement of the (out-of-loop) output stability was measured via an Allan deviation to be a factor of $20\times$ at 10 s , increasing to $\sim 110\times$ at 10^3 s and achieving a fractional uncertainty of $< 10^{-4}$ for $10 \text{ s} - 700 \text{ s}$ timescales within the stricter fault-tolerant QIP requirement for the timescales needed to complete a full spectroscopy routine. For shorter timescales, namely those at single pulse durations, the power stabilisation can be performed by the pulse shaping setup that follows the tuner. Evaluating this was outside of the scope of the work done here.

To ensure that the tuner subsystem does not negatively affect the frequency stability of the qubit laser a beat measurement is made on a spectrum analyser between a sample

of the laser at the output of the pulse shaping setup and the other functioning FNCS output at the laser source. Although this measurement was only relative and did not show the laser power spectrum that the ion experiences, it does give an indication of how much influence the systems downstream of the FNCS systems have on the laser frequency stability. Multiple measurements over different frequency ranges showed that any sidebands and noise were < -36.5 dBc. A fit with window function used by the spectrum analyser to the carrier of the highest resolution spectrum determined that the linewidth of the beat note was < 0.21 Hz, with the measurement being limited by the instrument.

The stability of the magnetic field and its influence on the Zeeman shift of the $S_{1/2}(m_j = -1/2) - D_{5/2}(m_j = -5/2)$ qubit transition was investigated. The attenuation to the external magnetic field provided by the mu-metal magnetic shield is examined through measurements of the power spectrum of the magnetic field taken inside and outside the shield. These show that the shield provides a $1065\times$ attenuation at 50 Hz, the largest component of the spectrum, which meets the specification of the shield. The effects of nearby electronic devices on the magnetic field stability were investigated by comparing Allan deviations measured with each device turned on in isolation and in conjunction with the other devices. These revealed the existence of ground loops in the voltage supply and connections to the DC electrodes and in the piezo adjusters used to steer the qubit laser pointing. Attempts to remove the ground loops from the DC electrodes resulted in the trap being unable to trap ions and as a consequence the ground loop had to be restored, with further investigation required on how to effectively remove it. Should the ground loop somehow not be easily removed and results in problems for future experiments, it would be possible to create a feed-forward to compute the expected frequency shift from the DC electrode voltage settings and to apply an offset to the frequency of the tuner system. No attempts were made to find or fix the ground loop in the piezo adjusters due to the rarity of their use. The effects of running the hotplate as though it were being used to load an ion were also investigated. During operation it could be seen that that the hotplate induced a magnetic field that would shift the qubit transition by -8 kHz. Once the

sequence finished, the magnetic field was offset from its initial value by $\sim +180$ Hz that decayed back to the initial value via a two-phase exponential with time constants of $\tau_{fast} = 911$ s and $\tau_{slow} = 7650$ s. Performing the same fit to a temperature measurements obtained via thermistor located inside the magnetic shield returned similar time constants ($\tau_{fast} = 1394$ s and $\tau_{slow} = 6552$ s). This indicated that this was likely due to the temperature and the fact the change in the magnetic field is only slightly above the expected change from the temperature sensitivity of the sensor, leaving this as a probable explanation. The stability of the magnetic field measured on an out-of-loop sensor, with all devices on and operating in a steady state fashion, determined that the system could stabilise the magnetic field to the level where there were < 10 Hz fluctuations in the qubit transition for 1 s – 7000 s timescales and < 1 Hz for 20 s – 350 s. The improvements to the magnetic field stability from the current feedback system were considered. However, the noise floor of the out-of-loop sensor prevented an accurate assessment of this capability.

Spectroscopy experiments on one and two ions has been demonstrated. The ability of the apparatus to nullify the magnetic field and initialise the ion into the $S_{1/2}(m_j = -1/2)$ state with efficiencies exceeding 99.6 % has been shown. Once in a bias field the one and two ion motional frequencies have been recorded and show good agreement with the expected values obtained from calculation. The application of amplitude shaped pulses to reduce the effects of off-resonant excitations has been demonstrated. Coherent control of the qubit state was performed via the generation of Rabi oscillations and the application of Ramsey spectroscopy on the carrier transition. Fitting the Bloch equations to the results of these allowed for the parameters of the experiment that could not be directly set or measured to be determined. A fit to a Rabi flopping spectroscopy sequence determined the the Rabi frequency to be $\Omega/2\pi = 15.257 \pm 0.001$ kHz and the mean vibrational level for a Doppler cooled ion to be $\bar{n} = 19.2 \pm 3.8$, which overlaps well with the calculated cooling limit of the expected limit of $n_{z,\min} = 17.3$. Fitting to the results of a Ramsey spectroscopy sequence gave and $\bar{n} = 17.4 \pm 2.7$ which also comes close to the cooling limit. The effective laser linewidth, Γ_L , was not able to be reliably determined from the fits to either the Rabi flopping nor Ramsey spectroscopy

due to the duration of the pulse sequences being far shorter than the coherence time that Γ_L provided. This indicates that Γ_L was not a limiting factor on the ability of the apparatus to perform coherent control of the qubit at timescales of hundreds of microseconds. To reduce the value of \bar{n} to zero sideband cooling is employed. Measuring the ratio of the red and blue sideband Rabi frequencies after a 230 μs gap between the sideband cooling pulse and the probe pulse gave $\bar{n}_z = 0.041 \pm 0.015$. Additionally, the Stark shift imposed by the 1033 nm quenching light was examined and determined to shift the red motional sideband from -0.893 MHz to -2.35 MHz. The work in this thesis concludes with a presentation of the methods that will be used to do the data analysis for the Mølmer-Sørensen entanglement gate, however the failure of the 532 nm pump for the qubit laser has prevented the execution of this. The routines used for data fitting iterate on previous work that have been previously used, allowing for the simulation of amplitude shaped pulses and reducing the computational overhead of the calculations by searching through the parameter space rather than raster scanning through it.

8.2 Conclusion

The experimental apparatus summarised and presented here represents within this thesis represents 25 years of continuous development in the field of ion trapping. Throughout its history the apparatus has continually given high-quality outcomes and results, which are reflected in both this thesis and in a long history of previous publications [76, 112, 119, 135, 142, 154, 156, 162], that compares well against its peers (see sections 1.1 - 1.3). This thesis summarises the current state of the apparatus and the contributions made by the author to its development. The extensive capabilities and high stability of the setup have been demonstrated, as has its ability to deliver high quality spectroscopy results. These have been verified via precise and detailed measurements that have been described in previous chapters. Additionally, a method for verifying that the RF properties of newly manufactured ion trap devices conform to rigorous expectations has been demonstrated, ensuring that future microtraps are capable of supplying a suitable bedrock for the development future experiments. Despite

the hindrance of the qubit laser’s pump diode failing, preventing the entanglement of two-ions from being realised during the author’s time as part of the microtrap team, the short- and long-term future of the experiment looks promising, with a wide variety of potential research avenues that could be explored.

8.3 Future Work

Once functionality is restored to the qubit laser the implementation of the Mølmer-Sørensen gate can be completed and the fidelity of the operation can be determined. Further steps to this work could involve the creation of Greenberger–Horne–Zeilinger states. Implementing this with a high fidelity may involve modifications to the qubit laser to ensure that the ions are exposed to equal laser intensities. Work on implementing laser-written waveguides [91,229] that mate to the vacuum chamber may be utilised to overcome the difficulty in implementing this and will be required if the complexity of the qubit operations is expanded to involve ions stored across multiple array segments of the trap. With the entanglement gate demonstrated, the apparatus will have proven that it is capable of providing a universal set of QIP gates and the focus can be directed to either implementing more robust gates by improving the gate fidelity or onto more complex QIP routines.

Improving trap loading times and extending the atomic source lifetime by implementing a loading routine based on laser ablation [227,228] is currently being investigated.

The RF pickup measurement used by the RF testbed could be applied to a trap that is in use for experimentation. The RF amplitude can be sampled on an unused compensation electrode, such as the transport zone or an endcap segment, and used as an error signal to stabilise the amplitude of the RF voltage. In turn this can stabilise the motional frequencies of the ion in a manner similar to [242].

The construction of a second apparatus for further QIP experiments is currently in preparation. This apparatus will utilise the second FNCS port as the source of its qubit laser and is expected to use copies of the optical frequency tuner and pulse shaping setups for coherent control of its ion qubits. Additionally, this new apparatus

Chapter 8. Conclusion

will utilise a similar, if not identical, magnetic shield and coil system as the current apparatus. This will be characterised in the same manner as in the work undertaken. As mentioned in section 3.7, the third FNCS system is intended to be used as an out-of-loop measurement of the laser frequency stability by performing a beat measurement against a frequency comb setup in the adjacent lab [192].

Bibliography

- [1] A. Franzen, “Componentlibrary (a vector graphics library for illustrations of optics experiments)”, <http://www.gwoptics.org/ComponentLibrary/>, 2006. Accessed: Dec 2019.
- [2] W. Paul, “Electromagnetic traps for charged and neutral particles”, *Rev. Mod. Phys.*, **62**(3):531–540, Jul 1990, doi:10.1103/RevModPhys.62.531.
- [3] R. P. Feynman, “Simulating physics with computers”, *International Journal of Theoretical Physics*, **21**(6):467–488, Jun 1982, doi:10.1007/BF02650179.
- [4] P. W. Shor, “Algorithms for quantum computation: discrete logarithms and factoring”, in *Proceedings 35th Annual Symposium on Foundations of Computer Science*, pages 124–134, Nov 1994, doi:10.1109/SFCS.1994.365700.
- [5] L. K. Grover, “Quantum mechanics helps in searching for a needle in a haystack”, *Phys. Rev. Lett.*, **79**(2):325–328, Jul 1997, doi:10.1103/PhysRevLett.79.325.
- [6] D. Deutsch and R. Jozsa, “Rapid solution of problems by quantum computation”, *Proceedings of the Royal Society of London. Series A: Mathematical and Physical Sciences*, **439**(1907):553–558, Dec 1992, doi:<http://doi.org/10.1098/rspa.1992.0167>.
- [7] D. P. DiVincenzo, “The physical implementation of quantum computation”, *Fortschritte der Physik*, **48**(9-11):771–783, Oct 2000, doi:10.1002/1521-3978(200009)48:9/11<771::AID-PROP771>3.0.CO;2-E.

Bibliography

- [8] C. D. Bruzewicz, J. Chiaverini, R. McConnell, and J. M. Sage, “Trapped-ion quantum computing: Progress and challenges”, *Applied Physics Reviews*, **6**(2):021314, May 2019, doi:10.1063/1.5088164.
- [9] C. Langer, R. Ozeri, J. D. Jost, J. Chiaverini, B. DeMarco, A. Ben-Kish, R. B. Blakestad, J. Britton, D. B. Hume, W. M. Itano, D. Leibfried, R. Reichle, T. Rosenband, T. Schaetz, P. O. Schmidt, and D. J. Wineland, “Long-lived qubit memory using atomic ions”, *Phys. Rev. Lett.*, **95**(6):060502, Aug 2005, doi:10.1103/PhysRevLett.95.060502.
- [10] Y. Wang, M. Um, J. Zhang, S. An, M. Lyu, J.-N. Zhang, L.-M. Duan, D. Yum, and K. Kim, “Single-qubit quantum memory exceeding ten-minute coherence time”, *Nature Photonics*, **11**(10):646–650, Sep 2017, doi:10.1038/s41566-017-0007-1.
- [11] T. Ruster, C. T. Schmiegelow, H. Kaufmann, C. Warschburger, F. Schmidt-Kaler, and U. G. Poschinger, “A long-lived Zeeman trapped-ion qubit”, *Applied Physics B*, **122**(10):254, Sep 2016, doi:10.1007/s00340-016-6527-4.
- [12] T. Monz, P. Schindler, J. T. Barreiro, M. Chwalla, D. Nigg, W. A. Coish, M. Harlander, W. Hänsel, M. Hennrich, and R. Blatt, “14-qubit entanglement: Creation and coherence”, *Phys. Rev. Lett.*, **106**(13):130506, Mar 2011, doi:10.1103/PhysRevLett.106.130506.
- [13] V. Letchumanan, M. A. Wilson, P. Gill, and A. G. Sinclair, “Lifetime measurement of the metastable $4d^2D_{5/2}$ state in $^{88}\text{Sr}^+$ using a single trapped ion”, *Phys. Rev. A*, **72**(1):012509, Jul 2005, doi:10.1103/PhysRevA.72.012509.
- [14] S. Gulde, M. Riebe, G. P. Lancaster, C. Becher, J. Eschner, H. Häffner, F. Schmidt-Kaler, I. L. Chuang, and R. Blatt, “Implementation of the Deutsch–Jozsa algorithm on an ion-trap quantum computer”, *Nature*, **421**:48–50, Jan 2003, doi:10.1038/nature01336.

Bibliography

- [15] K.-A. Brickman, P. C. Haljan, P. J. Lee, M. Acton, L. Deslauriers, and C. Monroe, “Implementation of Grover’s quantum search algorithm in a scalable system”, *Phys. Rev. A*, **72**(5):050306, Nov 2005, doi:10.1103/PhysRevA.72.050306.
- [16] F. Schmidt-Kaler, H. Häffner, S. Gulde, M. Riebe, G. Lancaster, T. Deuschle, C. Becher, W. Hänsel, J. Eschner, C. Roos, and R. Blatt, “How to realize a universal quantum gate with trapped ions”, *Applied Physics B*, **77**(8):789–796, Dec 2003, doi:10.1007/s00340-003-1346-9.
- [17] V. M. Schäfer, C. J. Ballance, K. Thirumalai, L. J. Stephenson, T. G. Ballance, A. M. Steane, and D. M. Lucas, “Fast quantum logic gates with trapped-ion qubits”, *Nature*, **555**(75):75–78, Feb 2018, doi:10.1038/nature25737.
- [18] D. Maslov, “Basic circuit compilation techniques for an ion-trap quantum machine”, *New Journal of Physics*, **19**(2):023035, feb 2017, doi:10.1088/1367-2630/aa5e47.
- [19] T. Sleator and H. Weinfurter, “Realizable universal quantum logic gates”, *Phys. Rev. Lett.*, **74**(20):4087–4090, May 1995, doi:10.1103/PhysRevLett.74.4087.
- [20] D. P. DiVincenzo, “Two-bit gates are universal for quantum computation”, *Phys. Rev. A*, **51**(2):1015–1022, Feb 1995, doi:10.1103/PhysRevA.51.1015.
- [21] H. G. Dehmelt, “Monoion oscillator as potential ultimate laser frequency standard”, *IEEE Transactions on Instrumentation and Measurement*, **IM-31**(2):83–87, June 1982, doi:10.1109/TIM.1982.6312526.
- [22] W. Nagourney, J. Sandberg, and H. Dehmelt, “Shelved optical electron amplifier: Observation of quantum jumps”, *Phys. Rev. Lett.*, **56**(26):2797–2799, Jun 1986, doi:10.1103/PhysRevLett.56.2797.
- [23] D. Wineland, C. Monroe, W. M. Itano, D. Leibfried, B. E. King, and D. M. Meekhof, “Experimental issues in coherent quantum-state manipulation of trapped atomic ions”, *Journal of Research of the National Institute of Standards and Technology*, **103**(3):259–328, June 1998, doi:10.6028/jres.103.019.

Bibliography

- [24] T. P. Harty, D. T. C. Allcock, C. J. Ballance, L. Guidoni, H. A. Janacek, N. M. Linke, D. N. Stacey, and D. M. Lucas, “High-fidelity preparation, gates, memory, and readout of a trapped-ion quantum bit”, *Phys. Rev. Lett.*, **113**(22):220501, Nov 2014, doi:10.1103/PhysRevLett.113.220501.
- [25] A. H. Myerson, D. J. Szwer, S. C. Webster, D. T. C. Allcock, M. J. Curtis, G. Imreh, J. A. Sherman, D. N. Stacey, A. M. Steane, and D. M. Lucas, “High-fidelity readout of trapped-ion qubits”, *Phys. Rev. Lett.*, **100**(20):200502, May 2008, doi:10.1103/PhysRevLett.100.200502.
- [26] M. Acton, K.-A. Brickman, P. C. Haljan, P. J. Lee, L. Deslauriers, and C. Monroe, “Near-perfect simultaneous measurement of a qubit register”, *Quantum Info. Comput.*, **6**(6):465–482, Sep 2006, doi:https://doi.org/10.26421/QIC6.6-1.
- [27] J. I. Cirac and P. Zoller, “Quantum computations with cold trapped ions”, *Phys. Rev. Lett.*, **74**(20):4091–4094, May 1995, doi:10.1103/PhysRevLett.74.4091.
- [28] D. Kielpinski, C. Monroe, and D. J. Wineland, “Architecture for a large-scale ion-trap quantum computer”, *Nature*, **417**:709–711, Jun 2002, doi:10.1038/nature00784.
- [29] B. Lekitsch, S. Weidt, A. G. Fowler, K. Mølmer, S. J. Devitt, C. Wunderlich, and W. K. Hensinger, “Blueprint for a microwave trapped ion quantum computer”, *Science Advances*, **3**(2):, Feb 2017, doi:10.1126/sciadv.1601540.
- [30] T. D. Ladd, F. Jelezko, R. Laflamme, Y. Nakamura, C. Monroe, and J. L. O’Brien, “Quantum computers”, *Nature*, **464**:45–53, Mar 2010, doi:10.1038/nature08812.
- [31] T. P. Spiller, W. J. Munro, S. D. Barrett, and P. Kok, “An introduction to quantum information processing: applications and realizations”, *Contemporary Physics*, **46**(6):407–436, Jul 2005, doi:10.1080/00107510500293261.
- [32] N. M. Linke, D. Maslov, M. Roetteler, S. Debnath, C. Figgatt, K. A. Landsman, K. Wright, and C. Monroe, “Experimental comparison of two quantum computing

Bibliography

- architectures”, *Proceedings of the National Academy of Sciences*, **114**(13):3305–3310, Mar 2017, doi:10.1073/pnas.1618020114.
- [33] I. Buluta, S. Ashhab, and F. Nori, “Natural and artificial atoms for quantum computation”, *Reports on Progress in Physics*, **74**(10):104401, Sep 2011, doi:10.1088/0034-4885/74/10/104401.
- [34] S. Debnath, N. M. Linke, C. Figgatt, K. A. Landsman, K. Wright, and C. Monroe, “Demonstration of a small programmable quantum computer with atomic qubits”, *Nature*, **536**(7614):63–66, Aug 2016, doi:10.1038/nature18648.
- [35] C. J. Ballance, T. P. Harty, N. M. Linke, M. A. Sepiol, and D. M. Lucas, “High-fidelity quantum logic gates using trapped-ion hyperfine qubits”, *Phys. Rev. Lett.*, **117**(6):060504, Aug 2016, doi:10.1103/PhysRevLett.117.060504.
- [36] M. Saffman, “Quantum computing with atomic qubits and Rydberg interactions: progress and challenges”, *Journal of Physics B: Atomic, Molecular and Optical Physics*, **49**(20):202001, 2016, doi:10.1088/0953-4075/49/20/202001.
- [37] J. T. Peltonen, P. C. J. J. Coumou, Z. H. Peng, T. M. Klapwijk, J. S. Tsai, and O. V. Astafiev, “Hybrid rf SQUID qubit based on high kinetic inductance”, *Scientific Reports*, **8**(1)(10033):, Jun 2018, doi:10.1038/s41598-018-27154-1.
- [38] J. Koch, T. M. Yu, J. Gambetta, A. A. Houck, D. I. Schuster, J. Majer, A. Blais, M. H. Devoret, S. M. Girvin, and R. J. Schoelkopf, “Charge-insensitive qubit design derived from the Cooper pair box”, *Phys. Rev. A*, **76**(4):042319, Oct 2007, doi:10.1103/PhysRevA.76.042319.
- [39] R. Barends, J. Kelly, A. Megrant, A. Veitia, D. Sank, T. C. White, J. Mutus, B. Campbell, Y. Chen, Z. Chen, B. Chiaro, A. Dunsworth, A. Dunsworth, C. Neill, P. O’Malley, P. Roushan, A. Vainsencher, J. Wenner, A. N. Korotkov, A. N. Cleland, and J. M. Martinis, “Superconducting quantum circuits at the surface code threshold for fault tolerance”, *Nature*, **508**(1):500–503, Feb 2014, doi:10.1103/RevModPhys.86.153.

Bibliography

- [40] G. Wendin, “Quantum information processing with superconducting circuits: a review”, *Reports on Progress in Physics*, **80**(10):106001, 2017, doi:10.1088/1361-6633/aa7e1a.
- [41] V. Cerletti, W. A. Coish, O. Gywat, and D. Loss, “Recipes for spin-based quantum computing”, *Nanotechnology*, **16**(4):R27–R49, 2005, doi:10.1088/0957-4484/16/4/R01.
- [42] T. Han, M. Chen, G. Cao, H. Li, M. Xiao, and G. Guo, “Radio-frequency measurement in semiconductor quantum computation”, *Science China Physics, Mechanics & Astronomy*, **60**(5):057301, Mar 2017, doi:10.1007/s11433-017-9019-9.
- [43] P. Kok, W. J. Munro, K. Nemoto, T. C. Ralph, J. P. Dowling, and G. J. Milburn, “Linear optical quantum computing with photonic qubits”, *Rev. Mod. Phys.*, **79**(1):135–174, Jan 2007, doi:10.1103/RevModPhys.79.135.
- [44] G. J. Milburn, “Photons as qubits”, *Physica Scripta*, **2009**(T137):014003, 2009, doi:10.1088/0031-8949/2009/T137/014003.
- [45] X.-L. Wang, Y.-H. Luo, H.-L. Huang, M.-C. Chen, Z.-E. Su, C. Liu, C. Chen, W. Li, Y.-Q. Fang, X. Jiang, J. Zhang, L. Li, N.-L. Liu, C.-Y. Lu, and J.-W. Pan, “18-qubit entanglement with six photons’ three degrees of freedom”, *Phys. Rev. Lett.*, **120**(26):260502, Jun 2018, doi:10.1103/PhysRevLett.120.260502.
- [46] A. Mizel, D. A. Lidar, and M. Mitchell, “Simple proof of equivalence between adiabatic quantum computation and the circuit model”, *Phys. Rev. Lett.*, **99**(7):070502, Aug 2007, doi:10.1103/PhysRevLett.99.070502.
- [47] T. Albash and D. A. Lidar, “Adiabatic quantum computation”, *Rev. Mod. Phys.*, **90**(1):015002, Jan 2018, doi:10.1103/RevModPhys.90.015002.
- [48] M. H. S. Amin, “Consistency of the adiabatic theorem”, *Phys. Rev. Lett.*, **102**(22):220401, Jun 2009, doi:10.1103/PhysRevLett.102.220401.
- [49] R. Raussendorf and H. J. Briegel, “A one-way quantum computer”, *Phys. Rev. Lett.*, **86**(22):5188–5191, May 2001, doi:10.1103/PhysRevLett.86.5188.

Bibliography

- [50] R. Raussendorf and T.-C. Wei, “Quantum computation by local measurement”, *Annual Review of Condensed Matter Physics*, **3**(1):239–261, Mar 2012, doi:10.1146/annurev-conmatphys-020911-125041.
- [51] T. Rosenband, D. B. Hume, P. O. Schmidt, C. W. Chou, A. Brusch, L. Lorini, W. H. Oskay, R. E. Drullinger, T. M. Fortier, J. E. Stalnaker, S. A. Diddams, W. C. Swann, N. R. Newbury, W. M. Itano, D. J. Wineland, and J. C. Bergquist, “Frequency ratio of Al^+ and Hg^+ single-ion optical clocks; metrology at the 17th decimal place”, *Science*, **319**(5871):1808–1812, Mar 2008, doi:10.1126/science.1154622.
- [52] A. D. Ludlow, M. M. Boyd, J. Ye, E. Peik, and P. O. Schmidt, “Optical atomic clocks”, *Rev. Mod. Phys.*, **87**(2):637–701, Jun 2015, doi:10.1103/RevModPhys.87.637.
- [53] C. W. Chou, D. B. Hume, J. C. J. Koelemeij, D. J. Wineland, and T. Rosenband, “Frequency comparison of two high-accuracy Al^+ optical clocks”, *Phys. Rev. Lett.*, **104**(7):070802, Feb 2010, doi:10.1103/PhysRevLett.104.070802.
- [54] P. B. R. Nisbet-Jones, S. A. King, J. M. Jones, R. M. Godun, C. F. A. Baynham, K. Bongs, M. Doležal, P. Balling, and P. Gill, “A single-ion trap with minimized ion–environment interactions”, *Applied Physics B*, **122**(3):57, Mar 2016, doi:10.1007/s00340-016-6327-x.
- [55] N. Huntemann, C. Sanner, B. Lipphardt, C. Tamm, and E. Peik, “Single-ion atomic clock with 3×10^{-18} systematic uncertainty”, *Phys. Rev. Lett.*, **116**(6):063001, Feb 2016, doi:10.1103/PhysRevLett.116.063001.
- [56] T. Nicholson, S. Campbell, R. Hutson, G. Marti, B. Bloom, R. McNally, W. Zhang, M. Barrett, M. Safronova, G. Strouse, W. Tew, and J. Ye, “Systematic evaluation of an atomic clock at 2×10^{-18} total uncertainty”, *Nature Communications*, **6**(1):6896, Apr 2015, doi:10.1038/ncomms7896.

Bibliography

- [57] J. Zhang, K. Deng, J. Luo, and Z.-H. Lu, “Direct laser cooling Al^+ ion optical clocks”, *Chinese Physics Letters*, **34**(5):050601, 2017, doi:10.1088/0256-307X/34/5/050601.
- [58] A. Kleczewski, M. R. Hoffman, J. A. Sherman, E. Magnuson, B. B. Blinov, and E. N. Fortson, “Coherent excitation of the $6S_{1/2}$ to $5D_{3/2}$ electric-quadrupole transition in $^{138}\text{Ba}^+$ ”, *Phys. Rev. A*, **85**(4):043418, Apr 2012, doi:10.1103/PhysRevA.85.043418.
- [59] A. A. Madej, P. Dubé, Z. Zhou, J. E. Bernard, and M. Gertsvolf, “ $^{88}\text{Sr}^+$ 445-THz single-ion reference at the 10^{-17} level via control and cancellation of systematic uncertainties and its measurement against the SI second”, *Phys. Rev. Lett.*, **109**(20):203002, Nov 2012, doi:10.1103/PhysRevLett.109.203002.
- [60] T. Rosenband, P. O. Schmidt, D. B. Hume, W. M. Itano, T. M. Fortier, J. E. Stalnaker, K. Kim, S. A. Diddams, J. C. J. Koelemeij, J. C. Bergquist, and D. J. Wineland, “Observation of the $^1S_0 \rightarrow ^3P_0$ clock transition in $^{27}\text{Al}^+$ ”, *Phys. Rev. Lett.*, **98**(22):220801, May 2007, doi:10.1103/PhysRevLett.98.220801.
- [61] K. Hosaka, S. A. Webster, P. J. Blythe, A. Stannard, D. Beaton, H. S. Margolis, S. N. Lea, and P. Gill, “An optical frequency standard based on the electric octupole transition in $^{171}\text{Yb}^+$ ”, *IEEE Transactions on Instrumentation and Measurement*, **54**:759–762, Apr 2005, doi:10.1109/TIM.2004.843319.
- [62] M. Roberts, P. Taylor, G. P. Barwood, W. R. C. Rowley, and P. Gill, “Observation of the $^2S_{1/2} - ^2F_{7/2}$ electric octupole transition in a single $^{171}\text{Yb}^+$ ion”, *Phys. Rev. A*, **62**(2):020501, Jul 2000, doi:10.1103/PhysRevA.62.020501.
- [63] N. Huntemann, M. Okhapkin, B. Lipphardt, S. Weyers, C. Tamm, and E. Peik, “High-accuracy optical clock based on the octupole transition in $^{171}\text{Yb}^+$ ”, *Phys. Rev. Lett.*, **108**(9):090801, Feb 2012, doi:10.1103/PhysRevLett.108.090801.
- [64] M. Delehaye and C. Lacroûte, “Single-ion, transportable optical atomic clocks”, *Journal of Modern Optics*, **65**(5-6):622–639, Apr 2018, doi:10.1080/09500340.2018.1441917.

Bibliography

- [65] H. S. Margolis, “Frequency metrology and clocks”, *Journal of Physics B: Atomic, Molecular and Optical Physics*, **42**(15):154017, Jul 2009.
- [66] E. A. Burt, L. Yi, B. Tucker, R. Hamell, and R. L. Tjoelker, “JPL ultra-stable trapped ion atomic frequency standards”, *IEEE Transactions on Ultrasonics, Ferroelectrics, and Frequency Control*, **63**(7):1013–1021, July 2016, doi:10.1109/TUFFC.2016.2572701.
- [67] D. L. Mills, “Internet time synchronization: the network time protocol”, *IEEE Transactions on Communications*, **39**(10):1482–1493, Oct 1991, doi:10.1109/26.103043.
- [68] D. T. Snyder, C. J. Pulliam, Z. Ouyang, and R. G. Cooks, “Miniature and fieldable mass spectrometers: Recent advances”, *Analytical Chemistry*, **88**(1):2–29, Jan 2016, doi:10.1021/acs.analchem.5b03070. PMID: 26422665.
- [69] P. A. Ivanov, “Force sensors with precision beyond the standard quantum limit”, *Phys. Rev. A*, **94**(2):022330, Aug 2016, doi:10.1103/PhysRevA.94.022330.
- [70] W. C. Campbell and P. Hamilton, “Rotation sensing with trapped ions”, *Journal of Physics B: Atomic, Molecular and Optical Physics*, **50**(6):064002, 2017.
- [71] I. Baumgart, J.-M. Cai, A. Retzker, M. B. Plenio, and C. Wunderlich, “Ultra-sensitive magnetometer using a single atom”, *Phys. Rev. Lett.*, **116**(24):240801, Jun 2016, doi:10.1103/PhysRevLett.116.240801.
- [72] H. Zhang, M. Gutierrez, G. H. Low, R. Rines, J. Stuart, T. Wu, and I. Chuang, “Iterative precision measurement of branching ratios applied to $5P$ states in $^{88}\text{Sr}^+$ ”, *New Journal of Physics*, **18**(12):123021, Dec 2016.
- [73] S. Kotler, N. Akerman, Y. Glickman, A. Keselman, and R. Ozeri, “Single-ion quantum lock-in amplifier”, *Nature*, **473**(61):61–65, May 2011, doi:10.1038/nature10010.

Bibliography

- [74] C. Schrama, E. Peik, W. Smith, and H. Walther, “Novel miniature ion traps”, *Optics Communications*, **101**(1):32 – 36, 1993, doi:[https://doi.org/10.1016/0030-4018\(93\)90318-Y](https://doi.org/10.1016/0030-4018(93)90318-Y).
- [75] S. R. Jefferts, C. Monroe, E. W. Bell, and D. J. Wineland, “Coaxial-resonator-driven rf (Paul) trap for strong confinement”, *Phys. Rev. A*, **51**(4):3112–3116, Apr 1995, doi:[10.1103/PhysRevA.51.3112](https://doi.org/10.1103/PhysRevA.51.3112).
- [76] A. Sinclair, M. Wilson, and P. Gill, “Improved three-dimensional control of a single strontium ion in an endcap trap”, *Optics Communications*, **190**(1):193 – 203, apr 2001, doi:[https://doi.org/10.1016/S0030-4018\(01\)01057-4](https://doi.org/10.1016/S0030-4018(01)01057-4).
- [77] R. B. Blakestad, C. Ospelkaus, A. P. VanDevender, J. M. Amini, J. Britton, D. Leibfried, and D. J. Wineland, “High-fidelity transport of trapped-ion qubits through an X-junction trap array”, *Phys. Rev. Lett.*, **102**(15):153002, Apr 2009, doi:[10.1103/PhysRevLett.102.153002](https://doi.org/10.1103/PhysRevLett.102.153002).
- [78] K. Wright, J. M. Amini, D. L. Faircloth, C. Volin, S. C. Doret, H. Hayden, C.-S. Pai, D. W. Landgren, D. Denison, T. Killian, R. E. Slusher, and A. W. Harter, “Reliable transport through a microfabricated X-junction surface-electrode ion trap”, *New Journal of Physics*, **15**(3):033004, Mar 2013.
- [79] D. L. Moehring, C. Highstrete, D. Stick, K. M. Fortier, R. Haltli, C. Tigges, and M. G. Blain, “Design, fabrication and experimental demonstration of junction surface ion traps”, *New Journal of Physics*, **13**(7):075018, 2011.
- [80] Z. D. Romaszko, S. Hong, M. Siegele, R. K. Puddy, F. R. Lebrun-Gallagher, S. Weidt, and W. K. Hensinger, “Engineering of microfabricated ion traps and integration of advanced on-chip features”, *Nature Reviews Physics*, **2**(6)(2522-5820):285–299, May 2020, doi:[10.1038/s42254-020-0182-8](https://doi.org/10.1038/s42254-020-0182-8).
- [81] D. Leibfried, R. Blatt, C. Monroe, and D. Wineland, “Quantum dynamics of single trapped ions”, *Rev. Mod. Phys.*, **75**(1):281–324, Mar 2003, doi:[10.1103/RevModPhys.75.281](https://doi.org/10.1103/RevModPhys.75.281).

Bibliography

- [82] J. M. Amini, H. Uys, J. H. Wesenberg, S. Seidelin, J. Britton, J. J. Bollinger, D. Leibfried, C. Ospelkaus, A. P. VanDevender, and D. J. Wineland, “Toward scalable ion traps for quantum information processing”, *New Journal of Physics*, **12**(3):033031, 2010.
- [83] N. D. Guise, S. D. Fallek, K. E. Stevens, K. R. Brown, C. Volin, A. W. Harter, J. M. Amini, R. E. Higashi, S. T. Lu, H. M. Chanhvongsak, T. A. Nguyen, M. S. Marcus, T. R. Ohnstein, and D. W. Youngner, “Ball-grid array architecture for microfabricated ion traps”, *Journal of Applied Physics*, **117**(17):174901, 2015, doi:10.1063/1.4917385.
- [84] S. Woodrow, “Linear paul trap design for high-fidelity, scalable quantum information processing”, Master’s thesis, University of Oxford, 2016.
- [85] C. Hempel, *Digital quantum simulation, Schrödinger cat state spectroscopy and setting up a linear ion trap*. PhD thesis, University of Innsbruck, 2014.
- [86] J. D. Siverns and Q. Quraishi, “Ion trap architectures and new directions”, *Quantum Information Processing*, **16**(12):1–42, Dec 2017, doi:10.1007/s11128-017-1760-2.
- [87] D.-I. D. Cho, S. Hong, M. Lee, and T. Kim, “A review of silicon microfabricated ion traps for quantum information processing”, *Micro and Nano Systems Letters*, **3**(1):2, Apr 2015, doi:10.1186/s40486-015-0013-3.
- [88] A. M. Eltony, D. Gangloff, M. Shi, A. Bylinskii, V. Vuletić, and I. L. Chuang, “Technologies for trapped-ion quantum information systems”, *Quantum Information Processing*, **15**(12):5351–5383, Dec 2016, doi:10.1007/s11128-016-1298-8.
- [89] D. Kielpinski, C. Volin, E. W. Streed, F. Lenzini, and M. Lobino, “Integrated optics architecture for trapped-ion quantum information processing”, *Quantum Information Processing*, **15**(12)(1573-1332):5315–5338, Nov 2016, doi:10.1007/s11128-015-1162-2.

Bibliography

- [90] K. K. Mehta, C. D. Bruzewicz, R. McConnell, R. J. Ram, J. M. Sage, and J. Chiaverini, “Integrated optical addressing of an ion qubit”, *Nature Nanotechnology*, **11**(12)(1748-3395):1066–1070, Aug 2016, doi:10.1038/mnano.2016.139.
- [91] M. L. Day, K. Choonee, Z. Chaboyer, S. Gross, M. J. Withford, A. G. Sinclair, and G. D. Marshall, “A micro-optical module for multi-wavelength addressing of trapped ions”, *Quantum Science and Technology*, **6**(2):024007, Feb 2021, doi:10.1088/2058-9565/abdf38.
- [92] R. J. Niffenegger, J. Stuart, C. Sorace-Agaskar, D. Kharas, S. Bramhavar, C. D. Bruzewicz, W. Loh, R. T. Maxson, R. McConnell, D. Reens, G. N. West, J. M. Sage, and J. Chiaverini, “Integrated multi-wavelength control of an ion qubit”, *Nature*, **586**(7830)(1476-4687):538–542, Oct 2020, doi:10.1038/s41586-020-2811-x.
- [93] S. Olmschenk, K. C. Younge, D. L. Moehring, D. N. Matsukevich, P. Maunz, and C. Monroe, “Manipulation and detection of a trapped Yb^+ hyperfine qubit”, *Phys. Rev. A*, **76**(5):052314, Nov 2007, doi:10.1103/PhysRevA.76.052314.
- [94] J. D. Wong-Campos, S. A. Moses, K. G. Johnson, and C. Monroe, “Demonstration of two-atom entanglement with ultrafast optical pulses”, *Phys. Rev. Lett.*, **119**(23):230501, Dec 2017, doi:10.1103/PhysRevLett.119.230501.
- [95] J. P. Gaebler, T. R. Tan, Y. Lin, Y. Wan, R. Bowler, A. C. Keith, S. Glancy, K. Coakley, E. Knill, D. Leibfried, and D. J. Wineland, “High-fidelity universal gate set for $^9\text{Be}^+$ ion qubits”, *Phys. Rev. Lett.*, **117**(6):060505, Aug 2016, doi:10.1103/PhysRevLett.117.060505.
- [96] J. A. Sherman, M. J. Curtis, D. J. Szwer, D. T. C. Allcock, G. Imreh, D. M. Lucas, and A. M. Steane, “Experimental recovery of a qubit from partial collapse”, *Phys. Rev. Lett.*, **111**(18):180501, Oct 2013, doi:10.1103/PhysRevLett.111.180501.
- [97] T. P. Harty, M. A. Sepiol, D. T. C. Allcock, C. J. Ballance, J. E. Tarlton, and D. M. Lucas, “High-fidelity trapped-ion quantum logic us-

Bibliography

- ing near-field microwaves”, *Phys. Rev. Lett.*, **117**(14):140501, Sep 2016, doi:10.1103/PhysRevLett.117.140501.
- [98] K. K. Mehta, A. M. Eltony, C. D. Bruzewicz, I. L. Chuang, R. J. Ram, J. M. Sage, and J. Chiaverini, “Ion traps fabricated in a CMOS foundry”, *Applied Physics Letters*, **105**(4):044103, Jul 2014, doi:10.1063/1.4892061.
- [99] S. X. Wang, J. Labaziewicz, Y. Ge, R. Shewmon, and I. L. Chuang, “Demonstration of a quantum logic gate in a cryogenic surface-electrode ion trap”, *Phys. Rev. A*, **81**(6):062332, Jun 2010, doi:10.1103/PhysRevA.81.062332.
- [100] A. Keselman, Y. Glickman, N. Akerman, S. Kotler, and R. Ozeri, “High-fidelity state detection and tomography of a single-ion Zeeman qubit”, *New Journal of Physics*, **13**(7):073027, 2011.
- [101] N. Akerman, N. Navon, S. Kotler, Y. Glickman, and R. Ozeri, “Universal gate-set for trapped-ion qubits using a narrow linewidth diode laser”, *New Journal of Physics*, **17**(11):113060, 2015.
- [102] M. Madsen, W. Hensinger, D. Stick, J. Rabchuk, and C. Monroe, “Planar ion trap geometry for microfabrication”, *Applied Physics B*, **78**(5):639–651, Mar 2004, doi:10.1007/s00340-004-1414-9.
- [103] A. Drakoudis, M. Söllner, and G. Werth, “Instabilities of ion motion in a linear Paul trap”, *International Journal of Mass Spectrometry*, **252**(1):61–68, Mar 2006, doi:https://doi.org/10.1016/j.ijms.2006.02.006.
- [104] D. J. Berkeland, J. D. Miller, J. C. Bergquist, W. M. Itano, and D. J. Wineland, “Minimization of ion micromotion in a Paul trap”, *Journal of Applied Physics*, **83**(10):5025–5033, 1998, doi:10.1063/1.367318.
- [105] A. M. and S. I.A., *Handbook of Mathematical Functions With Formulas, Graphs and Mathematical Tables*. National Bureau of Standards and Applied Mathematics Series-55, 9 ed., Dec 1972.

Bibliography

- [106] R. F. Wuerker, H. Shelton, and R. V. Langmuir, “Electrodynamic containment of charged particles”, *Journal of Applied Physics*, **30**(3):342–349, Mar 1959, doi:10.1063/1.1735165.
- [107] F. W. J. Olver, A. B. Olde Daalhuis, D. W. Lozier, B. I. Schneider, R. F. Boisvert, C. W. Clark, B. R. Miller, B. V. Saunders, H. S. Cohl, and M. A. McClain eds., “NIST Digital Library of Mathematical Functions”, <https://dlmf.nist.gov/28.6>. Chapter 28.6, Release 1.1.1 of 2021-03-15, Accessed: Apr 2021.
- [108] R. B. Blakestad, *Transport of Trapped-Ion Qubits within a Scalable Quantum Processor*. PhD thesis, University of Colorado, 2009.
- [109] J. Carrico, *Applications of Inhomogeneous Oscillatory Electric Fields in Ion Physics*. Heydon & Son LTD, 3rd ed., 1972.
- [110] M. Drewsen and A. Brøner, “Harmonic linear paul trap: Stability diagram and effective potentials”, *Phys. Rev. A*, **62**(4):045401, Sep 2000, doi:10.1103/PhysRevA.62.045401.
- [111] S. Gulde, *Experimental realization of quantum gates and the Deutsch-Josza algorithm with trapped $^{40}\text{Ca}^+$ -ions*. PhD thesis, Universität Innsbruck, 2003.
- [112] M. Akhtar, *Towards Improving the Quantum Coherence in Ion Microtraps*. PhD thesis, Universtiy of Strathclyde, 2019.
- [113] D. James, “Quantum dynamics of cold trapped ions with application to quantum computation”, *Applied Physics B*, **66**(2):181–190, Feb 1998, doi:10.1007/s003400050373.
- [114] R. J. Cook, D. G. Shankland, and A. L. Wells, “Quantum theory of particle motion in a rapidly oscillating field”, *Phys. Rev. A*, **31**(2):564–567, Feb 1985, doi:10.1103/PhysRevA.31.564.
- [115] J. Eschner, G. Morigi, F. Schmidt-Kaler, and R. Blatt, “Laser cooling of trapped ions”, *J. Opt. Soc. Am. B*, **20**(5):1003–1015, May 2003, doi:10.1364/JOSAB.20.001003.

Bibliography

- [116] R. Loudon, *The Quantum Theory of Light*. Oxford University Press, 2nd ed., 1983.
- [117] S. C. Doret, J. M. Amini, K. Wright, C. Volin, T. Killian, A. Ozakin, D. Denison, H. Hayden, C.-S. Pai, R. E. Slusher, and A. H. Harter, “Controlling trapping potentials and stray electric fields in a microfabricated ion trap through design and compensation”, *New Journal of Physics*, **14**:073012, Jul 2012, doi:10.1088/1367-2630/14/7/073012.
- [118] S. X. Wang, G. Hao Low, N. S. Lachenmyer, Y. Ge, P. F. Herskind, and I. L. Chuang, “Laser-induced charging of microfabricated ion traps”, *Journal of Applied Physics*, **110**(10):104901, 2011, doi:10.1063/1.3662118.
- [119] M. A. Wilson, *Quantum State Control of a Single Trapped Strontium Ion*. PhD thesis, University of Strathclyde, 2001.
- [120] R. G. DeVoe, J. Hoffnagle, and R. G. Brewer, “Role of laser damping in trapped ion crystals”, *Phys. Rev. A*, **39**(9):4362–4365, May 1989, doi:10.1103/PhysRevA.39.4362.
- [121] M. Brownnutt, V. Letchumanan, G. Wilpers, R. Thompson, P. Gill, and A. Sinclair, “Controlled photoionization loading of $^{88}\text{Sr}^+$ for precision ion-trap experiments”, *Applied Physics B*, **87**(3):411 – 415, May 2007, doi:10.1007/s00340-007-2624-8.
- [122] C. E. Moore, *Atomic Energy Levels, Volume II*. Washington D.C.: National Bureau of Standards, 1958.
- [123] K. Vogel, T. Dinneen, A. Gallagher, and J. Hall, “Narrow line cooling of strontium to the recoil limit”, in *1998 Conference on Precision Electromagnetic Measurements Digest (Cat. No.98CH36254)*, pages 303–304, Jul 1998, doi:10.1109/CPEM.1998.699919.
- [124] S. ul Haq, S. Mahmood, N. Amin, R. Ali, and M. A. Baig, “Measurements of photoionization cross sections from the $5s5p\ ^1P_1$ and $5s6s\ ^1S_0$ states of strontium”,

Bibliography

- Journal of Physics B: Atomic, Molecular and Optical Physics*, **39**(7):1587–1596, Mar 2006, doi:10.1088/0953-4075/39/7/003.
- [125] A. Gallagher, “Oscillator strengths of Ca II, Sr II, and Ba II”, *Phys. Rev.*, **157**(1):24–30, May 1967, doi:10.1103/PhysRev.157.24.
- [126] H. S. Margolis, G. Huang, G. P. Barwood, S. N. Lea, H. A. Klein, W. R. C. Rowley, P. Gill, and R. S. Windeler, “Absolute frequency measurement of the 674-nm $^{88}\text{Sr}^+$ clock transition using a femtosecond optical frequency comb”, *Phys. Rev. A*, **67**(3):032501, Mar 2003, doi:10.1103/PhysRevA.67.032501.
- [127] S. Mannervik, J. Lidberg, L.-O. Norlin, P. Royen, A. Schmitt, W. Shi, and X. Tordoir, “Lifetime measurement of the metastable $4d^2D_{3/2}$ level in Sr^+ by optical pumping of a stored ion beam”, *Phys. Rev. Lett.*, **83**(4):698–701, Jul 1999, doi:10.1103/PhysRevLett.83.698.
- [128] C. J. Foot, *Atomic physics*. OUP Oxford, Nov 2004.
- [129] I. I. Sobelman, *Atomic Spectra and Radiative Transitions*. Springer Series on Atoms and Plasmas, 2nd ed., 1952.
- [130] A. Corney, *Atomic and Laser Spectroscopy*. OUP Oxford, 2006.
- [131] D. J. Wineland and W. M. Itano, “Laser cooling of atoms”, *Phys. Rev. A*, **20**(4):1521–1540, Oct 1979, doi:10.1103/PhysRevA.20.1521.
- [132] W. M. Itano and D. J. Wineland, “Laser cooling of ions stored in harmonic and penning traps”, *Phys. Rev. A*, **25**(1):35–54, Jan 1982, doi:10.1103/PhysRevA.25.35.
- [133] R. Blatt, G. Lafyatis, W. D. Phillips, S. Stenholm, and D. J. Wineland, “Cooling in traps”, *Physica Scripta*, **1988**(T22):216–223, Jan 1988, doi:10.1088/0031-8949/1988/t22/032.
- [134] R. H. Dicke, “The effect of collisions upon the doppler width of spectral lines”, *Phys. Rev.*, **89**(2):472–473, Jan 1953, doi:10.1103/PhysRev.89.472.

Bibliography

- [135] V. Letchumanan, *Coherent Control and Ground State Cooling of a Single $^{88}\text{Sr}^+$ Ion*. PhD thesis, Imperial College London, 2004.
- [136] F. Diedrich, J. C. Bergquist, W. M. Itano, and D. J. Wineland, “Laser cooling to the zero-point energy of motion”, *Phys. Rev. Lett.*, **62**(4):403–406, Jan 1989, doi:10.1103/PhysRevLett.62.403.
- [137] L. Deslauriers, P. C. Haljan, P. J. Lee, K.-A. Brickman, B. B. Blinov, M. J. Madsen, and C. Monroe, “Zero-point cooling and low heating of trapped $^{111}\text{Cd}^+$ ions”, *Phys. Rev. A*, **70**(4):043408, Oct 2004, doi:10.1103/PhysRevA.70.043408.
- [138] V. Letchumanan, G. Wilpers, M. Brownnutt, P. Gill, and A. G. Sinclair, “Zero-point cooling and heating-rate measurements of a single $^{88}\text{Sr}^+$ ion”, *Phys. Rev. A*, **75**(6):063425, Jun 2007, doi:10.1103/PhysRevA.75.063425.
- [139] Q. A. Turchette, Kielpinski, B. E. King, D. Leibfried, D. M. Meekhof, C. J. Myatt, M. A. Rowe, C. A. Sackett, C. S. Wood, W. M. Itano, C. Monroe, and D. J. Wineland, “Heating of trapped ions from the quantum ground state”, *Phys. Rev. A*, **61**(6):063418, May 2000, doi:10.1103/PhysRevA.61.063418.
- [140] R. W. Boyd, *Nonlinear optics*. Academic press, 2nd ed., 2003.
- [141] V. Letchumanan, P. Gill, E. Riis, and A. G. Sinclair, “Optical Ramsey spectroscopy of a single trapped $^{88}\text{Sr}^+$ ion”, *Phys. Rev. A*, **70**(3):033419, Sep 2004, doi:10.1103/PhysRevA.70.033419.
- [142] J. A. Thom, *Agile and stable optical system for high-fidelity coherent control of a single $^{88}\text{Sr}^+$ ion*. PhD thesis, University of Strathclyde, 2015.
- [143] B. K. Sahoo, M. R. Islam, B. P. Das, R. K. Chaudhuri, and D. Mukherjee, “Lifetimes of the metastable $^2D_{3/2, 5/2}$ states in Ca^+ , Sr^+ , and Ba^+ ”, *Phys. Rev. A*, **74**(6):062504, Dec 2006, doi:10.1103/PhysRevA.74.062504.
- [144] H. Häffner, C. Roos, and R. Blatt, “Quantum computing with trapped ions”, *Physics Reports*, **469**(4):155–203, Dec 2008, doi:https://doi.org/10.1016/j.physrep.2008.09.003.

Bibliography

- [145] D. Wineland, C. Monroe, W. Itano, B. King, D. Leibfried, D. Meekhof, C. Myatt, and C. Wood, “Experimental primer on the trapped ion quantum computer”, *Fortschritte der Physik*, **46**(4-5):363–390, Apr 1998, doi:10.1002/(SICI)1521-3978(199806)46:4/5<363::AID-PROP363>3.0.CO;2-4.
- [146] D. F. V. James, “Theory of heating of the quantum ground state of trapped ions”, *Phys. Rev. Lett.*, **81**(2):317–320, Jul 1998, doi:10.1103/PhysRevLett.81.317.
- [147] D. Hite, K. McKay, D. Leibfried, D. Wineland, and D. Pappas, “Measurements of trapped-ion heating rates with exchangeable surfaces in close proximity”, *MRS Advances*, **2**:2189–2197, Jan 2017, doi:https://doi.org/10.1557/adv.2017.14.
- [148] M. Akhtar, G. Wilpers, K. Choonee, E. Riis, and A. G. Sinclair, “Radio-frequency microplasmas with energies suited to in situ selective cleaning of surface adsorbates in ion microtraps”, *Journal of Physics B: Atomic, Molecular and Optical Physics*, **52**(5):055001, Feb 2019, doi:10.1088/1361-6455/aaf704.
- [149] M. Brownnutt, M. Kumph, P. Rabl, and R. Blatt, “Ion-trap measurements of electric-field noise near surfaces”, *Rev. Mod. Phys.*, **87**(4):1419–1482, Dec 2015, doi:10.1103/RevModPhys.87.1419.
- [150] M. D. Hughes, B. Lekitsch, J. A. Broersma, and W. K. Hensinger, “Microfabricated ion traps”, *Contemporary Physics*, **52**(6):505–529, 2011, doi:10.1080/00107514.2011.601918.
- [151] T. A. Savard, K. M. O’Hara, and J. E. Thomas, “Laser-noise-induced heating in far-off resonance optical traps”, *Phys. Rev. A*, **56**(2):R1095–R1098, Aug 1997, doi:10.1103/PhysRevA.56.R1095.
- [152] J. B. Johnson, “Thermal agitation of electricity in conductors”, *Phys. Rev.*, **32**(1):97–109, Jul 1928, doi:10.1103/PhysRev.32.97.
- [153] D. J. Wineland and H. G. Dehmelt, “Principles of the stored ion calorimeter”, *Journal of Applied Physics*, **46**(2):919–930, Feb 1975, doi:10.1063/1.321602.

Bibliography

- [154] G. Wilpers, P. See, P. Gill, and A. G. Sinclair, “A compact UHV package for microfabricated ion-trap arrays with direct electronic air-side access”, *Applied Physics B*, **111**(1):21–28, Apr 2013, doi:10.1007/s00340-012-5302-4.
- [155] J. D. Siverns, L. R. Simkins, S. Weidt, and W. K. Hensinger, “On the application of radio frequency voltages to ion traps via helical resonators”, *Applied Physics B*, **107**(4):921–934, Jun 2012, doi:10.1007/s00340-011-4837-0.
- [156] M. Brownnutt, *⁸⁸Sr⁺ ion trapping techniques and technologies for quantum information processing*. PhD thesis, Imperial College London, 2007.
- [157] L. Deslauriers, S. Olmschenk, D. Stick, W. K. Hensinger, J. Sterk, and C. Monroe, “Scaling and suppression of anomalous heating in ion traps”, *Phys. Rev. Lett.*, **97**(10):103007, Sep 2006, doi:10.1103/PhysRevLett.97.103007.
- [158] J. Labaziewicz, Y. Ge, P. Antohi, D. Leibbrandt, K. R. Brown, and I. L. Chuang, “Suppression of heating rates in cryogenic surface-electrode ion traps”, *Phys. Rev. Lett.*, **100**(1):013001, Jan 2008, doi:10.1103/PhysRevLett.100.013001.
- [159] J. Chiaverini and J. M. Sage, “Insensitivity of the rate of ion motional heating to trap-electrode material over a large temperature range”, *Phys. Rev. A*, **89**(1):012318, Jan 2014, doi:10.1103/PhysRevA.89.012318.
- [160] R. McConnell, C. Bruzewicz, J. Chiaverini, and J. Sage, “Reduction of trapped-ion anomalous heating by in situ surface plasma cleaning”, *Phys. Rev. A*, **92**(2):020302, Aug 2015, doi:10.1103/PhysRevA.92.020302.
- [161] P. B. Antohi, D. Schuster, G. M. Akselrod, J. Labaziewicz, Y. Ge, Z. Lin, W. S. Bakr, and I. L. Chuang, “Cryogenic ion trapping systems with surface-electrode traps”, *Review of Scientific Instruments*, **80**(1):013103, 2009, doi:10.1063/1.3058605.
- [162] G. Wilpers, P. Gill, and A. G. Sinclair, “A monolithic array of three-dimensional ion traps fabricated with semiconductor technology”, *Nature Nanotechnology*, **7**:572–576, Jul 2012, doi:10.1038/nnano.2012.126.

Bibliography

- [163] M. Kumph, C. Henkel, P. Rabl, M. Brownnutt, and R. Blatt, “Electric-field noise above a thin dielectric layer on metal electrodes”, *New Journal of Physics*, **18**(2):023020, Feb 2016, doi:10.1088/1367-2630/18/2/023020.
- [164] D. A. Hite, Y. Colombe, A. C. Wilson, K. R. Brown, U. Warring, R. Jördens, J. D. Jost, K. S. McKay, D. P. Pappas, D. Leibfried, and D. J. Wineland, “100-fold reduction of electric-field noise in an ion trap cleaned with in situ argon-ion-beam bombardment”, *Phys. Rev. Lett.*, **109**(10):103001, Sep 2012, doi:10.1103/PhysRevLett.109.103001.
- [165] A. Safavi-Naini, P. Rabl, P. F. Weck, and H. R. Sadeghpour, “Microscopic model of electric-field-noise heating in ion traps”, *Phys. Rev. A*, **84**(2):023412, Aug 2011, doi:10.1103/PhysRevA.84.023412.
- [166] D. T. C. Allcock, L. Guidoni, T. P. Harty, C. J. Ballance, M. G. Blain, A. M. Steane, and D. M. Lucas, “Reduction of heating rate in a microfabricated ion trap by pulsed-laser cleaning”, *New Journal of Physics*, **13**(12):123023, Dec 2011, doi:10.1088/1367-2630/13/12/123023.
- [167] D. T. C. Allcock, J. A. Sherman, D. N. Stacey, A. H. Burrell, M. J. Curtis, G. Imreh, N. M. Linke, D. J. Szwer, S. C. Webster, A. M. Steane, and D. M. Lucas, “Implementation of a symmetric surface-electrode ion trap with field compensation using a modulated Raman effect”, *New Journal of Physics*, **12**(5):053026, May 2010, doi:10.1088/1367-2630/12/5/053026.
- [168] C. O’Dwyer, S. J. Ingleby, I. C. Chalmers, P. F. Griffin, and E. Riis, “A feed-forward measurement scheme for periodic noise suppression in atomic magnetometry”, *Review of Scientific Instruments*, **91**(4):045103, Apr 2020, doi:10.1063/5.0002964.
- [169] B. Merkel, K. Thirumalai, J. E. Tarlton, V. M. Schäfer, C. J. Ballance, T. P. Harty, and D. M. Lucas, “Magnetic field stabilization system for atomic physics experiments”, *Review of Scientific Instruments*, **90**(4):044702, Apr 2019, doi:10.1063/1.5080093.

Bibliography

- [170] M. F. Brandl, M. W. van Mourik, L. Postler, A. Nolf, K. Lakhmanskiy, R. R. Paiva, S. Möller, N. Daniilidis, H. Häffner, V. Kaushal, T. Ruster, C. Warschburger, H. Kaufmann, U. G. Poschinger, F. Schmidt-Kaler, P. Schindler, T. Monz, and R. Blatt, “Cryogenic setup for trapped ion quantum computing”, *Review of Scientific Instruments*, **87**(11):113103, Nov 2016, doi:10.1063/1.4966970.
- [171] A. Hesse, K. Köster, J. Steiner, J. Michl, V. Vorobyov, D. Dasari, J. Wrachtrup, and F. Jendrzejewski, “Direct control of high magnetic fields for cold atom experiments based on NV centers”, *New Journal of Physics*, **23**(2):023037, Feb 2021, doi:10.1088/1367-2630/abe1e5.
- [172] J. Benhelm, G. Kirchmair, C. F. Roos, and R. Blatt, “Towards fault-tolerant quantum computing with trapped ions”, *Nature Physics*, **4**(6):463–466, Jun 2008, doi:10.1038/nphys961.
- [173] E. L. Hahn, “Spin echoes”, *Phys. Rev.*, **80**(4):580–594, Nov 1950, doi:10.1103/PhysRev.80.580.
- [174] M. J. Biercuk, H. Uys, A. P. VanDevender, N. Shiga, W. M. Itano, and J. J. Bollinger, “Optimized dynamical decoupling in a model quantum memory”, *Nature*, **458**(7241):996–1000, Apr 2009, doi:10.1038/nature07951.
- [175] J. Thom, G. Wilpers, E. Riis, and A. G. Sinclair, “Accurate and agile digital control of optical phase, amplitude and frequency for coherent atomic manipulation of atomic systems”, *Opt. Express*, **21**(16):18712–18723, Aug 2013, doi:10.1364/OE.21.018712.
- [176] F. Harris, “On the use of windows for harmonic analysis with the discrete fourier transform”, *Proceedings of the IEEE*, **66**(1):51–83, Jan 1978, doi:10.1109/PROC.1978.10837.
- [177] J. Alnis, A. Matveev, N. Kolachevsky, T. Udem, and T. W. Hänsch, “Subhertz linewidth diode lasers by stabilization to vibrationally and thermally compensated

Bibliography

- ultralow-expansion glass Fabry-Pérot cavities”, *Phys. Rev. A*, **77**(5):053809, May 2008, doi:10.1103/PhysRevA.77.053809.
- [178] T. Kessler, C. Hagemann, C. Grebing, T. Legero, U. Sterr, F. Riehle, M. J. Martin, L. Chen, and J. Ye, “A sub-40-mHz-linewidth laser based on a silicon single-crystal optical cavity”, *Nature Photonics*, **6**(10):687–692, Sep 2012, doi:10.1038/nphoton.2012.217.
- [179] E. Mount, C. Kabytayev, S. Crain, R. Harper, S.-Y. Baek, G. Vrijsen, S. T. Flammia, K. R. Brown, P. Maunz, and J. Kim, “Error compensation of single-qubit gates in a surface-electrode ion trap using composite pulses”, *Phys. Rev. A*, **92**(6):060301, Dec 2015, doi:10.1103/PhysRevA.92.060301.
- [180] F. Tricot, D. H. Phung, M. Lours, S. Guérandel, and E. de Clercq, “Power stabilization of a diode laser with an acousto-optic modulator”, *Review of Scientific Instruments*, **89**(11):113112, Nov 2018, doi:10.1063/1.5046852.
- [181] J. Thom, B. Yuen, G. Wilpers, E. Riis, and A. G. Sinclair, “Intensity stabilisation of optical pulse sequences for coherent control of laser-driven qubits”, *Applied Physics B*, **124**(5):90, May 2018, doi:10.1007/s00340-018-6955-4.
- [182] K. Mølmer and A. Sørensen, “Multiparticle entanglement of hot trapped ions”, *Phys. Rev. Lett.*, **82**(9):1835–1838, Mar 1999, doi:10.1103/PhysRevLett.82.1835.
- [183] A. Sørensen and K. Mølmer, “Entanglement and quantum computation with ions in thermal motion”, *Phys. Rev. A*, **62**(2):022311, Jul 2000, doi:10.1103/PhysRevA.62.022311.
- [184] A. Sørensen and K. Mølmer, “Quantum computation with ions in thermal motion”, *Phys. Rev. Lett.*, **82**(9):1971–1974, Mar 1999, doi:10.1103/PhysRevLett.82.1971.
- [185] P. See, G. Wilpers, P. Gill, and A. G. Sinclair, “Fabrication of a monolithic array of three dimensional Si-based ion traps”, *Journal of Microelectromechanical Systems*, **22**(5):1180–1189, Oct 2013, doi:10.1109/JMEMS.2013.2262573.

Bibliography

- [186] M. Brownnutt, G. Wilpers, P. Gill, R. C. Thompson, and A. G. Sinclair, “Monolithic microfabricated ion trap chip design for scaleable quantum processors”, *New Journal of Physics*, **8**(10):232, Oct 2006, doi:10.1088/1367-2630/8/10/232.
- [187] M. T. Baig, M. Johanning, A. Wiese, S. Heidbrink, M. Ziolkowski, and C. Wunderlich, “A scalable, fast, and multichannel arbitrary waveform generator”, *Review of Scientific Instruments*, **84**(12):124701, 2013, doi:10.1063/1.4832042.
- [188] T. Hansch and B. Couillaud, “Laser frequency stabilization by polarization spectroscopy of a reflecting reference cavity”, *Optics Communications*, **35**(3):441–444, Sep 1980, doi:https://doi.org/10.1016/0030-4018(80)90069-3.
- [189] A. Madej, L. Marmet, and J. Bernard, “Rb atomic absorption line reference for single Sr+ laser cooling systems”, *Applied Physics B*, **67**(2)(1432-0649):229–234, Aug 1998, doi:10.1007/s003400050498.
- [190] R. W. P. Drever, J. L. Hall, F. V. Kowalski, J. Hough, G. M. Ford, A. J. Munley, and H. Ward, “Laser phase and frequency stabilization using an optical resonator”, *Applied Physics B*, **31**(2):97–105, Jun 1983, doi:10.1007/BF00702605.
- [191] M. J. Ehrlich, L. C. Phillips, and J. W. Wagner, “Voltage-controlled acousto-optic phase shifter”, *Review of Scientific Instruments*, **59**(11):2390–2392, Aug 1988, doi:10.1063/1.1139915.
- [192] L. A. M. Johnson, P. Gill, and H. S. Margolis, “Evaluating the performance of the NPL femtosecond frequency combs: agreement at the 10^{-21} level”, *Metrologia*, **52**(1):62–71, Jan 2015, doi:10.1088/0026-1394/52/1/62.
- [193] R. G. DeVoe and C. Kurtsiefer, “Experimental study of anomalous heating and trap instabilities in a microscopic ^{137}Ba ion trap”, *Phys. Rev. A*, **65**(6):063407, Jun 2002, doi:10.1103/PhysRevA.65.063407.
- [194] J. T. Höffges, H. W. Baldauf, W. Lange, and H. Walther, “Heterodyne measurement of the resonance fluorescence of a single ion”, *Journal of Modern Optics*, **44**(10):1999–2010, Jun 1997, doi:10.1080/09500349708231861.

Bibliography

- [195] G. Barwood, P. Gill, G. Huang, H. Klein, and W. Rowley, “Sub-kHz “clock” transition linewidths in a cold trapped $^{88}\text{Sr}^+$ ion in low magnetic fields using 1092-nm polarisation switching”, *Optics Communications*, **151**(1):50–55, 1998, doi:[https://doi.org/10.1016/S0030-4018\(97\)00743-8](https://doi.org/10.1016/S0030-4018(97)00743-8).
- [196] T. Hasegawa and T. Shimizu, “Limiting temperature of sympathetically cooled ions in a radio-frequency trap”, *Phys. Rev. A*, **67**(1):013408, Jan 2003, doi:[10.1103/PhysRevA.67.013408](https://doi.org/10.1103/PhysRevA.67.013408).
- [197] M. Guggemos, D. Heinrich, O. A. Herrera-Sancho, R. Blatt, and C. F. Roos, “Sympathetic cooling and detection of a hot trapped ion by a cold one”, *New Journal of Physics*, **17**(10):103001, sep 2015, doi:[10.1088/1367-2630/17/10/103001](https://doi.org/10.1088/1367-2630/17/10/103001).
- [198] J. Labaziewicz, *High fidelity quantum gates with ions in cryogenic microfabricated ion traps*. PhD thesis, Massachusetts Institute of Technology, 2008.
- [199] T. Navickas, *Towards high-fidelity microwave driven multi-qubit gates on micro-fabricated surface ion traps*. PhD thesis, University of Sussex, Sep 2018.
- [200] S. Hong, M. Lee, Y. D. Kwon, D. Cho, and T. Kim, “Experimental methods for trapping ions using microfabricated surface ion traps”, *Journal of Visualized Experiments*, **126**:56060, August 2017, doi:[10.3791/56060](https://doi.org/10.3791/56060).
- [201] R. Sterling, H. Rattanasonti, S. Weidt, K. Lake, P. Srinivasan, S. C. Webster, M. Kraft, and W. K. Hensinger, “Fabrication and operation of a two-dimensional ion-trap lattice on a high-voltage microchip”, *Nature Communications*, **5**:3637, April 2014, doi:[10.1038/ncomms4637](https://doi.org/10.1038/ncomms4637).
- [202] R. C. Sterling, M. D. Hughes, C. J. Mellor, and W. K. Hensinger, “Increased surface flashover voltage in microfabricated devices”, *Applied Physics Letters*, **103**(14):143504, Oct 2013, doi:[10.1063/1.4824012](https://doi.org/10.1063/1.4824012).

Bibliography

- [203] R. C. Gonzalez and R. E. Woods, *Digital Image Processing*. Prentice Hall, Upper Saddle River, New Jersey, 07458, United States of America: Prentice Hall, 2nd ed., 2002.
- [204] M. S. Nixon and A. S. Aguado, *Feature Extraction and Image Processing*. Linacre House, Jordan Hill, Oxford, OX2 8DP, United Kingdom: Academic Press, Elsevier, 2 ed., 2008.
- [205] M. Paine, S. Gabriel, C. Schabmueller, and A. Evans, “Realisation of very high voltage electrode–nozzle systems for MEMS”, *Sensors and Actuators A: Physical*, **114**(1):112 – 117, August 2004, doi:<https://doi.org/10.1016/j.sna.2004.02.013>.
- [206] Y. Zhang, O. Dary, and A. Shashurin, “Low energy surface flashover for initiation of electric propulsion devices”, *Plasma Research Express*, **1**(1):015010, jan 2019, doi:[10.1088/2516-1067/aaf659](https://doi.org/10.1088/2516-1067/aaf659).
- [207] P. Carazzetti and H. R. Shea, “Electrical breakdown at low pressure for planar microelectromechanical systems with 10- to 500- μm gaps”, *Journal of Micro/Nanolithography, MEMS, and MOEMS*, **8**(3):1 – 9, July 2009, doi:[10.1117/1.3152368](https://doi.org/10.1117/1.3152368).
- [208] Y. Wu, Q. Ye, X. Li, and D. Tan, “Classification of dielectric barrier discharges using digital image processing technology”, *IEEE Transactions on Plasma Science*, **40**(5):1371–1379, 2012.
- [209] Y. Liu, B. X. Du, and D. Du, “Pattern analysis on dielectric breakdown characteristics of biodegradable polyethylene film under nonuniform electric field”, *International Transactions on Electrical Energy Systems*, **23**(1):72–82, october 2011, doi:[10.1002/etep.645](https://doi.org/10.1002/etep.645).
- [210] G. Meng, Y. Cheng, X. Gao, K. Wang, C. Dong, and B. Zhu, “In-situ optical observation of dynamic breakdown process across microgaps at atmospheric pressure”, *IEEE Transactions on Dielectrics and Electrical Insulation*, **25**(4):1502–1507, august 2018.

Bibliography

- [211] H. Kirkici, M. Serkan, and K. Koppisetty, “Nano/micro dielectric surface flashover in partial vacuum”, *IEEE Transactions on Dielectrics and Electrical Insulation*, **14**(4):790–795, August 2007.
- [212] B. Du and Y. Liu, “Pattern analysis of discharge characteristics for hydrophobicity evaluation of polymer insulator”, *IEEE Transactions on Dielectrics and Electrical Insulation*, **18**(1):114–121, Jan 2011, doi:10.1109/TDEI.2011.5704500.
- [213] P. Kwee, C. Bogan, K. Danzmann, M. Frede, H. Kim, P. King, J. Pödl, O. Puncken, R. L. Savage, F. Seifert, P. Wessels, L. Winkelmann, and B. Willke, “Stabilized high-power laser system for the gravitational wave detector advanced LIGO”, *Opt. Express*, **20**(10):10617–10634, Apr 2012, doi:10.1364/OE.20.010617.
- [214] M. J. V. Streeter, S. J. D. Dann, J. D. E. Scott, C. D. Baird, C. D. Murphy, S. Eardley, R. A. Smith, S. Rozario, J.-N. Gruse, S. P. D. Mangles, Z. Najmudin, S. Tata, M. Krishnamurthy, S. V. Rahul, D. Hazra, P. Pourmoussavi, J. Osterhoff, J. Hah, N. Bourgeois, C. Thornton, C. D. Gregory, C. J. Hooker, O. Chekhlov, S. J. Hawkes, B. Parry, V. A. Marshall, Y. Tang, E. Springate, P. P. Rajeev, A. G. R. Thomas, and D. R. Symes, “Temporal feedback control of high-intensity laser pulses to optimize ultrafast heating of atomic clusters”, *Applied Physics Letters*, **112**(24):244101, Jun 2018, doi:10.1063/1.5027297.
- [215] S. A. King, R. M. Godun, S. A. Webster, H. S. Margolis, L. A. M. Johnson, K. Szymaniec, P. E. G. Baird, and P. Gill, “Absolute frequency measurement of the $^2S_{1/2} - ^2F_{7/2}$ electric octupole transition in a single ion of $^{171}\text{Yb}^+$ with 10^{-15} fractional uncertainty”, *New Journal of Physics*, **14**(1):013045, Jan 2012, doi:10.1088/1367-2630/14/1/013045.
- [216] M. A. Nielsen and I. L. Chuang, *Quantum Computation and Quantum Information*. Cambridge University Press, 10th anniversary ed., Dec 2010.
- [217] E. Knill, “Quantum computing with realistically noisy devices”, *Nature*, **434**(7029):39–44, Mar 2005, doi:10.1038/nature03350.

Bibliography

- [218] D. Bacon, “Operator quantum error-correcting subsystems for self-correcting quantum memories”, *Phys. Rev. A*, **73**(1):012340, Jan 2006, doi:10.1103/PhysRevA.73.012340.
- [219] P. Aliferis and A. W. Cross, “Subsystem fault tolerance with the Bacon-Shor code”, *Phys. Rev. Lett.*, **98**(22):220502, May 2007, doi:10.1103/PhysRevLett.98.220502.
- [220] E. W. Iverson and M. Feng, “Transistor laser power stabilization using direct collector current feedback control”, *IEEE Photonics Technology Letters*, **24**(1):4–6, Jan 2012, doi:10.1109/LPT.2011.2171679.
- [221] M. Ohtsu, “Frequency stabilization in semiconductor lasers”, *Optical and Quantum Electronics*, **20**(4):283–300, jul 1988, doi:10.1007/BF00620246.
- [222] Y. Zhao, J. Zhang, J. Stuhler, G. Schuricht, F. Lison, Z. Lu, and L. Wang, “Sub-Hertz frequency stabilization of a commercial diode laser”, *Optics Communications*, **283**(23):4696–4700, 2010, doi:https://doi.org/10.1016/j.optcom.2010.06.079.
- [223] E. A. Donley, T. P. Heavner, F. Levi, M. O. Tataw, and S. R. Jefferts, “Double-pass acousto-optic modulator system”, *Review of Scientific Instruments*, **76**(6):063112, Jun 2005, doi:10.1063/1.1930095.
- [224] M. Gunawardena, P. W. Hess, J. Strait, and P. K. Majumder, “A frequency stabilization technique for diode lasers based on frequency-shifted beams from an acousto-optic modulator”, *Review of Scientific Instruments*, **79**(10):103110, 2008, doi:10.1063/1.3006386.
- [225] D. Świerad, S. Häfner, S. Vogt, B. Venon, D. Holleville, S. Bize, A. Kulosa, S. Bode, Y. Singh, K. Bongs, E. Maria Rasel, J. Lodewyck, R. Le Targat, C. Lisdat, and U. Sterr, “Ultra-stable clock laser system development towards space applications”, *Scientific Reports*, **6**(1):33973, Sep 2016, doi:10.1038/srep33973.

Bibliography

- [226] W. Riley and D. J. Howe, *Handbook of Frequency Stability Analysis*. NIST SP, Jul 2008. Special Publication (NIST SP) - 1065.
- [227] D. R. Leibbrandt, R. J. Clark, J. Labaziewicz, P. Antohi, W. Bakr, K. R. Brown, and I. L. Chuang, “Laser ablation loading of a surface-electrode ion trap”, *Phys. Rev. A*, **76**(5):055403, Nov 2007, doi:10.1103/PhysRevA.76.055403.
- [228] G. Vrijsen, Y. Aikyo, R. F. Spivey, I. V. Inlek, and J. Kim, “Efficient isotope-selective pulsed laser ablation loading of $^{174}\text{Yb}^+$ ions in a surface electrode trap”, *Opt. Express*, **27**(23):33907–33914, Nov 2019, doi:10.1364/OE.27.033907.
- [229] M. Day, *Microfabricated Optics for Quantum Control of Trapped Ions*. PhD thesis, University of Bristol, Nov 2018.
- [230] R. Blatt and D. Wineland, “Entangled states of trapped atomic ions”, *Nature*, **453**(7198):1008 – 1015, Jun 2008, doi:10.1038/nature07125.
- [231] V. Giovannetti, S. Lloyd, and L. Maccone, “Quantum-enhanced measurements: Beating the standard quantum limit”, *Science*, **306**(5700):1330–1336, 2004, doi:10.1126/science.1104149.
- [232] C. F. Roos, M. Chwalla, K. Kim, M. Riebe, and R. Blatt, “Designer atoms’ for quantum metrology”, *Nature*, **443**:316–319, Sep 2006, doi:https://doi.org/10.1038/nature05101.
- [233] P. Harris. Private communications.
- [234] Y. Pawitan, *In all likelihood: statistical modelling and inference using likelihood*. Oxford University Press, 2001.
- [235] O. M. Brastein, B. Lie, C. F. Pfeiffer, and N.-O. Skeie, “Estimating uncertainty of model parameters obtained using numerical optimisation”, *Modeling, Identification and Control*, **40**(4):213–243, 2019, doi:10.4173/mic.2019.4.3.
- [236] W. M. Itano, J. C. Bergquist, J. J. Bollinger, J. M. Gilligan, D. J. Heinzen, F. L. Moore, M. G. Raizen, and D. J. Wineland, “Quantum projection noise:

Bibliography

- Population fluctuations in two-level systems”, *Phys. Rev. A*, **47**(5):3554–3570, May 1993, doi:10.1103/PhysRevA.47.3554.
- [237] N. F. Ramsey, “A molecular beam resonance method with separated oscillating fields”, *Phys. Rev.*, **78**(6):695–699, Jun 1950, doi:10.1103/PhysRev.78.695.
- [238] N. F. Ramsey, “Experiments with separated oscillatory fields and hydrogen masers”, *Rev. Mod. Phys.*, **62**(3):541–552, Jul 1990, doi:10.1103/RevModPhys.62.541.
- [239] G. Kirchmair, J. Benhelm, F. Zähringer, R. Gerritsma, C. F. Roos, and R. Blatt, “Deterministic entanglement of ions in thermal states of motion”, *New Journal of Physics*, **11**(2):023002, Feb 2009, doi:10.1088/1367-2630/11/2/023002.
- [240] J. Randall, A. M. Lawrence, S. C. Webster, S. Weidt, N. V. Vitanov, and W. K. Hensinger, “Generation of high-fidelity quantum control methods for multilevel systems”, *Phys. Rev. A*, **98**(4):043414, Oct 2018, doi:10.1103/PhysRevA.98.043414.
- [241] C. F. Roos, “Ion trap quantum gates with amplitude-modulated laser beams”, *New Journal of Physics*, **10**(1):013002, Jan 2008, doi:10.1088/1367-2630/10/1/013002.
- [242] K. G. Johnson, J. D. Wong-Campos, A. Restelli, K. A. Landsman, B. Neyenhuis, J. Mizrahi, and C. Monroe, “Active stabilization of ion trap radiofrequency potentials”, *Review of Scientific Instruments*, **87**(5):053110, May 2016, doi:10.1063/1.4948734.

Bibliography